北京大学

博士研究生学位论文

题目：CMS 实验上双希格斯粒子寻找与探测器升级

姓　　名：章立诚

学　　号：1901110115

院　　系：物理学院

专　　业：粒子物理与原子核物理

研究方向：高能物理实验

导　　师：班勇教授，孙小虎助理教授

Tabarelli De Fatis Tommaso 教授

☑ 学术学位　　☐ 专业学位

二〇二四 年 六 月

版权声明

摘要

粒子物理的标准模型（Standard Model，SM）是一种可重整化的量子场论，为描述亚原子尺度上的现象提供了一个全面系统的理论框架。它统一地描述了强相互作用、弱相互作用和电磁相互作用，揭示了它们的基本原理，实现这一统一的数学基础是其拉格朗日量在 $SU(3) \times SU(2) \times U(1)$ 规范群下的局部规范不变性。在标准模型框架下，基本粒子包括了构成物质的费米子（自旋为 $\frac{1}{2}$）和传递相互作用的玻色子（自旋为 1）。实验上已经发现了标准模型所预言的 12 种费米子，包括 6 种轻子和 6 种夸克。这些费米子被分类为 3 代，每一代都包含有两种电荷为 $+\frac{2}{3}$ 和 $-\frac{1}{3}$ 的夸克，以及两种电荷分别为 -1 和 0 的轻子。基本粒子中还有 4 种规范玻色子作为传递相互作用的媒介，传递强相互作用（胶子）、电磁相互作用（光子）和弱相互作用（W/Z 玻色子）。此外，还有一个在 2012 年被发现的希格斯玻色子，其发现宣告了标准模所预言的所有基本粒子均被发现，具有重大的物理意义。另外，希格斯玻色子所引入的规则是希格斯机制（Brout-Engler-Higgs Mechanism, BEH mechanism），是整个标准模型框架的重要组成部分，该机制为玻色子及费米子质量起源提供了一种理论上的解决方案，对我们理解电弱对称性自发破缺和宇宙的起源起至关重要的作用。因此，深入研究并且测量希格斯玻色子相关物理，成为了进一步完善和理解标准模型所需的重要实验工作。通过计算 BEH 机制的拉格朗日量，我们发现重要的两个自由参数是真空势能期望值（Vacuum Expectation Value，VEV）和希格斯玻色子质量，他们也成为实验测量希格斯玻色子性质的重要对象。希格斯玻色子质量从粒子被发现时开始就不断地通过逐渐积累的实验数据被更为精确地测量，而 VEV 更加复杂，它直接关联于希格斯粒子的自相互作用或者说自耦合强度，实验上测量希格斯自耦合强度对我们进一步验证标准模型至关重要。

本论文介绍的物理实验，基于紧凑型缪子螺线管（Compact Muon Solenoid，CMS）实验，该实验是坐落于欧洲核子研究中心（Conseil européen pour la Recherche nucléaire, CERN）的大型强子对撞机（Large Hadron Collider，LHC）上进行的众多实验中的一个，其主要任务是追踪难以捉摸的希格斯物理，并驾驭 TeV 能级物理的复杂性。

在 LHC 上直接测量希格斯玻色子自耦合强度只能通过测量双希格斯粒子（HH）和三希格斯粒子（HHH）的产生过程，而在目前的对撞质心系能量下，只有双希格斯粒子过程能积累可供研究的统计量。当前在对撞机实验中寻找 HH 并限制相关耦合系数允许范围的主要挑战是 HH 过程在当前对撞的质心系能量下只有很小的产生截面。对此，物理学家主要可以从三个不同方面提高对撞机实验的物理结果：

1. 提高探测器直接测量的物理对象（例如轻子、喷注、丢失横动量等）等的标定

效率，进而提升希格斯粒子的重建效率。

2. 优化对撞事例分析策略与数据分析技术以提高信号与背景比，例如采用有效的事例分类优化流程以及合理应用机器学习的技术。

3. 在实验上通过提高亮度累积更多实验数据，升级探测器以提高测量精度和维度。

双希格斯粒子在 LHC 上有 5 种产生模式，按照产生截面由大到小分别是胶子对融合产生（ggF），矢量玻色子融合产生（VBF），矢量玻色子联合产生（VHH），顶夸克对联合产生（ttHH）和单顶夸克联合产生（tjHH）。其中 ggF 模式产生截面大，被广泛使用于 HH 物理的研究，VBF 模式包含希格斯粒子与矢量玻色子相互作用的顶点，也在实验中被测量，用以限制希格斯粒子与矢量玻色子相互作用的强度参数。本论文的主要工作是对 VHH 模式进行寻找，该模式是双希格斯粒子与一个矢量玻色子 (Z/W) 联合产生的过程（VHH 过程），和 VBF 模式一样，VHH 过程同样涉及了希格斯粒子与矢量玻色子的耦合顶点，另外由于矢量玻色子的轻子道衰变，让我们可以分别对 Z 玻色子和 W 玻色子进行独立的研究。此外，虽然相对 ggF 和 VBF，VHH 模式的产生截面较小，但同样由于其矢量玻色子末态的存在，不同的产生过程干涉加强，使得 VHH 产生截面在归一化的自耦合系数为正的情况下迅速增大，可能可以与其他 HH 产生模式一起，更好地限制参数的允许范围。

本文介绍首次在 CMS 实验中寻找 VHH 过程的工作，分析使用完整的 LHC 第二期运行数据（于 2016-2018 年期间收集，质心能量为 13TeV）进行研究。为了增加统计量，该分析包括了矢量玻色子所有的轻子和强子衰变通道，同时聚焦于 HH 衰变到 4b 末态以获得最大的衰变分支比。如前文提到，矢量玻色子的轻子衰变特性使我们能够分别从统计上限制 HHZZ 和 HHWW 顶点的耦合强度。这项复杂的分析还独立研究了高横动量区域内的物理性能，由于统计量的限制，结果只覆盖了在矢量玻色子单轻子和中微子衰变通道中的高横动量区域。**本分析的亮点有**二，首先是精细的事例分类，尽可能使被选择条件淘汰的事例得到运用，使得其在信号区域内的本底建模、结果拟合中限制主要本底涨落等方面发挥重要的作用，前者压低了结果计算中的统计学误差，后者压低了有关本底涨落的系统误差，而这两个误差恰好是全部误差中最重要的组成部分。第二个亮点是机器学习技术的运用，我们使用了增强决策树方法（Boosted Decision Trees，BDTs）和基于 ResNet 的深度神经网络方法，分别在数据分类、本底建模和信号提取三个关键步骤中依次发挥了重大的作用。

本工作发现 VHH 信号的多个动力学分布对耦合系数 κ_λ（HHH 耦合强度参数）、κ_{VV}（HHVV 耦合强度参数）的变化非常敏感，因此采用了 BDT 方法对信号与本底事例进行分类，建立了 κ_λ 富集区域和 κ_{VV} 富集区。在两个区域中独立进行信噪比优化，目的是提高在整个 kappa 参数扫描范围中的敏感性，对最终结果有明显的提升。

另外，BDT 模型和 DNN 模型在不同的矢量玻色子衰变道中进行独立的训练和优化，以用于信号提取。在最后的结果拟合中，我们没有传统地采用 HH 分析中使用的例如 HH 质量等动力学变量，而是直接使用了机器学习输出值进行联合拟合，在折算得分偏向于信号的区域内，获得了更大的信噪比，从而进一步提升了物理结果。

值得一提的是，在本底建模过程中，研究遇到了统计量不足的困境，在高横动量区域以及 Z 玻色子双轻子道的信号区域无法通过蒙特卡洛方法模拟的事例进行有效的本底建模。对此，我们创新性地使用了 BDT 赋权的方法，使用 BDT 模型提取信号区域本底和未通过筛选的本底之间动力学指标分布的差异，进而量化该差异，给不满足信号选择标准的事件加权，使其在动力学指标分布和事例产量上都非常接近信号区的本底，用以在信号区域内为本底过程建模。这种方法使我们可以获得更加稳定的本底模型，同时极大地减小统计误差。

实验观测到（预期的）在 95% 置信水平的 VHH 产生截面设上限为 294（124）倍标准模型预测值。此外，在假设 κ_{VV} 等于 1 的情况下，对 κ_λ 的范围进行了限制，反之亦然。这些耦合强度系数在 95% 置信区间观测的（预期的）允许范围分别为-37.7 < κ_λ < 37.2（-30.1 < κ_λ < 28.9）和-12.2 < κ_{VV} < 13.5（-7.2 < κ_{VV} < 8.9）。另外，还在 CMS 首次对 κ_{WW} 和 κ_{ZZ} 进行了独立的扫描和约束，得到了-17.4 < κ_{ZZ} < 18.5（-10.5 < κ_{ZZ} < 11.6）和-14.0 < κ_{WW} < 15.4（-10.2 < κ_{WW} < 11.6）的允许区间。

前文提到了提高物理结果水平的三种方法，我们想进一步探索机器学习在粒子物理研究中的重要性。我们通过对 HH 衰变到 $b\bar{b}\tau^+\tau^-$ 和 $b\bar{b}\mu^+\mu^-$ 末态物理过程进行前瞻性研究，以探索机器学习算法在物理对象标定和事例分类、信号提取中的重要作用。

首先，在基于 CMS 实验在为 2018 年数据产生的蒙特卡洛模拟样本的 $b\bar{b}\tau^+\tau^-$ **高横动量区域预研**中，我们通过采用最先进的 ParticleNet 双陶子大半径喷注鉴别器与之前的单陶子重建鉴别方法进行比较。**非常大地提升了含有双陶子大喷注的标定效率**。我们发现，新鉴别器的使用可以使我们在高横动量区域专注于大半径喷注的重建和分类，而不需要考虑更加复杂的物理对象，非常大的减轻了数据分析的压力。此外，更重要的是，由于 ParticleNet 为所有的喷注计算了其为双陶子喷注的可能性，从而不需要考虑对单陶子重建的效率，尤其是在高横动量区域，同一个喷注内的两个陶子方向非常一致，以致于它们的子结构互相纠缠到了一起，单陶子重建和鉴别效率会急剧下降，从而直接浪费了可能的希格斯衰变到陶子对的候选喷注。根据我们的预研，总体上，通过使用 ParticleNet，我们至少可以增加 20% 的统计数据，同时，这增加的 20% 统计量并不会影响鉴别器鉴别信号和本底的能力。我们在原有的统计量内，将 ParticeNet 方法和传统方法进行了直接的对比，发现我们可以挖掘出在同等信号接收效率的情况下，将本底信号压低能力提高一个数量级以上的潜力。为我们后续使用第二期运行或者第

三期运行的 CMS 数据进行物理分析提供了动力，打下了扎实的基础。

在 HH 衰变到 $b\bar{b}\mu^+\mu^-$ 末态过程的唯象学研究中，我们面向的是高亮度大型强子对撞机（High-Luminosity LHC, HL-LHC）场景，证明了机器学习算法的运用可以显著提升物理结果。CMS 和 ATLAS 基于第二期运行的数据，分别观测到希格斯粒子衰变到缪子对信号关于无信号假设的超出。随着探测器的升级计划，缪子探测分辨率会进一步增加，这些都为我们将来研究 $b\bar{b}\mu^+\mu^-$ 末态提供了动力。本研究的核心是使用基于传统的线性筛选的分析方法和采用增强决策树的机器学习分析进行分类和优化的分析方法进行结果比较。我们针对 ggF 和 VBF 的 HH 产生过程，使用动力学指标进行了基本的事例分类，在子类中分别进行优化，最终联合拟合得到结果。使用传统分析方法，我们精心挑选了重要的动力学指标，并且对筛选条件进行了细致的优化，尽可能提高最终信号区域内的信噪比。而在基于 BDT 的分析方法中，我们聚集了高敏感度的指标，进行了仔细的训练和优化，最终使用 BDT 输出值进行了结果拟合。在 95% 置信水平上，我们使用基于传统（增强决策树）方法对胶子-胶子融合产生的双希格斯玻色子过程的预期产生截面上限计算结果为 47（28）倍的标准模型截面预测值。在未来对撞机 3000 fb^1 的积分亮度下，使用传统（增强决策树）方法计算了 95% 置信水平下的耦合常数范围为-13.8 < κ_λ < 19.1（-10.0 < κ_λ < 15.5）。我们可以看到在 HL-LHC 场景下，该衰变通道相对于具有更大分支比的衰变通道不具有很强的竞争力，但是也可以作为一个重要的补充对耦合系数进行限制。更重要的是，我们在该研究中，看到了简单的机器学习算法例如 BDT 一方面可以非常大地降低数据分析的复杂度，实现在更高维空间内的数据分类，另一方面可以提高信号区域内的信噪比，从而显著提高物理结果，为我们在今后的物理分析工作中提供有效的指导。

提升物理分析性能的第三个方法是在更高的亮度下累积更多实验数据，同时升级探测器以提高测量精度和维度。由于大型强子对撞机复杂的结构和极高的运行成本，这样的机会并不常见。但是在未来的运行中，现有 LHC 将会提高亮度和对撞质心系能量，升级为上文提到的 HL-LHC，以极大地增加数据的统计量，将现有的大约 150fb^{-1} 积分亮度提升至 3000fb^{-1}，稀有信号的寻找和物理量的精确测量将会大受裨益。于此同时，例如 CMS 和 ATLAS 等实验的探测器也必须为此进行升级，以应对高亮度 LHC 运行带来的挑战。挑战主要具体为以下的两个方面：

1. 高辐射剂量的运行环境，高亮度直接带来高辐照强度，升级后的探测器必须可以在强的辐射环境中稳定长期的运行，而不是迅速地老化和损坏，从而影响物理结果的精度甚至大量损失事例接收度。

2. 更高的事例堆积率，高亮度的运行会将事例的堆积率提高 5 至 10 倍，如果探测系统无法对小范围内的大量对撞顶点进行区分，那么重建效率将大打折扣，更高的

亮度也只能是得不偿失。因此有必要引入新型探测器，这些探测器具有很短的死时间，同时可以帮助减小堆积效应带来的影响。

我们在本论文中介绍了端盖缪子探测系统的升级，将通过增加新的基于气体电子倍增器 (Gaseous Electron Multiplier，GEM) 的探测器进行升级，一方面提升探测器的质量，另一方面提高缪子探测系统在端盖的覆盖率，以提高缪子触发的接受度和效率。

论文介绍了大面积三层 GEM 探测器的组装和质量控制程序的确立和在组装中心搭建平台的细节，包含了 GEM 探测器的组成，组装中心需要进行的组装流程，以及包括腔体气密性测试、高压与噪声测试以及有效增益测试的具体实现，其中的一个模型 (GE1/1) 已经被安装在 CMS 上并且在第三期运行期间进行了安装并完成了部分测试。

此外，为了进一步研究 GEM 探测器的原理，为未来的优化和升级作指导，我们对多层 GEM 探测器进行了模拟研究，探索了与当前设计的三层 GEM 探测器具有相同外尺寸的四层 GEM 探测器应用在 CMS 实验的可能性，研究在同等条件下，四层 GEM 探测器能否保持相同的物理性能，但是降低运行时的高压数值，这可以进一步减小打火率和空间电荷效应，同时，四层 GEM 的结构相比三层 GEM，可以更大的压低离子回流效应对结果造成的干扰。作为模拟研究的衍生结果，我们在模拟的过程中发现了当前的气体探测器模拟软件在 CPU 占用和时长上的低效率，创新性地提出了分步模拟法的概念，使用物理模型和数学函数对探测器运行的各个阶段进行分步模拟，从而在更短的时间和资源消耗的情况下，得到相同精度的模拟结果。

论文还介绍了桶部时间探测器（MIP Timing Detector, MTD），为了缓解事例堆积问题，未来 CMS 将在桶部和端盖安装新的时间探测层。额外的时间测量维度可以显著减少高堆积率的影响，提高重建效率，另外，该探测系统所提供的物理对象的时间信息，将带来额外的物理分析潜力，对于 HH 分析以及与时间密不可分的长寿命粒子寻找等都有巨大的提升。

桶部 MTD 主要采用闪烁晶体和硅光电倍增器的组合，从而实现能量沉积到光信号，再转化为电信号实现测量的过程，期待实现 30 至 60ps 的高时间分辨率。探测器基本结构的组装测量已经具有一定的基础，对于基本单位的束流测试非常重要，对我们为优化探测器性能作调整或者为未来的软件设计作指导都必不可少。论文介绍了对于单个粒子同时穿过多个闪烁晶体并沉积能量的现象的研究，由于 MTD 探测器覆盖角分布大，因此对撞顶点飞出的粒子可能以不同的角度穿过时间层，在多根闪烁晶体中沉积能量的现象不可避免，而之前的重建模式并不能很好地重建这部分事例。因此我们研究并提出了重建的流程和方法，能够针对这一部分事例获得更好的时间重建，提升时间分辨率。

关键词：标准模型, CMS 实验, 双希格斯玻色子，缪子探测器，时间探测器。

Ricerca di coppie di bosoni di Higgs e aggiornamento del rilevatore CMS

Licheng Zhang (Fisica delle particelle)
Diretto da Prof. Ban Yong, Prof. Sun Xiaohu, Prof. Tabarelli De Fatis Tommaso

RIASSUNTO

Il Modello Standard della Fisica delle Particelle (SM) è una teoria quantistica dei campi rinormalizzabile che fornisce un quadro comprensivo per descrivere i fenomeni che si verificano a scale subatomiche. Come pezzo fondamentale dell'intero mosaico, il meccanismo di Brout-Englert-Higgs (BEH) funge da soluzione per generare le masse dei bosoni di gauge e per chiarire le origini delle masse dei fermioni. Questo meccanismo ha le sue radici nel concetto di rottura spontanea di simmetria. La chiave per comprendere meglio il meccanismo e i concetti correlati è misurare l'autoaccoppiamento del bosone di Higgs e gli accoppiamenti con altre particelle fondamentali. L'unica prova diretta dell'autoaccoppiamento del bosone di Higgs al Large Hadron Collider (LHC) è la misurazione dei processi di produzione di Higgs doppio o triplo, con vertici di interazione caratterizzati da accoppiamenti che sono normalizzati da un quadro kappa negli esperimenti.

La principale sfida degli esperimenti attuali nella ricerca di coppie di bosoni di Higgs (HH) e nel vincolare gli accoppiamenti è rappresentata dalle piccole sezioni d'urto dei processi di produzione HH. I fisici possono potenziare le prestazioni fisiche dagli esperimenti al collider in tre diversi aspetti:

1. Migliorare l'efficienza di etichettatura degli oggetti fisici.

2. Migliorare la strategia di analisi a livello di evento per aumentare il rapporto segnale/rumore.

3. Accumulare dati aggiuntivi e aggiornamenti del rilevatore per migliorare la precisione e l'accettazione.

Il processo di produzione di coppie di bosoni di Higgs (HH) associato a un bosone vettore (Z/W) è stato studiato per la prima volta nell'esperimento CMS con i dati completi di Run-2 (raccolti nel 2016-2018 a un'energia nel centro di massa di 13 TeV). L'analisi include tutti i canali di decadimento del bosone vettore e si concentra sul decadimento di HH nello stato

finale 4b. Il decadimento leptonico del bosone vettore ci permette di vincolare separatamente l'accoppiamento HHZZ e HHWW. Questa analisi comprensiva incorpora anche la topologia potenziata, impiegando Alberi Decisionali Potenziati (BDTs) per stabilire una regione arricchita da κ_λ (modificatore di accoppiamento HHH) e una regione arricchita da κ_{VV} (modificatore di accoppiamento HHVV). L'ottimizzazione dei processi successivi in parallelo mira a migliorare la sensibilità su un ampio intervallo di parametri kappa. Tecniche di apprendimento automatico dedicate sono utilizzate per l'estrazione del segnale. Gli BDT potenziano il processo di modellazione dello sfondo attraverso la rivalutazione degli eventi che non soddisfano i criteri di selezione. Questo metodo favorisce modelli di sfondo più robusti con una ridotta incertezza statistica. Riportiamo un limite superiore osservato (atteso) al livello di confidenza del 95% sulla sezione d'urto della produzione di VHH fissata a 294 (124) volte la previsione del Modello Standard. Inoltre, vengono imposti vincoli su κ_λ, assumendo che κ_{VV} sia uguale a 1, e viceversa. Gli intervalli di confidenza del 95% osservati (attesi) per questi modificatori di accoppiamento sono delineati come -37.7 < κ_λ < 37.2 (-30.1 < κ_λ < 28.9) e -12.2 < κ_{VV} < 13.5 (-7.2 < κ_{VV} < 8.9), rispettivamente.

Esploriamo ulteriormente il potenziale dell'adattamento degli algoritmi di apprendimento automatico mediante uno studio prospettico sul decadimento di HH nei stati finali $b\bar{b}\tau^+\tau^-$ e $b\bar{b}\mu^+\mu^-$. Nello studio potenziato $b\bar{b}\tau^+\tau^-$, basato sui campioni MC del CMS del 2018, potremmo ottenere almeno il 20% in più di statistica e un potere di soppressione dello sfondo nettamente superiore adattando un tagger di-tau potenziato all'avanguardia ParticleNet. Nello studio $b\bar{b}\mu^+\mu^-$, vengono eseguite un'analisi basata su tagli e un'analisi di apprendimento automatico utilizzando BDT, con categorizzazioni e ottimizzazioni a seconda delle variazioni di questi accoppiamenti. Le sensibilità attese sono estratte con diverse luminosità integrate assunte fino alle corse complete ad alta luminosità dell'LHC. Il limite superiore atteso al livello di confidenza del 95% sulla produzione di coppie di bosoni di Higgs è calcolato come 47 (28) volte la sezione d'urto del Modello Standard utilizzando il metodo basato su tagli (BDT) per la produzione di fusione gluon-gluon. I vincoli attesi sugli accoppiamenti al livello di confidenza del 95% sono calcolati essere -13.8 < κ_λ < 19.1 (-10.0 < κ_λ < 15.5) utilizzando il metodo basato su tagli (BDT), rispettivamente, assumendo una luminosità integrata di 3000 fb^1.

Nell'ultima ma importante parte, introduciamo il significativo progetto di aggiornamento dei sistemi di sottodetettori del CMS, affrontando la sfida dell'ambiente operativo dell'LHC ad alta luminosità, ovvero l'alta dose di radiazione che potrebbe influenzare la durata dei rilevatori e l'alto tasso di pile-up che potrebbe influenzare la precisione della ricostruzione e delle

misurazioni. Il sistema Muon Endcap sarà aggiornato aggiungendo una nuova camera basata su moltiplicatore di elettroni gassosi (GEM) per migliorare l'accettazione e l'efficienza dei trigger. Le procedure di assemblaggio e controllo di qualità sono stabilite e uno dei modelli (GE1/1) è già stato installato e testato durante la Run-3. Per la mitigazione del pile-up, verrà assemblato un nuovo strato temporale sia nel barile che nell'endcap. La dimensione temporale aggiuntiva può diminuire significativamente l'impatto dall'alto pile-up e apportare ulteriore potenziale fisico. Test sui fasci e algoritmi di ricostruzione dedicati sono in fase di sviluppo per affrontare lo scenario pratico futuro.

PAROLE CHIAVE: Modello Standard, CMS, Coppia di Bosoni di Higgs, Rilevatore di Muoni, Rilevatore Temporale.

Search for Higgs Boson Pair and Detector Upgrade on the CMS Experiment

Licheng Zhang (Particle Physics)
Directed by Prof. Ban Yong, Prof. Sun Xiaohu, Prof. Tabarelli De Fatis Tommaso

ABSTRACT

The Standard Model of Particle Physics (SM) is a renormalizable quantum field theory that provides a comprehensive framework for describing phenomena occurring at subatomic scales. As a very important piece of the whole puzzle, the Brout-Engler-Higgs (BEH) mechanism serves as a solution for generating the masses of gauge bosons and elucidating the origins of fermion masses. This mechanism is rooted in the concept of spontaneous symmetry breaking. The key to understand the mechanism and the concepts better is to measure the higgs boson self-coupling and couplings with other fundamental particles. The only direct prob of the Higgs boson self-coupling at the LHC is the measurement of double or triple Higgs production processes, with interaction vertices characterized by couplings that are normalized by a kappa framework in experiments.

The main challenge of the current experiments in searching Higgs boson pair (HH) and constrain the couplings is the small cross sections of the HH production processes. Physicists can enhance the physics performance from collider experiments in three different aspects:

1. Enhance the physics object tagging efficiency.

2. Enhance the event-level analysis strategy to increase the signal-to-background ratio.

3.Accumulate additional data and detector upgrades to enhance precision and acceptance.

The process of HH production associated with one vector boson (Z/W) is first time studied at CMS experiment with the full Run-2 (collected 2016-2018 at a center-of-mass energy of 13 TeV) data. The analysis includes all the vector boson decay channels and focuses on the HH decay to 4b final state. The leptonic decay of the vector boson allow us to constrain the HHZZ and HHWW coupling separately. This comprehensive analysis also incorporates the boosted topology, employing Boosted Decision Trees (BDTs) to establish a κ_λ (HHH coupling modifier) enriched region and a κ_{VV} (HHVV coupling modifier) enriched region. Optimization of the subsequent processes in parallel aims to enhance sensitivity across a wide range of

kappa parameters. Dedicated machine learning techniques are used for the signal extraction. BDTs enhance background modeling process by re-weighting events that not meeting selection criteria. This method fosters more robust background models with diminished statistical uncertainty. We report an observed (expected) upper limit at 95% confidence level of VHH production cross section setting at 294 (124) times the SM prediction. Additionally, constraints are imposed on the κ_λ, under the assumption that κ_{VV} equals 1, and conversely. The observed (expected) 95% confidence intervals for the Higgs self-coupling modifier is delineated as -37.7 < κ_λ < 37.2 (-30.1 < κ_λ < 28.9).

We further explore the power of the adaption of the machine learning algorithms by doing prospective study in the HH decay into $b\bar{b}\tau^+\tau^-$ and $b\bar{b}\mu^+\mu^-$ final states. In the $b\bar{b}\tau^+\tau^-$ boosted study, based on CMS 2018 MC samples, we could gain at least 20% statistics and magnitudes higher background suppress power by adapting a state-of-the-art ParticleNet boosted di-tau tagger. In the $b\bar{b}\mu^+\mu^-$ study, a cut-based analysis and a machine-learning analysis using BDT are performed with categorizations and optimizations depending on the variations of these couplings. The expected sensitivities are extracted with different integrated luminosity assumed up to the full high luminosity LHC runs. The expected upper limit at 95% confidence level on the Higgs boson pair production is calculated as 47 (28) times the Standard Model cross section using the cut-based (BDT) method for the gluon-gluon fusion production. The expected constraints on the couplings at 95% confidence level are calculated to be -13.8 < κ_λ < 19.1 (-10.0 < κ_λ < 15.5) using the cut-based (BDT) method, respectively, assuming an integrated luminosity of 3000 fb^1.

In the last but important part, **we introduce the important upgrade project of the CMS sub-detector systems** facing the challenge of the high-luminosity LHC operation environment, namely the high radiation dose that could effect the life time of the detectors and the high pile up rate that could effect the precision of the reconstruction and measurements. The Endcap Muon system will be upgraded by adding new gaseous electron multiplier (GEM) based chamber to improve the acceptance and the efficient of the triggers. The assembly and quality control procedures are settled and one of the model (GE1/1) has already been installed and tested during Run-3. For pile up mitigation, a new timing layer will be assembled at both barrel and endcap. The extra time dimension can significantly decrease the impact from the high pile up and bring extra physics potential. Test beam and dedicate reconstruction algorithms are under developing to deal with the future practical scenario.

KEY WORDS: Standard Model, CMS, Higgs Boson Pair, Muon detector, Timing detector.

Contents

Chapter 1 Standard Model and Higgs Boson Pair Production

In the annals of history, humanity has harbored an enduring and innate conviction regarding the cosmic mechanisms, firmly convinced that beneath the bewildering array of phenomena in the universe resides an elegant and profoundly symmetrical order. This order can be distilled and extrapolated through human intellect, enabling us to anticipate events in our immediate environment by drawing upon these foundational principles.

Fueled by this conviction, Kepler authored celestial laws, Newton formulated the three foundational laws of motion, and Maxwell ushered symmetrical principles into the domain of electromagnetic interactions. As human science and technology have progressed, our ability to observe an ever-expanding panorama of cosmic phenomena has grown, encompassing the extremes of the macroscopic and the intricacies of the microscopic realms. Along this journey, the theories we employ to encapsulate the universe have evolved into intricate constructs, yet they retain remarkable conciseness when juxtaposed with the natural phenomena they elucidate.

1.1 The Standard Model for Particle Physics

The Standard Model of Particle Physics (SM) is a renormalizable quantum field theory that provides a comprehensive framework for describing phenomena occurring at subatomic scales. It offers a unified depiction of the strong, weak, and electromagnetic forces, incorporating a minimal scalar sector responsible for both the spontaneous breaking of the electroweak symmetry and the generation of fermion masses.

The mathematical foundation of the Standard Model relies on the local gauge invariance of its Lagrangian under the gauge group $\mathrm{SU}(3)_C \times \mathrm{SU}(2)_L \times \mathrm{U}(1)_Y$, elucidating the underlying principles governing the strong, weak, and electromagnetic interactions.

The fundamental particles included in the Standard Model are fermions with spin $\frac{1}{2}$ that describe matter and bosons with spin -1 that describe the interactions. As shown in Figure 1.1, experiments since J.J. Thomson have witnessed the existence of 12 fermions, which includes 6 'leptons' and 6 'quarks'. The fermions are organized into 3 'generations', with each containing 2 quarks with electric charges $+\frac{2}{3}$ and $-\frac{1}{3}$ and two leptons with electric charges -1 and 0. Additionally, there are 4 gauge bosons that act as mediators, facilitating the transmission of forces between fermions to realize the strong force (gluons) or the electromagnetic force

(photons) and the weak force (W/Z bosons). Apart from these, there exists a boson called the Higgs boson, which we will focus on in the following sections.

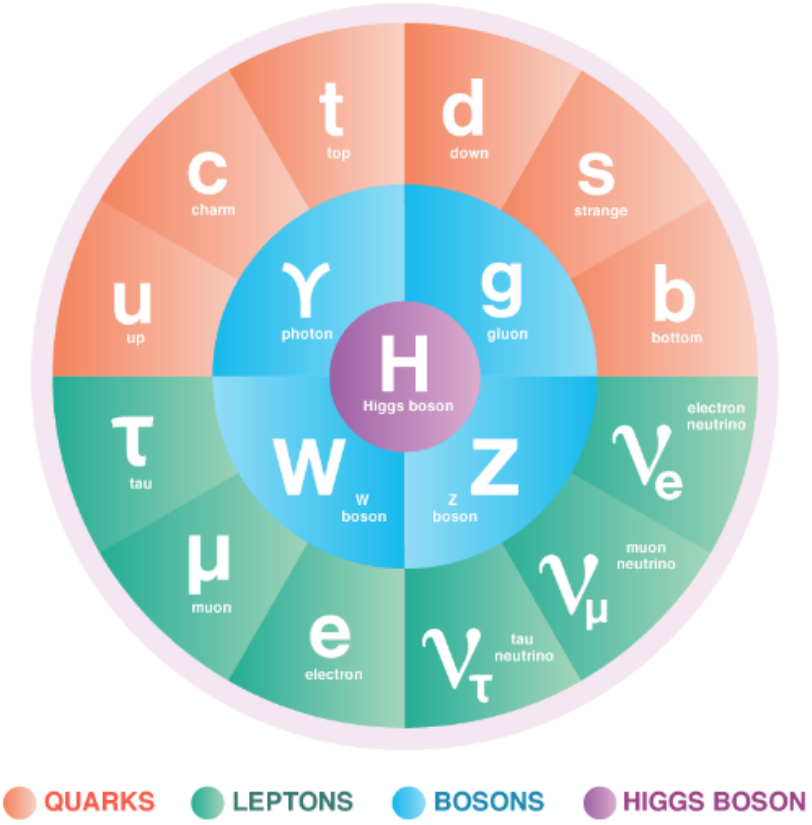

Figure 1.1 The Standard Model includes the matter particles (quarks and leptons), the force carrying particles (bosons), and the Higgs boson.[1]

Strong interaction and gluon

$SU(3)_C$ constitutes the initial component of the symmetrical gauge group, providing the local gauge invariance upon which Quantum Chromodynamics (QCD) is founded. The free-field Dirac Lagrangian density of a massless spin $-\frac{1}{2}$ fermion could be written as the follow:

$$\mathcal{L} = \bar{\psi}(x)(i\gamma^\mu \partial_\mu)\psi(x) \tag{1.1}$$

, in which $\psi(x)$ is the fermion field and γ^μ are the Dirac matrices. Then the fermion field transforms in the presence of a mass term:

$$\psi(x) \rightarrow e^{ig\frac{\lambda^a}{2}\theta_a(x)}\psi(x) \tag{1.2}$$

, where the $\frac{\lambda^a}{2}$ are the 8 Gell-Mann matrices that generate the group. In order to make the Lagrangian in 1.1 to be invariant through the transformation is to redefine the ∂_μ to be a covariant

derivatives:

$$D_\mu = \partial_\mu - igA^a_\mu(x)\frac{\lambda^a}{2} \tag{1.3}$$

, where the gauge vector fields $A^a_\mu(x)$ correspond to the eight **gluons** as the strong force carrier and they transform as:

$$A^a_\mu \rightarrow A^a_\mu + \partial_\mu\theta^a + g_s f^{abc}A^c_\mu\theta^c \tag{1.4}$$

$$\text{with} \quad [\frac{\lambda^a}{2}, \frac{\lambda^b}{2}] = if^{abc}\frac{\lambda^c}{2}, \quad a, b, c = 1, \ldots, 8 \tag{1.5}$$

In this equation, the f^{abc} are the structure constant of the gauge group. Substituting these terms into the Dirac Lagrangian, we get the Lagrangian density:

$$\mathcal{L}_{\text{QCD}} = -\frac{1}{4}F^{\mu\nu}_a F^a_{\mu\nu} + \bar{\psi}(i\gamma^\mu\partial_\mu)\psi - g_s\bar{\psi}\gamma^\mu\frac{\lambda^a}{2}\psi A^a_\mu, \tag{1.6}$$

where the field strength tensor is

$$F^a_{\mu\nu} = \partial_\mu A^a_\nu - \partial_\nu A^a_\mu + g_s f^{abc}A^b_\mu A^c_\nu \tag{1.7}$$

The first term of 1.6 represents the kinetic term for the gluon fields. It is notable for its non-linearity in terms of the gluon potential, giving rise to trilinear and quadrilinear terms within the Lagrangian, which correspond to the self-interactions of gluons. The coupling constant g_s determines the strength of the interaction and is frequently redefined as $\alpha_s = \frac{g_s^2}{4\pi}$. The mandate for local gauge invariance necessitated the introduction of gauge bosons, specifically the **gluons**, to describe their interactions with the fermion fields, namely the **quarks**. The selection of the $\text{SU}(3)_C$ group implies the existence of eight generators, corresponding to the eight gluons. Mathematically, these gluons are described by the adjoint representation of the group (**8**) and are distinguished by the color charges they carry. In contrast, quarks and anti-quarks are described by the simplest non-trivial representations of $\text{SU}(3)_C$, denoted as **3** and $\overline{\mathbf{3}}$, respectively. This elucidates the origin of the three distinct color quantum numbers associated with quarks.

Quarks

QCD is named due to the concept of "colors" mentioned earlier, which are associated with different quarks. However, quarks are influenced by all three fundamental forces.

The first family of quarks consists of the up (u) and down (d) quarks, both with masses

on the order of a few MeV. The up quark carries a positive electric charge of +2/3, while the down quark bears a negative electric charge of −1/3. As the lightest quarks, they are stable and constitute the fundamental building blocks of ordinary matter. In the second family, we find the charm (c) and strange (s) quarks, with masses approximately around 1.28 GeV and 95 MeV, respectively. Lastly, the third family comprises the top (t) and bottom (b) quarks, with masses of about 173 and 4.2 GeV, respectively.

Due to the color confinement properties of QCD, quarks do not exist in isolated, free states but can only be observed experimentally when they are in bound states. In collider experiments, the detections primarily involve "mesons," composed of a quark-antiquark pair, or "baryons," composed of three quarks. Stable examples of the latter are the proton and neutron, which make up ordinary matter. Mesons and baryons are collectively referred to as hadrons. The process by which hadrons are created from a single quark produced in a collider experiment is a complex phenomenon known as "hadronization." Due to the timescales involved, which are linked to QCD energy scales and on the order of 10^{-24} seconds, the hard scattering and hadronization processes can be treated separately, thanks to a factorization of their effects. An exception to this pattern is the top quark, whose extraordinarily short lifetime (approximately 0.5×10^{-24} seconds) results in its decay before bound states can form.

Quark flavor conservation holds true in electromagnetic and strong interactions, but it does not apply in weak interactions. This is because the quark mass eigenstates do not align with the weak interaction eigenstates. The mixing of these eigenstates is mathematically described by the Cabibbo–Kobayashi–Maskawa (CKM) matrix.

Electroweak interaction, photon and vector bosons

The $SU(2)_L \times U(1)_Y$ gauge group collectively describes the electromagnetic and weak interactions, and is thus commonly referred to as the electroweak (EW) group. The electromagnetic interaction is succinctly represented by the Quantum Electrodynamics (QED) Lagrangian, which remains invariant under the local $U(1)_{\text{em}}$ symmetry:

$$\mathcal{L}_{\text{QED}} = \bar{\psi}(i\gamma^\mu \partial_\mu - m)\psi - \frac{1}{4}F^{\mu\nu}F_{\mu\nu}. \tag{1.8}$$

In a manner analogous to the QCD Lagrangian, a kinetic term, proportional to $F^{\mu\nu}$, describes the propagation of the gauge boson (in this case, the **photon**). The covariant derivative, denoted as ($D^\mu = \partial^\mu - ieA^\mu$), introduces the interaction term:

$$\mathcal{L}^{\text{int}}_{\text{QED}} = e\bar{\psi}\gamma^\mu \psi A_\mu. \tag{1.9}$$

A theoretical description of the weak interaction poses a greater challenge due to the need to accommodate experimental evidence of parity violation. This challenge is addressed by assigning distinct interaction terms to left- and right-handed fermion fields. Theoretically, this is accomplished by utilizing the gamma matrix $\gamma^5 = i\gamma^0\gamma^1\gamma^2\gamma^3$ to define left and right chirality projection operators:

$$P_L = \frac{1-\gamma^5}{2}; \quad P_R = \frac{1+\gamma^5}{2}. \tag{1.10}$$

Ultimately, the weak interaction is characterized by two quantum numbers: weak isospin (T_3) and hypercharge (Y). The weak isospin (T_3) quantum number is associated with the non-abelian group $SU(2)_L$ and corresponds to one of the group generators. More precisely, the group possesses three generators, denoted as $T_i = \frac{\sigma_i}{2}$, where σ_i represents the Pauli matrices. Gauge invariance is reflected in the presence of three gauge fields W_i^μ within the $SU(2)_L$ group. Left-handed fermions are described by a doublet, while right-handed particles are $SU(2)_L$ singlets that do not interact with the W_i^μ fields. Both left- and right-handed fields are derived from the chirality projection operators defined earlier:

$$\Psi_L = P_L\psi = \frac{1-\gamma^5}{2}\begin{pmatrix}\psi\\ \psi'\end{pmatrix} = \begin{pmatrix}\psi_L\\ \psi'_L\end{pmatrix}, \tag{1.11}$$

$$\psi_R = P_R\psi = \frac{1+\gamma^5}{2}\psi, \tag{1.12}$$

$$\psi'_R = \frac{1+\gamma^5}{2}\psi', \tag{1.13}$$

where the ψ and ψ' fields can represent either the neutrino and charged lepton fields or the up- and down-type quark fields. The weak hypercharge (Y) quantum number is associated with the $U(1)_Y$ abelian group, which has a single generator $Y/2$. The presence of the B_μ gauge field reflects the $U(1)_Y$ gauge invariance. The Gell-Mann-Nishijima formula establishes a relationship between weak hypercharge, isospin, and the electric charge associated with the $U(1)_{\text{em}}$ group:

$$Q = T_3 + \frac{Y}{2}. \tag{1.14}$$

Hence, the Electroweak (EW) Lagrangian density can be expressed as:

$$\mathcal{L} = \bar{\Psi}_L(i\gamma^\mu D_\mu)\Psi_L + \bar{\psi}_R(i\gamma^\mu D_\mu)\psi_R + \bar{\psi}'_R(i\gamma^\mu D_\mu)\psi'_R, \tag{1.15}$$

In order to maintain $SU(2)_L$ invariance, the mass terms have been omitted. Following the same methodology as applied in the QED and QCD Lagrangians, the inclusion of the covariant derivative (D^μ) guarantees a local symmetry under $SU(2)_L \times U(1)_Y$:

$$D^\mu = \partial^\mu - ig\frac{\vec{\tau}}{2} \cdot \vec{W}^\mu - ig'\frac{Y}{2}B^\mu, \tag{1.16}$$

with g and g' governing the strength of these interactions.

Equation 1.15 can be reformulated by isolating the kinetic term from those accountable for the charged(C) and neutral(N) currents:

$$\mathcal{L} = \mathcal{L}_{\text{kin}} + \mathcal{L}_{\text{CC}} + \mathcal{L}_{\text{NC}}, \tag{1.17}$$

where:

$$\begin{aligned}
\mathcal{L}_{\text{kin}} &= \bar{\Psi}_L(i\gamma^\mu\partial_\mu)\Psi_L + \bar{\psi}_R(i\gamma^\mu\partial_\mu)\psi_R + \bar{\psi}'_R(i\gamma^\mu\partial_\mu)\psi'_R, \\
\mathcal{L}_{\text{CC}} &= \frac{g}{\sqrt{2}}W^+_\mu\bar{\Psi}_L\gamma^\mu\sigma^+\Psi_L + \frac{g}{\sqrt{2}}W^-_\mu\bar{\Psi}_L\gamma^\mu\sigma^-\Psi_L \\
&= \frac{g}{\sqrt{2}}W^+(\bar{\psi}_L\gamma^\mu\psi'_L) + \frac{g}{\sqrt{2}}W^-(\bar{\psi'}_L\gamma^\mu\psi_L), \\
\mathcal{L}_{NC} &= -\frac{g}{\sqrt{2}}W^3_\mu\left[\bar{\psi}_L\gamma^\mu\psi_L - \bar{\psi}'_L\gamma^\mu\psi'_L\right] \\
&\quad + \frac{g'}{\sqrt{2}}B_\mu\left[Y(\bar{\psi}_L\gamma^\mu\psi_L + \bar{\psi}'_L\gamma^\mu\psi'_L) + Y\bar{\psi}_R\gamma^\mu\psi_R + Y\bar{\psi}'_R\gamma^\mu\psi'_R\right]
\end{aligned}$$

where the $W^\pm$ **charged bosons** can be represented as linear combinations of the W_1 and W_2 gauge bosons:

$$W^\pm_\mu = \frac{1}{\sqrt{2}}(W^1_\mu \mp iW^2_\mu), \tag{1.18}$$

The Pauli's matrices:

$$\sigma^\pm = \frac{1}{\sqrt{2}}(\sigma^1 \pm i\sigma^2). \tag{1.19}$$

The neutral current Lagrangian is formulated as a function of W^3_μ and B_μ, neither of which can be initially interpreted as a physical neutral boson. To address this, Z_μ and A_μ fields are

introduced, directly representing the **neutral Z boson** and the **photon**. This is achieved through a Weinberg's angle (θ_W) rotation of the W^3_μ and B_μ fields:

$$\begin{pmatrix} A_\mu \\ Z_\mu \end{pmatrix} = \begin{pmatrix} \cos\theta_w & \sin\theta_w \\ -\sin\theta_w & \cos\theta_w \end{pmatrix} \begin{pmatrix} B_\mu \\ W_\mu \end{pmatrix}, \tag{1.20}$$

This enables us to reformulate the neutral current Lagrangian of Eq. 1.17 by segregating the terms related to the photon and the Z boson fields:

$$\mathcal{L}^Z_{NC} = \bar{\psi}_L \gamma^\mu Z_\mu \left(g \frac{\sigma_3}{2} \cos\theta_\omega - g' \frac{Y}{2} \sin\theta_\omega \right) \psi_L \tag{1.21}$$

$$\mathcal{L}^\gamma_{NC} = \bar{\psi}_L \gamma^\mu A_\mu \left(g \frac{\sigma_3}{2} \sin\theta_\omega + g' \frac{Y}{2} \cos\theta_\omega \right) \psi_L, \tag{1.22}$$

Here, the two neutral currents associated with the Z_μ and A_μ fields are explicitly expressed as functions of weak isospin ($T_3 = \frac{\sigma_3}{2}$) and hypercharge (Y). Furthermore, in accordance with the Gell-Mann-Nishijima formula, the following relation is valid:

$$e = g' \sin\theta_\omega = g \cos\theta_\omega, \tag{1.23}$$

It relates the value of the fundamental electric charge e to the coupling constants g and g', as well as to the Weinberg's angle θ_ω.

To complete the description of the Electroweak Lagrangian, one must introduce a kinetic term for the gauge fields:

$$\mathcal{L}_{EW} = \bar{\Psi}_L (i\gamma^\mu D_\mu) \Psi_L + \bar{\psi}_R (i\gamma^\mu D_\mu) \psi_R + \bar{\psi}'_R (i\gamma^\mu D_\mu) \psi'_R - \frac{1}{4} W^{\mu\nu}_i W^i_{\mu\nu} - \frac{1}{4} B^{\mu\nu} B_{\mu\nu}, \tag{1.24}$$

with the fields strength tensors $W^i_{\mu\nu}$ and $B_{\mu\nu}$ defined as:

$$B_{\mu\nu} = \partial_\mu B_\nu - \partial_\nu B_\mu, \quad W^i_{\mu\nu} = \partial_\mu W^i_\nu - \partial_\nu W^i_\mu + g \epsilon^{ijk} W^j_\mu W^k_\nu, \tag{1.25}$$

where ϵ^{ijk} represents the Levi-Civita tensor. This additional kinetic term leads to the self-interaction of the gauge bosons, predicting the existence of trilinear (ZW^+W^-, γW^+W^-) and quadrilinear (ZZW^+W^-, $\gamma\gamma W^+W^-$, $Z\gamma W^+W^-$, $W^+W^-W^+W^-$) self-couplings involving the Z, $W^\pm$, and γ bosons.

Leptons

Leptons do not possess color charge and interact solely through the electromagnetic and

weak forces that introduced above. The charged leptons of the three families are denoted as follows: the electron (e), muon (μ), and tau lepton (τ). The electron is stable, being the lightest lepton with a mass of 511 keV. The muon has a mass of 105.7 MeV and a lifetime of 2.2 μs, which is long enough to consider it stable for LHC experiments, given the detector size and typical muon momenta. On the other hand, the tau lepton has a mass of 1.8 GeV and a very short lifetime of 2.9×10^{-13} s, making it observable only through its decay products. Notably, the tau is the only lepton with sufficient mass to undergo semi-leptonic decay.

Each lepton is associated with a neutrino, denoted as ν_e, ν_μ, and ν_τ, respectively. Neutrinos are electrically neutral, and they interact with matter solely through the weak force, making them undetectable directly at collider experiments. While their masses remain poorly known, evidence from flavor oscillations confirms that they are not zero. The mixing of weak and mass eigenstates is described by the Pontecorvo–Maki–Nakagawa–Sakata (PMNS) matrix.

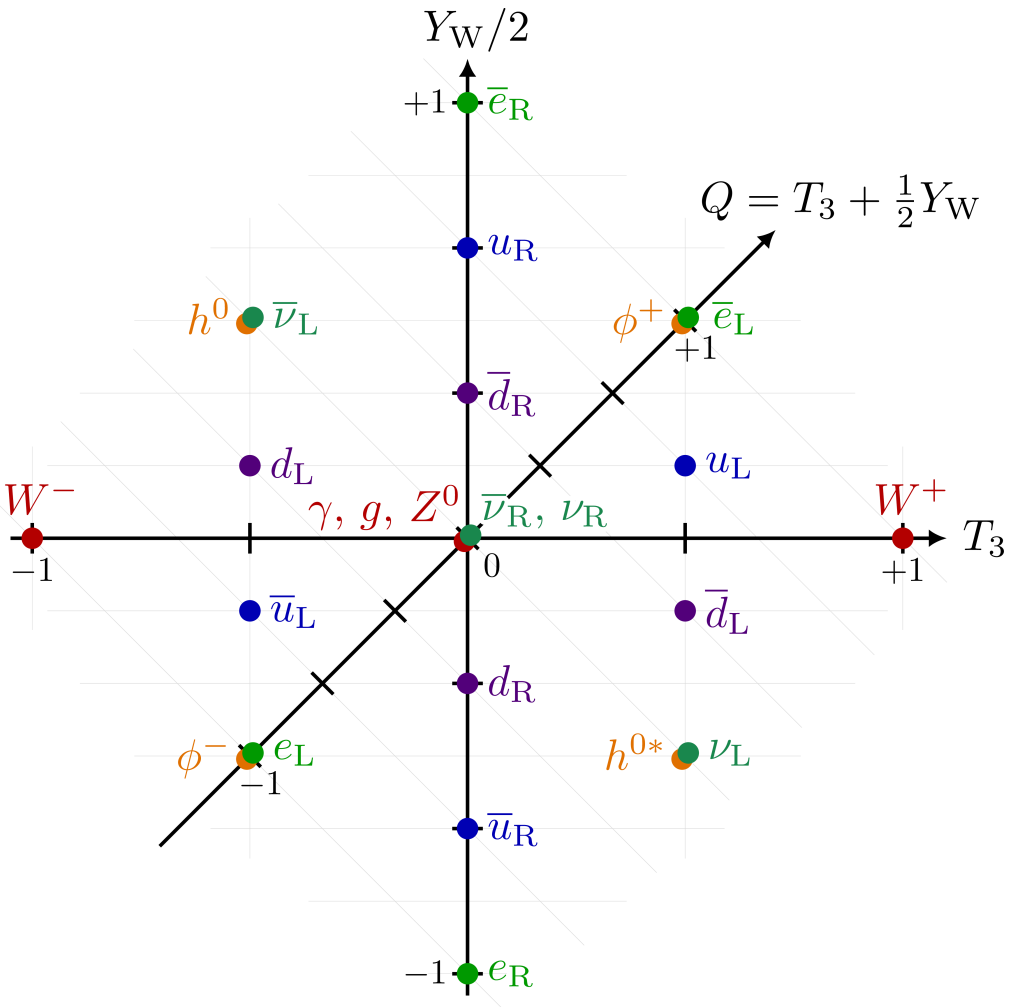

Figure 1.2 The summary plot of all SM field.[2]

Hence, the electroweak and strong interactions can be represented by a Lagrangian comprising two terms, $\mathcal{L}_{QCD}$ and $\mathcal{L}_{EW}$, resulting in a gauge theory with $SU(3)_C \times SU(2)_L \times U(1)_Y$ symmetry. However, neither $\mathcal{L}_{QCD}$ nor $\mathcal{L}_{EW}$ contains explicit mass terms for either the gauge or the fermion fields, as such terms would break gauge invariance. While this is consistent with the observed masslessness of photons and gluons, it does not account for the existence of massive gauge bosons, such as the $W^{\pm}$ and Z, and massive fermions.

To preserve the gauge invariance of the theory while accounting for the experimental presence of massive gauge bosons and fermions, the electroweak symmetry must undergo breaking. In the Standard Model, this phenomenon occurs through the Brout-Englert-Higgs (BEH) mechanism, which will be discussed in detail in the following section.

1.2 The Brout-Englert-Higgs mechanism and the Higgs Boson

The Brout-Engler-Higgs (BEH) mechanism, independently proposed in 1964 by physicists Englert and Brout[3], Higgs[4], and also by Guralnik, Hagen, and Kibble[5], serves as a solution for generating the masses of gauge bosons and elucidating the origins of fermion masses. This mechanism is rooted in the concept of spontaneous symmetry breaking, a phenomenon frequently observed in nature when the individual ground states of a system fail to conform to the symmetries inherent to the system itself.

A familiar illustration of this concept is a pencil positioned vertically on a table. In this scenario, the gravitational force exhibits rotational symmetry around the vertical axis. However, the actual ground state of the pencil is one where it lies horizontally on the table, pointing in a specific direction. This ground state doesn't adhere to the symmetry of the gravitational force, resulting in what is termed "spontaneous symmetry breaking." This term is coined "spontaneous" because the chosen ground state is just one among many possible ground states. These states are interconnected through the original symmetry of the system, which remains "hidden" among these diverse options.

In the BEH mechanism, spontaneous symmetry breaking is achieved by introducing a complex scalar doublet of fields:

$$\Phi = \begin{pmatrix} \phi_+ \\ \phi_0 \end{pmatrix} \tag{1.26}$$

It's worth noting that the field must be scalar to maintain spatial isotropy, ensuring that the expectation value in the vacuum is frame-independent. Additionally, to achieve spatial homogeneity, the expectation value in the vacuum must remain constant. The field carries a

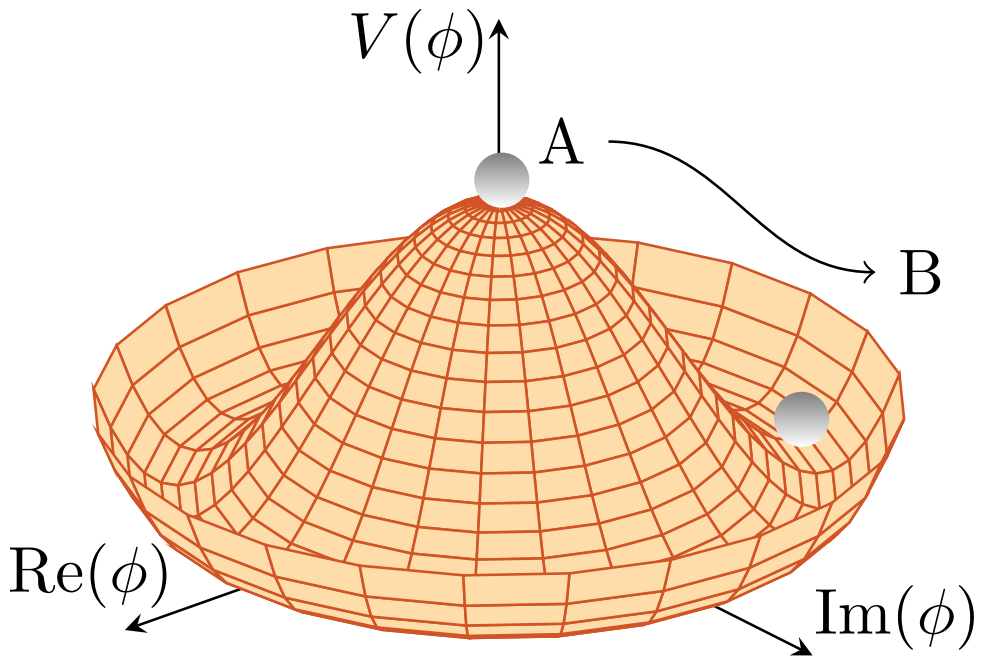

Figure 1.3 Schematic illustration of the Higgs potential $V(\phi)$

hypercharge $Y_\Phi = 1$, and thus, its covariant derivative is expressed as follows:

$$D_\mu = \partial_\mu - igW_\mu^i \frac{\sigma_i}{2} - \frac{1}{2}ig'B_\mu \tag{1.27}$$

The BEH lagrangian can consequently be written as:

$$\mathcal{L}_{BEH} = (D_\mu \Phi)^\dagger (D^\mu \Phi) - V(\Phi^\dagger \Phi) \tag{1.28}$$

where the potential $V(\Phi^\dagger\Phi)$ is defined as:

$$V(\Phi^\dagger\Phi) = -\mu^2\Phi^\dagger\Phi + \lambda(\Phi^\dagger\Phi)^2 \quad \text{with} \quad \mu^2, \lambda > 0 \tag{1.29}$$

The functional form of the potential is illustrated in Fig. 1.3, resembling a 'Mexican Hat' shape, where the states naturally gravitate toward the minimum points of the potential field which are expressed in the following equations.

All the doublets that satisfy the condition:

$$|\Phi^\dagger\Phi| = \frac{\mu^2}{2\lambda} \equiv \frac{v^2}{2} \tag{1.30}$$

The selected minima are linked by gauge transformations that alter the phase of the field Φ but leave its magnitude unchanged. The term v denotes the vacuum expectation value (VEV) of the scalar potential. When a particular ground state is chosen, the symmetry is explicitly

broken, but the Lagrangian remains gauge-invariant, resulting in significant implications for the existence of gauge interactions.

If the symmetry spontaneously breaks to the ground state aligned with the ϕ^0 component of the doublet, it can be demonstrated that this particular ground state remains invariant under the $U(1)_{em}$ symmetry group. Consequently, the field expansion around this minimum takes the form:

$$\Phi(x) = \frac{1}{\sqrt{2}} e^{\left[\frac{i\sigma_i \theta^i(x)}{v}\right]} \begin{pmatrix} 0 \\ v + H(x) \end{pmatrix} \tag{1.31}$$

This results in the existence of a real scalar massive field H and three massless fields θ^i. The presence of these massless fields is a consequence of the Goldstone theorem[6], which asserts that the spontaneous breaking of a continuous symmetry produces an equal number of massless bosons (known as Goldstone bosons) as the number of broken generators of the symmetry. However, these massless bosons are not observed in the natural world. They can be eliminated through an $SU(2)_L$ transformation, specifically by adopting a particular gauge known as the "unitary gauge":

$$\Phi(x) \rightarrow \Phi'(x) = e^{\left[-i\frac{\theta_i(x)}{v}\right]} \Phi(x) = \frac{1}{\sqrt{2}} = \begin{pmatrix} 0 \\ v + H(x) \end{pmatrix} \tag{1.32}$$

Following this transformation, only the real scalar field $H(x)$ remains, and its quanta correspond to a new physical massive particle known as the Higgs boson (H).

Then the BEH Lagrangian could be written as:

$$\begin{aligned} \mathcal{L}_{BEH} = & \frac{1}{2}\partial^\mu H \partial_\mu H - \frac{1}{2}(2\lambda v^2)H^2 \\ & + \left[(\frac{gv}{2})^2 W^{\mu+} W^-_\mu + \frac{1}{2}\frac{(g^2 + g'^2)v^2}{4} Z^\mu Z_\mu \right] \left(1 + \frac{H}{v}\right)^2 \\ & + \lambda v H^3 + \frac{\lambda}{4}H^4 - \frac{\lambda}{4}v^4 \end{aligned} \tag{1.33}$$

The first line represents the evolution of the scalar Higgs field, which has a mass $m_H^2 = 2\lambda v^2 = 2\mu^2$. It is a free parameter of the theory, directly related to the parameter μ of the scalar potential. The second line represents the mass terms of the weak bosons (those that multiply the constant term), with a mass:

$$m_W^2 = \frac{g^2 v^2}{4};\ m_Z^2 = \frac{(g^2 + g'^2)v^2}{4} = \frac{m_W^2}{\cos^2\theta_W} \tag{1.34}$$

It can be observed that the Goldstone bosons, removed with the transformation, are absorbed as additional degrees of freedom of the $W^{\pm}$ and Z bosons, corresponding to their longitudinal polarizations. This mechanism confers mass to the weak bosons.

The second line of the Lagrangian also describes the interactions of the weak bosons with the Higgs field. It includes interactions such as HWW and HZZ arising from the $\frac{2H}{v}$ term, as well as $HHWW$ and $HHZZ$ interactions originating from the $\frac{H^2}{v^2}$ term. The third line reveals the presence of cubic and quartic self-interactions of the Higgs boson. Consequently, the Brout-Englert-Higgs (BEH) potential can be reformulated in terms of trilinear and quadrilinear couplings as:

$$\begin{aligned} V(H) &= \frac{1}{2}m_{\mathrm{H}}^2 H^2 + \lambda_{\mathrm{HHH}} v H^3 + \frac{1}{4}\lambda_{\mathrm{HHHH}} H^4 - \frac{\lambda}{4}v^4 \\ \lambda_{\mathrm{HHH}} &= \lambda_{\mathrm{HHHH}} = \lambda = \frac{m_{\mathrm{H}}^2}{2v^2} \end{aligned} \tag{1.35}$$

From the equation above, it becomes evident that both Higgs boson self-couplings are intricately linked to the parameters of the scalar potential and are entirely dependent on the Higgs boson mass and the vacuum expectation value (VEV). The measurement of these self-couplings serves as a critical assessment of the consistency and validity of the Standard Model (SM). In a broader perspective, the Higgs boson self-couplings hold a unique position within the SM: unlike the self-interactions of the weak bosons, which possess a gauge nature, the Higgs boson self-interactions are exclusively associated with the scalar sector of the theory. They bear the responsibility for determining the Higgs boson's own mass, as demonstrated in the mass term of the Lagrangian. Hence, the experimental determination of these self-couplings assumes paramount importance, as it contributes significantly to the reconstruction of the Higgs boson potential and offers valuable insights into the nature of Electroweak Symmetry Breaking (EWSB).

The presence of a constant term in the BEH Lagrangian density carries significant implications for vacuum energy, which holds a close connection to the cosmological constant governing the curvature of the Universe. The predicted value of this cosmological constant, as computed within the framework of the Standard Model (SM), does not align with the values derived from astronomical observations. This disparity presents a formidable challenge that demands attention. One potential avenue to resolve this issue is the development of a quantum theory of gravity that incorporates additional interactions. Alternatively, another approach involves the implementation of a mechanism designed to mitigate the vacuum energy density associated with the Higgs field.

At this stage, the BEH mechanism introduces two essential free parameters: the Vacuum Expectation Value (v) and the Higgs boson mass (m_H). The former parameter represents the energy scale at which electroweak symmetry breaking occurs and can be calculated from the precisely determined Fermi constant (G_F), derived from the muon lifetime:

$$\frac{G_F}{\sqrt{2}} = \left(\frac{g}{2\sqrt{2}}\right)^2 \frac{1}{m_W^2} \Rightarrow v = \left(\sqrt{\frac{1}{\sqrt{2}G_F}}\right) \approx 246\,\text{GeV} \tag{1.36}$$

Until this point, fermions have been considered massless. Mass terms for fermions are generated by the Higgs field through a Yukawa interaction that couples the left and right chiral fields. If we denote the up-type ($I_3 = 1/2$) and down-type ($I_3 = -1/2$) fermions as ψ and ψ', respectively, the Yukawa Lagrangian density takes the form:

$$\mathcal{L}_{Yukawa} = -y'_f \left(\bar{\Psi}_L \tilde{\Phi} \psi'_R + \bar{\psi}'_R \tilde{\Phi}^\dagger \Psi_L\right) - y_f \left(\bar{\Psi}_L \tilde{\Phi} \psi_R + \bar{\psi}_R tilde \Phi^\dagger \Psi_L\right) \tag{1.37}$$

with

$$\tilde{\Phi} = i\sigma_2 \Phi^* = \begin{pmatrix} \phi_0^* \\ \phi_+^* \end{pmatrix} \xrightarrow{\text{EWSB}} \frac{1}{\sqrt{2}} \begin{pmatrix} v + H(x) \\ 0 \end{pmatrix} \tag{1.38}$$

While we have omitted the discussion for the sake of simplicity in this context, it is worth noting that the Yukawa Lagrangian can be extended to incorporate fermion mixing by utilizing combinations of the mass eigenstates of the fields Ψ_L, ψ_R, and ψ'_R. This extended Yukawa Lagrangian density maintains Lorentz and gauge invariance and retains its renormalizability, allowing it to be seamlessly integrated into the Standard Model (SM) Lagrangian density. Following Electroweak Symmetry Breaking (EWSB), the Lagrangian takes on the following expression:

$$\mathcal{L}_{Yukawa} = -\sum_f m_f (\bar{\psi}_L \psi_R + \bar{\psi}_R \psi_L) \left(1 + \frac{H}{v}\right) \tag{1.39}$$

where the summation is carried out over both up- and down-type fermions, and the mass terms are defined as follows:

$$m_{f'}(\psi) = y_{f'}(\psi) \frac{v}{\sqrt{2}} \tag{1.40}$$

In the SM, fermion masses find their explanation in the interaction between fermion fields and the Higgs field, which induces a chirality change in the fermions. The magnitudes of these

interactions are directly correlated with the fermion masses and are treated as free parameters within the theory. It is worth emphasizing that the SM does not provide an explanation for the origin of these couplings, and as a result, it does not elucidate the hierarchical structure of the three fermion families.

In conclusion, the Brout-Englert-Higgs (BEH) mechanism offers solutions to the previously mentioned issues within the electroweak theory of the Standard Model (SM). Upon electroweak symmetry breaking, the scalar field generates Goldstone bosons that are absorbed as degrees of freedom by the vector boson fields, rendering them massive. The Higgs boson's contributions to quantum loops in the scattering of longitudinally polarized vector bosons serve to regularize the process, ensuring unitarity at the TeV scale and beyond. Moreover, the Higgs boson couples the left and right chiral components of fermion fields through a Yukawa interaction, ultimately determining fermion masses via a purely quantum-relativistic mechanism. Lastly, it is noteworthy that the theory resulting from the incorporation of the BEH mechanism into the electroweak theory is renormalizable, a fact established by 't Hooft and Veltman[7].

1.3 Higgs Boson Pair Production in the SM

A direct measurement of the Higgs boson self-coupling at the LHC can be derived from the measurement of double and triple Higgs production processes, which are the only processes at the lowest order involving the Higgs boson HHH and HHHH interaction vertices characterized by couplings $\lambda = \lambda_{\mathrm{HHH}} = \lambda_{\mathrm{HHHH}}$. While the cross-section for triple Higgs production remains exceedingly low (approximately 80 ab at $\sqrt{s} = 13$ TeV), making it currently beyond the experimental reach of the LHC, the challenging nature of Higgs boson pair (HH) production, with a cross-section of around 30 fb, allows for experimental probing at the LHC.

In a general context, a pair of on-shell Higgs bosons can be generated in the final state of a collision through any of the diagrams depicted in Fig. 1.4.

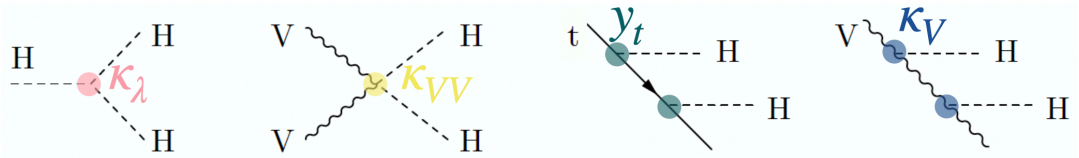

Figure 1.4 On-shell Higgs boson pair productions' final states and vertices.

At the Large Hadron Collider (LHC), the production of Higgs boson pairs (HH) predominantly takes place through five distinct mechanisms[8, 9], listed below in descending order of cross-section. The leading-order (LO) diagrams illustrating the primary mechanisms of

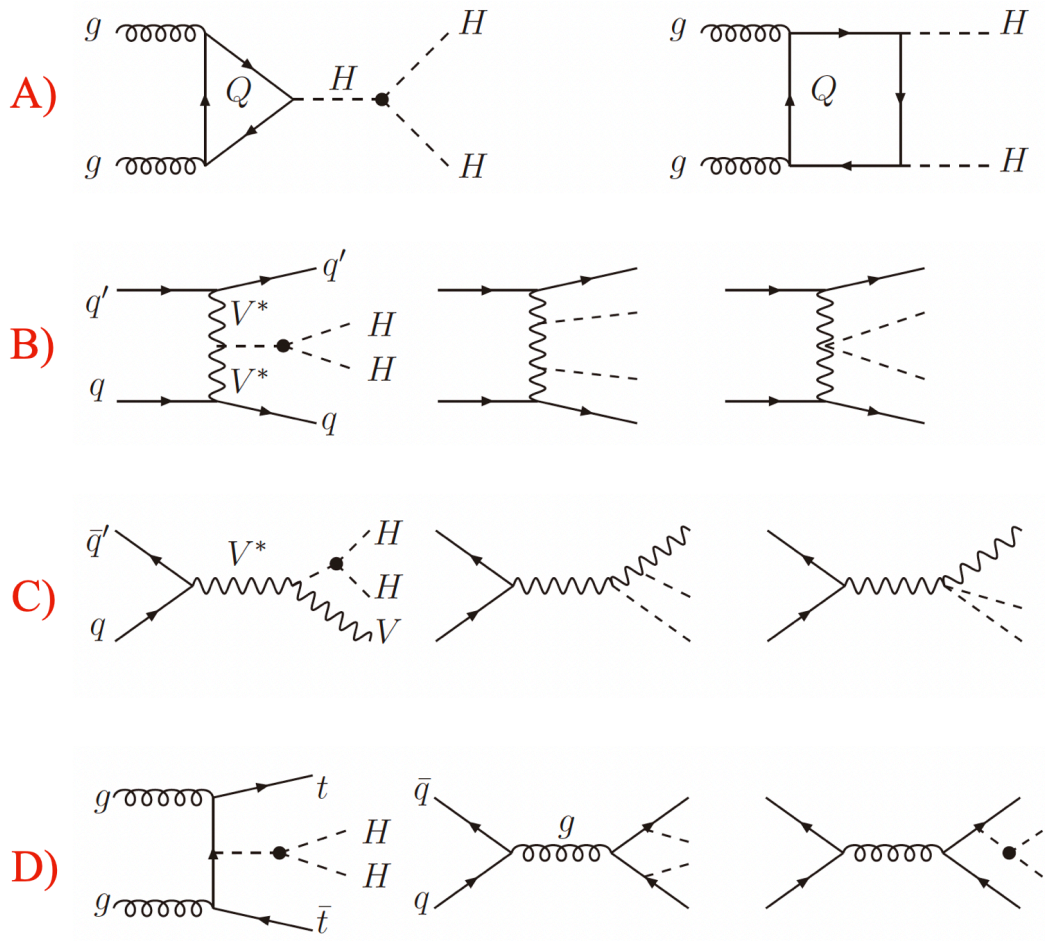

Figure 1.5 Some generic Feynman diagrams contributing to Higgs pair production processes that can be studied at current LHC experiments.

leading 4 HH production are presented in Fig. 1.5. Additionally, we consider the fifth production process illustrated in Fig. 1.5, albeit its cross-section at the current LHC energy is too minuscule to be subjected to comprehensive study. Furthermore, the involved production mechanisms and vertices closely align with those of the preceding four processes.

These mechanisms include:

'A)' Gluon-gluon double-Higgs fusion ($gg \rightarrow HH$).

'B)' Vector boson (WW/ZZ) double-Higgs fusion ($qq' \rightarrow HH\,qq'$).

'C)' Double Higgs-strahlung ($qq' \rightarrow ZHH/WHH$).

'D)' Associated production with top-quarks ($qq'/gg \rightarrow t\bar{t}HH$).

'E)' Single top quark associated production ($qq' \rightarrow tjHH$).

A) gluon-gluon double-Higgs fusion($gg \rightarrow HH$)

At hadron colliders, the dominant production mechanism for Higgs boson pairs (HH) is the loop-induced gluon-fusion (ggF) process, which primarily occurs through a top quark loop,

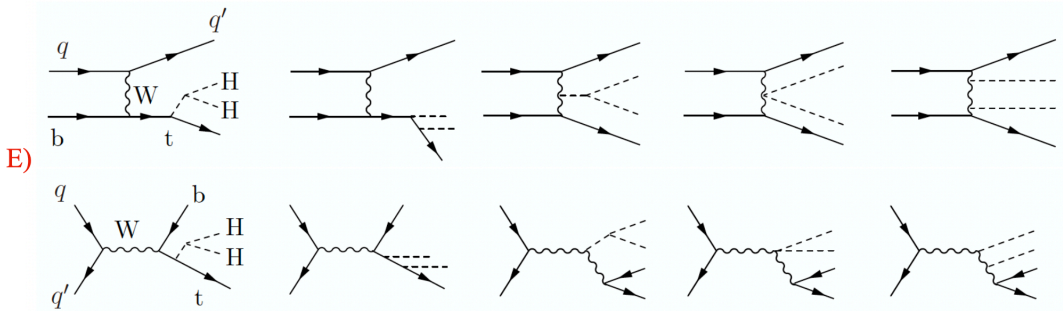

Figure 1.6 Feynman diagrams of $qq' \to tjHH$ production mode.

similar to the single Higgs boson production in ggH production. At the leading order (LO), two diagrams are involved in this process: a box diagram (Fig. 1.5 (A) left), which entails the radiation of two on-shell Higgs bosons from a heavy quark loop, and a triangle diagram (Fig. 1.5 (A) right), involving a trilinear self-coupling λ_{HHH}. As a result, the cross-section for ggF HH production is influenced by both the Yukawa top quark coupling $y_t$and the Higgs boson self-coupling λ_{HHH}. The relative contributions of these two diagrams, along with their interference and total sum, are illustrated in Fig. 1.7, which displays the distribution of the invariant mass of the Higgs boson pair (m_{HH}). Notably, a substantial destructive interference between the two diagrams is observed, resulting in an extremely small total cross-section (approximately 31.05 fb at $\sqrt{s}$ = 13 TeV[10]), which is nearly three orders of magnitude lower than the single Higgs ggH production.

An essential characteristic of the gluon fusion production channel warrants special attention at this point. The two production diagrams we previously examined possess amplitudes of nearly equal magnitude but engage in destructive interference. This, combined with the confined phase space governing the production of two Higgs bosons, leads to the small cross-section we discussed earlier. However, it is imperative to recognize that this destructive interference endows HH production with an exceptional sensitivity to physics beyond the Standard Model (BSM). Contributions from BSM physics have the potential to significantly modify this destructive interference, resulting in substantial alterations that can be probed using available LHC data. Consequently, we shift from regarding HH production primarily as a test of the Standard Model to considering it as a valuable probe into the realm of BSM physics.

B) WW/ZZ double-Higgs fusion ($qq' \to HHqq'$)

This constitutes the second-largest production mechanism, primarily driven by W and Z exchange processes radiated off the colliding quarks. The corresponding diagrams closely resemble those of single Higgs Vector Boson Fusion (VBF) production. This production mode

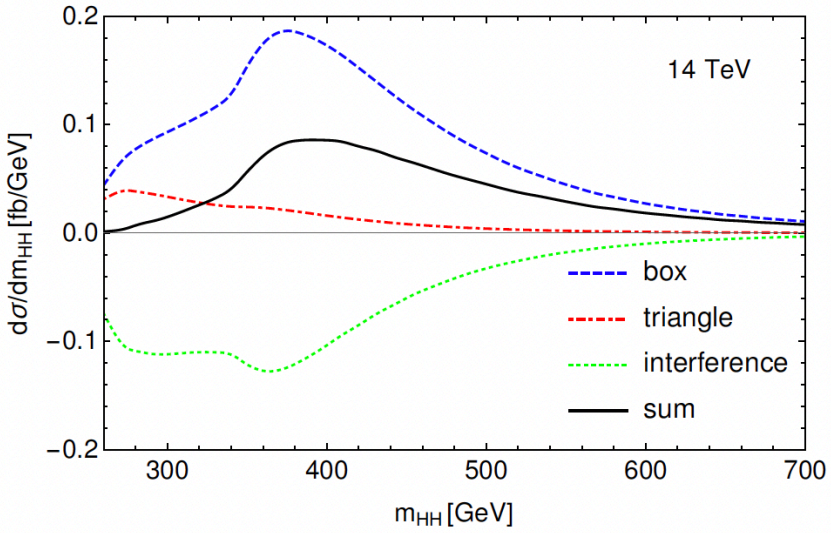

Figure 1.7 The Higgs pair invariant mass distribution at the leading order reflects the distinct contributions from the gluon fusion production mechanism, including the box and triangle diagrams, as well as their interference effects.[11]

not only provides insight into the Higgs boson self-coupling (λ_{HHH}) but also offers access to the coupling between two vector bosons and the Higgs boson (HVV) as well as the coupling between a pair of Higgs bosons and a pair of vector bosons (HHVV). Particularly, the HHVV coupling serves as a valuable probe of the nature of electroweak symmetry breaking dynamics within the Standard Model (SM) and is directly observable exclusively through the VBF HH production mode. Despite having a cross-section approximately 10 times smaller than that of ggF HH production, similar to VBF Higgs production, the distinctive final state featuring two jets with significant invariant mass and pseudorapidity separation enables efficient signal-background discrimination.

C) Double Higgs-strahlung ($qq' \rightarrow ZHH/WHH$)

Associated production of Higgs pairs with a W or a Z boson entails the same couplings as in the VBF HH production mechanism, but the cross-section is notably lower. This final state includes an on-shell vector boson, and when it decays leptonically, it offers a relatively clean experimental signature. Nevertheless, this channel presents unique characteristics both from experimental and theoretical perspectives, making it a valuable subject for investigation at the LHC. The examination of this production process will constitute a significant portion of this thesis and will be thoroughly expounded upon in Chapter 3.

As the combined production process with the third-largest cross-section, following gluon fusion and vector boson fusion, it also exhibits a substantial interference effect, but in the opposite direction. When considering the large quark mass limit to simplify the matrix element

expression, for gluon fusion:

$$\mathcal{M}_{\mathrm{ggF}} = \frac{4m_H^2\hat{s}}{\hat{s}-m_H^2}\kappa_\lambda - \frac{4\hat{s}}{3} \tag{1.41}$$

In this expression, the first term signifies the contribution originating from the triangle diagram, while the second term signifies that arising from the box diagram. Consequently, the positive value of κ_λ causes these two terms to have opposite signs, leading to the cancellation of the amplitude. Conversely, a negative κ_λ enhances the cross-section.

For vector boson fusion, the matrix element is:

$$\mathcal{M}_{\mathrm{VBF}} = g^{\mu\nu}\left[\frac{4m_V^4}{v^2}\left(\frac{1}{\hat{t}-m_V^2}+\frac{1}{\hat{u}-m_V^2}\right)+\kappa_\lambda\frac{m_V^2}{v^2}\frac{6m_H^2}{\hat{s}-m_H^2}+\frac{2m_V^2}{v^2}\right]+others \tag{1.42}$$

The three terms in equation 1.42 are the contribution from the three VBF diagrams respectively. Near the HH production threshold, $\hat{s}\sim 4m_H^2, \hat{t}\simeq\hat{u}\sim 0$. It give rise to:

$$\mathcal{M}_{\mathrm{VBF}} \sim \frac{2m_V^2}{v^2}(\kappa_\lambda - 3)g^{\mu\nu} + others \tag{1.43}$$

yielding a small cross section around κ_λ around 3.

The VHH production mode shares precisely the same vertices (subprocess) as the VBF production mode involving $V^\mu V^\nu \rightarrow HH$, and these two modes are interrelated by crossing symmetry. However, in the VHH production mode, a vector boson appears in the final state. Consequently, in proximity to the Higgs boson pair production threshold, where $\hat{s}\sim 4m_H^2$ and $\hat{t}=\hat{u}\sim(m_H+m_V)^2$, the matrix element exhibits (from equation 1.42):

$$\mathcal{M}_{\mathrm{VHH}} \sim \frac{2m_V^2}{v^2}(\kappa_\lambda + 1 + \frac{4m_V^2}{m_H(m_H+2m_V)})g^{\mu\nu} + others \tag{1.44}$$

In this case the positive κ_λ enhance the cross section which output a 'constructive interference'.

D) Associated production with top-quarks ($qq'/gg \rightarrow t\bar{t}HH$) The production mechanism bears a resemblance to $t\bar{t}H$ production, where two Higgs bosons are either radiated from the top quarks or produced via the Higgs boson self-coupling. However, this mode exhibits an low cross-section owing to the negative higher-order QCD corrections.

E) Single top quark associated production ($qq' \rightarrow tjHH$) This process can proceed through either the t-channel or s-channel, depicted in the top and bottom rows of the diagrams below. The t-channel diagrams are illustrated in the so-called 5F scheme[12] for simplicity.

Remarkably, it is the sole process that simultaneously probes the HH couplings to vector bosons and top quarks, as well as their relative phase. However, due to its minuscule cross-section, it poses a formidable challenge for investigation at the LHC, but it holds the potential for study in a future, higher-energy collider.

The cross-sections for these production mechanisms at various center-of-mass energies are summarized in Table 1.1. The cross-section for gluon fusion is computed at the next-to-next-to-leading order (NNLO) of the theoretical perturbative QCD calculation, encompassing next-to-next-to-leading-logarithm (NNLL) corrections and finite top quark mass effects at the next-to-leading order (NLO). The theoretical uncertainties encompass variations in the QCD factorization and renormalization scales, α_s, parton distribution functions (PDFs), and unaccounted effects originating from the finite top quark mass at NNLO. The cross-sections for VHH are computed at the NNLO, while those for the other processes are calculated at the NLO of the perturbative QCD framework.

Production mode	$\sqrt{s}$ = 8 TeV	$\sqrt{s}$ = 13 TeV	$\sqrt{s}$ = 14 TeV
Gluon fusion	$10.15^{+4.1\%}_{-5.7\%}$	$33.49^{+4.3\%}_{-6.0\%}$	$39.59^{+4.4\%}_{-6.0\%}$
VBF	$0.459^{+3.2\%}_{-3.6\%}$	$1.62^{+2.3\%}_{-2.7\%}$	$1.95^{+1.8\%}_{-2.3\%}$
W+HH	$0.145^{+0.43\%}_{-0.52\%}$	$0.329^{+0.32\%}_{-0.41\%}$	$0.368^{+0.33\%}_{-0.39\%}$
W-HH	$0.0677^{+1.0\%}_{-1.2\%}$	$0.173^{+1.2\%}_{-1.3\%}$	$0.197^{+1.2\%}_{-1.3\%}$
ZHH	$0.143^{+2.7\%}_{-2.3\%}$	$0.362^{+3.4\%}_{-2.6\%}$	$0.414^{+3.5\%}_{-2.7\%}$
ttHH	$0.174^{+2.8\%}_{-10.6\%}$	$0.772^{+1.7\%}_{-4.5\%}$	$0.949^{+1.8\%}_{-4.8\%}$
tjHH	$0.00540^{+5.4\%}_{-3.1\%}$	$0.0281^{+5.2\%}_{-3.2\%}$	$0.0364^{+3.7\%}_{-1.3\%}$

Table 1.1 Cross section for different HH production modes assuming a Higgs boson mass of 125.09 GeV. The gluon fusion cross section is computed at NNLO of perturbative QCD calculation, with NNLL corrections and finite top quark mass effects at NLO. The cross section of the VHH, $V = W\pm, Z$ are computed at NNLO QCD and those of the other processes at NLO QCD. The values are taken from Ref.[13]

By extending the range of scans to encompass a wider center-of-mass energy spectrum, we can glean insights into the projected cross-section predictions for various HH decay modes, ranging from the current LHC center-of-mass energy to 100 TeV, as illustrated in Fig. 1.8. Additionally, an exploration of the κ parameter (κ_λ) scan is depicted in Fig. 1.9. Both figures comes from reference[9].

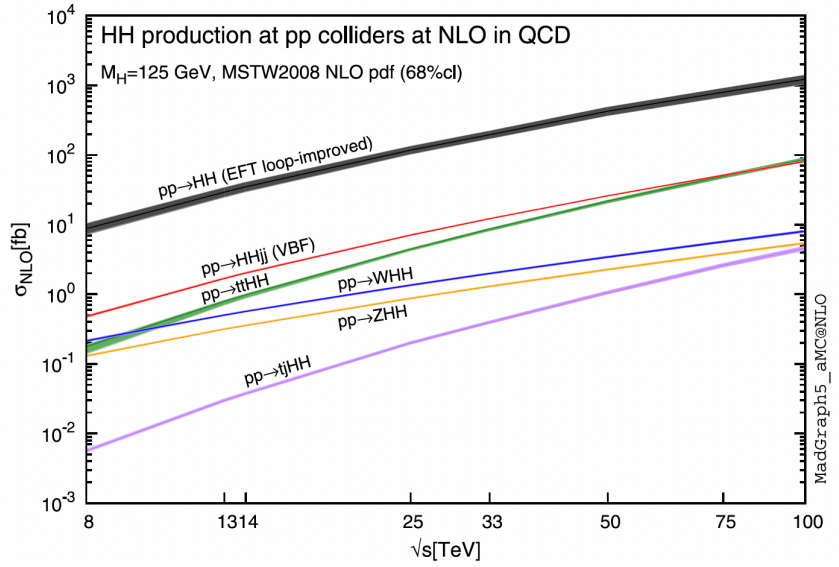

Figure 1.8 The total cross-sections at the next-to-leading order (NLO) in QCD for the six most significant HH production channels at proton-proton (pp) colliders are depicted, with the line thickness representing the combined uncertainties from scale and PDF added linearly.

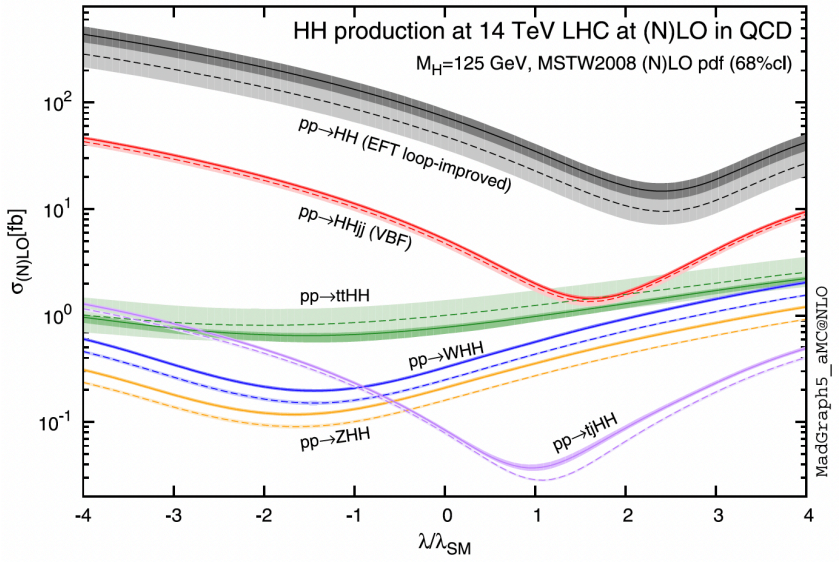

Figure 1.9 The total cross-sections for HH production channels at both the leading order (LO) and next-to-leading order (NLO) in QCD are presented, focusing on the $\sqrt{s}$ = 14TeV Large Hadron Collider (LHC) as a function of the self-interaction coupling λ (κ_λ). In this representation, dashed (solid) lines correspond to the LO (NLO) results, while light-colored (dark-colored) bands denote the uncertainties originating from scale and PDF variations added linearly. The standard model (SM) values of the cross-sections are established at $\lambda/\lambda_{\mathrm{SM}} = 1$.

1.4 Higgs boson pair searches at the LHC

While the previous section primarily delved into the theoretical aspect of HH production modes in the context of current LHC experiments, it is crucial to shift our focus towards the experimental exploration of HH physics. This entails an in-depth examination of the decay channels of HH, or, in terms of collider experiments, the final states. Final states involving a pair of Higgs bosons exhibit substantial phenomenological richness and can be investigated through various decay channels.

Measuring the production of Higgs boson pairs at the LHC necessitates the reconstruction of their decay products within the detector and the differentiation of these signals from the substantial background noise. The selection of the HH system's decay channel plays a pivotal role in this regard, as it dictates a distinct trade-off between the branching fraction and background contamination. In the context of the Standard Model (SM), Higgs boson pair production is distinguished by remarkably small cross-sections, underscoring the preference for decay channels characterized by substantial branching fractions.

The decay branching fractions for some selected HH final states are shown in fig. 1.10 [14].

With an integrated luminosity of 36.3 fb^{-1}, both ATLAS and CMS experiments have conducted searches for non-resonant gluon fusion HH production in various decay channels, including $bbbb$ [15, 16], $b\bar{b}\tau^+\tau^-$ [17, 18], $bbVV$ [19, 20], and $bb\gamma\gamma$ [21, 22]. Furthermore, ATLAS has investigated the $WW\gamma\gamma$ [23] and $WWWW$ [24] channels. Both ATLAS and CMS experiments separately combined results from all available channels. These combined results have constrained the Standard Model (SM) production cross section to be less than approximately 7 times (ATLAS) and 22 times (CMS) the SM prediction, with expected limits of about 10 and 13, respectively.

The full Run2 results, utilizing the integrated luminosity of 138 fb^{-1}, have been published for the $bbWW$ [25], $bb\gamma\gamma$ [26] and multi-leptonic [27] channels. In the $bb\gamma\gamma$ channel, a limit on the SM HH production is set at 7.7 times the SM prediction, and constraints on κ_λ are established with values ranging from -3.3 to 8.5 at the 95% confidence level (CL). Additionally, the VBF HH production has been thoroughly examined in the $bbbb$ [28] and $bb\gamma\gamma$ [26] channels. The former provides the most stringent constraint at the 95% CL on κ_{VV}, with a range of $(-0.43, 2.56)$, while the latter establishes a 95% CL upper limit of 225 times the SM prediction.

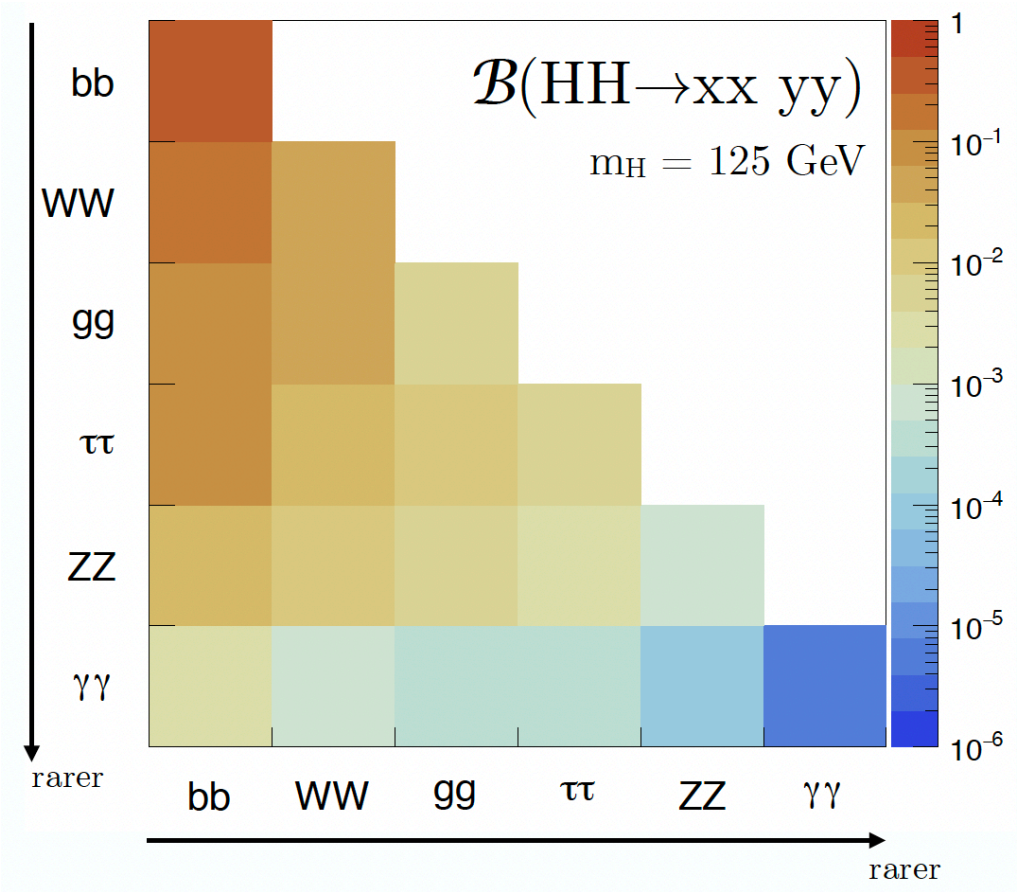

Figure 1.10 The branching fractions for the decay of an HH pair into a specified set of final states are depicted, with the decays of the two Higgs bosons indicated on the respective axes of the figure.

Chapter 2 Experimental apparatus

The European Organization for Nuclear Research (**Conseil européen pour la Recherche nucléaire, CERN**) currently stands at the forefront of particle physics research and technology development, fostering international collaboration and education. CERN serves as a catalyst for scientific activities in the domain of high-energy physics, boasting the participation of more than 10,000 individuals from over 800 institutes and universities across the globe.

Scientists at CERN analyze data from proton-proton collisions in the **Large Hadron Collider (LHC)**, operating at a design center-of-mass energy of 14 TeV. This colossal particle accelerator stands as the largest ever constructed, spanning a subterranean tunnel measuring 27 kilometers in length. Constructed between 1998 and 2008, the LHC occupies the same tunnel that previously housed its predecessor, the Large Electron-Positron (LEP) collider, necessitating meticulous considerations in infrastructure design and installation.

Situated underground at depths ranging between 45 meters and 170 meters, the tunnel accommodates two vacuum beam-pipes where proton beams circulate in opposing directions before converging at four interaction points. It is at these points where the primary experimental facilities are situated.

Given the breadth of the LHC scientific agenda, each experiment was meticulously crafted to investigate distinct physics scenarios. Among them, **A Toroidal LHC Apparatus (ATLAS)** and **the Compact Muon Solenoid (CMS)** detectors stand as two versatile instruments, originally tailored to pursue the Higgs boson and scrutinize potential Beyond Standard Model (BSM) scenarios at the TeV energy scale. Meanwhile, **A Large Ion Collider Experiment (ALICE)** and **the LHC beauty (LHCb)** detectors are dedicated to the study of heavy ions and b-quark physics, respectively.

The CMS Collaboration involves the participation of more than 5746 scientists from 58 different countries. The primary physics results presented in this thesis stem from the analysis of proton-proton collisions recorded by the **CMS** experiment at a center-of-mass energy of $\sqrt{s} = 13\,\text{TeV}$, corresponding to the total integrated luminosity of $138\,\text{fb}^{-1}$collected during the Run2 Phase-I of the LHC. The implications for physics research, along with the ongoing detector upgrade efforts, are pertinent to the forthcoming **High-Luminosity LHC (HL-LHC)** experiments Phase-II operation and data acquisition.

2.1 The Large Hadron Collider

The LHC [29] represents the final component of the CERN accelerator complex. Within its confines, proton beams are generated, progressively accelerated to energies of up to 7 TeV, and then injected into two distinct beam pipes. These pipes intersect at designated interaction points (IP), where the detectors are strategically positioned. The arrangement of the four primary experiments around the collider ring, along with the various components of the accelerator complex, is depicted in Figure 2.1 [30].

2.1.1 Design

Hydrogen atoms undergo electron stripping within a dual plasma source before being accelerated to an energy of 50 MeV in the Linear Accelerator 2 (LINAC2). Subsequently, the protons are further accelerated to 1.4 GeV in the Proton Synchrotron Booster (PSB). The beam is then injected into the Proton Synchrotron (PS), where additional acceleration occurs, ultimately reaching 25 GeV. Following this stage, the protons enter the Super Proton Synchrotron (SPS), where their energy is boosted to 450 GeV. Finally, the proton beam is directed into two separate beam pipes of the Large Hadron Collider (LHC). Within the LHC, operation within 400 MHz radiofrequency cavities accelerates and shapes the protons into proton bunches. Upon reaching their designated energy levels and achieving stable beam dynamics, collisions occur at four distinct points along the LHC ring.

The beam optics within the LHC ring are meticulously controlled by superconducting NbTi magnets. These magnets maintain the beams on their circular trajectory using 1232 dipoles distributed across eight arcs, each spanning 2.45 km. Operating at a current of approximately 11 kA, these dipoles generate an 8.3 T magnetic field, crucial for keeping the beams on course.

A critical requirement for the accelerator is the narrow size of the bunches, which is maintained constant with the aid of additional magnets known as quadrupoles. These quadrupoles further focus the beams. To ensure their superconducting state, the magnets are cooled with superfluid He-4 to 1.9 K.

The beams are directed to collide at four interaction points (IP), where the primary experiments are situated. Before reaching each IP, additional quadrupoles are strategically placed to enhance focusing.

The number of events per unit time $\partial N/\partial t$ for a process with given cross section σ is determined by the **instantaneous luminosity** $\mathcal{L}$:

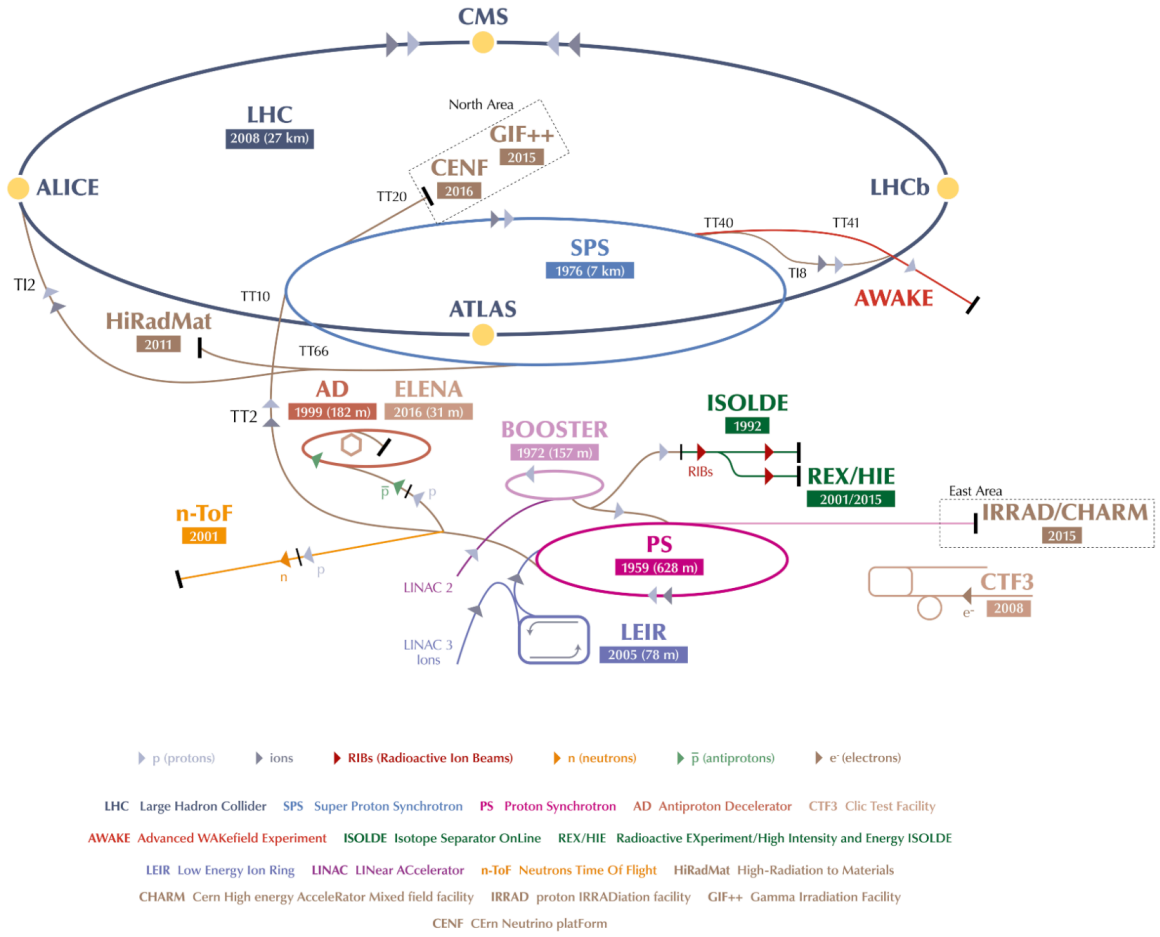

Figure 2.1 Schematic representation of the accelerator complex locate at CERN. [30]

$$\frac{\partial N}{\partial t} = \mathcal{L} \times \sigma \tag{2.1}$$

It is common practice to report the integral of $\mathcal{L}$ over time, denoted as integrated luminosity, $L = \int \mathcal{L} dt$. This quantity represents the amount of data recorded over a specific period, typically spanning a year of data-taking. Instantaneous luminosity is measured in units of $\mathrm{cm}^{-2}\mathrm{s}^{-1}$, with the nominal value for the LHC machine typically represented as $\mathcal{L} = 10^{34}\mathrm{cm}^{-2}\mathrm{s}^{-1}$. Integrated luminosity is often expressed in inverse femtobarns (fb^{-1}) or picobarns (pb^{-1}).

Table 2.1 Nominal parameters of the LHC in proton-proton collisions.

Parameter	**Meaning**	**Nominal value**
$\sqrt{s}$	Center-of-mass energy	14 TeV
Δt	Bunch separation	25 ns
n_b	Number of bunches	2808
N_p	Number of protons per bunches	$1.15 \cdot 10^{11}$
f_{rev}	Revolution frequency	11245 Hz
σ_z	Transverse bunch r.m.s. at the IP	16.7 μm
σ_{xy}	Longitudinal bunch r.m.s.	7.55 cm
β^*	Beta function at the IP	0.55 m
θ_c	Crossing angle at the IP	285 μrad
ϵ_n	Transverse emittance	3.75 μm

The operations of the accelerator are often characterized by quoting the instantaneous luminosity, which can be defined from the beam parameters as follows:

$$L = \frac{N_p^2 n_b f_{\mathrm{rev}} \gamma_r F}{4\pi \varepsilon_n \beta^*}, \tag{2.2}$$

Here, N_p denotes the quantity of particles per n_b bunch within the beam, with f_{rev} representing the revolution frequency and γ_r the relativistic gamma factor. The beam's optical properties are encapsulated by the $\varepsilon_n \beta^*$ term, in which ε_n signifies the emittance and β^* the beta function, indicating beam focusing at the interaction point (IP) [29]. The factor F reflects the instantaneous luminosity adjustment due to the beam's crossing angle (θ_c), alongside the beams' transverse and longitudinal root-mean-square (r.m.s.) dimensions (σ_{xy} and σ_z):

$$F = \left(1 + \frac{\theta_c \sigma_z}{2\sigma_{xy}}\right)^{-1/2} \tag{2.3}$$

The specified nominal values for these parameters are catalogued in Table 2.1. As highlighted, the LHC's elevated luminosity is crucial for detecting processes with low cross sec-

tions. Nonetheless, this high luminosity also implies the potential for multiple interactions within a single bunch crossing, a scenario known as pileup, with its mean value described as follows:

$$< \text{P.U.} >= \frac{L\sigma_{\text{pp}}^{\text{inel}}}{n_b \cdot f_{\text{rev}}} \tag{2.4}$$

Here, $\sigma_{\text{pp}}^{\text{inel}}$ denotes the inelastic proton-proton (pp) cross-section. With the LHC's design energy of $\sqrt{s} = 14$ TeV, the $\sigma_{\text{pp}}^{\text{inel}}$ stands at 69 mb, yielding an initial pileup rate of approximately 22 interactions per bunch crossing [31]. Over time, the LHC has steadily increased its operational intensity, currently observing a pileup rate near 60 interactions per event. This figure is anticipated to rise significantly with the commencement of the High Luminosity LHC (HL-LHC) phase in 2027, expecting an average pileup of (P.U.) = 140/200 events. Such escalation in pileup rates directly impacts detector efficiency, notably diminishing particle identification fidelity and resolution. To address these challenges in preparation for the HL-LHC era, LHC experiments are undergoing comprehensive upgrades [32]. Among the primary objectives of these modifications is the reduction of pileup effects and the mitigation of radiation damage. Innovations such as the CMS endcap GEM system upgrade and the integration of new timing detectors are pivotal to these efforts, with this thesis delving into their development, assembly, simulation, and empirical validation. An in-depth exploration of the CMS upgrade initiatives in anticipation of the HL-LHC, focusing on design considerations, assembly processes, simulation methodologies, and test beam data analysis, is presented in Chapter 5.

2.1.2 Operation

Following over a decade of preparatory work and setup, the LHC witnessed the introduction of its first proton beams in September 2008. However, this initial endeavor was abruptly halted due to a significant mechanical malfunction caused by an extensive helium leak, attributed to a defective electrical link between two magnets. This incident necessitated a comprehensive technical pause that lasted until November 2009, marking the moment when proton beams, each carrying an energy of 450 GeV, were reintroduced. Subsequently, the energy level was elevated to 1.18 TeV per beam, positioning the LHC as the most powerful particle accelerator globally.

By 2010, the beam energy saw progressive increments, achieving 3.5 TeV per beam. March of the same year recorded the inaugural high-energy proton-proton collision at a center-of-mass energy of 7 TeV ($\sqrt{s} = 7$ TeV). The ensuing years, 2011 and 2012, signified the Run-I

epoch of the LHC operations: the initial year witnessed the delivery of 6 fb^{-1}at a center-of-mass energy of $\sqrt{s}$ = 7 TeV, followed by a delivery of 23 fb^{-1}in 2012 at $\sqrt{s}$ = 8 TeV. These data enabled the ATLAS and CMS collaborations to narrow down the search parameters for the Higgs boson. The latter year, with its increased luminosity and combined with data from $\sqrt{s}$ = 7 TeV, led to the landmark discovery of the Higgs boson in July 2012. The subsequent period saw a steady enhancement in the machine's luminosity to match its intended design specifications. The initiation of Run-II in 2015 brought the LHC to operate at a center-of-mass energy of $\sqrt{s}$ = 13 TeV, culminating in a total gathered luminosity of 139 $fb^{-1}$by the end of 2018. The trajectory of both integrated and peak luminosities captured by the CMS detector through the last eight years is depicted in Fig. 2.2.

Fig. 2.3 provides an overview of the LHC's operational history and future trajectory. Following Run-I, the LHC entered a two-year hiatus known as the first long shutdown (LS1), aimed at gearing up for Run-II through significant updates across its infrastructure, focusing on magnets and specific sub-detectors of the experiments.

As depicted in Fig. 2.2, with the luminosity's incremental rise, an increase in the average collision rate per bunch crossing is anticipated. According to Fig. 2.4, the Run-II phase witnessed a surge in pileup rates; the average collision rate per bunch crossing nearly tripled from a pileup of <P.U.> = 13 in 2015 to <P.U.> = 40 in 2018. The timeline from 2011 to 2024 is denoted as Phase 1, transitioning into Phase 2 from 2027 to 2037, marking the High-Luminosity LHC era (HL-LHC).

Post-LS1, LHC operations recommenced in 2015, continuing through to the end of 2018, a period commonly recognized as Run-II. The 2015 operations were chiefly aimed at commissioning the machine to operate at a new record center-of-mass energy, thus paving the path to novel physics explorations. That year, CMS was allocated 4.2 fb^{-1}at an initial luminosity of $\mathcal{L} = 5 \times 10^{33} cm^2 s^1$, but by June 2016, the design instantaneous luminosity of $\mathcal{L} = 1.5 \times 10^{34} cm^2 s^1$ was achieved and subsequently surpassed. Over the years 2016 to 2018, CMS documented integrated luminosities of 41.0 fb^{-1}, 49.8 fb^{-1}, and 67.9 fb^{-1}, respectively.

Following the pivotal discovery of the Higgs boson during Run-I, the subsequent Run-II phase of LHC operations has been focused on meticulously measuring the Higgs boson's attributes: spanning its production and decay phenomena to detailing its interactions with other Standard Model (SM) particles.

To date, analyses conducted during CMS Run-II have yet to uncover signs of beyond the Standard Model (BSM) phenomena. Expected BSM processes are likely to manifest through

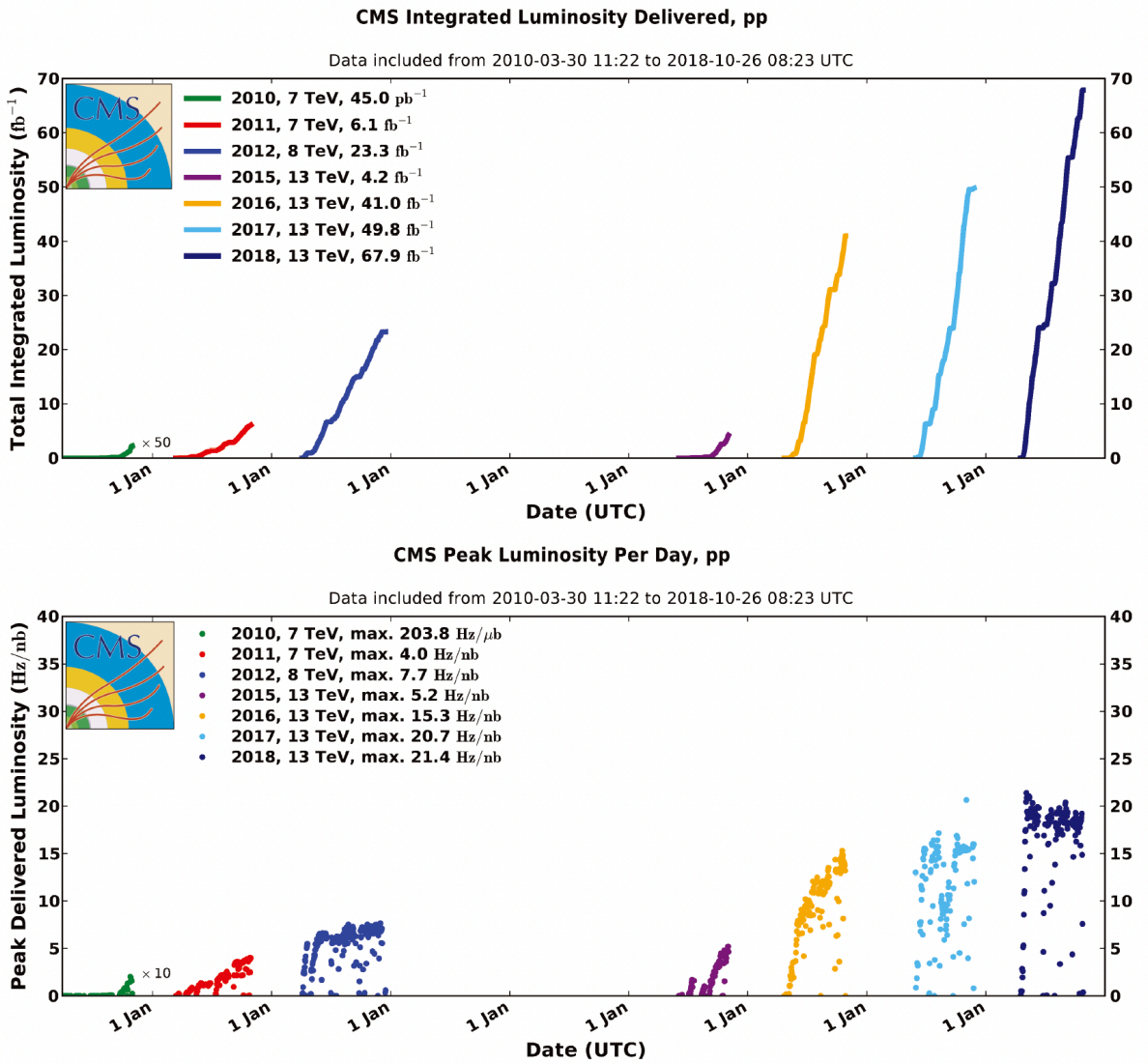

Figure 2.2 Total integrated luminosity (top) and peak instantaneous luminosity (bottom) delivered to CMS as a function of the date. The plots include both the Run-1 (2010-2012) and the Run-II (2015-2018) operations of the LHC. [33]

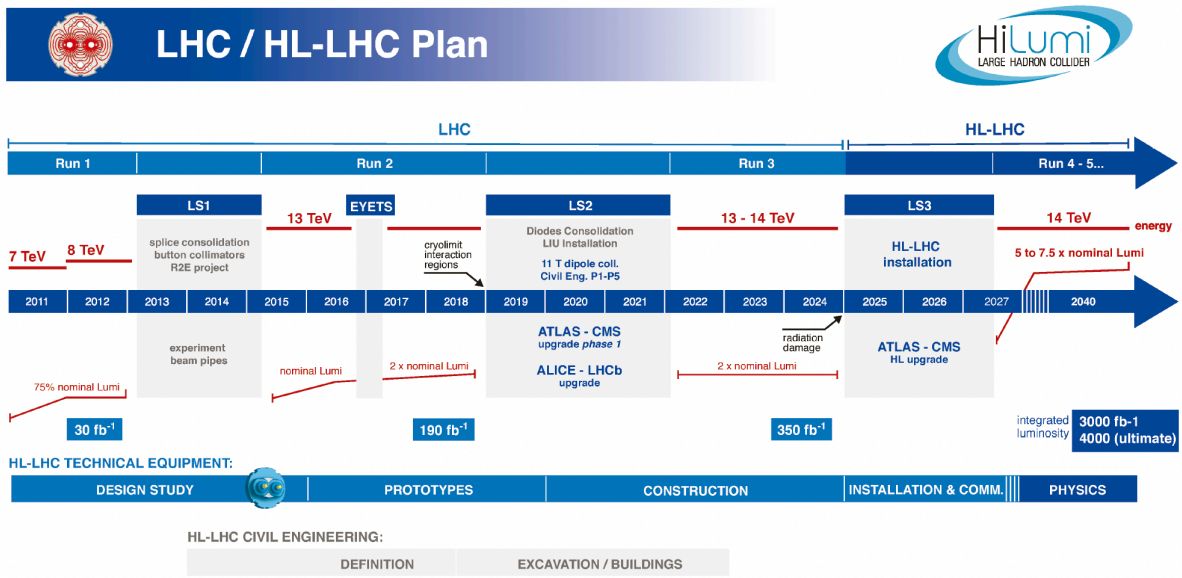

Figure 2.3 Subdivision of the past LHC activities and future plans for the LHC and L-LHC programs. [33]

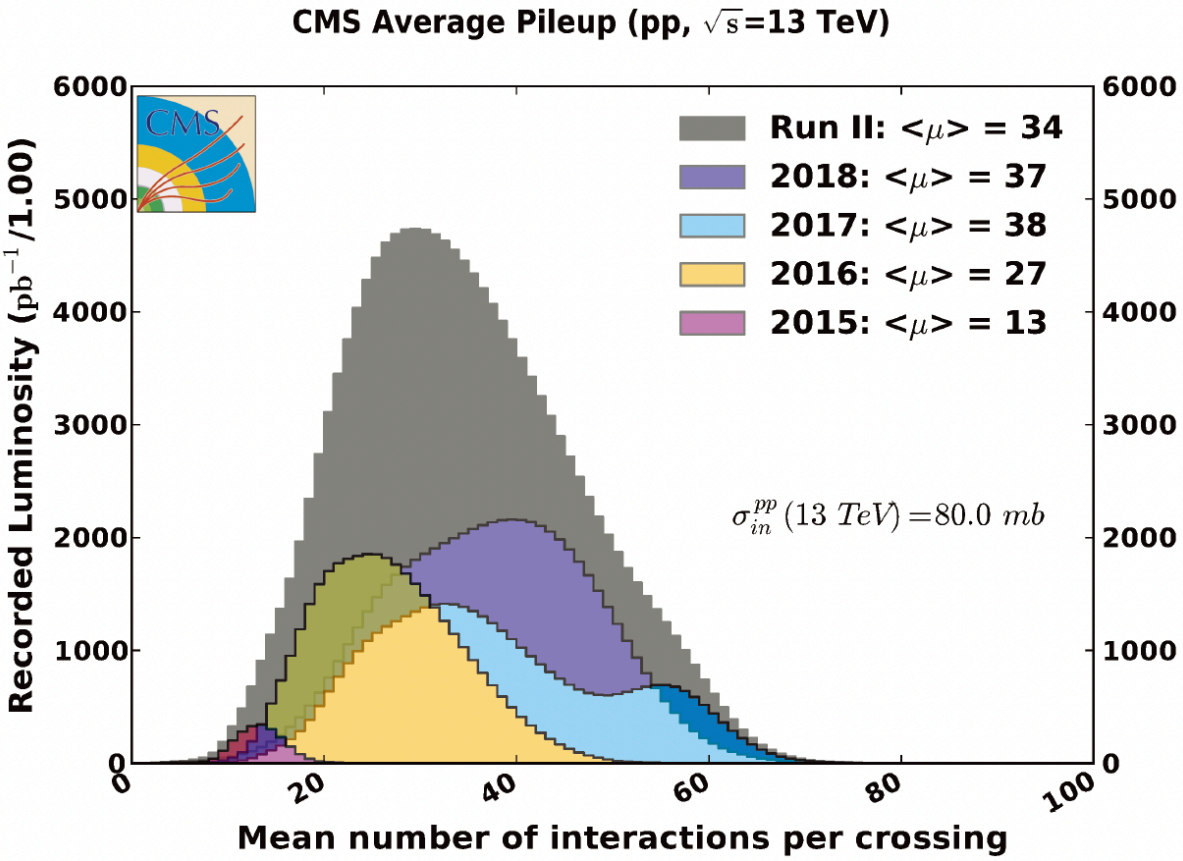

Figure 2.4 The average pileup profile registered by the CMS detector during the Run-II (2015-2018) period is depicted in the figure. The average pileup value <μ> is determined relative to the σ_{pp}^{inel} values illustrated in the figure for each center-of-mass energy. [33]

subtler cross-sections and predominantly influence the extremities of distributions, where currently available statistical data remains sparse. Therefore, to thoroughly explore potential BSM scenarios or to utilize the Higgs boson as a conduit to new physics discoveries, an augmentation of the data pool is imperative, necessitating enhanced precision in event selection, identification, and reconstruction methodologies.

As this thesis is being penned, the LHC is undergoing its second *long shutdown* (LS2), a period dedicated to the enhancement and maintenance of both the accelerator's complex and its supporting infrastructure, setting the stage for Run-III. This upcoming phase anticipates operations at the LHC's peak design energy of $\sqrt{s} = 14$ TeV. The conclusion of Run-III in 2024 will signify the end of LHC Phase 1, by which point it is projected that the experiments will have accumulated an impressive integrated luminosity of approximately 350 fb^{-1}, facilitating in-depth analyses of infrequent events and affording even more precise measurements of the Higgs boson's characteristics. Nonetheless, by this juncture, significant radiation-induced degradation is expected across the experimental detectors, necessitating extensive upgrades to preserve their operational efficiency and to broaden the scope for new discoveries. In anticipation, the LHC is gearing up for the High Luminosity phase (HL-LHC), expected to achieve a total integrated luminosity close to 3000 fb^{-1}along with a peak instantaneous luminosity of 5×10^{34} cm^{-2} s^{-1}, ushering in an era of heightened radiation exposure and pileup rates in the vicinity of 140/200 events per bunch crossing. This phase is poised to dramatically increase the annual Higgs boson yield to approximately 15 million, a significant leap from the three million recorded in 2017, thereby enabling exhaustive investigations into the Higgs boson's properties and potentially uncovering previously undetected physics phenomena.

2.1.3 Experiments

As previously mentioned, the CERN accelerator complex encompasses a variety of experimental setups along its acceleration sequence. The Proton Synchrotron (PS) functions as a low-energy proton feeder for the East Area, while the Super Proton Synchrotron (SPS) accelerates protons to 450 GeV for use in the North Area. These areas serve dual purposes, facilitating test beam experiments and housing detectors for research into non-Higgs phenomena such as dark matter, crystallography, and irradiation effects.

Proton beams circulate in opposite directions within two distinct beam lines, converging at four interaction points (IPs) where the primary experiments are stationed. The ALICE and LHCb detectors utilize two of the former LEP IPs, whereas the ATLAS and CMS detectors

reside in expanded caverns, repurposed from their original designs. At each IP, the beam lines intersect to enable collisions, which are then observed and analyzed by the respective experiments:

`Interaction point IP1` is the site for **A Toroidal LHC Apparatus (ATLAS)** [34], a versatile detector designed for various purposes, including the search and analysis of the Standard Model (SM) Higgs boson, conducting Quantum Chromodynamics (QCD) research, and exploring physics beyond the Standard Model (BSM). The ATLAS detector features a range of sub-detectors, each specialized in detecting and reconstructing specific particles or phenomena. Structurally, ATLAS is built around the interaction point with a series of concentric layers: an inner tracker followed by a Transition Radiation Tracker (TRT) utilizing both silicon and gaseous detection technologies. At its heart lies a sampling calorimeter, with an inner electromagnetic component using liquid Argon and an outer calorimeter made of steel tiles. This architectural decision marks a significant distinction from the CMS detector, which employs a homogeneous $PbWO_4$ electromagnetic calorimeter. Encircling the apparatus are muon chambers that give ATLAS its notable dimensions of 25 m in diameter and 46 m in length, highlighting another primary divergence from CMS. A 2 T solenoid magnet surrounds the interaction zone, while additional toroidal coils generate magnetic fields of up to 4 T beyond the solenoid.

Within the same vault as ATLAS, the **Large Hadron Collider forward (LHCf)** experiment [35] positions its detectors roughly 140 m from the IP. Comprising two detectors, each with a mass of 40 kg and dimensions of 30cm $\times$ 80cm $\times$ 10cm, LHCf's mission is to study the characteristics of ultra-high-energy cosmic rays.

`Interaction point IP2` is home to **A Large Ion Collider Experiment (ALICE)** [36], located at one of the sites previously used by LEP. ALICE has been specifically engineered for heavy-ion research, primarily to explore and understand the quark-gluon plasma (QGP), a form of matter believed to have existed in the early Universe. Distinguished by its suite of sub-detectors, which are not found in any other LHC experiment, ALICE's standout feature is its Time Projection Chamber (TPC). This TPC works alongside the inner tracking system to achieve accurate particle identification and separation. This capability is further enhanced by an array of calorimeters, along with Time of Flight (TOF) and Ring-imaging Cherenkov (RICH) detectors. Situated in the detector's very forward region is a muon spectrometer, offering additional insights into QGP through the analysis of heavy quarkonium state decay products.

`Interaction point IP5` serves as the site for the **Compact Muon Solenoid (CMS)** [37], positioned opposite to the ATLAS detector across the LHC ring. Both CMS and ATLAS function as multi-purpose detectors with the aim of probing a broad spectrum of physics phenomena. Despite their core mission alignment, the structural differences between the two facilities allow for the generation of complementary data. Further insights into CMS are elaborated in Sec. 2.2.

Co-located with CMS, and in part, integrated within its structure, is the **TOtal Elastic and diffractive cross section Measurement (TOTEM)** experiment [38]. TOTEM's name reflects its research objectives: the quantification of total cross section, elastic scattering, and diffractive processes in proton-proton collisions. The experiment utilizes cathode strip chambers (CSC) and Gas Electron Multipliers (GEM) across several stations to track particles emanating from the IP, assembling them into two telescopic arrays. Additionally, the TOTEM experiment employs Roman Pots—silicon-based sensors tasked with the detection of scattered protons.

`Interaction point IP8` is the venue for the **LHC beauty (LHCb)** experiment [39], situated in one of the erstwhile LEP caverns, similar to ALICE. LHCb's primary focus is on the intricacies of b-quark phenomena, probing for new physics beyond the Standard Model (BSM) or evidence of CP violation. Unlike ATLAS or CMS, LHCb is designed uniquely as a single-arm forward spectrometer to suit its specific research needs, given that b-hadrons are predominantly generated in the forward direction. The detector array extends over 20 m, starting from a sub-detector placed proximal to the IP. A key feature of LHCb is the Vertex Locator (VELO), a silicon-based movable tracking apparatus situated near the beam pipe, adept at identifying secondary decay vertices of b-hadrons.

Co-located with the LHCb, the **Monopole & Exotics Detector At the LHC (MoEDAL)** experiment [40] embarks on the quest to directly detect magnetic monopoles, theoretical entities endowed with magnetic charge. MoEDAL distinguishes itself as the seventh experiment to receive approval and installation at the LHC, underscoring its unique investigative purview.

Among the LHC experiments discussed, not all are equipped to handle the same levels of instantaneous luminosity and pileup rates. Specifically, ALICE and LHCb face constraints that preclude their operation at the standard LHC intensities. For ALICE, the limitation arises from the Time Projection Chamber (TPC) dead-time, and for LHCb, the bottleneck is due to the high particle flux overwhelming its data acquisition system. To manage these restrictions, a technique known as luminosity leveling is applied, wherein the beams are strategically sepa-

rated and directed to the detectors once the predefined luminosity thresholds are met. ALICE operates at a controlled instantaneous luminosity of approximately $L = 10^{27}\text{cm}^{-2}\text{s}^{-1}$, whereas LHCb is adjusted to a slightly higher rate of $L = 10^{32}\text{cm}^{-2}\text{s}^{-1}$.

2.2 The CMS experiment

Nestled 100 meters beneath the surface at Interaction Point 5, within the confines of Cessy, France, the Compact Muon Solenoid (CMS) detector stands as one of two versatile experiments stationed at the CERN LHC. Its mission: to track down the elusive Higgs boson and navigate the complexities of TeV-scale physics. Characterized by a cylindrical form, the CMS fully encapsulates IP5, measuring 15 meters in diameter and extending 21.5 meters in length. The term ”compact” in its name highlights its relatively smaller size compared to the ATLAS experiment, despite possessing a significantly heavier mass of 12,500 tons.

At the heart of CMS lies a superconducting solenoid magnet, generating a magnetic field of 4 T and encompassing various sub-detectors, each specialized in capturing specific particle types or measuring particular observables. Positioned immediately beyond the IP and within 6 meters of the coil, the inner tracking system is flanked by electromagnetic and hadronic calorimeters. Encircling the magnet, with an additional span of 7 meters, is the extensive muon detection subsystem, accounting for roughly 80% of the detector's total volume—hence, the ”muon” component of the CMS nomenclature. A cross-sectional view of the CMS setup, detailing these subsystems and more, is illustrated in Fig. 2.5.

2.2.1 Coordinate system

The CMS experiment utilizes a right-handed coordinate system, anchoring its origin at the nominal interaction point. The x-axis extends toward the LHC's center, the y-axis ascends vertically, and the z-axis aligns with the direction of the anticlockwise-moving proton beam. Accommodating the detector's cylindrical design, a polar coordinate framework is adopted alongside the Cartesian system. Here, the azimuthal angle ϕ represents the angle in the transverse plane relative to the x-axis, with r denoting the radial distance from the origin.

A graphical depiction of both the CMS Cartesian and polar coordinate systems is presented in Fig. 2.6(left).

This coordinate setup effectively delineates the detector's layout and large-scale measurements. However, it proves inadequate for pinpointing proton-proton collisions, which occur at the parton level, where the momentum fractions along the z-axis and the longitudinal colli-

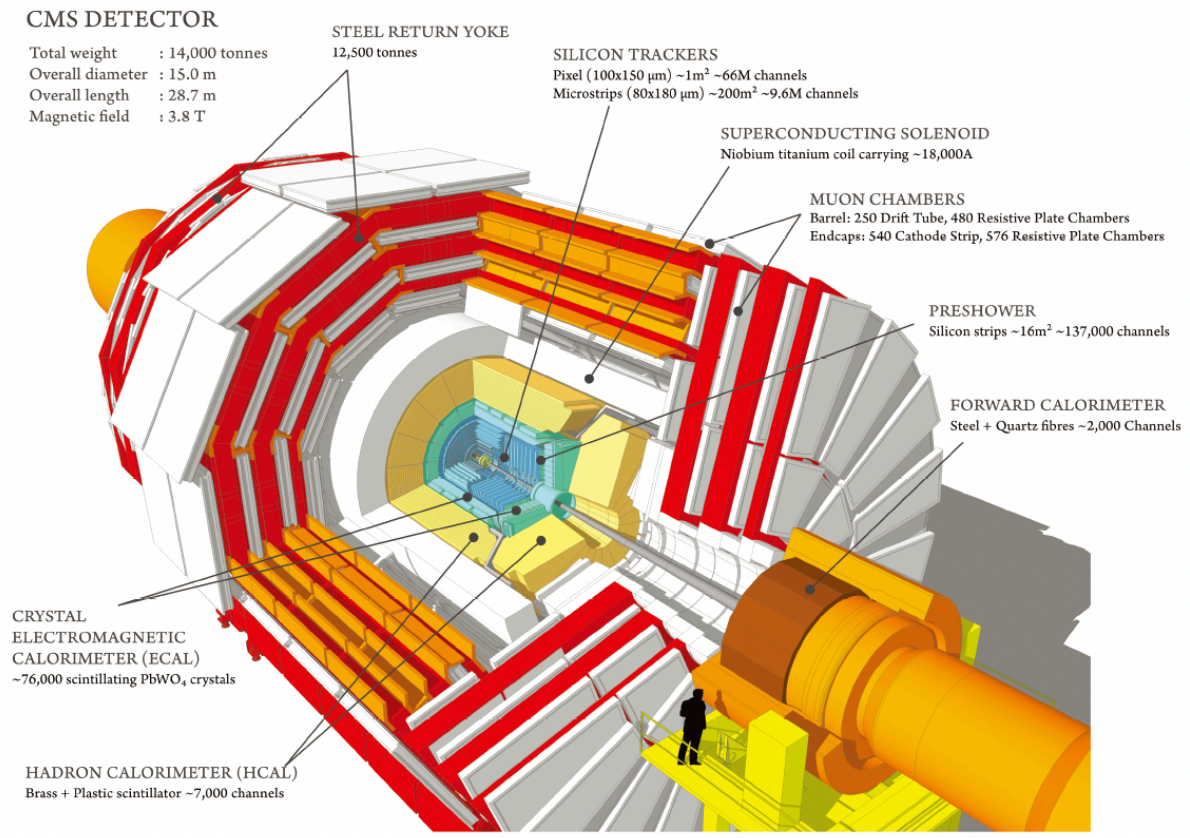

Figure 2.5 Schematic illlustration of the CMS at the CERN LHC. [41]

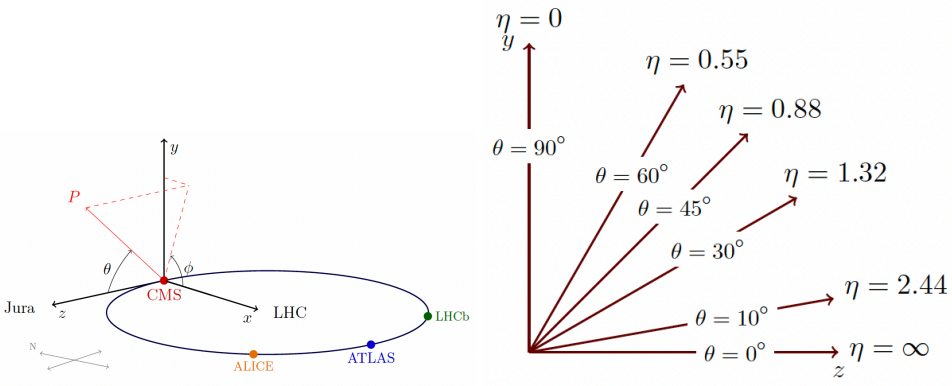

Figure 2.6 Left: Schematic representation of the CMS coordinate systems. [42] Right: Relation between the pseudorapidity η and the polar angle θ.

sion boost remain indeterminate. Consequently, collision events are better characterized using Lorentz boost-invariant metrics, focusing on transverse plane projections. This approach introduces the concepts of **transverse momentum** (p_T) and **transverse mass** (m_T), with the latter ranging from 0 at $\theta = \frac{\pi}{2}$ to $\pm\infty$ at $\theta = 0(\pi)$, as depicted in Fig. 2.6 (right). Particle spatial separation within a Lorentz boost-invariant context is determined based on their angular disparity.

$$\mathrm{p}_T^2 = \mathrm{p}_x^2 + \mathrm{p}_y^2 \tag{2.5}$$

$$m_T^2 = m^2 + \mathrm{p}_x^2 + \mathrm{p}_y^2 = E^2 - \mathrm{p}_z^2 \tag{2.6}$$

The rapidity of a particle is expressed as:

$$y = \frac{1}{2} \ln \left(\frac{E + \mathrm{p}_z}{E - \mathrm{p}_z} \right) \tag{2.7}$$

The polar angle is usually converted into **pseudorapidity**, i.e. the rapidity for ultra-relativistic ($m/E \ll 1$) particles:

$$\eta = -\ln \left[\tan \left(\frac{\theta}{2} \right) \right] = \frac{1}{2} \ln \left(\frac{p + p_z}{p - p_z} \right) \tag{2.8}$$

which varies from 0 at $\theta = \frac{\pi}{2}$ to $\pm\infty$ at $\theta = 0(\pi)$, as shown in Fig. 2.6 (right). The spatial separation between two particles is expressed, in a Lorentz boost-invariant frame, as a function of their angular distance as:

$$\Delta R = \sqrt{(\Delta\eta)^2 + (\Delta\phi)^2}. \tag{2.9}$$

Event topology gains an additional dimension through the negative aggregate of all reconstructed particles' transverse momenta, dubbed missing transverse momentum p_T^{miss}. Given the detector's symmetrical and enclosed nature around the interaction point, this variable is typically inferred as the collective transverse momentum of neutrinos or other undetectable non-interactive entities eluding detection.

2.2.2 Detector structure

The CMS detector is centered on a 4 T superconducting solenoid, which serves to curve the trajectories of particles passing through the various sub-modules comprising CMS. In the

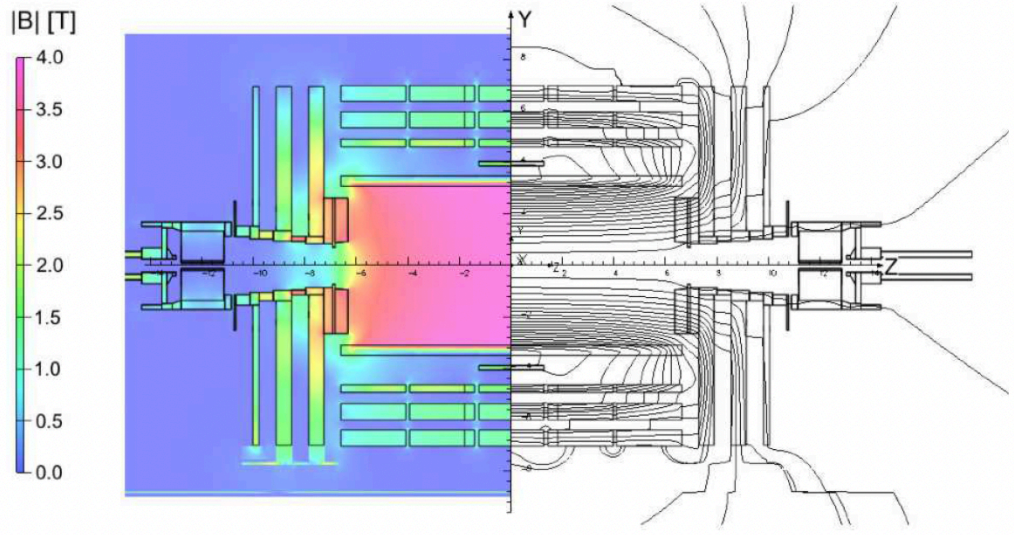

Figure 2.7 Longitudinal view of the CMS detector showing the magnetic $|B|$ field (left) and field lines (right). Central magnetic flux density of 3.8 T. Each field line represents an increment of 6 Wb of the total flux. Figure taken from [44].

subsequent sections, the diverse components will be delineated, with a special focus on their functions in detecting specific types of particles.

Superconducting magnet

At the heart of the CMS experiment lies its niobium-titanium (NbTi) superconducting solenoid magnet [43], a critical architectural and functional feature. This magnet, boasting a diameter of 6 meters and maintained at a chilly 4.5 K, is pivotal to the CMS detector's overall design. It encases the tracking and calorimetric apparatuses within its domain, providing a stable 3.8 T magnetic field. The iron return yoke, integral for containing this potent magnetic field, is interleaved with the muon detection array and positioned exterior to the NbTi magnet, subjecting the muon chambers to a 2 T magnetic environment. This arrangement yields distinct muon trajectories with varying curvature prior to and subsequent to their passage through the magnet.

In light of the magnet's innovative design and its prospective longevity concerns, the CMS team opted to maintain the magnetic field at a slightly reduced operational strength of 3.8 T, deviating from the initially proposed 4 T. The distribution and intensity of the magnetic field, deduced via Monte Carlo simulations, are illustrated in Fig. 2.7.

Inner tracking system

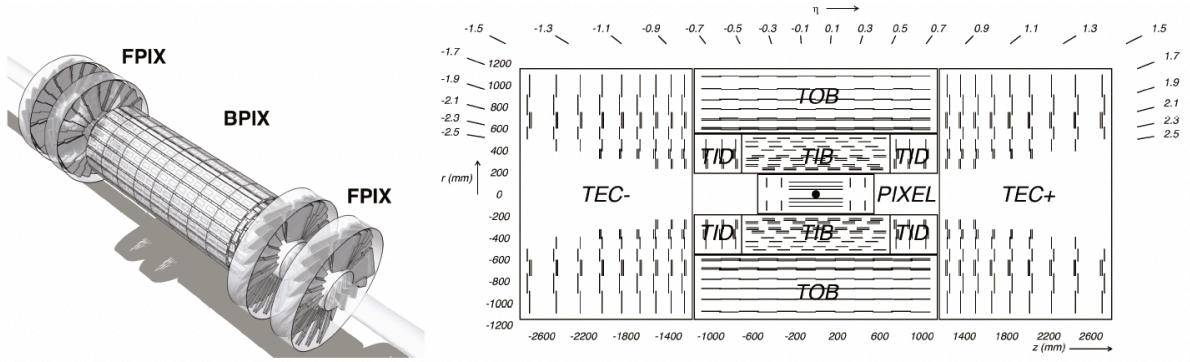

Figure 2.8 Left: Illustration of the CMS pixel tracking sub-system,three sylindrical layers are disposed in the barrel(BPix), while the endcaps are covered by two disks(FPix) on each side. Right: Schematic representation of the CMS tracking systems' cross section in the r-z plane. [47, 48]

Placed directly around the interaction point, the tracking system [45, 46] is the innermost part of the CMS detector. The CMS tracker covers a volume of 5.6 m in length and 2.4 m in diameter, and it is instrumented with silicon sensors, sensitive to the passage of charged particles originating from the interaction vertex. A uniform magnetic field of 3.8 T permeates the tracking volume, and it is used as an additional handle in the particles identification and reconstruction. The tracker also has to identify the in-flight decays and discriminate the hard scattering interactions vertex, also referred to as primary vertex, from additional pile-up collisions. As a result, the tracker is the sub-detector that has to cope with the most stringent requirements in terms of design, detection efficiency, and radiation hardness. The tracking system is dubdivided into two components to cope with these chanllenges: the pixel detectors and the silicon strip tracker, shown in Fig. 2.8.

`Electromagnetic calorimeter (ECAL)`

Enveloping the inner tracking apparatus, the Electromagnetic CALorimeter (ECAL) [49] is tasked with the high-precision energy determination of incoming electrons and photons. This homogeneous calorimeter is densely packed with nearly 70,000 lead tungstate ($PbWO_4$) crystals, a selection motivated by the necessity for a material of high density (ρ = 8.29 g/cm^3), minimal radiation length (X_0 = 0.89 cm), and compact Molière radius ($R_M \approx$ 2.2 cm). These characteristics are crucial for the complete absorption of electromagnetic showers and swift response, crucially emitting about 80

Divided into two semi-cylindrical segments, the ECAL Barrel (EB) is flanked by two endcap discs (EE). The EB is segmented into 18 super-modules, each clustering around 1700

crystals and weighing approximately 1.5 tons, arranged across 20 in ϕ and 85 in η. This configuration ensures an $|\eta| < 1.479$ and 20° coverage in ϕ. The EB in total harbors 62,000 crystals, with each crystal spanning 0.0174×0.0174 in $\eta \times \phi$, equivalent to a 22×22 mm^2 front face. The EE segments comprise 5×5 crystal groupings, or super-crystals, extending coverage from $1.479 < |\eta| < 3.0$. To achieve comprehensive coverage, ECAL crystals are angled up to 3° from the direct line of sight from the interaction point, though some gaps or *cracks* persist between modules and in critical areas like the $\eta = 0$ junction and the EB to EE transition zones.

To further refine spatial resolution in the $1.65 < |\eta| < 2.6$ region, an electromagnetic preshower detector (ES) is positioned ahead of the EE sections. Comprising two lead layers succeeded by a plane of silicon sensors equipped with 22 m long strips, the ES adds approximately $1X_0$ to the calorimeter's depth, complementing the tracker's $2X_0$. This setup ensures initiation of photon showers within the sensors for the majority of single incident photons. The ES's principal function is to discern di-photon emissions from $\pi^0 \to \gamma\gamma$ decays from singular, high-energy photons advancing forward. Silicon is chosen for its durability under high radiation, with the ES achieving optimal performance at temperatures ranging from $-15°$ C to $-10°$ C. Contributing significantly to electromagnetic shower reconstruction, the ES captures about 6% to 8% of the total shower energy.

The CMS ECAL intrinsic energy resolution was measured on a 3×3 crystals matrix in a test beam environment and it is parametrized as:

$$\left(\frac{\sigma_E}{E}\right)^2 = \left(\frac{2.8\%}{\sqrt{E}}\right)^2 + \left(\frac{12\%}{E}\right)^2 + (0.3\%)^2 \tag{2.10}$$

The initial component, termed *stochastic*, pertains to the statistical variances inherent in the shower's physical progression. The subsequent *noise* aspect derives from the electronic readout chain's background, closely tied to the Data Acquisition (DAQ) system's intricacies. Given its inverse relation to the energy of the shower, this noise becomes notably impactful at energies beneath the GeV threshold. The *constant* segment, unaffected by energy levels, mirrors the calorimeter's inherent characteristics, including response non-uniformities, potential energy losses, and lingering calibration discrepancies.

The CMS ECAL's homogeneous nature yields enhanced precision in energy reconstruction compared to sampling calorimeters, albeit at the sacrifice of detailed shower shape analysis or supplementary tracking points beyond those gleaned from the tracker's pixel and strips. Despite these design considerations, the primary challenge for the CMS ECAL lies in its initial

design to withstand luminosities up to 500 fb^{-1}, beyond which crystal degradation due to radiation becomes a significant concern. With the CMS poised to accumulate roughly 350 fb^{-1} by LHC Run-III's conclusion, an upgrade is imperative for the forthcoming High-Luminosity LHC (HL-LHC) phase. Plans include substituting the endcap calorimeters with a High Granularity Calorimeter (HGCAL), transitioning to a sampling architecture that facilitates comprehensive shower shape analysis. Moreover, the HGCAL will inaugurate precise timing capabilities, warranting its distinction as a *5D*, or *imaging calorimeter*.

Hadronic calorimeter (HCAL)

Hadronic showers typically impart no more than 30% of their energy into the ECAL. Positioned directly behind the ECAL, the CMS hadronic calorimeter (HCAL) [49] is engineered to completely capture the energy from hadronic showers. Its pivotal role in event reconstruction, particularly for hadronic jets and their neutral components, necessitates a substantial amount of material for full energy absorption. Hence, the HCAL is constructed as a sampling calorimeter, with alternating brass absorber layers and plastic scintillator tiles. The HCAL barrel (HB), located immediately beyond the ECAL within the solenoid's confines, extends the reach of the ECAL barrel (EB) in the barrel section, complemented by the HCAL endcap (HE) system adjacent to the ECAL endcaps (EE). The solenoid magnet imposes a significant design challenge for the HCAL, as the available depth of about 10 λ_i within the HB is insufficient for hadronic shower containment. An outer hadron calorimeter (HO), situated just outside the solenoid, addresses this by increasing the total depth to 11 λ_i, as depicted in Fig. 2.10(upper), enhancing hadronic jet absorption capabilities.

Additionally, the HCAL includes a very forward calorimeter (HF) located just beyond the CMS detector at a distance of 11.2 m from the interaction point, offering extended coverage in high-η regions. Fig. 2.10(lower) provides a detailed schematic of the CMS HCAL layout.

Muon detector system

Reflecting its moniker, the CMS detector is meticulously engineered for the precise identification and reconstruction of muons. Muons generated in typical LHC interactions span a broad energy spectrum, from a few to several hundred GeV, traversing the detector with relatively minimal interaction, save for slight imprints in the tracker and subsequent sub-systems. Their accurate identification, alongside the determination of their charge and momentum, is crucial for analyses involving W, Z, or H bosons, as well as in searches for novel physics phenomena.

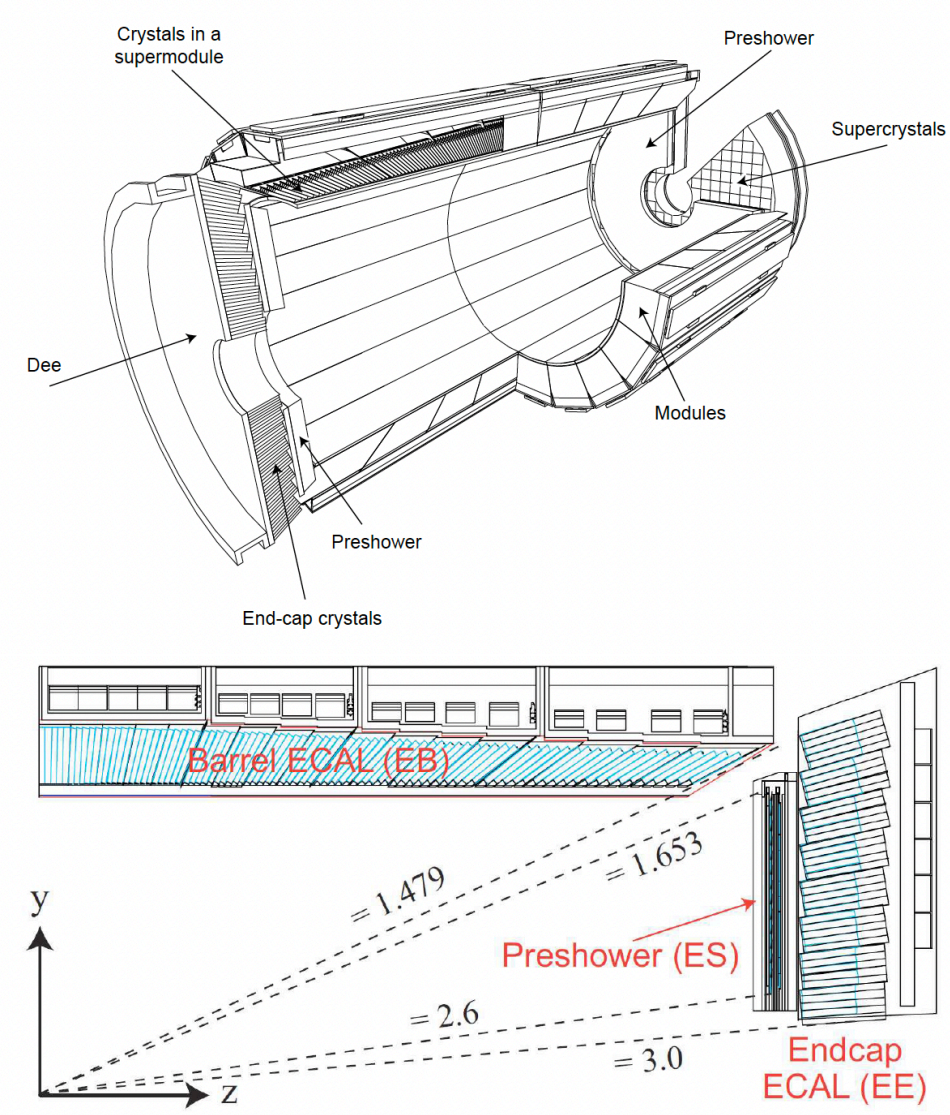

Figure 2.9 Upper: Schematic view of the CMS ECAL mechanical structure. The $PbWO_4$ crystals in the barrel are organized into modules and super-modules. In the endcaps a preshower is followed by two half-disks, or "Dees", on each side. [49] Lower: Schematic illustration of the spatial coverage of an ECAL quarter. The three sub-components of the ECAL are shown: barrel, preshower and endcap systems. $PbWO_4$ crystals are depicted in blue. [50]

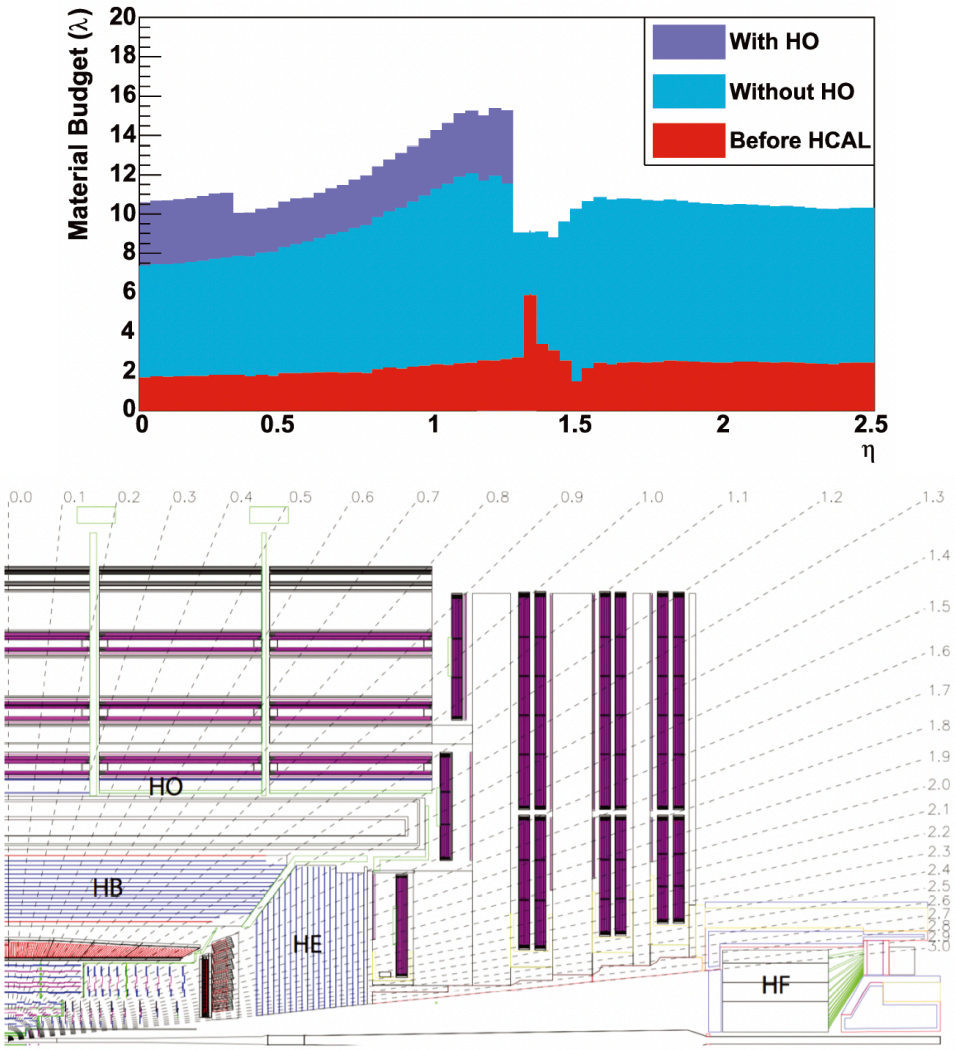

Figure 2.10 Upper: Material budget of the HCal with and without the HO. The introduction of the HO brings the material budget up to 11 λ_i everywhere in η, thus ensuring the complete absorption of the hadronic showers. [49] Lower: Illustration of a HCal quarter: the sub-modules that compose the detector are indicated, along with their coverage in pseudorapidity. [49]

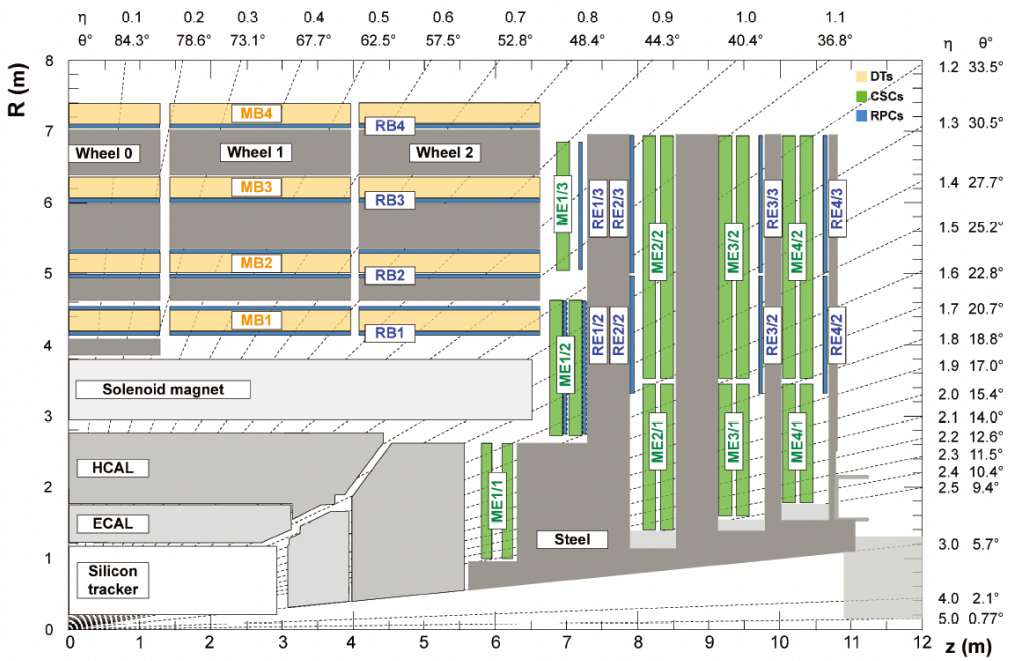

Figure 2.11 Schematic longitudinal view of a quater of the CMS detector with the layout of the muon detection systems. DTs, CSCs and RPCs are represented in onrange, green, and blue, respectively. [51]

Positioned in the detector's outermost layer, the muon detection system [51] consists of four stations nestled within the iron yokes, or *wheels*, leveraging the 2 T return magnetic field to deduce particle momentum based on trajectory curvature. The system's design navigates the balance between extensive coverage needs and cost efficiency. Incorporating three distinct gaseous detector technologies, the CMS muon detection ensemble features 1400 chambers arrayed to mitigate background rates and optimize magnetic field efficacy: Drift Tubes (DTs) envelop the barrel region up to $|\eta| < 1.2$, complemented by Cathode Strip Chambers (CSCs) in the endcaps for $0.9 < |\eta| < 2.4$, and Resistive Plate Chambers (RPCs) extending coverage to $|\eta| < 1.6$, thereby enhancing trigger functionality and providing system redundancy. Collectively, these components constitute approximately 25,000 m^2 of detection surfaces and achieve a depth of 20 λ_i in regions of low pseudorapidity. Fig. 2.11 illustrates the CMS muon detection system's layout.

The CMS detector's muon system employs 250 rectangular (2x2.5 m^2) Drift Tubes (DTs), organized into clusters of four stations across five *wheels* spanning the barrel area, with three illustrated in Fig. 2.16. Situated centrally, DTs cover up to $|\eta| < 1.2$, the low muon rates and magnetic fields in this sector ensuring satisfactory performance utilizing standard rectangular drift cells. Each cell, a drift tube of 2.4 m length and 1.3x4.2 cm^2 cross-section, comprises

an anode wire flanked by cathode strips, bathed in an Argon (85%) and CO_2 (15%) mix. DTs effectuate two-dimensional muon path tracing by measuring electron drift times to the anode. Beyond angle and position precision for muons, DTs also activate muon triggers independently from tracker data. Their layers, staggered with half-cell offsets, attain sub-3 ns time resolution, 99.8% cell efficiency, and around 180 μm spatial accuracy per cell, cumulating in 80-120 μm overall positional precision.

In the more challenging endcap region, subjected to heightened background activity and erratic magnetic fields as depicted in Fig. 2.8, finely segmented Multi Wire Proportional Cathode Strip Chambers (MWP CSCs) are deployed for $0.9 < |\eta| < 2.4$ coverage. CSCs' trapezoidal form and organization into four stations between iron yokes facilitate muon detection. Alternating anode wires and cathode strips layers yield η and r, ϕ data, respectively. Encompassing around 5000 m^2 and filled with an Argon (45%), CO_2 (50%), and CF_4 (10%) gas mix, CSCs offer fine resolution down to 40-150 μm and approximately 3 ns timing accuracy, enhancing trigger efficacy.

Supporting DTs and CSCs, Resistive Plate Chambers (RPCs) offer a standalone trigger system and clarify tracking in multi-hit scenarios. Positioned within both barrel and endcaps, RPCs supplement measurement redundancy. Barrel configurations see RPCs alongside the first two DT stations and preceding the drift chambers in the final pair, optimizing low-momentum muon trigger performance. Each endcap station hosts an RPC layer, all upgraded to four stations post-LS1. RPCs, double-gap chambers in avalanche mode with a $C_2H_2F_4$, $i-C_4H_{10}$, and SF_6 blend, surpass DT and CSC response speeds with under 3 ns time resolution and circa 1 cm spatial precision, proving invaluable for high-pileup muon event triggers.

By 2017's close, the muon system expansion included Gas Electron Multiplier (GEM) detectors within $1.6 < |\eta| < 2.2$, elevating endcap redundancy through superior rate capability and radiation tolerance. The initial 10 GEM prototypes set the stage for further additions during LS2, aiming for 144 detectors aligned with HL-LHC expectations. Further insights into GEM principles and enhancements are detailed in Chapter 5.

[51]

2.2.3 Luminosity measurement

For CMS, precise monitoring of both integrated and instantaneous luminosities is vital for real-time operations and detailed physics analysis. Instantaneous luminosity feedback plays a pivotal role in the Data Acquisition (DAQ) and trigger systems, guiding beam intensity adjust-

ments. Concurrently, the tally of reconstructed events is intrinsically linked to experimental luminosity levels.

Online luminosity measurement employs the Hadron Forward (HF) calorimeter in conjunction with two specialized luminometers: the Fast Beam Conditions Monitor (BCM1f) [52] and the Pixel Luminosity Telescope (PLT), the latter introduced before Run-II to enhance luminosity measurement precision [53–55]. This trio of detectors yields *in situ* insights into integrated luminosity. Offline analyses benefit from a more refined approach, integrating data from the pixel tracker and Drift Tubes (DTs), both of which are paired with a specialized readout system for expedited processing.

Luminosity calculations are conducted for each data collection phase, with systematic uncertainties ranging from 2.3% to 2.5%, varying by year. The influence of these uncertainties on analysis outcomes, along with their associated correlations, is thoroughly examined within the analysis segments.

Chapter 3 Search for the Higgs boson pair production associated with a vector boson

The discovery of the Higgs boson by the ATLAS and CMS collaborations in 2012 [56, 57] marked a pivotal milestone. Consequently, the focus of the scientific community has shifted towards conducting precise measurements of the properties of this newfound particle and its interactions.

To date, the experimentally determined characteristics of the Higgs boson are in concordance with the predictions of the standard model (SM). In Chapter 1, we introduced the production of a pair of Higgs bosons (HH) as an infrequent process that presents a unique opportunity to investigate specific couplings.

Of particular significance is the trilinear self-interaction coupling, which has the potential to provide a model-independent measurement of the shape of the scalar potential. This measurement could have implications for models involving a strong first-order phase transition, a pivotal element in baryogenesis [58]. Additionally, there is the four-boson coupling VVHH (ZZHH and WWHH), as predicted by the SM but not yet directly observed in experiments.

3.1 The properties of the VHH production mode

HH production predominantly occurs through gluon-gluon fusion (ggF), vector boson fusion (VBF), and vector boson-associated production (VHH). This analysis specifically focuses on VHH, complementing the findings obtained from ggF and VBF production processes.

In the SM, at a center-of-mass energy of $\sqrt{s} = 13$ TeV and for a Higgs boson mass of $m_H = 125$ GeV, the ggF cross section is calculated to be $\sigma_{ggF} = 31.05^{+2.2\%}_{-5.0\%}$ (scale) $\pm 3\%$ (PDF+α_s) $\pm 2.6\%$ (m_t) fb [59, 60]. This cross section is relatively small due to a significant destructive interference between the two leading-order diagrams. One of these diagrams is governed by the Higgs self-coupling (denoted as κ_λ), while the other involves a top-quark loop and depends solely on the top quark Yukawa coupling (y_t).

In the SM, at the same center-of-mass energy and for $m_H = 125$ GeV, the VBF cross section is calculated to be $\sigma_{VBF} = 1.726^{+0.03\%}_{-0.04\%}$ (scale) $\pm 2.1\%$ (PDF+α_s) fb, computed at the next-to-next-to-next-to-leading order (N3LO) of the QCD perturbative expansion [59, 60].

The SM cross section for VHH production mode is calculated to be $\sigma_{ZHH} = 0.363^{+3.4\%}_{-2.7\%}$

(scale) ±1.9% (PDF+α_s) fb, $\sigma_{W^+HH} = 0.329^{+0.32\%}_{-0.41\%}$ (scale) ±2.2% (PDF+α_s) fb, and $\sigma_{W^-HH} = 0.173^{+1.2\%}_{-1.3\%}$ (scale) ±2.8% (PDF+α_s) fb at NNLO QCD.

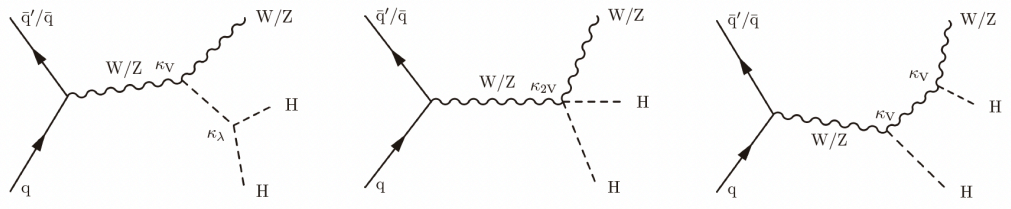

Figure 3.1 Leading-order diagrams for nonresonant di-Higgs production via VHH.

This analysis focuses on the final state with both Higgs bosons decaying into a b quark-antiquark pair, with a total branching fraction of $B(HH \to 4b) = 33.9 \pm 0.85\%$. The analysis is based on data from proton-proton collisions by the CERN LHC at a $\sqrt{s} = 13$ TeV, collected by the CMS experiment in 2016–2018, with an integrated luminosity of 138 fb^{-1}.

In Fig. 3.1, we present the three leading-order diagrams for nonresonant HH production via VHH. These diagrams encompass three distinct types of Higgs boson couplings: the Higgs boson self-coupling (HHH), the quartic coupling between two vector bosons and two Higgs bosons ($VVHH$), and the Higgs-vector-boson coupling (VVH). To describe the relative strength of these couplings compared to their Standard Model (SM) values, we introduce the coupling modifiers κ_λ, κ_{VV}, and κ_V for the HHH, VVHH, and VVH couplings, respectively. In the mean time, we also consider the box diagram contribution, which is also significant, shown and described in detail in the next section in Fig. 3.2.

Here, we emphasize three distinctive properties of this production mode, which also serve as compelling motivations for initiating this analysis with CMS Run-2 data.

The constructive interference: As discussed in Chapter 1.3, from Equation 1.41 to Equation 1.44, it is noteworthy that, in contrast to the leading cross-section production modes, the VHH production process exhibits constructive interference. With this particular property, as illustrated in Fig. 1.9, we anticipate that the analysis of this process could impose a relatively more stringent constraint on the positive side of κ_λ . Given the findings from existing analyses on the ggF and VBF processes, which suggest the absence of a "golden channel" akin to single Higgs studies in the HH investigation, the utilization of LHC Run-2 data for the study of the VHH production process holds significant value.

The HHWW and HHZZ vertex: As elucidated in Chapter 1.3, the VHH production process shares identical vertices with the VBF production, rendering it an apt candidate for the study and constraint of the HHVV coupling. Remarkably, in contrast to VBF, which solely

incorporates virtual vector bosons, VHH production provides a distinctive opportunity to disentangle the κ_{WW} and κ_{ZZ} couplings, contingent on the decay products of the vector bosons in the ”final states”.

The final states of W/Z boson: The presence of W/Z bosons in the final state not only affords the opportunity to unveil the HHWW/HHZZ vertices but also empowers analysts to capitalize on the reconstruction of the decay products of the W/Z bosons, particularly the leptons, for enhanced background constraint. From this perspective, the investigation of the VHH process represents a judicious trade-off between the challenges posed by its low cross section and the relatively purer signal it offers.

In summary, this analysis centers its attention on the VHH production process, encompassing all V decaying channels. The selection of the HH decay into a 4b final state is driven by its largest branching ratio. The overarching strategy involves segregating events into distinct V decaying channels, supplemented by other categorization techniques. Simultaneously, efforts are directed towards optimizing the signal-background ratios, with the overarching goal of attaining maximum significance.

3.2 Data sample and simulated events

This analysis relies on proton-proton collision data obtained during the years 2016 to 2018, within the framework of LHC Run 2, operating at a center-of-mass energy of $\sqrt{s}$ = 13 TeV. Only data that has been certified as high-quality, as specified in the golden JSON files listed in Table 3.1, has been chosen for inclusion in the analysis. Also the corresponding integrated luminosities for each year are listed. The total Run-2 luminosity sums up to 138 fb^{-1}. The datasets used for the analysis are listed in Table 3.2. In the table, various expressions pertain to the conditions of the data: "UL" stands for Ultra Legacy, which refers to the latest officially reconstructed dataset. The terms "HIPM" and "pre(post)-VFP" denote different phases of data collection. During these phases, certain events or objects may be excluded due to malfunctioning detectors.

Table 3.1 Golden JSON files used in the analysis and the corresponding integrated luminosities.

Year	File name	$\mathcal{L}$ (fb^{-1})
2016	`Cert_271036-284044_13TeV_Legacy2016_Collisions16_JSON.txt`	36.3 fb^{-1}
2017	`Cert_294927-306462_13TeV_UL2017_Collisions17_GoldenJSON.txt`	41.5 fb^{-1}
2018	`Cert_314472-325175_13TeV_Legacy2018_Collisions18_JSON.txt`	59.8 fb^{-1}

3.2.1 VHH signals

Simulated samples used for obtaining various VHH signal hypotheses are listed in Table 3.3. They are all generated at leading order (LO) in perturbative QCD using MadGraph generator. The signal cross sections σ multiplied by the branching fraction $\mathcal{B}$ into 4b final state are also provided. In signal sample names, the chosen benchmark values of the coupling modifiers are denoted as follows: `CV` refers to κ_V, `C2V` refers so κ_{VV} and `C3` refers to κ_λ.

In the analysis, the cross sections for signal samples featuring Standard Model-like couplings (`CV_1_C2V_1_C3_1`) are set to the current-best theoretical cross sections of 0.3657 fb (for ZHH, up to NNLO, which includes the contribution from the loop-induced gg $\rightarrow$ ZHH process) and 0.5193 fb (for WHH, at NLO). These values align with the cross sections provided by the LHCHWGHH [60] within uncertainties. The slight discrepancy arises from the use of the nominal PDF set, as our signals are generated with NNPDF 3.1 instead. Upon multiplication by the branching fraction $\mathcal{B}(\text{HH} \rightarrow \text{4b}) = 33.92\%$, these cross sections yield 0.1240 fb (for ZHH, NNLO) and 0.1761 fb (for WHH, NLO).

As mentioned, the cross sections of the ZHH and WHH production processes have been

Table 3.2 Primary Datasets

1L and 2L channels		
2016	2017	2018
/SingleMuon/Run2016B-ver1_HIPM_UL2016_[1]-v1	/SingleMuon/Run2017B-UL2017_[1]-v1	/SingleMuon/Run2018A-UL2018_[1]-v2
/SingleMuon/Run2016B-ver2_HIPM_UL2016_[1]-v1	/SingleMuon/Run2017C-UL2017_[1]-v1	/SingleMuon/Run2018B-UL2018_[1]-v2
/SingleMuon/Run2016C-UL2016_[1]-v1	/SingleMuon/Run2017D-UL2017_[1]-v1	/SingleMuon/Run2018C-UL2018_[1]-v2
/SingleMuon/Run2016D-UL2016_[1]-v1	/SingleMuon/Run2017E-UL2017_[1]-v2	/SingleMuon/Run2018D-UL2018_[1]-v2
/SingleMuon/Run2016E-UL2016_[1]-v1	/SingleMuon/Run2017F-UL2017_[1]-v2	
/SingleMuon/Run2016F-HIPM_UL2016_[1]-v1		
/SingleMuon/Run2016F-UL2016_[1]-v4		
/SingleMuon/Run2016G-UL2016_[1]-v1		
/SingleMuon/Run2016H-UL2016_[1]-v1		
/SingleElectron/Run2016B-ver1_HIPM_UL2016_[1]-v1	/SingleElectron/Run2017B-UL2017_[1]-v1	/EGamma/Run2018A-UL2018_[1]-v1
/SingleElectron/Run2016B-ver2_HIPM_UL2016_[1]-v1	/SingleElectron/Run2017C-UL2017_[1]-v1	/EGamma/Run2018B-UL2018_[1]-v1
/SingleElectron/Run2016C-UL2016_[1]-v1	/SingleElectron/Run2017D-UL2017_[1]-v1	/EGamma/Run2018C-UL2018_[1]-v1
/SingleElectron/Run2016D-UL2016_[1]-v1	/SingleElectron/Run2017E-UL2017_[1]-v2	/EGamma/Run2018D-UL2018_[1]-v2
/SingleElectron/Run2016E-UL2016_[1]-v2	/SingleElectron/Run2017F-UL2017_[1]-v3	
/SingleElectron/Run2016F-HIPM_UL2016_[1]-v1		
/SingleElectron/Run2016F-UL2016_[1]-v2		
/SingleElectron/Run2016G-UL2016_[1]-v1		
/SingleElectron/Run2016H-UL2016_[1]-v1		
/DoubleMuon/Run2016B-ver1_HIPM_UL2016_[1]-v1	/DoubleMuon/Run2017B-UL2017_[1]-v1	/DoubleMuon/Run2018A-UL2018_[1]-v1
/DoubleMuon/Run2016B-ver2_HIPM_UL2016_[1]-v1	/DoubleMuon/Run2017C-UL2017_[1]-v1	/DoubleMuon/Run2018B-UL2018_[1]-v2
/DoubleMuon/Run2016C-UL2016_[1]-v1	/DoubleMuon/Run2017D-UL2017_[1]-v1	/DoubleMuon/Run2018C-UL2018_[1]-v1
/DoubleMuon/Run2016D-UL2016_[1]-v1	/DoubleMuon/Run2017E-UL2017_[1]-v1	/DoubleMuon/Run2018D-UL2018_[1]-v1
/DoubleMuon/Run2016E-UL2016_[1]-v1	/DoubleMuon/Run2017F-UL2017_[1]-v1	
/DoubleMuon/Run2016F-HIPM_UL2016_[1]-v1		
/DoubleMuon/Run2016F-UL2016_[1]-v2		
/DoubleMuon/Run2016G-UL2016_[1]-v1		
/DoubleMuon/Run2016H-UL2016_[1]-v1		
/DoubleEG/Run2016B-ver1_HIPM_UL2016_[1]-v1	/DoubleEG/Run2017B-UL2017_[1]-v1	
/DoubleEG/Run2016B-ver2_HIPM_UL2016_[1]-v2	/DoubleEG/Run2017C-UL2017_[1]-v1	
/DoubleEG/Run2016C-UL2016_[1]-v1	/DoubleEG/Run2017D-UL2017_[1]-v1	
/DoubleEG/Run2016D-UL2016_[1]-v1	/DoubleEG/Run2017E-UL2017_[1]-v1	
/DoubleEG/Run2016E-UL2016_[1]-v1	/DoubleEG/Run2017F-UL2017_[1]-v1	
/DoubleEG/Run2016F-HIPM_UL2016_[1]-v1		
/DoubleEG/Run2016F-UL2016_[1]-v2		
/DoubleEG/Run2016G-UL2016_[1]-v1		
/DoubleEG/Run2016H-UL2016_[1]-v1		
MET channel		
2016	2017	2018
/MET/Run2016B-ver1_HIPM_UL2016_[1]-v1	/MET/Run2017B-UL2017_[1]-v1	/MET/Run2018A-UL2018_[1]-v2
/MET/Run2016B-ver2_HIPM_UL2016_[1]-v1	/MET/Run2017C-UL2017_[1]-v1	/MET/Run2018B-UL2018_[1]-v5
/MET/Run2016C-UL2016_[1]-v1	/MET/Run2017D-UL2017_[1]-v1	/MET/Run2018C-UL2018_[1]-v1
/MET/Run2016D-UL2016_[1]-v1	/MET/Run2017E-UL2017_[1]-v3	/MET/Run2018D-UL2018_[1]-v1
/MET/Run2016E-UL2016_[1]-v1	/MET/Run2017F-UL2017_[1]-v1	
/MET/Run2016F-HIPM_UL2016_[1]-v1		
/MET/Run2016F-UL2016_[1]-v2		
/MET/Run2016G-UL2016_[1]-v1		
/MET/Run2016H-UL2016_[1]-v1		
Full Hadronic channel		
2016	2017	2018
/BTagCSV/Run2016B-ver1_HIPM_UL2016_[1]-v1	/BTagCSV/Run2017B-UL2017_[1]-v1	/JetHT/Run2018A-UL2018_[1]-v1
/BTagCSV/Run2016B-ver2_HIPM_UL2016_[1]-v1	/BTagCSV/Run2017C-UL2017_[1]-v1	/JetHT/Run2018B-UL2018_[1]-v1
/BTagCSV/Run2016C-UL2016_[1]-v1	/BTagCSV/Run2017D-UL2017_[1]-v1	/JetHT/Run2018C-UL2018_[1]-v1
/BTagCSV/Run2016D-UL2016_[1]-v1	/BTagCSV/Run2017E-UL2017_[1]-v2	/JetHT/Run2018D-UL2018_[1]-v1
/BTagCSV/Run2016E-UL2016_[1]-v1	/BTagCSV/Run2017F-UL2017_[1]-v1	
/BTagCSV/Run2016F-HIPM_UL2016_[1]-v1		
/BTagCSV/Run2016F-UL2016_[1]-v2		
/BTagCSV/Run2016G-UL2016_[1]-v1		
/BTagCSV/Run2016H-UL2016_[1]-v1		

[1] MiniAODv2_NanoAODv9

corrected to NNLO and NLO, respectively. In practice, the (N)NLO k-factors have been derived using specially requested official production of signal NNLO and NLO samples with

Table 3.3 List of the simulated VHH signal samples and the corresponding cross sections times branching ratios ($\sigma \times \mathcal{B}$).

Dataset name	$\sigma \times \mathcal{B}$ [fb]
/ZHHTo4B_CV_0_5_C2V_1_0_C3_1_0_TuneCP5_13TeV-madgraph-pythia8/[1,2,3,4]	0.0788
/ZHHTo4B_CV_1_0_C2V_0_0_C3_1_0_TuneCP5_13TeV-madgraph-pythia8/[1,2,3,4]	0.0432
/ZHHTo4B_CV_1_0_C2V_1_0_C3_0_0_TuneCP5_13TeV-madgraph-pythia8/[1,2,3,4]	0.0729
/ZHHTo4B_CV_1_0_C2V_1_0_C3_1_0_TuneCP5_13TeV-madgraph-pythia8/[1,2,3,4]	0.1240
/ZHHTo4B_CV_1_0_C2V_1_0_C3_2_0_TuneCP5_13TeV-madgraph-pythia8/[1,2,3,4]	0.1990
/ZHHTo4B_CV_1_0_C2V_2_0_C3_1_0_TuneCP5_13TeV-madgraph-pythia8/[1,2,3,4]	0.3195
/ZHHTo4B_CV_1_5_C2V_1_0_C3_1_0_TuneCP5_13TeV-madgraph-pythia8/[1,2,3,4]	0.2713
/ZHHTo4B_CV_1_0_C2V_1_0_C3_20_0_TuneCP5_13TeV-madgraph-pythia8/[1,2,3,4]	5.6211
/WHHTo4B_CV_0_5_C2V_1_0_C3_1_0_TuneCP5_13TeV-madgraph-pythia8/[1,2,3,4]	0.1229
/WHHTo4B_CV_1_0_C2V_0_0_C3_1_0_TuneCP5_13TeV-madgraph-pythia8/[1,2,3,4]	0.0647
/WHHTo4B_CV_1_0_C2V_1_0_C3_0_0_TuneCP5_13TeV-madgraph-pythia8/[1,2,3,4]	0.1010
/WHHTo4B_CV_1_0_C2V_1_0_C3_1_0_TuneCP5_13TeV-madgraph-pythia8/[1,2,3,4]	0.1761
/WHHTo4B_CV_1_0_C2V_1_0_C3_2_0_TuneCP5_13TeV-madgraph-pythia8/[1,2,3,4]	0.2896
/WHHTo4B_CV_1_0_C2V_2_0_C3_1_0_TuneCP5_13TeV-madgraph-pythia8/[1,2,3,4]	0.4755
/WHHTo4B_CV_1_5_C2V_1_0_C3_1_0_TuneCP5_13TeV-madgraph-pythia8/[1,2,3,4]	0.3790
/WHHTo4B_CV_1_0_C2V_1_0_C3_20_0_TuneCP5_13TeV-madgraph-pythia8/[1,2,3,4]	8.9292
NLO and NNLO samples	$\sigma \times \mathcal{B}$ [fb]
/ZHHTo4B_CV_1_0_C2V_1_0_C3_1_0_TuneCP5_13TeV-amcatnlo-pythia8/[4]	0.1093
/WHHTo4B_CV_1_0_C2V_1_0_C3_1_0_TuneCP5_13TeV-amcatnlo-pythia8/[4]	0.1761
/ggHHTo4B_CV_1_0_C2V_1_0_C3_1_0_TuneCP5_13TeV-madgraph-pythia8/[4]	0.0148

[1] `RunIISummer20UL16NanoAODAPVv9-106X_mcRun2_asymptotic_preVFP_v11-v*`
[2] `RunIISummer20UL16NanoAODv9-106X_mcRun2_asymptotic_v17-v*`
[3] `RunIISummer20UL17NanoAODv9-106X_mc2017_realistic_v9-v*`
[4] `RunIISummer20UL18NanoAODv9-106X_upgrade2018_realistic_v16_L1v1-v*`

SM-like couplings, as listed in Table 3.3. Utilizing the MadGraph generator, the LO cross sections are calculated to be 0.2701 fb for ZHH and 0.4253 fb for WHH, in SM-like couplings, without considering the branching fraction. The (N)NLO k-factors, approximately 1.354 and approximately 1.221, are derived and scaled to the signal ZHH and WHH samples for normalization. These values can be easily computed using the cross section provided at each level, as specified in Table 3.4.

Table 3.4 Cross section of SM ZHH and WHH processes

Process	LO (fb)	NLO (fb)	NNLO (fb)	NLO+NNLO (fb)
ZHH	0.2701	0.3222	0.0435	0.3657
WHH	0.4253	0.5193	-	0.5193

The (N)NLO k-factor is further determined as a function of the transverse momentum of the Z and W bosons at the generator level, owing to the differences in kinematics induced by the NLO and gluon fusion processes, as depicted in Fig. 3.3. Specifically, the vector boson experiences greater boosting when the loop-induced process is included, while the NLO correction predominantly contributes to a larger cross section. For the ZHH process, the NNLO k-factor increases up to approximately 1.5 starting from a p_T of around 150 GeV, whereas the NLO k-factor of the WHH sample remains approximately 1.2 across the p_T spectrum of the W boson. Following signal selection, any residual discrepancy from NNLO reweighting is factored in as a systematic uncertainty on the ZHH signals. Further details are elaborated upon in Appendix .1.

The gluon-fusion ZHH process (ggZHH) typically exhibits a larger average transverse momentum ($p_T(Z)$) than ZHH production at NLO. A representative diagram for ggZHH is shown in Fig. 3.2 on the left. Both the NLO and ggZHH contributions are accounted for by adjusting the LO ZHH samples. Initially, the LO simulated signals are scaled to NLO in perturbative QCD using a constant factor. Subsequently, they are reweighted as functions of $p_T(Z)$ to differentially incorporate the NNLO cross section enhancement. The comparison between NLO and NLO+ggZHH is depicted on the right of Fig. 3.2, where the ratios in the bottom panel represent the function utilized to reweight the NLO signals.

Regarding other signal samples with modified couplings, the LO cross sections provided by the MadGraph generator are likewise adjusted using the same k-factor. This scaling methodology, along with the resulting values, is in line with other non-resonant double Higgs analyses.

The continuous scans of Higgs couplings, such as the κ_λ coupling, are conducted using the

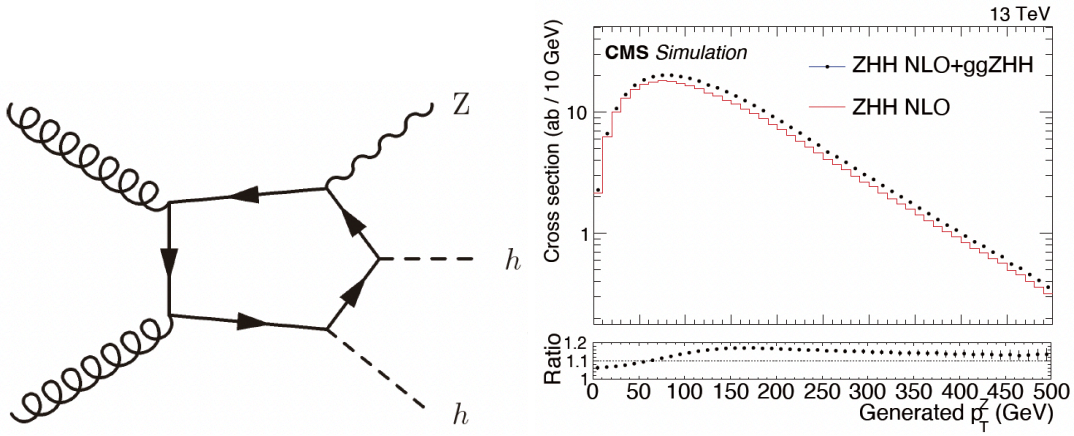

Figure 3.2 Left: A representative diagram illustrating ZHH production initiated by gluon-fusion via a quark loop, constituting approximately 14% of the total cross section for ZHH production. Right: Distribution of $p_T(Z)$ with and without the ggZHH process. The ratio is applied to NLO to incorporate the ggZHH cross section enhancement.

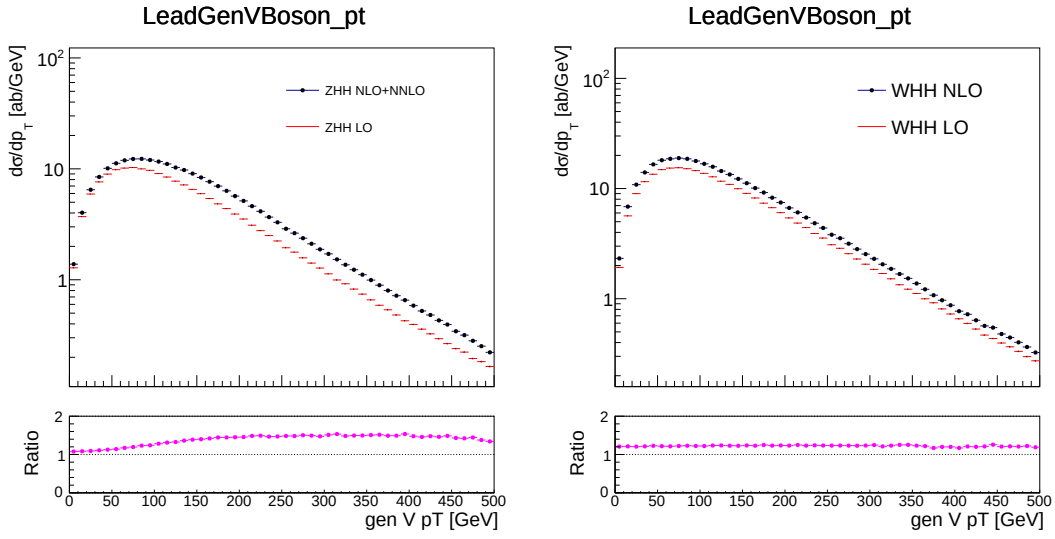

Figure 3.3 Distributions of transverse momentum of the Z and W bosons comparing between (N)NLO and LO at generator level and scale to 1 ab^{-1}. The ratio plots are used as the k-factor to scale all signal samples (both normalisation and shape corrections).

`HHinference` toolkit [61], which relies on a specific `HHModel`, a physics model implemented in the Combine tool. With these tools, any particular signal hypothesis (with desired values of κ_V, κ_{VV}, and κ_λ) can be constructed as a linear combination of six signal hypotheses with specific combinations of these couplings, corresponding to six signal samples provided as input.

Alternatively, we can utilize more than six signal samples through the Moore–Penrose inverse method [62, 63]. In this analysis, we opt to utilize all the signal samples to better model signal hypotheses at large coupling values. To ensure that this reweighting method adequately models all coupling points, we have conducted a validation of this method in the subsequent subsection.

The VHH signal samples are generated at LO [64] using `MG5_aMCNLO` v2.4.2. The simulated samples are generated for different combinations of the coupling modifier values (κ_λ , κ_V, κ_{VV}). Similarly to what is done for the ggF HH samples generated at NLO, samples corresponding to any point in the (κ_λ , κ_V, κ_{VV}) parameter space can be obtained as a linear combination of any six of the generated samples. The cross section can be described as:

$$\sigma(\kappa_\lambda, \kappa_V, \kappa_{VV}) = \left(\kappa_V^2\kappa_\lambda^2, \kappa_V^4, \kappa_{VV}^2, \kappa_V^2\kappa_\lambda^3, \kappa_V\kappa_\lambda\kappa_{VV}, \kappa_V^2\kappa_{VV}\right) \cdot \begin{pmatrix} a \\ b \\ c \\ i_{ab} \\ i_{ac} \\ i_{bc} \end{pmatrix} \tag{3.1}$$

where a, b and c are the squared amplitude terms and i_{ab}, i_{ac}, and i_{bc} are the interference terms. We can rewrite Eq. 3.1 as:

$$\sigma(\kappa_\lambda, \kappa_V, \kappa_{VV}) = c(\kappa_\lambda, \kappa_V, \kappa_{VV})\mathbf{v} \tag{3.2}$$

where $c(\kappa_\lambda, \kappa_V, \kappa_{VV}) = (\kappa_V^2\kappa_\lambda^2, \kappa_V^4, \kappa_{VV}^2, \kappa_V^2\kappa_\lambda^3, \kappa_V\kappa_\lambda\kappa_{VV}, \kappa_V^2\kappa_{VV})$ is a vector of the coupling functions and $\mathbf{v} = (a, b, c, i_{ab}, i_{ac}, i_{bc})$ is a vector of the values of the six components. Therefore, the total cross section corresponding to $(\kappa_\lambda, \kappa_V, \kappa_{VV})$ can be obtained as a linear combination of the six samples generated with different values of couplings as:

$$\sigma(\kappa_\lambda, \kappa_V, \kappa_{VV}) = \mathbf{c}^T(\kappa_\lambda, \kappa_V, \kappa_{VV})\mathbf{C}^{-1}\sigma \tag{3.3}$$

Signal reweighting validation

Validation plots of signal reweighting are presented in Fig. 3.4.

For each of the 8 signal samples, the distribution of some observables is compared with their reweighted counterpart. The original distribution is shown with solid circular dots, and the reweighted distribution is shown with open rectangular markers. From the ratio plots at the bottom of each plot, we can see that the difference between MC and reweighted signals is less than 10% across all observables.

The implementation of this signal reweighting in `HHinference` is validated and shown in Section 3.8.

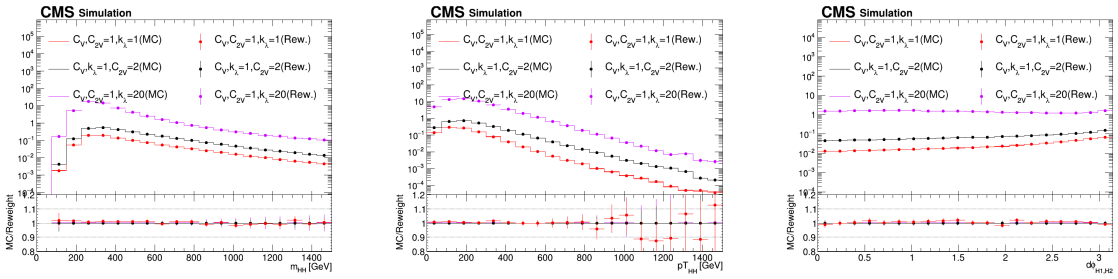

Figure 3.4 A comparison between true signals and reweighted signals (WHH+ZHH). The solid lines represent the original signal and dots represent the corresponding reweighted signal at each coupling point.

3.2.2 Backgrounds Processes

There are several background processes that significantly contribute to the analysis. We treat them differently to achieve the best background modeling performance before proceeding to the final fit, as effective background modeling can be crucial to the final results. Table 3.5 lists the main samples generated using Monte Carlo methods for further study, with the `DY+Jets` process listed separately due to specific operations.

In general, three dominant background processes are identified: $t\bar{t}$, `DY+Jets`, and QCD Multijets. The QCD process will be modeled using a data-driven method, while simulation samples will be employed for the other two. Various measurements are conducted for the $t\bar{t}$ and `DY+Jets` processes to enhance their modeling accuracy. In this paragraph, we introduce the most significant measurements; the minor ones will be introduced in the following sections.

$t\bar{t}$+jets Samples

$t\bar{t}$+jets production constitutes the primary background process in this analysis within the leptonic channels. It is simulated using Monte Carlo (MC) methods. Of particular significance are $t\bar{t}$ events accompanied by additional b-jet production: the count of b-jets mirrors that of

Table 3.5 List of partial simulated Background samples and the corresponding cross sections times branching ratios ($\sigma \times \mathcal{B}$).

Dataset name	$\sigma \times \mathcal{B}$ [fb]	k-factor
/TTToHadronic_TuneCP5_13TeV-powheg-pythia8/[1,2,3,4]	377.96	
/TTTo2L2Nu_TuneCP5_13TeV-powheg-pythia8/[1,2,3,4]	88.29	
/TTToSemiLeptonic_TuneCP5_13TeV-powheg-pythia8/[1,2,3,4]	365.34	
/TTbb_4f_TTTo2L2Nu_TuneCP5-Powheg-Openloops-Pythia8/[1,2,3,4]	2.74	
/TTbb_4f_TTToSemiLeptonic_TuneCP5-Powheg-Openloops-Pythia8/[1,2,3,4]	11.33	
/TTbb_4f_TTToHadronic_TuneCP5-Powheg-Openloops-Pythia8/[1,2,3,4]	11.72	
/TTWJetsToLNu_TuneCP5_13TeV-amcatnloFXFX-madspin-pythia8/[1,2,3,4]	0.2043	
/TTWJetsToQQ_TuneCP5_13TeV-amcatnloFXFX-madspin-pythia8/[1,2,3,4]	0.4062	
/TTZToLLNuNu_M-10_TuneCP5_13TeV-amcatnlo-pythia8/[1,2,3,4]	0.2529	
/TTZToQQ_TuneCP5_13TeV-amcatnlo-pythia8/[1,2,3,4]	0.5297	
/ttHTobb_M125_TuneCP5_13TeV-powheg-pythia8/[1,2,3,4]	0.295	
/ST_tW_antitop_5f_NoFullyHadronicDecays_TuneCP5_13TeV-powheg-pythia8/[1,2,3,4]	19.56	
/ST_tW_top_5f_NoFullyHadronicDecays_TuneCP5_13TeV-powheg-pythia8/[1,2,3,4]	19.56	
/ST_s-channel_4f_leptonDecays_TuneCP5_13TeV-amcatnlo-pythia8/[1,2,3,4]	3.36	
/ST_t-channel_eleDecays_TuneCP5_13TeV-comphep-pythia8/[1,2,3,4]	24.8	
/ST_t-channel_muDecays_TuneCP5_13TeV-comphep-pythia8/[1,2,3,4]	24.8	
/ST_t-channel_tauDecays_TuneCP5_13TeV-comphep-pythia8/[1,2,3,4]	24.8	
/ST_t-channel_antitop_4f_InclusiveDecays_TuneCP5_13TeV-powheg-madspin-pythia8/[1,2,3,4]	80.95	
/ST_t-channel_top_4f_InclusiveDecays_TuneCP5_13TeV-powheg-madspin-pythia8/[1,2,3,4]	136.02	
/ZJetsToNuNu_HT-100To200_TuneCP5_13TeV-madgraphMLM-pythia8/[1,2,3,4]	302.8	0.93
/ZJetsToNuNu_HT-200To400_TuneCP5_13TeV-madgraphMLM-pythia8/[1,2,3,4]	92.59	0.93
/ZJetsToNuNu_HT-400To600_TuneCP5_13TeV-madgraphMLM-pythia8/[1,2,3,4]	13.18	0.93
/ZJetsToNuNu_HT-600To800_TuneCP5_13TeV-madgraphMLM-pythia8/[1,2,3,4]	3.257	0.93
/ZJetsToNuNu_HT-800To1200_TuneCP5_13TeV-madgraphMLM-pythia8/[1,2,3,4]	1.496	0.93
/ZJetsToNuNu_HT-1200To2500_TuneCP5_13TeV-madgraphMLM-pythia8/[1,2,3,4]	0.3419	0.93
/ZJetsToNuNu_HT-2500ToInf_TuneCP5_13TeV-madgraphMLM-pythia8/[1,2,3,4]	0.005146	0.93

[1] `RunIISummer20UL16NanoAODAPVv9-106X_mcRun2_asymptotic_preVFP_v11-v*`
[2] `RunIISummer20UL16NanoAODv9-106X_mcRun2_asymptotic_v17-v*`
[3] `RunIISummer20UL17NanoAODv9-106X_mc2017_realistic_v9-v*`
[4] `RunIISummer20UL18NanoAODv9-106X_upgrade2018_realistic_v16_L1v1-v*`

the VHH signal events, and modeling these events presents theoretical challenges due to the multi-parton final state with two vastly different energy scales.

A sophisticated $t\bar{t}$+jets Background Model was devised in the $t\bar{t}/t\bar{t}H(bb)$ Analysis. We will adopt their methodology in this study.

The overarching approach is as follows: An exclusive $t\bar{t}+b\bar{b}$ simulation at next-to-leading order (NLO) in the four flavor scheme (4FS) is dedicated to modeling the $t\bar{t}$ + b jets events, while an inclusive $t\bar{t}$ simulation at NLO in the five flavor scheme (5FS) is utilized to depict the entire $t\bar{t}$+jets background, encompassing the $t\bar{t}$ + b-jets events already accounted for in the exclusive $t\bar{t}$ + $b\bar{b}$ simulation. A merging technique has been devised to amalgamate both sets of samples, ensuring comprehensive coverage of the $t\bar{t}$+jets phase space without redundancies. This amalgamated dataset is denoted as the merged $t\bar{t}$+jets sample.

While the $t\bar{t}$ + $b\bar{b}$ simulation is expected to provide a more accurate modeling of the kinematics of such events, the same cannot be assumed for the cross-section prediction. Hence, the merged $t\bar{t}$+ jets sample is scaled to match the latest $t\bar{t}$ inclusive cross-section calculation (NNLO+NNLL) computed in the 5FS scheme. Essentially, the dedicated $t\bar{t}$ + $b\bar{b}$ simulation is employed to characterize the shapes of the kinematic distributions of $t\bar{t}$ + b-jets events, while the normalization of this process is adjusted to align with the yield predicted by the inclusive $t\bar{t}$+ jets 5FS sample.

The merging procedure has been outlined in Refs. [65, 66]. $t\bar{t}$ + B events are defined as events with at least one additional b jet satisfying $p_T > 20$ GeV and $\eta < 2.4$. Essentially, it involves substituting the $t\bar{t}$ + B events from the dedicated $t\bar{t}$ + $b\bar{b}$ sample into the inclusive $t\bar{t}$ sample.

The $t\bar{t}$ + B events (i.e., those being replaced) are weighted such that their yield matches the yield of the corresponding (replaced) $t\bar{t}$ + B component in the inclusive $t\bar{t}$ sample. Consequently, the overall yield of all $t\bar{t}$ + X events remains constant. The normalization of the $t\bar{t}+B$ component is kept free-floating in the final fit. The procedure is depicted in Fig. 3.5, and Table. 3.6 illustrates the weight for the exclusive $t\bar{t}+b\bar{b}$ sample, with an average value of 1.32.

Table 3.6 ttbb 4FS initial normalization factor to match tt 5FS yield.

Sample	ttbb_AllHadronic	ttbb_DiLep	ttbb_SingleLep
2018	1.26	1.26	1.16
2017	1.05	1.18	1.20
2016PreVFP	1.21	1.16	1.18
2016PostVFP	1.26	1.20	1.20

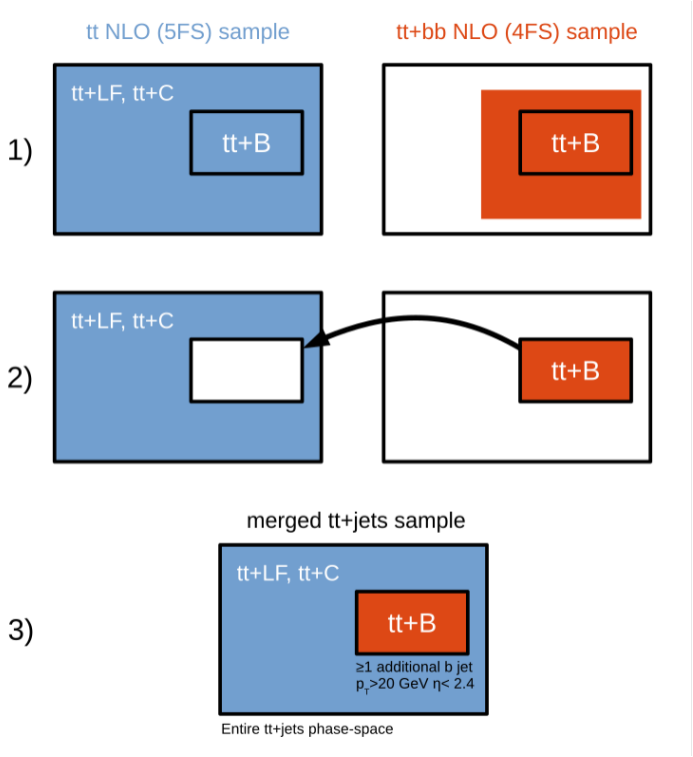

Figure 3.5 Illustration of the procedure to merge the $t\bar{t} + b\bar{b}$ and $t\bar{t}$ samples.

V+jets Samples

V+jets constitutes an irreducible background for the VHH signal, particularly prominent in the 2-lepton channel. The cross-section of single V boson production is known at next-to-next-to-leading order (NNLO) precision at 13 TeV:

- $\sigma(pp \rightarrow Z + X) = 1906\text{pb}$
- $\sigma(pp \rightarrow W^{\pm} + X) = 20080\text{pb}$

The VHH analysis encompasses phase spaces corresponding to high p_T of the V boson or large values of the invariant mass, especially in boosted topologies. To fully exploit the sensitivity of all regions, it is crucial to minimize statistical fluctuations of the background prediction compared to those in the data. To achieve this, the generation of the MadGraph V+jets samples involves splitting the events according to the scalar sum of the p_T of the jets in the event, denoted as H_T:

[0-70, 70-100, 100-200, 200-400, 400-600, 600-800, 800-1200, 1200-2500, >2500] GeV

All LO samples are subsequently reweighted to match the NLO samples over $p_T(V)$ (LHE_Vpt), resulting in softer samples and improved agreement with data. The NLO samples used are detailed in Table 3.8. Following this, the effect of the NNLO correction is incorporated

Table 3.7 2018 simulation summary for V+ jets

Sample Name	**Xsec(pb)**	**KFactor**
DYJetsToLL_M-10to50[1]	15810.0	0.93
DYJetsToLL_M-50[1]	5343.0	0.93
DYJetsToLL_M-50_HT70to100[1]	146.5	0.93
DYJetsToLL_M-50_HT100to200[1]	160.8	0.93
DYJetsToLL_M-50_HT200to400[1]	48.63	0.93
DYJetsToLL_M-50_HT400to600[1]	6.982	0.93
DYJetsToLL_M-50_HT600to800[1]	1.756	0.93
DYJetsToLL_M-50_HT800to1200[1]	0.8094	0.93
DYJetsToLL_M-50_HT1200to2500[1]	0.1931	0.93
DYJetsToLL_M-50_HT2500toInf[1]	0.003513	0.93

[1] `_TuneCP5_PSweights_13TeVmadgraphMLM-pythia8`

through the k-Factor, as shown in Table 3.7.

The weights are derived individually for each vector boson decay channel and jet flavor composition. Jet flavor is determined by generator-level jets above 20 GeV within the detector acceptance $|\eta| < 2.4$. The same jet selection criteria are applied to categorize the nB multiplicity as detailed in Table 3.9.

Table 3.8 NLO sample

Sample Name	**Xsec(pb)**	**KFactor**
DYJetsToLL_0J[1]	-	1.0
DYJetsToLL_1J[1]	-	1.0
DYJetsToLL_2J[1]	-	1.0
DYJetsToLL_M-50[1]	-	1.0
DYJetsToLL_Pt-50To100[2]	-	1.0
DYJetsToLL_Pt-100To250[2]	-	1.0
DYJetsToLL_Pt-250To400[2]	-	1.0
DYJetsToLL_Pt-400To650[2]	-	1.0
DYJetsToLL_Pt-650ToInf[2]	-	1.0

[1] `_TuneCP5_13TeV-amcatnloFXFX-pythia8`
[2] `_MatchEWPDG20_TuneCP5_13TeV-amcatnloFXFX-pythia8`

Table 3.9 NLO sample

Channel	**nB**	**NLO/LO**
DYJetsToLL	0	$1.650 \pm 0.002 - (1.707 \pm 0.020) \times 10^3 pT(\mathrm{V})$
DYJetsToLL	1	$1.534 \pm 0.010 - (1.458 \pm 0.080) \times 10^3 pT(\mathrm{V})$
DYJetsToLL	2	$1.519 \pm 0.019 - (1.916 \pm 0.140) \times 10^3 pT(\mathrm{V})$

Linear functions, specified in Table 3.9, are applied as event weights to the LO samples. Their uncertainties are primarily driven by the limited size of the NLO sample. Figure 3.6 illustrates the effect of the NLO correction on the `DY+Jets` sample.

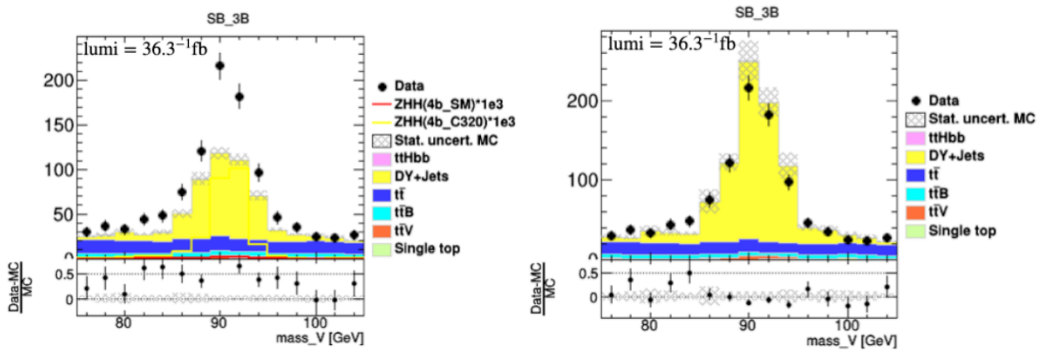

Figure 3.6 The comparison of Data and MC estimated background in some certain regions without(left) and with(right) the NLO correction on `DY+Jets` sample with 2016 data and MC.

3.3 Event reconstruction and selection

Global event reconstruction, employing the particle-flow (PF) algorithm [67], aims to reconstruct and identify individual particles within an event by optimizing information from sub-detectors. Particle identification is crucial in determining the particle direction and energy.

Photons are identified as energy clusters in the electromagnetic calorimeter (ECAL) not associated with charged particle trajectories. Electrons are identified as primary tracks with corresponding ECAL energy clusters, accounting for bremsstrahlung photons within the tracker material. Muons are recognized as tracks consistent with either muon system hits or tracks with calorimeter deposits consistent with the muon hypothesis. Charged hadrons are identified as tracks distinct from electrons or muons, while neutral hadrons are recognized as HCAL energy clusters without associated charged hadron trajectories or as an aggregate of ECAL and HCAL energy exceeding the expected charged hadron energy deposit.

3.3.1 The VHH decay channels

In this VHH study, the leptons, jets (especially b-jets), and missing transverse momentum are the most important objects.

With the aim of achieving improved performance, we segment the entire analysis into different vector boson decay channels and make further modifications based on their individual characteristics. For the standard model (SM) vector boson decays, we consider both leptonic and hadronic decays. This includes $W^{\pm}$ boson decays into a single lepton and a neutrino(**1L channel**), Z boson decays into two leptons(**2L channel**) or two neutrinos(**MET channel**), and $W^{\pm}/Z$ decays into quarks(**FH channel**).

Electron

Electrons are reconstructed with the Gaussian Sum Filter algorithm (GSF Electrons). They are pre-selected by requiring $p_T > 7$ GeV, $|\eta| < 2.4$, $d_{xy} < 0.05\,\text{cm}$, $d_z < 0.2\,\text{cm}$ (where both distances are measured with respect to the primary vertex), and a very loose relative isolation cut of 0.4, where the ρ-subtracted PF isolation in a cone of radius 0.3 is used.

A general-purpose multivariate discriminator is trained for electrons that pass a set of cuts intended to include all electrons desired for standard analyses. A set of offline cuts on ECAL-based electron quantities is then applied on top of the multivariate discriminator to reproduce the conditions of the training sample:

```
    pt>15 & (
(abs(superCluster().eta)<1.4442 & full5x5_sigmaIetaIeta<0.012 &
```

```
hcalOverEcal<0.09 &
(ecalPFClusterIso/pt)<0.4 & (hcalPFClusterIso/pt)<0.25 &
(dr03TkSumPt/pt)<0.18 & abs(deltaEtaSuperClusterTrackAtVtx)<0.0095 &
abs(deltaPhiSuperClusterTrackAtVtx)<0.065) ||
(abs(superCluster().eta)>1.5660 & full5x5_sigmaIetaIeta<0.033 &
hcalOverEcal<0.09 &
(ecalPFClusterIso/pt)<0.45 & (hcalPFClusterIso/pt)<0.28 &
(dr03TkSumPt/pt)<0.18)
).
```

Two cuts on the MVA ID discriminator are applied to define two different working points based on the expected selection efficiency of either 90% (loose, WP90) or 80% (tight, WP80).

The loose WP90 working point is utilized for global event classification (based on vector boson type and decay), in the counting of additional leptons for the veto requirement, and in the event selection of the $Z(ee)$HH channel. The tighter WP80 working point is employed in the $W(e\nu)$HH channel to suppress the fake background in that final state. The p_T threshold in the $W(e\nu)$HH channel is 32 GeV (2017/2018) and 28 GeV (2016). For the $Z(ee)$HH channel, thresholds are looser at 23 GeV and 14 GeV for the two electrons. For the 2017 analysis, we use the mvaFall17V2Iso_WPXX working points with channel-specific isolation cuts (pfRelIso03_all < 0.06 for $W(e\nu)$HH and pfRelIso03_all < 0.15 for $Z(ee)$HH). Working points and isolation cuts for 2-lepton channels are generally looser because requiring two leptons virtually eliminates all QCD background, whereas in the 1-lepton channels, tighter cuts are necessary to remove QCD background.

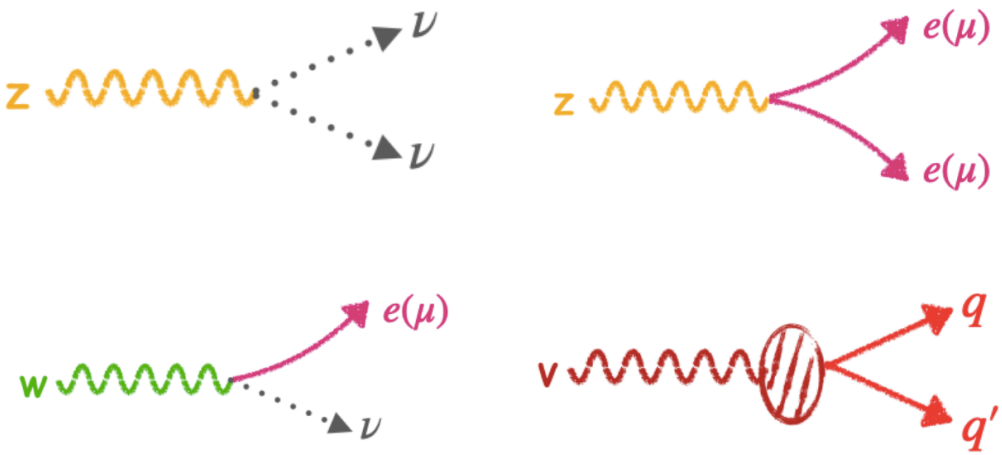

Figure 3.7 Sketches of the vector bosons decay modes, we separate events into different analysis channels based on these decay modes.

Muon

Muons are reconstructed from combined tracker and muon-chamber information (global muons). They are preselected by requiring the loose muon physics object group (POG) identification (see below), $p_T > 5$GeV, $|\eta| < 2.4$, $d_{xy} < 0.5$cm, $d_z < 1.0$cm (where both distances are measured with respect to the primary vertex), and a very loose relative isolation cut of 0.4, where the $\Delta\beta$-subtracted PF isolation in a cone of radius 0.4 is used (isolation will be introduced in the next section). They are further required to pass standard criteria suggested by the Muon POG. Two working points are used: a loose and tight.

- Loose muon:
  - Particle-Flow Muon:
    `isPFMuon()`
  - is Global or Tracker Muon:
    `isGlobalMuon() || isTrackerMuon()`
- Tight muon:
  - the candidate is reconstructed as a Global Muon:
    `isGlobalMuon()`
  - Particle-Flow Muon:
    `isPFMuon()`
  - $\chi^2/ndof$ of the global-muon track fit:
    `globalTrack()->normalizedChi2() < 10.`
  - at least one muon-chamber hit included in the global-muon track fit:
    `globalTrack()->hitPattern().numberOfValidMuonHits() > 0`
  - muon segments in at least two muon stations; this implies that the muon is also an arbitrated tracker muon:
    `numberOfMatchedStations() > 1`
  - tracker track transverse impact parameter w.r.t. the primary vertex:
    `fabs(muonBestTrack()->dxy(vertex->position())) < 0.2`
  - longitudinal distance of the tracker track wrt. the primary vertex:
    `fabs(muonBestTrack()->dz(vertex->position())) < 0.5`
  - number of pixel hits:
    `innerTrack()->hitPattern().numberOfValidPixelHits() > 0`
  - cut on number of tracker layers with hits:
    `innerTrack()->hitPattern().trackerLayersWithMeasurement() > 5`

The p_T threshold in the $W(\mu\nu)$HH channel is 25GeV. For the $Z(\mu\mu)$HH channel thresholds are looser at 25GeV and 15GeV for the two muons.

Lepton isolation

Lepton isolation is the primary criterion for selecting prompt muons and electrons generated in the electroweak decay of massive particles such as Z or W bosons, and for rejecting the numerous leptons produced in jets through the decay of heavy-flavour hadrons or the decay in flight of charged pions and kaons. Isolation is quantified by estimating the total transverse momentum (p_T) of the particles emitted around the direction of the lepton:

$$I_{\text{PF}} \equiv \frac{1}{p_T^{\ell}}\Big(\sum p_T^{\text{charged}} + \max\Big[0, \sum p_T^{\text{neutral}} + \sum p_T^{\gamma} - p_T^{\text{PU}}(\ell)\Big]\Big) \tag{3.4}$$

where the sums run over charged hadrons (p_T^{charged}), photons (p_T^{γ}), and neutral hadrons (p_T^{neutral}) within a distance ΔR of 0.3 (0.4) in the (η, φ) plane around the electron (muon) momentum. The $\sum p_T^{\text{charged}}$ is the scalar sum of the transverse momenta of charged hadrons originating from the chosen primary vertex of the event. The $\sum p_T^{\text{neutral}}$ and $\sum p_T^{\gamma}$ are the scalar sums of the transverse momenta for neutral hadrons and photons, respectively. Since the isolation variable is particularly sensitive to energy deposits from pileup interactions, a $p_T^{\text{PU}}(\ell)$ contribution is subtracted, using two different techniques. For muons, we define $p_T^{\text{PU}}(\mu) \equiv 0.5 \times \sum_i p_T^{\text{PU},i}$, where i runs over the momenta of the charged hadron PF candidates not originating from the primary vertex, and the factor of 0.5 corrects for the different fraction of charged and neutral particles in the cone. For electrons, the FASTJET technique is used, in which $p_T^{\text{PU}}(\text{e}) \equiv \rho \times A_{\text{eff}}$, where the effective area A_{eff} is the geometric area of the isolation cone scaled by a factor that accounts for the residual dependence of the average pileup deposition on the η of the electron, and ρ is the median of the p_T density distribution of neutral particles within the area of any jet in the event.

Both muon and electron channels are required to have a relative isolation smaller than 0.06. In both cases, the cuts were tightened to remove excess data in poorly isolated distribution tails. Although the cuts are tight, there is no loss in expected sensitivity, and the data/MC agreement is very good in the bulk of the isolation distribution.

Jets

Jets are reconstructed from particle-flow candidates using the anti $-\, k_T$ clustering algorithm with distance parameter $R = 0.4$. Reconstructed jets require a small additional energy correction, mostly due to thresholds on reconstructed tracks and clusters in the PF algorithm and various reconstruction inefficiencies.

Loose jet identification criteria are also applied to reject mis-reconstructed jets resulting from detector noise, as well as jets heavily contaminated with pileup energy. Jets that overlap geometrically ($\Delta R < 0.4$) with preselected electrons or muons are discarded. Jets calibrated using the official Jet/MET (JME) physics object group (POG) prescriptions are considered for the analysis if $|\eta| < 2.5$.

A dedicated algorithm to estimate the b-jet energy by accounting for the undetected energy from neutrinos in the B hadron decays is applied. This is referred to as the b-jet energy regression, and the method is detailed in [68]. Energy scale and resolution uncertainties associated with the regression are considered by adding additional scale and smearing. The numbers in Table 3.10 are conservatively taken from previous VHbb analyses, where large smearing (+10%) with generous systematic coverage is provided. Scale uncertainties are also based on previous measurements from VHbb and are 2%.

Step1: $p_T^{diff} = p_T^{reco} - p_T^{gen}$;

Step2: $p_T^{new} = (p_T^{diff} * (1 + f_{smear}) + p_T^{gen}) * (1 + f_{scale})$

Table 3.10 b jet energy regression Scale and Smear

Year	Scale (correction)	Scale (uncertainty)	Smear (correction)	Smear (uncertainty)
2018	0.0	±0.02	0.10	±0.10
2017	0.0	±0.02	0.10	±0.10
2016	0.0	±0.02	0.10	±0.10

Identification of b-jets

The identification of jets originating from the hadronization of b quarks is performed with the output of a multiclass flavor tagging algorithm called DeepJet [69].

The DeepJet algorithm relies on low-level variables and loose selection of the inputs, using an architecture capable of efficiently processing these inputs. When compared with fully connected models using a smaller set of engineered features, a gain in performance is observed in all topologies of flavor tagging, in some cases exceeding a two-fold efficiency gain for the same misidentification rate.

The DeepJet output can be used to select optimal working points with respect to this analysis, in addition to the standard Loose/Medium/Tight working points defined by the BTV POG and listed in Table 3.11.

The b-tagging information can be utilized in two ways within the training of the final signal vs background discriminator in the signal region: either as a shape variable or in its

Table 3.11 Definition of b-tagging working points (WP). The WPs are selected such that a specific target for the mis-tag is achieved. That efficiency target is listed in the table per WP.

WP Name	Mistag efficiency	DeepJet
Loose (2018)	10%	0.0490
Medium(2018)	1%	0.2783
Tight (2018)	0.1%	0.7100
Loose (2017)	10%	0.0532
Medium(2017)	1%	0.3040
Tight (2017)	0.1%	0.7476
Loose (2016pre)	10%	0.0508
Medium(2016pre)	1%	0.2598
Tight (2016pre)	0.1%	0.6502
Loose (2016post)	10%	0.0480
Medium(2016post)	1%	0.2489
Tight (2016post)	0.1%	0.6377

binned working point configuration. Depending on the usage, a set of different uncertainties are applied to the calibration central values. The binned working point b-jet calibration extracts central values and uncertainties using a combination of calibration methods that exploit b-jet enriched phase-spaces through the presence of semi-leptonic decays in the jet or $t\bar{t}$ topologies.

In signal events where the Higgs boson has a boost of more than 250GeV, two AK04 jets will begin to overlap as the opening angle shrinks. These events can be interpreted as a single "fat jet" with a wider cone. A cone size of 0.8 is selected because this is geometrically the point where AK04 jets would start to overlap, so AK08 jets are referred to in this analysis as FatJets.

A novel multivariate classifier based on graph neural networks, ParticleNet, is applied to identify the jets corresponding to Higgs decays [70].

The ParticleNet tagger is a multiclassifier algorithm, assigning a set of output scores for each jet. Each score corresponds to the probability of this jet originating from a W, Z, Higgs, or top decay, and can further classify each jet based on the decay modes with different flavor content (e.g., $H \to b\bar{b}$, $H \to c\bar{c}$, $H \to q\bar{q}q\bar{q}$). This translates to 17 scores per jet, making ParticleNet a very versatile boosted-jet algorithm. In the context of the VHH analysis, we define the bb-tagging discriminant D_{bb} by aggregating the scores to provide separation of b quark pairs against background jets stemming from QCD radiation, formulated as:

$$D_{bb} = \frac{\text{ParticleNetMD\_score}(X \to b\bar{b})}{\text{ParticleNetMD\_score}(X \to b\bar{b}) + \text{ParticleNetMD\_score}(QCD)} \tag{3.5}$$

Three working points (WPs) are defined for the bb-tagging discriminant D_{bb}, correspond-

ing to D_{bb} values larger than 0.90 (Loose WP), 0.94 (Medium WP), and 0.98 (Tight WP).

These are the same working points used in the search for nonresonant Higgs boson pair production via vector boson fusion in the boosted 4b final state at $\sqrt{s} = 13\,\text{TeV}$ (AN-20-231). By choosing the same working points, we can directly use the ParticleNet-bb calibration in that analysis. Table 3.12 summarizes the scale factors (SFs) for the three data-taking years, which are taken from the CMS internal note AN-20-231. ParticleNet Regressed jet mass is also used, and the jet mass scale (JMS) and jet mass resolution (JMR) uncertainties are 1% and 5%, respectively.

Table 3.12 Summary of the ParticleNet-bb scale factors obtained with proxy jets from gluon splitting. (AN-20-231)

WP	AK8 jet [GeV] p_{T}					
	$200-250$	$250-300$	$300-350$	$350-400$	$400-500$	>500
				2016		
LP	1.10 ± 0.06	1.05 ± 0.04	1.16 ± 0.04	1.12 ± 0.04	1.15 ± 0.03	1.09 ± 0.03
MP	1.08 ± 0.06	1.06 ± 0.04	1.14 ± 0.04	1.14 ± 0.04	1.16 ± 0.03	1.10 ± 0.03
HP	1.09 ± 0.06	1.01 ± 0.05	1.14 ± 0.05	1.14 ± 0.05	1.19 ± 0.04	1.09 ± 0.04
				2017		
LP	1.11 ± 0.05	1.10 ± 0.05	1.08 ± 0.05	1.10 ± 0.04	1.07 ± 0.03	1.05 ± 0.02
MP	1.11 ± 0.05	1.09 ± 0.04	1.07 ± 0.05	1.09 ± 0.05	1.06 ± 0.03	1.06 ± 0.03
HP	1.12 ± 0.06	1.11 ± 0.05	1.09 ± 0.06	1.11 ± 0.06	1.13 ± 0.04	1.09 ± 0.03
				2018		
LP	0.96 ± 0.04	1.06 ± 0.05	1.06 ± 0.05	1.03 ± 0.05	1.05 ± 0.03	1.02 ± 0.02
MP	0.96 ± 0.04	1.03 ± 0.05	1.08 ± 0.05	1.05 ± 0.05	1.04 ± 0.03	1.03 ± 0.03
HP	0.99 ± 0.05	1.06 ± 0.05	1.07 ± 0.05	1.14 ± 0.05	1.09 ± 0.04	1.06 ± 0.03

3.3.2 Trigger requirement

As introduced in the previous chapters, there are levels of triggers designed to reduce the data volume while retaining events with 'physics meaning' for analysis. The data events recorded offline for this analysis are selected with a set of L1 triggers and high-level trigger (HLT) triggers that require the presence of muons, electrons, or jets.

The selection criteria for triggers utilized in this analysis adapted to the data-taking conditions across the 2016 (36.3 fb^{-1}), 2017 (41.5 fb^{-1}), and 2018 (59.8 fb^{-1}) datasets. The figures in parentheses denote the integrated luminosities [71–73]. The MET channel requires a substantial L1 missing transverse momentum signature, exceeding 120 GeV (110 GeV for early 2016), derived from roughly constructed calorimeter energy deposits. The minimum $p_{\text{T}}^{\text{miss}}$ threshold at the HLT is 170 GeV (180 GeV for 2017–2018 data) for 2016. Anomalous high-$p_{\text{T}}^{\text{miss}}$ events

may arise from various sources, such as reconstruction failures, detector malfunctions, or non-collision backgrounds. To mitigate such occurrences, event filters are implemented, aiming to identify over 85–90% of spurious high-$p_{\mathrm{T}}^{\mathrm{miss}}$ events with a mis-tagging rate of less than 0.1% [74]. In the 1L channel, a single electron or muon is mandated, whereas the 2L channel necessitates two electrons or muons. The transverse momentum (pT) thresholds for these leptons vary annually, with muons subjected to less stringent criteria compared to electrons, owing to the higher probability of jets being misidentified as electrons rather than muons. In the FH channel, the trigger strategy directly addresses the decay products of the Higgs boson: four jets, of which at least two or three are consistent with originating from b quarks.

The selection requirements imposed at the trigger level are listed in Table 3.13 and Table 3.14. The criteria for the FH and MET channels are more stringent than those for the other two channels, as necessitated by the significant background noise originating from SM processes, particularly QCD multijet events, characterized by the exclusive production of jets through strong interactions.

Table 3.13 The L1 Triggers.

Channel	Year	L1 trigger
MET	2016	$p_{\mathrm{T,L1}}^{\mathrm{miss}} > 110$ or 120 GeV
	2017/2018	$p_{\mathrm{T,L1}}^{\mathrm{miss}} > 120$GeV
1 electron	2016	$E_{T,\mathrm{L1}} > 27$GeV
	2017/2018	$E_{T,\mathrm{L1}} > 30$GeV
1 muon	2016	$p_{T,\mathrm{L1}}(\mu) > 22$GeV
	2017/2018	$p_{T,\mathrm{L1}}(\mu) > 25$GeV
2 electrons	2016–2018	$E_{T,\mathrm{L1}}(1) > 22$ and $E_{T,\mathrm{L1}}(2) > 10$GeV
2 muons	2016–2018	$p_{T,\mathrm{L1}}(\mu_1) > 15$ and $p_{T,\mathrm{L1}}(\mu_2) > 8$GeV
FH	2016	Four $E_{T,\mathrm{L1}} > 50$ or $H_{\mathrm{T}} > 280$GeV Two $E_{T,\mathrm{L1}} > 100$ or one $E_{T,\mathrm{L1}} > 200$GeV Two $E_{T,\mathrm{L1}} > 100$ or one $E_{T,\mathrm{L1}} > 170$GeV or $H_{\mathrm{T}} > 280$GeV
	2017	Four $E_{T,\mathrm{L1}} > 60$ or $H_{\mathrm{T}} > 380$ or $E_{T,\mathrm{L1},1} > 70$, $E_{T,\mathrm{L1},2} > 55$, $E_{T,\mathrm{L1},3} > 40$, $E_{T,\mathrm{L1},4} > 35$ and $H_{\mathrm{T,L1}} > 280$GeV Two $E_{T,\mathrm{L1}} > 100$GeV with $\Delta\eta_{1,2} < 1.6$
	2018	Four $E_{T,\mathrm{L1}} > 60$ or $H_{\mathrm{T}} > 380$GeV or $E_{T,\mathrm{L1},1} > 70$, $E_{T,\mathrm{L1},2} > 55$, $E_{T,\mathrm{L1},3} > 40$GeV, $E_{T,\mathrm{L1},4} > 40$ and $H_{\mathrm{T,L1}} > 320$GeV Two $E_{T,\mathrm{L1}} > 112$GeV with $\Delta\eta_{1,2} < 1.6$ or two $E_{T,\mathrm{L1}} > 150$GeV

Table 3.14 The HLT Triggers.

Channel	Year	HLT
MET	2016	$p_{\mathrm{T}}^{\mathrm{miss}} > 170$GeV
	2017/2018	$p_{\mathrm{T}}^{\mathrm{miss}} > 180 GeV$
1 electron	2016	$p_T(\mathrm{e}) > 32$GeV
	2017/2018	$p_T(\mathrm{e}) > 35 GeV$
1 muon	2016	$p_T(\mu) > 24$GeV
	2017/2018	$p_T(\mu) > 27$GeV
2 electron	$p_T(\mathrm{e}_1) > 22$ and $p_T(\mathrm{e}_2) > 10$GeV	
2 muons	$p_T(\mu_1) > 17$ and $p_T(\mu_2) > 8$GeV	
FH	2016	Four jets with $p_T > 45$GeV Two jets with $p_T > 100$GeV and $\Delta\eta_{1,2} < 1.6$ Two jets with $p_T > 90\ GeV$ and two jets with $p_T > 30$GeV
	2017	Four jets with $p_{T,1} > 75$GeV, $p_{T,3} > 45$, $p_{T,4} > 40$GeV, and $H_{\mathrm{T}} > 300$GeV Two jets with $p_T > 100$GeV and $\Delta\eta_{1,2} < 1.6$
	2018	Four jets with $p_{T,1} > 75$, $p_{T,2} > 60$GeV, $p_{T,3} > 45$, $p_{T,4} > 40$GeV, and $H_{\mathrm{T}} > 330$GeV Two jets with $p_T > 116$GeV and $\Delta\eta_{1,2} < 1.6$

3.3.3 Object reconstruction and selection

The basic PF object candidates are described in previous sections of this chapter, while the truth-level objects consist of one vector boson and two Higgs bosons.

Table 3.15 summarizes the kinematic thresholds for the selection of leptons (MET) and jets, as well as the pre-selection criteria for the vector bosons. The vector bosons are reconstructed with either 2 "good leptons" (2L), 1 "good lepton" with MET (1L), MET (MET), or 2 jets (FH). The collision events lacking a sufficient number of eligible candidates will be filtered out.

The reconstruction of the Higgs Bosons

We are investigating a scenario where both Higgs bosons decay into a pair of bottom quarks. This analysis comprehensively considers various topologies, including the Resolved, Semi-Boosted, and Boosted topologies. However, our primary focus is on the Resolved and Boosted topologies, as the contribution from the Semi-Boosted topology is negligible. Figure 3.8 illustrates a cartoon of the resolved and boosted topologies.

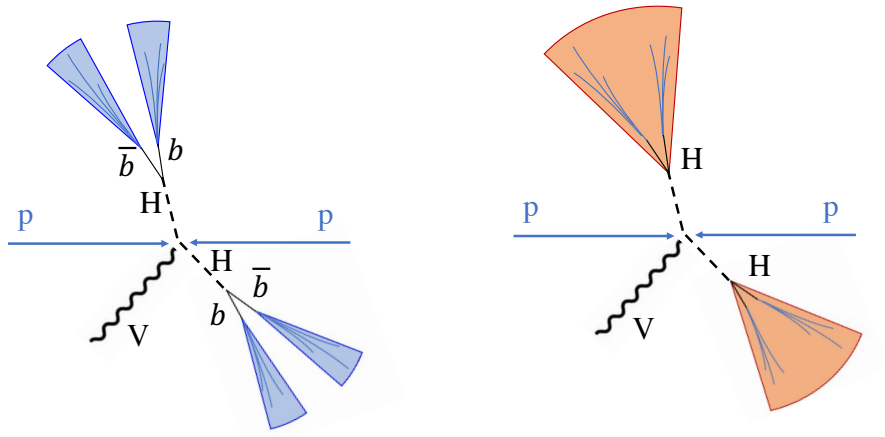

Figure 3.8 Cartoon of Resolved (left) and Boosted (right) topologies. The resolved category requires 4 AK4 Jets and pairing 2 Jets to form a Higgs candidate. The boosted category needs 2 AK8 Jets and each Jet is a boosted Higgs candidate.

In the **resolved topology**, each of the two Higgs bosons is reconstructed with a pair of eligible b-jet candidates. In all **V-leptonic** channels, although the selection criteria vary slightly, they all require at least four eligible jets, and among them, the four jets with the highest b-tagging scores are referred to as 'Higgs Candidate Jets'. In this topology, the DeepJet score introduced in Section 3.3.1, which based on the CMS standard jet reconstruction techniques, is utilized.

After obtaining the 4 Higgs candidate jets, the subsequent jet pairings are crucial and non-trivial in order to minimize potential combinatorial background. Once the four final candidates are selected, their pairing is performed by calculating the invariant mass of the two di-jet candidates. All combinations are checked, and the one presenting the minimal $D_{\mathrm{HH}}$is considered final, where $D_{\mathrm{HH}}$is defined by the following equation:

$$D_{\mathrm{HH}} = \frac{|m_{H1jj} - k m_{H2jj}|}{\sqrt{1 + (k)^2}} \tag{3.6}$$

where $k = 1.05$ is a constant that can be optimized based on significance. m_{H1jj} is the invariant mass of two jets that can be reconstructed as the leading p_T Higgs boson, and m_{H2jj} is that of the sub-leading Higgs boson. This can be visualized in the 2-D mass plot shown in Figure 3.9, where A, B, and C represent three different pairings of the four candidate jets, and B has the minimal D_{HH}.

There is a different reconstruction strategy applied in the **V-hadronic** channel. Among the 6 jet candidates required by the pre-selection, the combination that satisfies the most stringent

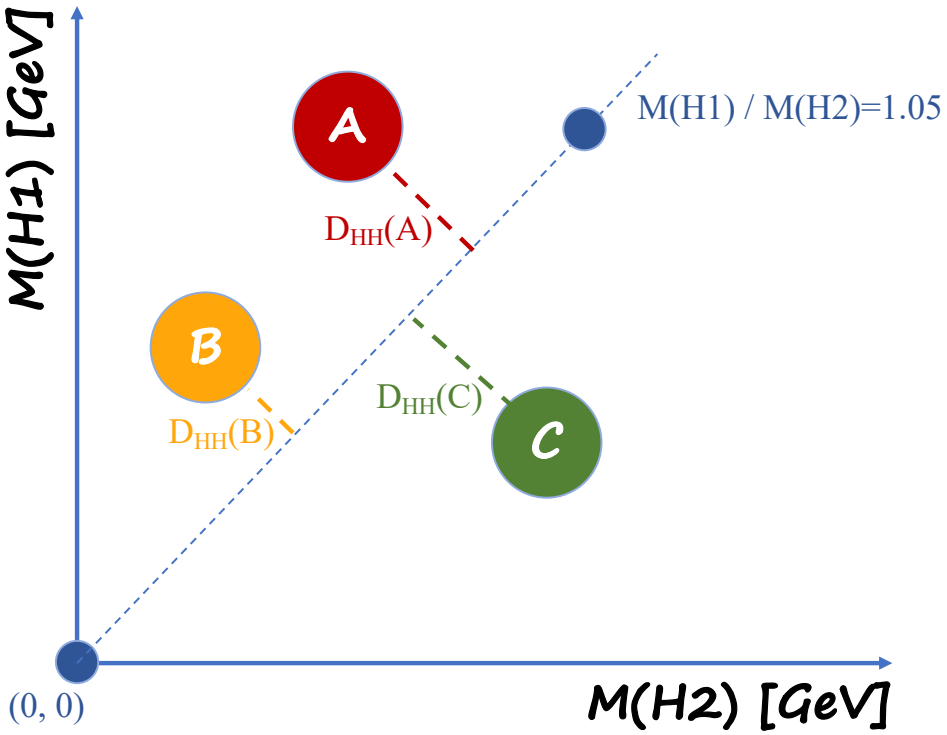

Figure 3.9 The definition of D_{HH} where A,B,C represent three different pairing of the four candidate jets.

criteria for jet separation, $\Delta R(j,j)$ ($\Delta R = \sqrt{(\Delta\eta)^2 + (\Delta\phi)^2}$), will be selected for reconstructing the two Higgs bosons. (S_T in the equation is defined as the combined transverse momemtum of the jets.)

$$\begin{aligned} \frac{360\text{GeV}}{m_{4j}} - 0.5 < \quad & \text{Leading } S_T \text{ dijet } \Delta R(j,j) < \max\left(1.5, \frac{650\text{GeV}}{m_{4j}} + 0.5\right) \\ \frac{235\text{GeV}}{m_{4j}} \quad < \quad & \text{Sub-leading } S_T \text{ dijet } \Delta R(j,j) < \max\left(1.5, \frac{650\text{GeV}}{m_{4j}} + 0.7\right) \end{aligned}$$

If more than one view is selected, only one will be kept at random, which will not effect the final result and the reason will be explained in detail in the following sections. The distributions of $\Delta R(j,j)$ in SM signal and background are shown in Figure 3.10.

In the **boosted topology**, at least 2 capable fat jets or, using CMS standard reconstruction terminology, 2 AK8 jets are selected for the events in this topology. They will be ranked according to the machine learning (ParticleNet) score obtained by equation 3.5. The top 2 candidates will be used to reconstruct the two higgs bosons respectively.

The reconstruction of the Vector Boson

In the **2L channel**, events must contain 2 'good electrons' or 2 'good muons'. These two same-flavor and opposite-charged leptons are used to reconstruct the Z boson. To suppress background contributions, the Z boson is required to have a transverse momentum (p_T) threshold of 50 GeV.

In the **1L channel**, events must contain 1 'good electron' or 1 'good muon' along with a well-reconstructed missing transverse energy (MET) object. These components are combined to reconstruct the leptonic decay of the W boson. To suppress background contributions, the W boson is required to have a transverse momentum (p_T) threshold of 125 GeV.

In the **MET channel**, events must contain a well-reconstructed missing transverse energy (MET) object, which is directly used to reconstruct the Z boson.

In the **FH channel**, at least 6 AK4 jet candidates are selected to reconstruct the Higgs bosons and the vector boson. The Higgs boson part has already been introduced. After selecting the 4 jets with the leading DeepJet scores as the 'Higgs candidate jets', we pick the 2 leading HT jets from the remaining capable jets to reconstruct the vector boson. To improve the purity of the signal, the reconstructed vector boson should fit within the mass window between 65 GeV and 105 GeV.

Table 3.15 Thresholds on kinematic variables for all selected objects are listed for each channel. Objects are always required to be within the acceptance of the CMS sub-detectors, which is $|\eta| < 2.5$ for electrons and 2.4 for all other objects, as well as outside of barrel-endcap transition regions near $|\eta| \sim 1.5$. The di-jet mass of the two jets with the lowest b tagging scores in the FH channel is denoted $m_{j_1 j_2}$.

Channel	Vector boson decay products selection	Vector boson selection	Jet selection
MET small-radius		$p_{\mathrm{T}}^{\mathrm{miss}} > 150$GeV	≥4 small-radius jets with $p_T > 35$GeV
MET large-radius		$p_{\mathrm{T}}^{\mathrm{miss}} > 250$GeV	≥2 large-radius jets with $p_T > 200$GeV
1L	$p_T(\mathrm{e}) > 32$ (28)GeV 2018/2017 (2016) OR $p_T(\mu) > 25$ GeV	$p_T(W) > 125$GeV	≥3 small-radius jets with $p_T > 25$GeV AND ≥4 small-radius jets with $p_T > 15$GeV OR ≥2 large-radius jets with $p_T > 200$GeV
2L	$p_T(\mu_{1[2]}) > 20$ [20]GeV OR $p_T(e_{1[2]}) > 25$ [20]GeV	$p_T(\ell\ell) > 50$GeV	≥4 small-radius jets with $p_T > 20$GeV
FH	$p_T(\mathrm{j}_i) > 20$GeV	$65 < m_{j_1 j_2} < 105$GeV	≥4 small-radius jets with $p_T > 40$GeV and ≥6 small-radius jets with $p_T > 20$GeV

3.3.4 Event selection

As introduced in the previous section (Section 3.3.3) and summarized in Table 3.15, only events containing a sufficient number of capable object candidates can pass the 'pre-selection' and proceed to the reconstruction process.

In the MET channel, additional cuts are applied to all Higgs candidate jets in the resolved topology to further suppress the QCD MultiJets background. Figure 3.11 shows the distribution of $|(\Delta\phi(\mathrm{Jet}, p_{\mathrm{T}}^{\mathrm{miss}}))|$ vs. $p_{\mathrm{T}}^{\mathrm{miss}}$, where the red line represents our cuts. The z-axis denotes the ratio between MC and Data. Events below the red line have a low ratio, indicating a higher abundance of data compared to MC in this phase space. Therefore, we choose to remove these events. The ratio along the red line is approximately 0.8.

Figure 3.12 displays the distribution with this cut reversed, i.e., selecting events below the red line. Not only is the overall normalization incorrect, but also the shape of the kinematics does not agree. Therefore, it is crucial to have these additional cuts in the MET channel.

Then, events in different vector boson decay channels and different topologies will be selected separately. The baseline selection criteria for the Higgs bosons and vector boson are listed as follows:

- 2L channel(resolved):
  $p_{\mathrm{T}}(V) \geq$ 50GeV
- 1L channel(resolved):
  $p_{\mathrm{T}}(V) \geq$ 125GeV
- 1L channel(boosted):
  $p_{\mathrm{T}}(V) \geq$ 125GeV ,
  $p_T(\mathrm{H}) \geq$ 200GeV
- MET channel(resolved):
  $p_{\mathrm{T}}(V) \geq$ 150GeV ,
  $|(\Delta\phi(Jet, p_{\mathrm{T}}^{\mathrm{miss}}))| > 0.4e^{4-p_{\mathrm{T}}^{\mathrm{miss}}/50\mathrm{GeV}} + 0.07$
- MET channel(boosted):
  $p_{\mathrm{T}}(V) \geq$ 250GeV ,
  $p_T(\mathrm{H}) \geq$ 200GeV ,
  $|(\Delta\phi(Jet, p_{\mathrm{T}}^{\mathrm{miss}}))| > 0.4e^{4-p_{\mathrm{T}}^{\mathrm{miss}}/50\mathrm{GeV}} + 0.07$
- FH channel(resolved):
  65GeV $\leq p_{\mathrm{T}}(V) \leq$ 105GeV

It is notable that a key concept in our analysis strategy, which will be elaborated on in detail in the next section (Section 3.4, Analysis strategy), is to retain events and categorize them rather than filtering them out directly. This approach is adopted because we are investigating a rare process with stringent object requirements, meaning that events in different categories may contribute differently to enhance the final results.

If we only consider the higher-level triggers and the basic selections outlined in this section, we can observe the dependence of the absolute efficiencies (acceptance times trigger and analysis selection efficiencies) on the mass of the HH at the generator level, $m_{\mathrm{HH}}^{\mathrm{gen}}$, in Figure 3.13. The leptonic channels generally exhibit high efficiency after the HLT selection because no jets are required. However, the FH selection necessitates four jets at the HLT, resulting in a generally lower efficiency. Even after applying all the analysis selections, the 1L and MET channels still maintain relatively high efficiencies at high $m_{\mathrm{HH}}^{\mathrm{gen}}$ due to the inclusion of the large-radius regions.

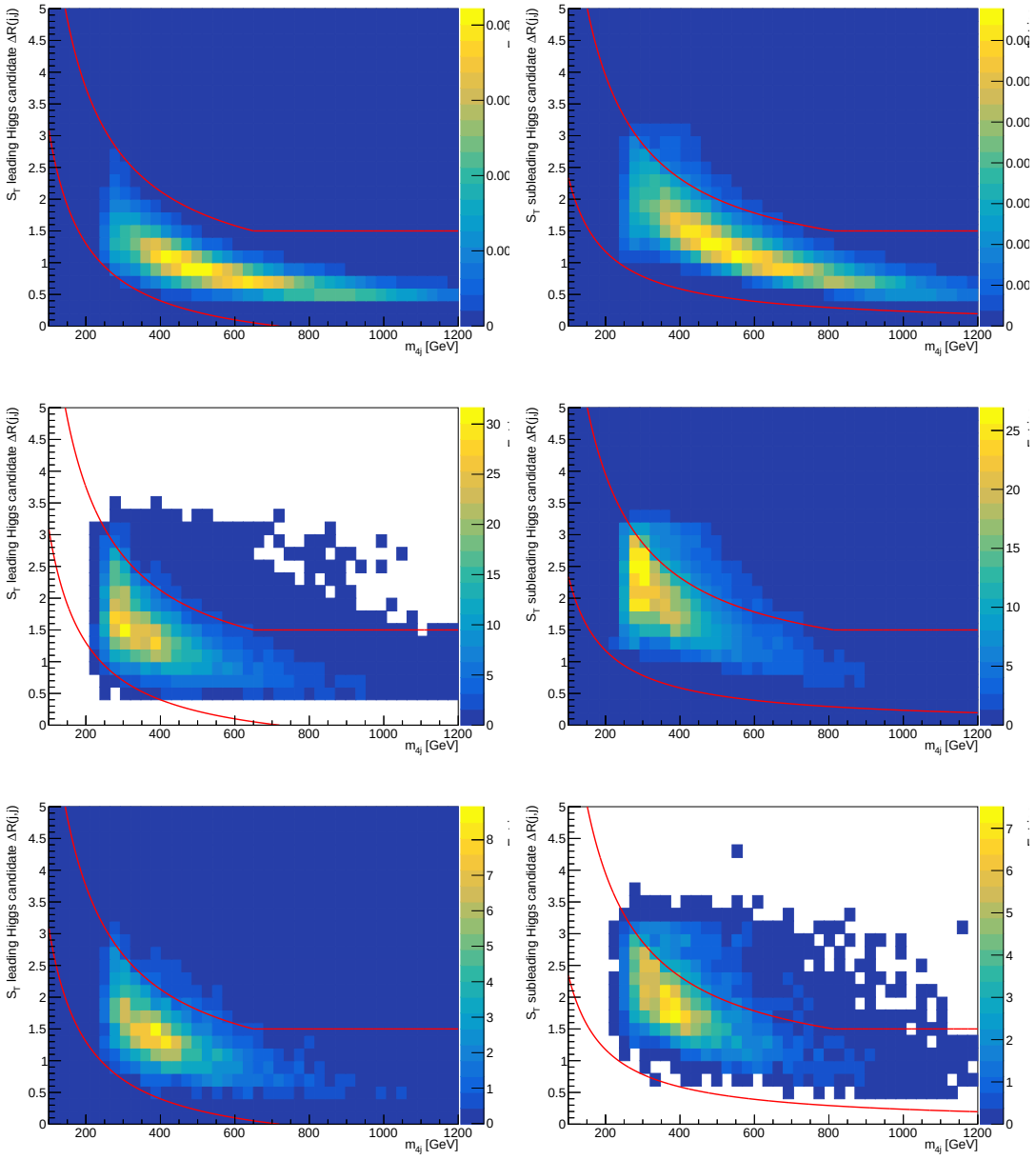

Figure 3.10 $\Delta R(j,j)$ distributions of the leading S_T dijet **(Left)** and sub-leading S_T dijet **(Right)** for SM signal **(Top)**, multijet background **(Middle)**, and $t\bar{t}$ background **(Bottom)**. The red curves represent the boundaries of the $\Delta R(j,j)$ criteria.

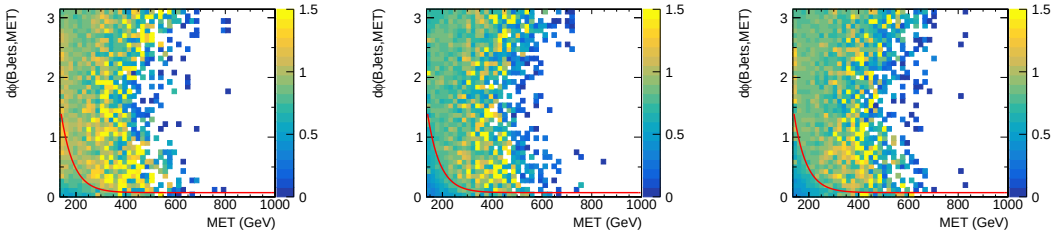

Figure 3.11 $|\Delta\phi(Jet, p_{\mathrm{T}}^{\mathrm{miss}})|$ vs. $p_{\mathrm{T}}^{\mathrm{miss}}$ for $\frac{MC}{Data}$. Plots from left to right are 2016,2017,2018. Selected events are in sideband, 3B or 4B. Excessive MultiJets events cluster in the bottom left corner. The red line represents $|(\Delta\phi(Jet, p_{\mathrm{T}}^{\mathrm{miss}}))| > 0.4e^{4-p_{\mathrm{T}}^{\mathrm{miss}}/50\mathrm{GeV}} + 0.07$ and events below this line are removed.

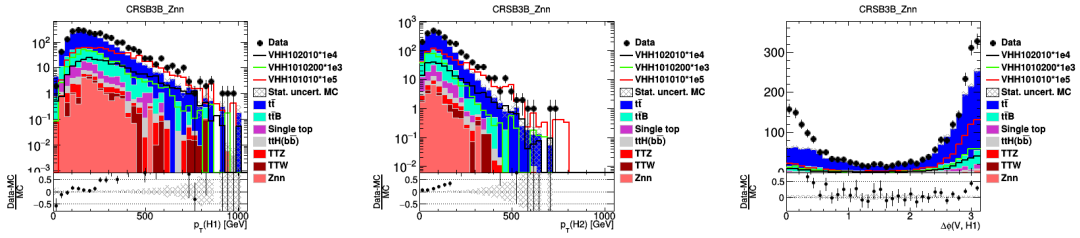

Figure 3.12 Kinematics distributions with the aforementioned cuts reversed.(failed selection events)

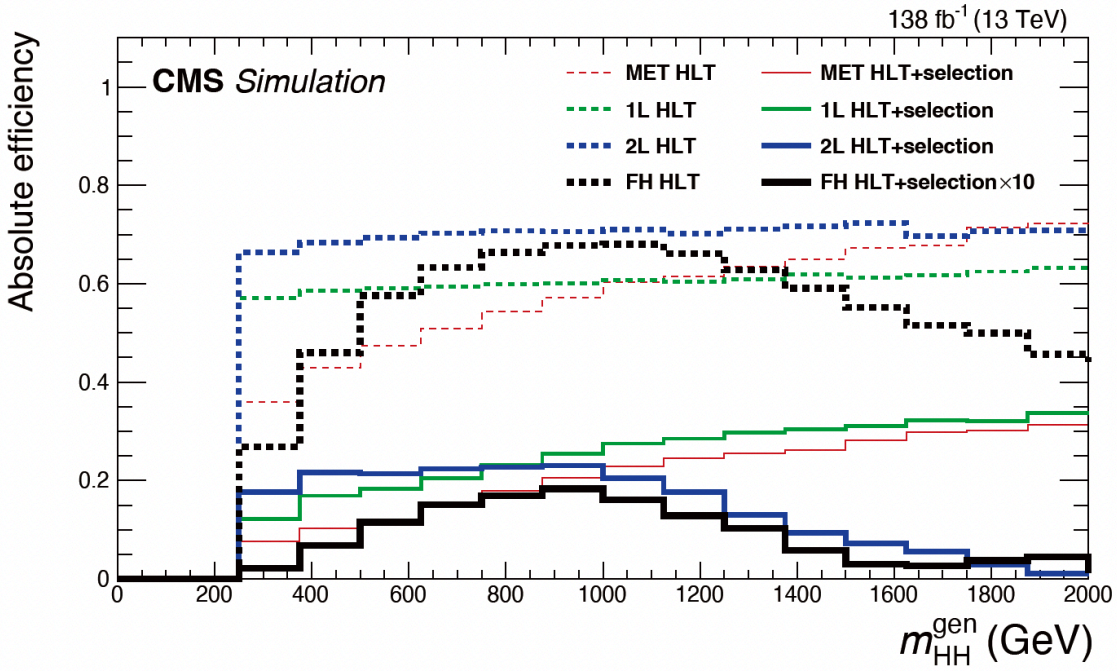

Figure 3.13 The SM VHH efficiencies of trigger selections (dashed lines) and full selections (solid lines) are illustrated for all four analysis channels. The full selection efficiency in the FH channel is scaled up by a factor of 10 for visibility. Both sets of efficiencies represent absolute efficiencies (acceptance times selection efficiencies).

3.4 Analysis strategy

Unlike traditional high-energy physics analyses, event categorization is a crucial concept in this VHH analysis. Events are subdivided into various phase spaces based on kinematics or higher-level parameters to fully exploit their information.

As mentioned in previous sections, events are divided into four orthogonal channels based on the decay modes of the vector boson. This approach enables us to fully utilize the available information and optimize separately for each channel. In this section, we will outline the general strategy and discuss specific measurements tailored to each channel.

3.4.1 Resolved and Boosted topologies

This analysis encompasses both the resolved and boosted topologies, allowing for the proper study of events both within and outside of very large transverse momentum regions, as briefly discussed in Section 3.3.3 and illustrated in Figure 3.8.

In the actual analysis, we focus solely on the boosted topology in the 1L and MET channels. This decision is driven by the fact that the 1L channel involves $W \pm HH$, which has a relatively large cross section, while the MET channel necessitates $Z \rightarrow \nu\nu$, which boasts the largest branching ratio among Z leptonic decays.

As outlined in the preceding section, the reconstruction of Higgs bosons varies between these two topologies, necessitating orthogonality between events or the events could go into more than one topologies. This raises the question of priority: which topology takes precedence in selecting events from the pool?

This question is addressed by comparing the outcomes of a "resolved prioritized (R priority)" study with those of a "boosted prioritized (B priority)" study, selecting the approach that yields the more accurate final result. Since the final results depend on the processes outlined in the subsequent sections, this aspect is detailed in Appendix .2.

The conclusion drawn is that the "B priority" strategy delivers superior performance in the analysis. Therefore, we proceed with this strategy for the subsequent steps.

3.4.2 Research regions

Signal regions

After obtaining the two reconstructed Higgs bosons (sec. 3.3.3), for ease of analysis and understanding, we rank them by their p_T. The leading one is denoted as H_1 , and the subleading one is denoted as H_2 . With these two Higgs bosons, we define **signal regions**. The

definitions vary slightly between the V-leptonic channels and the V-hadronic channel. The utilization of these signal regions will be detailed in subsequent sections.

In all **V-leptonic channels**, we firstly define r_{HH} as a distance on a two dimensional mass plot as shown in Fig.3.14(right):

$$r_{\mathrm{HH}} = \sqrt{(m_{H1} - 125 \times r_1)^2 + (m_{H2} - 125 \times r_2)^2} \tag{3.7}$$

In this case, we choose $r_1 = r_2 = 1$, it is easy to find that the r_{HH} is the distance between the reconstructed mass of two Higgs bosons and the SM Higgs boson mass. With different r_{HH} areas, we define the signal region, the control region and the side band as shown in Fig.3.14(left).

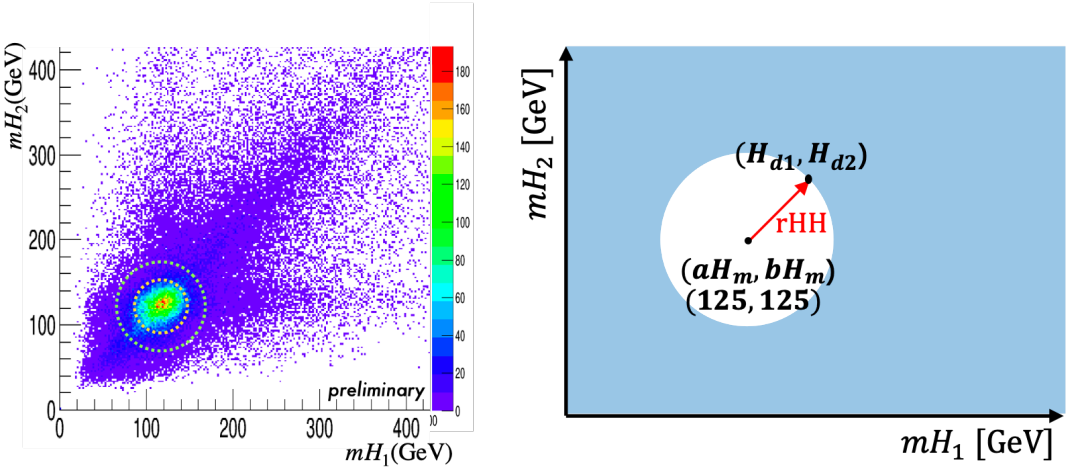

Figure 3.14 The definition of r_{HH} (right) and the definitions of signal region, control region and side band based on r_{HH} (left).

- Signal Region (SR):
  $r_{\mathrm{HH}} \leq 25\mathrm{GeV}$
- Control Region (CR):
  $25\mathrm{GeV} < r_{\mathrm{HH}} \leq 50\mathrm{GeV}$
- Side Band (SB):
  $50\mathrm{GeV} < r_{\mathrm{HH}} \leq 75\mathrm{GeV}$

In the **V-hadronic channel**, we define a δ_{HH} and choose $r_1 = 1.02$ and $r_2 = 0.98$:

$$\delta_{\mathrm{HH}} = \sqrt{\left(\frac{m_{\mathrm{H1}} - 125.0\mathrm{GeV} \times r_1}{m_{\mathrm{H1}}}\right)^2 + \left(\frac{m_{\mathrm{H2}} - 125.0\mathrm{GeV} \times r_2}{m_{\mathrm{H2}}}\right)^2} \tag{3.8}$$

and the signal region is defined as following, and the territories on the 2-D plots is illus-

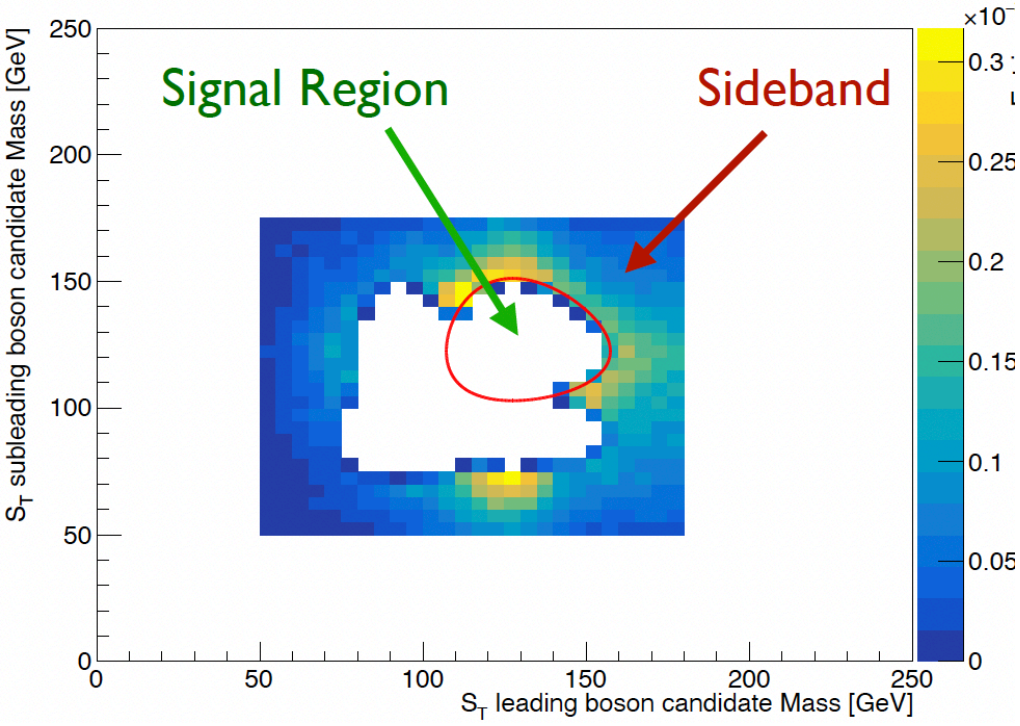

Figure 3.15 The signal region and side band of the signal in the FH channel. The signal events in the signal regions are blinded during the process of modeling.

trated in figure 3.15.

- Signal Region (SR):

  $\delta_{\mathrm{HH}} \leq 0.19$

- Side Band (SB):

  $0.19 < \delta_{\mathrm{HH}}$,

  $m_{\mathrm{H1}} \in (52, 180)\mathrm{GeV}$, $m_{\mathrm{H2}} \in (50, 173)\mathrm{GeV}$

In the large-radius jet analysis (boosted topology) in the MET and 1L channels, events are divided into three regions using the D_{bb} defined with equation 3.5 as sketched in figure 3.16.

- High-purity Region (HP):

  $min(D_{bb,1}, D_{bb,2}) > 0.94$

- Low-purity Region (LP):

  $0.90 < min(D_{bb,1}, D_{bb,2}) < 0.94$

- Failed Region:

  $0.80 < min(D_{bb,1}, D_{bb,2}) < 0.90$

b-jet multiplicity

Principally, only events containing equal to or more than 4 b-tagged jets could possibly be considered signal events. However, the existence of mis-tagging rates and other minor nui-

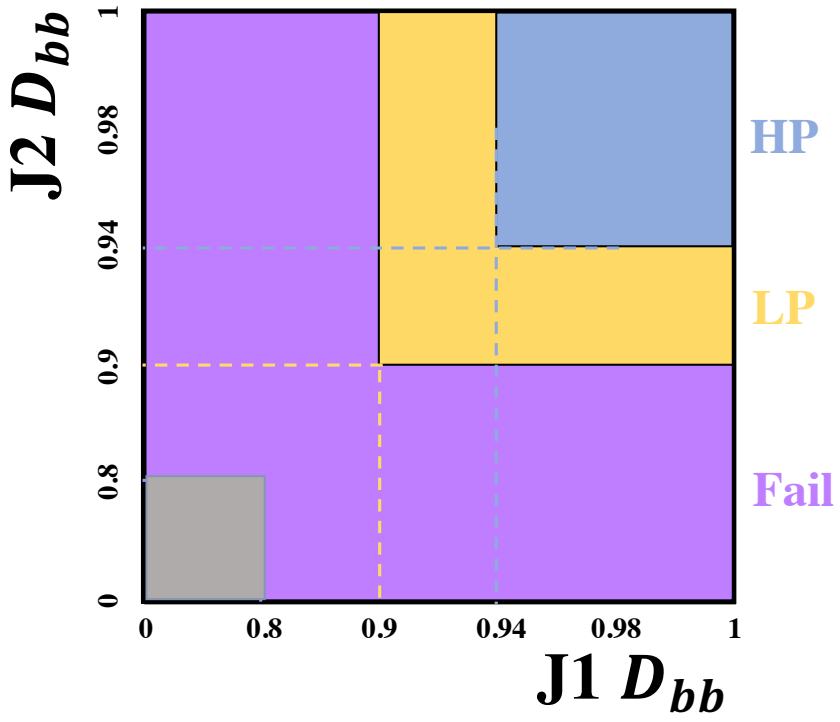

Figure 3.16 llustration of the ParticleNet score cuts used to define the Low Purity(LP) and High Purity (HP) D_{bb} search categories

sances may result in genuine signal events being filtered out.

According to our simulation study, in the leptonic channels, SRs with 3 or 4 b jets both exhibit significant signal yields, with the 4 b-jets region being the most significant. In the 2L channel, $N_b = 4$ and 3 are optimized and statistically analyzed separately, while in other leptonic channels, they are validated separately but analyzed together. The FH channel will only consider the $N_b = 4$ region for calculating the signal region.

3.4.3 Kappa parameter categorization

In this analysis, the most important objective is to explore and constrain the values of the kappa parameters, thereby maximizing sensitivity to enhanced SM coupling strengths. To achieve this goal, a viable approach is to utilize kinematic variables whose distributions exhibit significant differences when one or the other coupling of interest exceeds the SM prediction.

In the previous study of ggF or VBF HH production modes, we have already observed that κ_λ leads to significant differences in the distributions of kinematic variables such as m_{HH}. In this VHH study, we leverage this feature to explore additional kinematics. Simultaneously, κ_{VV} is another coupling we aim to constrain. As shown in Equation 1.44, the diagrams of VHH

interfere with each other, and as calculated at leading order (Equation 3.3), the absence of the tri-linear HHH diagram will naturally enhance the HHVV diagram.

Kinematic dependence on κ_λ

The dependence of signal kinematics on κ_λ is illustrated in Fig. 3.17 and Fig. 3.18. Signals are re-weighted to different κ_λ values, ranging from 0 to 20. The most distinguishing features include the HH mass, transverse momentum (p_T), and angular separations between V, H_1, and H_2. These features enable us to identify an enhanced region for κ_λ and, correspondingly, another region enhance κ_{VV}.

Meanwhile, the 2-D distribution of some main backgrounds is shown in Fig. 3.19. Notably, the background is independent of the kappa parameters, providing a stronger motivation to optimize our analysis in different 'kappa-enriched' regions. It can also be observed that, in the 2-D mass distributions, the background events are concentrated along the diagonal line. This is a side effect of the HH reconstruction strategy, as we tend to select reconstructions that match the distance from the diagonal line, as shown in Fig. 3.9. Consequently, the kinematics tend to align with this line. Fortunately, the signal distribution is concentrated around the (125, 125) point as expected, allowing our signal regions (SRs) to effectively limit the background yields.

Our basic strategy is to utilize reinforcement learning technology, specifically Boosted Decision Trees (BDT) [75, 76], to exploit the differences in kinematic distributions between κ_λ -enriched signal events and κ_{VV}-enriched signal events. This categorization allows us to classify signal events into different super-parameter categories accordingly. Subsequently, we can optimize the signal extraction process within these two categories based on the differing kinematics of signals and backgrounds. This approach enables us to achieve the best sensitivity to both κ_λ and κ_{VV} simultaneously.

The BDTs are trained separately in different V-decaying channels to maximize sensitivity enhanced by the varying mass resolution and kinematic effects of the trigger and selection criteria. The training samples consist of BSM simulation events with $\kappa_\lambda = 0$ against $\kappa_\lambda = 20$ events. Additionally, other pairs of enhanced coupling samples were tested in the training of candidate categorization BDTs. The selected pair was chosen from several equally optimal pairs in terms of separating signal kinematics. Moreover, the $\kappa_\lambda = 20$ point is closer to our expected boundary of the allowed interval for the upper limit scan of κ_λ .

Notably, the categorization BDTs are optimized and trained in all channels using the small-radius jets topology (resolved topology). In the boosted channel, no κ_λ -enrichment

is possible since the two large-radius jets tend to have $\Delta\phi \approx \pi$. As a result, boosted regions are inherently considered κ_{VV}-enriched by construction.

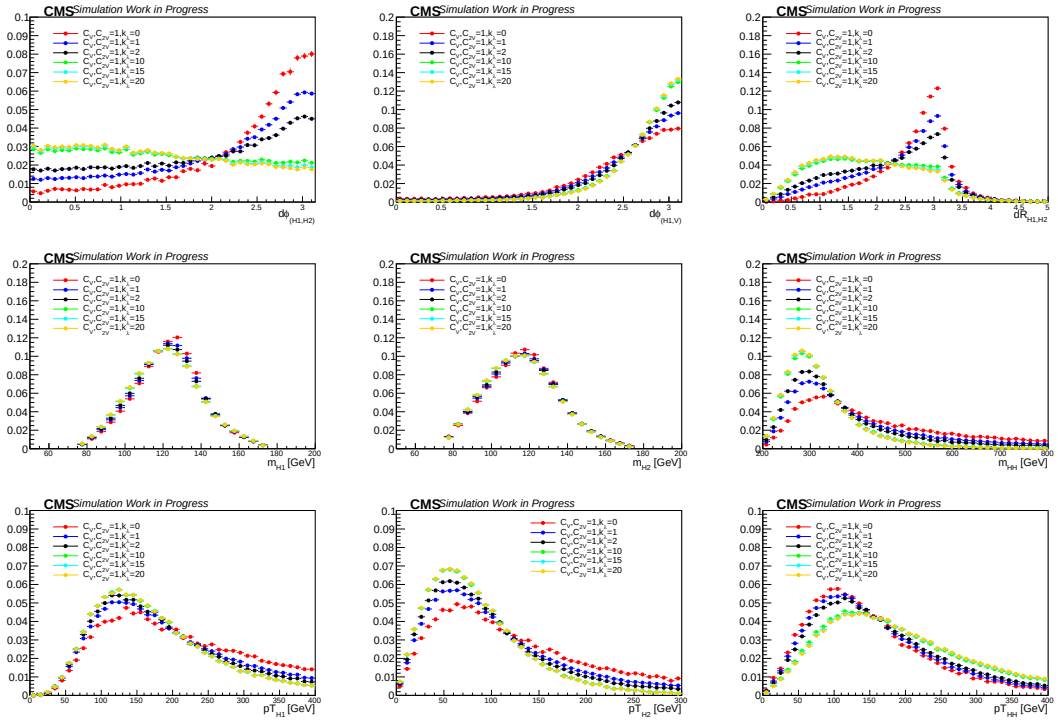

Figure 3.17 κ_λ dependence of different variables.

The BDTs are trained separately using the SCIKIT-LEARN software [77] and TMVA [76]. To enhance training performance, all three years' simulated signal samples in the signal regions are combined to increase the amount of training data. Figure 3.20 illustrates that the kinematic distributions are consistent across different years.

In the 2L channel, several sensitive variables are shown in Fig. 3.21 shows the distributions of the kinematics in the truth level, where various κ_λ values are displayed for continuous comparison of the signals, while κ_{VV} and κ_V are both fixed to their SM values.

The trained BDT distribution is shown in Fig. 3.22.

In 1L channel, the leading importance variable and the output of the BDT score are shown in figure 3.23 as an example.

In MET and 1L channel, an AdaBoost classifier is utilized, and the score returned represents the mean accuracy of the prediction. A BDT score < 0 or > 0 indicates that the event is more likely to belong to the corresponding categories. Thus, naturally, 0 is chosen as the division point, where the mean prediction correctness is 50%. With the categorization BDT, events are classified into κ_λ-enhanced (cateBDT score > 0, High score) and κ_{VV}-enriched (cateBDT

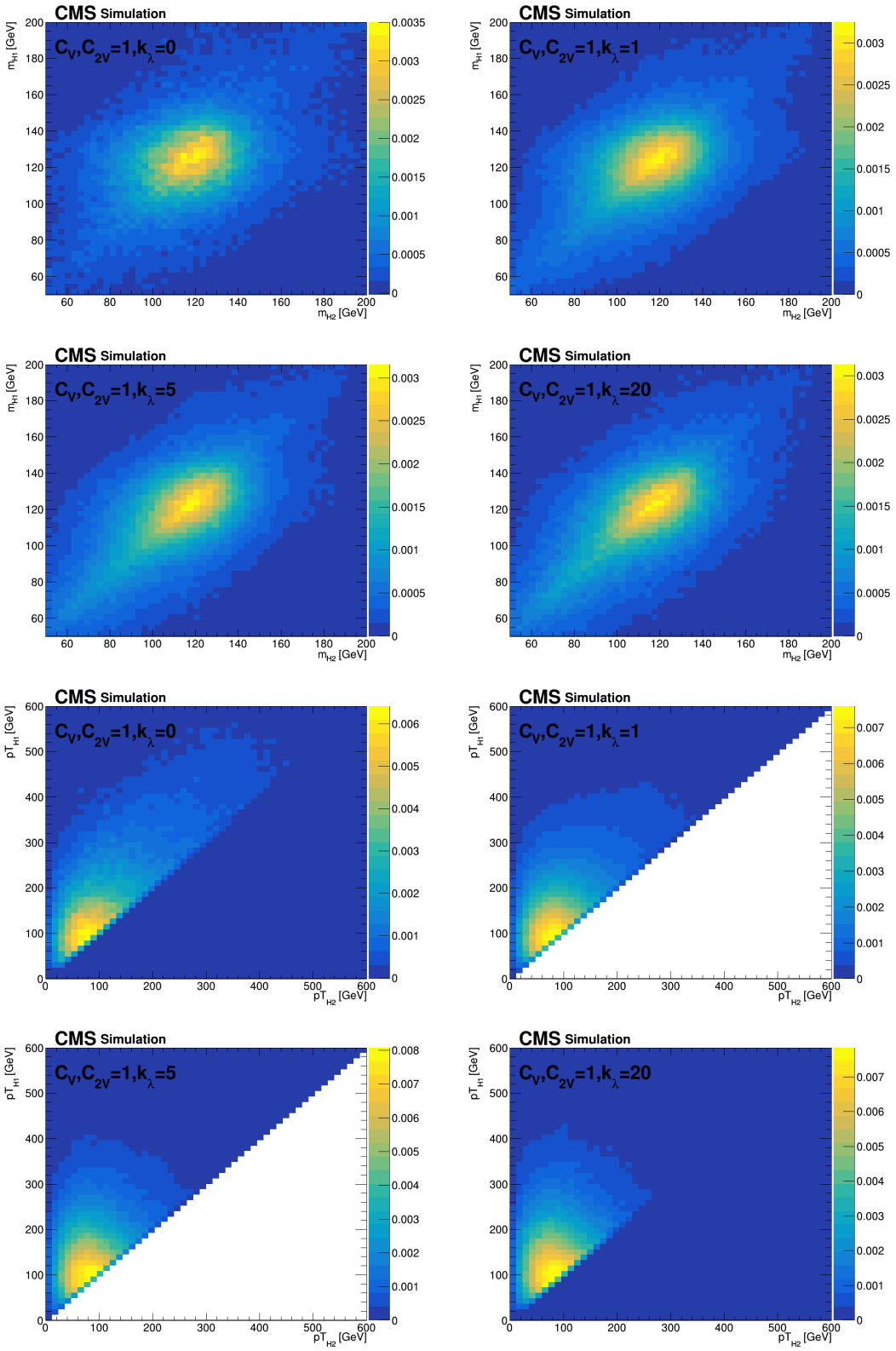

Figure 3.18 m_{H1} vs m_{H2} (top) and pT_{H1} vs pT_{H2} (bottom) distributions at different coupling points.

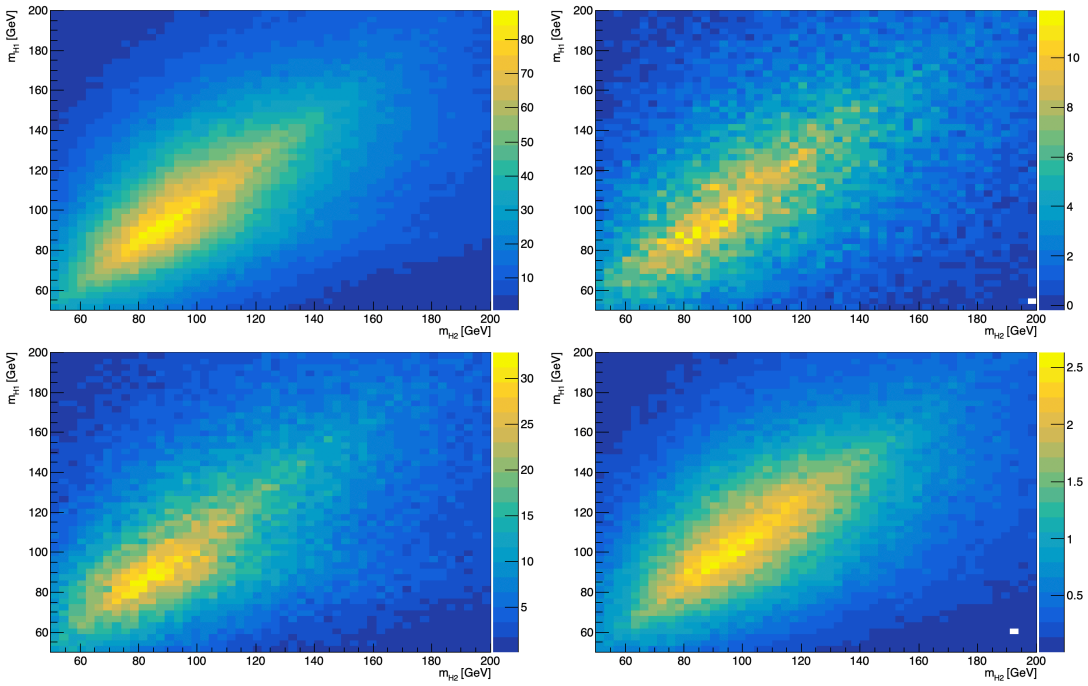

Figure 3.19 m_{H1} vs m_{H2} distributions of different major backgrounds: $t\bar{t}$ (top left), $t\bar{t} + b\bar{b}$ (top right), single top (bottom left), and $t\bar{t}V$ (bottom right).

score $\leq$ 0, Low score) regions. Fig. 3.24 also shows the distinct distribution of some input variables when we separate them using the BDT score.

As a summary, based on the different kinematic features and objects (e.g., lepton multiplicity) involved in different V-decay channels, we train 4 categorization BDTs to construct κ_λ -enriched and κ_{VV}-enriched categories in each channel. The variables used for these BDTs are listed in Table 3.16.

3.4.4 Background control

In different channels, the dominant backgrounds are different. For the FH channel, the dominant background is mainly QCD multi-jets process and majority $t\bar{t}$. In the MET and 1L channel, the main background is $t\bar{t}$ include $t\bar{t} + b\bar{b}$ process. In the 2L channel, the main backgrounds are both `DY+Jets` and $t\bar{t}$.

The FH channel differs from the leptonic channels in that the QCD multi-jet process is challenging to describe accurately using Monte Carlo simulation. Therefore, the background estimation will be accomplished using a data-driven method, which will be introduced in detail in the next section (Section 3.5, Background Modeling).

In all channels, Sidebands (SBs) are employed for studying background models, while Control Regions (CRs, not in the FH channel) serve to validate these models. Signal Regions

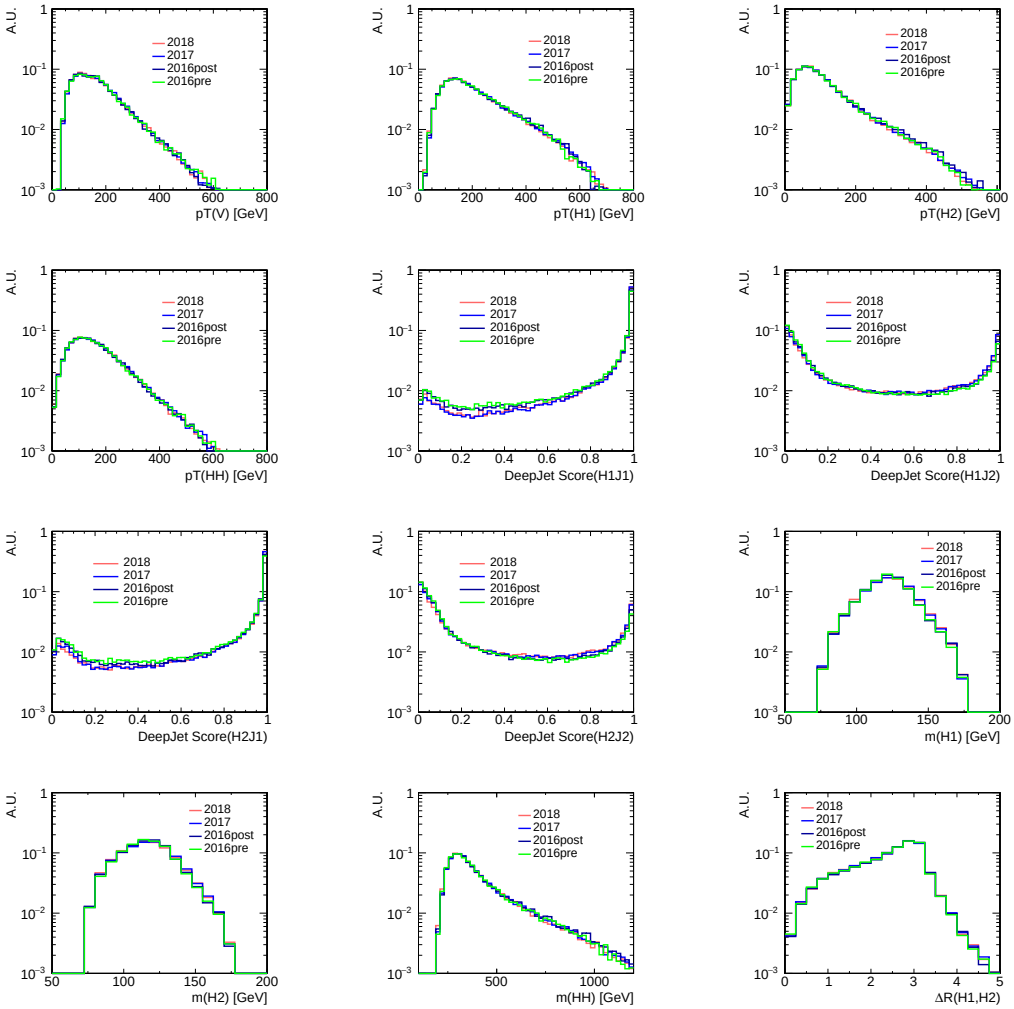

Figure 3.20 Comparison of the basic kinematics distributions of SM signal sample across 3 years in CMS Run2.

(SRs) are of paramount importance, as they yield the highest signal contributions and significantly enhance sensitivity analyses. In the boosted topology, the Failed selection Region(FR) is used as background control region, and the LP/HP regions are the signal regions.

Specially, due to the high precision reconstruction of the two leptons, the invariant mass of the vector boson can be accurately reconstructed with good resolution in the 2L channel. Leveraging this capability, we employ a 'mass window' to establish upper and lower limits of the vector boson mass (m_{V}). With this window, the two main backgrounds (`DY+Jets` and $t\bar{t}$, including $t\bar{t} + b\bar{b}$) can be studied separately.

According to the Monte Carlo (MC) simulation study, the principal background processes in the 2L channel consist of `DY+Jets`, $t\bar{t}$, and $t\bar{t} + b\bar{b}$. These backgrounds are estimated using MC simulations as detailed in Section 3.2.2. An overview of the background components

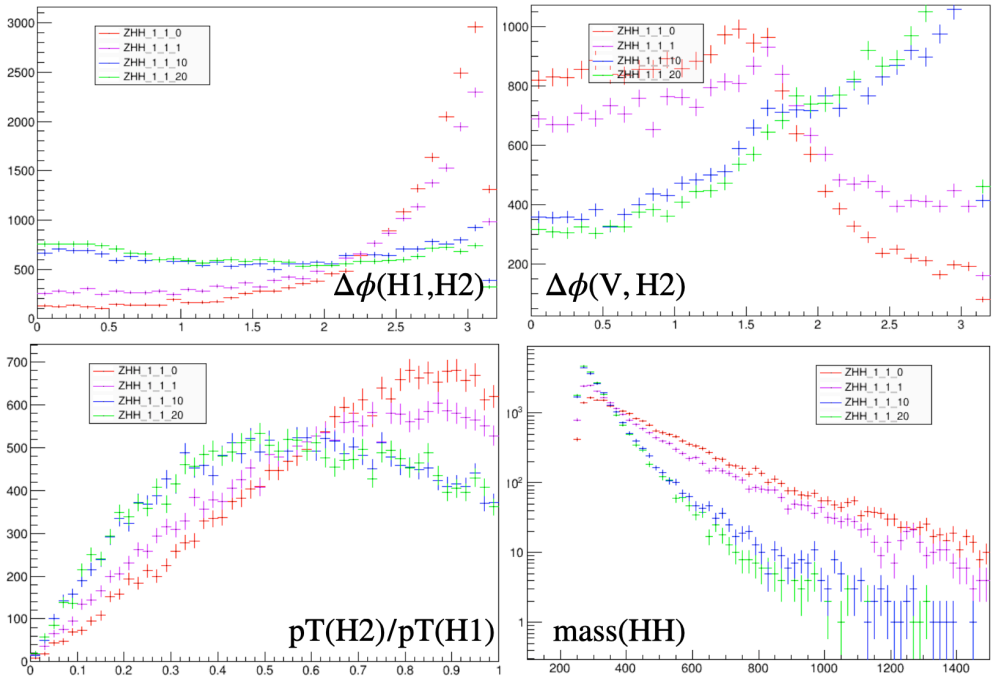

Figure 3.21 There are some of the kinematics that differ between signals with different couplings (blue: $\kappa_\lambda = 0$; red: $\kappa_\lambda = 20$) from the truth level.

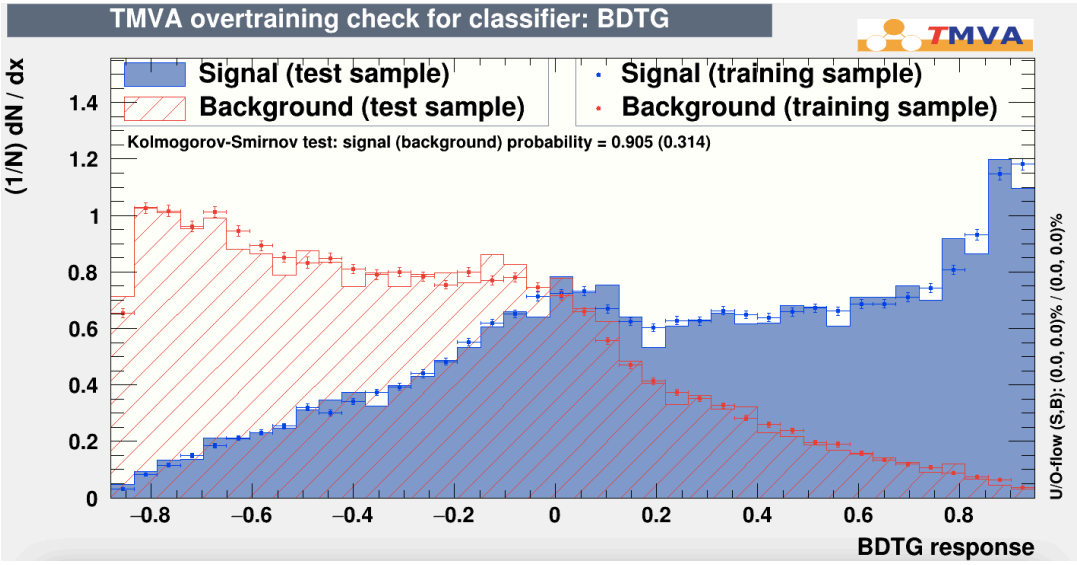

Figure 3.22 Distribution of the κ_λ BDT score of the $\kappa_\lambda = 0$ events(blue) vs. $\kappa_\lambda = 20$ events(red) and over training test.

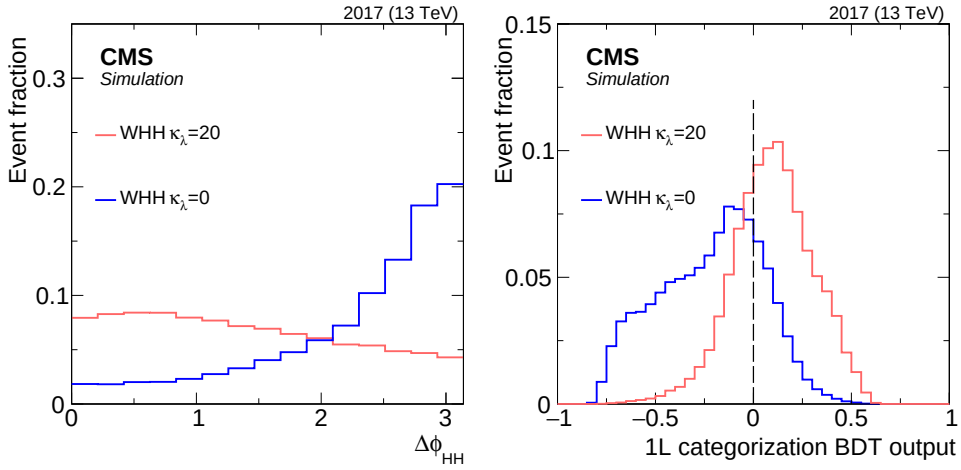

Figure 3.23 Kinematic distributions vary for different coupling strengths. On the left: azimuthal angle between the two reconstructed Higgs boson candidates, $\Delta\phi_{\mathrm{HH}}$, in the 1L SR for two different coupling models, $\kappa_\lambda = 20$ and 0. On the right: the categorization BDT output for the same two models. The dashed vertical line indicates where the categorization boundary is set.

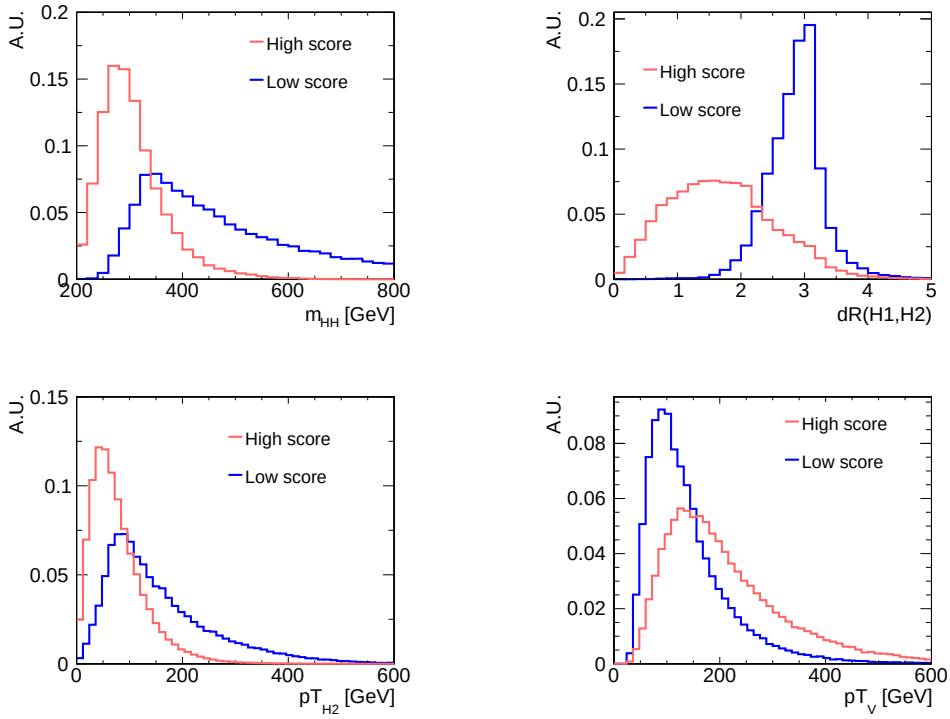

Figure 3.24 Distribution of some input variables in κ_λ -enhanced and κ_{VV}-enhanced region with SM signal. Events with lower HH mass, smaller angle between H1,H2 and more boosted vector boson are easier to have higher catgeorization BDT score.

is presented in Figure 3.27 based on events within and outside the Z mass window. As the number of b-jets increases, contributions from DY+Jets and $t\bar{t}$ decrease, while $t\bar{t}+b\bar{b}$ becomes

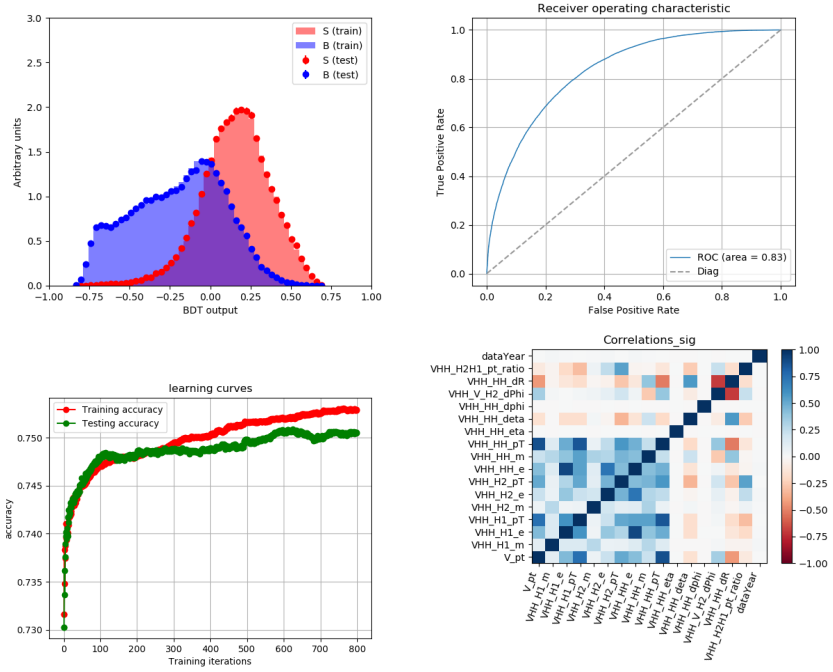

Figure 3.25 Categorization BDT (κ_λ =20 vs κ_λ =0) used in single lepton channel

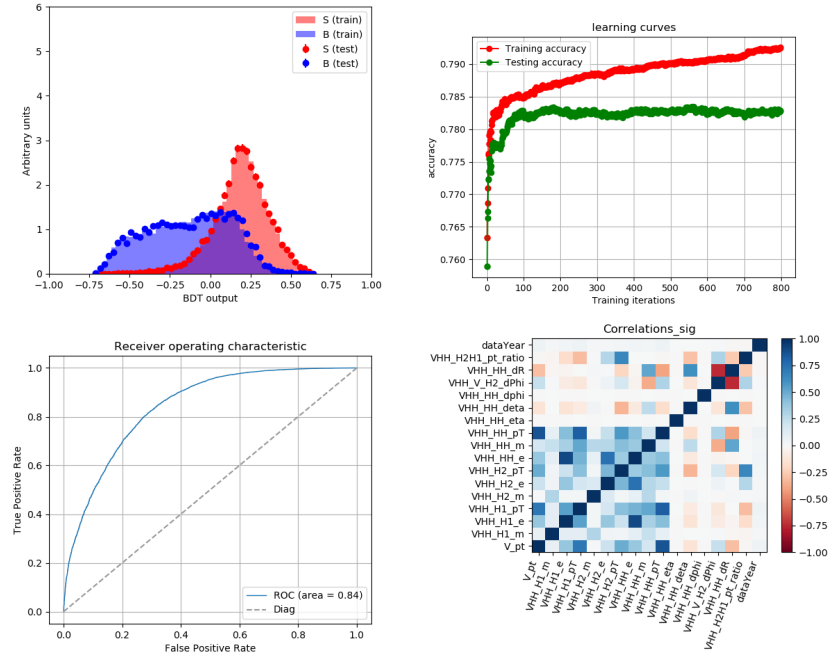

Figure 3.26 Categorization BDT (κ_λ =20 vs κ_λ =0) used in MET channel

dominant, as demonstrated in Figure 3.28 using events from the $t\bar{t}$ _CR. Due to the limited statistics of `DY+Jets` and $t\bar{t}$ MC samples in high b-multiplicity bins, 2b MC events are utilized to model events in 3b and 4b bins. A BDT-based reweighting method is developed to correct

Table 3.16 Variables used in the categorization BDTs for the separation of the κ_λ - and κ_{VV}-enriched regions and in $BDT_{SvB}$for extracting signal-like events. The ✓symbol indicates that the BDTs include the variable. These variables include the reconstructed Higgs boson with higher transverse momentum (H1) and the lower one (H2), the Higgs candidate jets ordered by the DeepJet b tagging score ($j_{1,2,3,4}$), the scalar sum of the transverse energy of all the jets excluding $j_{1,2,3,4}$ (H_T^{ex}), the number of jets (N_{jets}), the selected leptons in the 2L channel (ℓ_1, ell_2), the N-subjettiness [78] ratio τ_2/τ_1 and τ_3/τ_2. The small-radius (large-radius) regions are designated with an "S" ("L") in parentheses. Table come from public analysis summary [79].

	Cats.		SvB				Cat.	SvB
Input variable	MET/1L	FH	MET (S)	1L (S)	MET/1L (L)	Input variable	2L	2L
$p_T(V)$, p_T(H1)	✓	✓	✓	✓	✓	$p_T(V)$, p_T(H1)	✓	✓
p_T(H2), p_T(HH)	✓		✓	✓	✓	m_{HH}	✓	✓
m_{H1}, m_{H2}	✓		✓	✓	✓	ΔR(H1, H2)	✓	✓
m_{HH}	✓	✓	✓	✓	✓	$\Delta\phi$(V, H2)	✓	✓
ΔR(H1, H2)	✓	✓				p_T(H2)/p_T(H1)	✓	
$\Delta\phi$(V, H2)	✓	✓	✓	✓	✓	p_T(HH)		✓
p_T(H2)/p_T(H1)	✓	✓				m_{H1}, m_V		✓
$\Delta\eta$(H1, H2)	✓	✓	✓			$\Delta\eta$(H1, H2)		✓
$\Delta\phi$(H1, H2)	✓	✓	✓	✓	✓	Energy of H1		✓
Energy of H1	✓	✓				Energy of HH		✓
Energy of H2	✓	✓				$p_T(ell_2)/p_T(\ell_1)$	✓	✓
Energy of HH	✓	✓				$\Delta\phi(\ell_1, ell_2)$	✓	✓
η_{HH}	✓	✓				$\Delta\eta(\ell_1, ell_2)$	✓	✓
η_{H1}		✓	✓			$\Delta R(j_{1,H2}, j_{2,H2})$	✓	
ϕ(V)			✓	✓	✓	$\Delta R(j_{1,H1}, j_{2,H1})$	✓	
$s_{b-tag}(j_{1,2,3,4})$			✓	✓		$p_T(\ell_1)/m_V$	✓	
H_T^{ex}			✓			$p_T(\ell_1)$	✓	
N_{jets}			✓			$p_T(j_{3,4})$		✓
τ_2/τ_1(H1, H2)					✓	H_T^{VHH}		✓
τ_3/τ_2(H1, H2)					✓	p_T(V)/p_T(HH)		✓
						$\Delta\phi$(V, HH)		✓
						$p_T(\ell_1)/m_V$		✓

kinematic differences between the b-jet bins, although a detailed description will be provided in the next section (Background Modeling, Section 3.5).

The fitting topology in the 2L channel is depicted in the diagram shown in Fig. 3.29. For the template fit, we combine events from three years and categorize them into four regions based on the κ_λ BDT score and b-tag multiplicity, as follows: κ_λ -enriched with 3b-tags (3, 7), κ_λ -enriched with 4b-tags (2, 6), κ_{VV}-enriched with 3b-tags (4, 8), κ_{VV}-enriched with 4b-tags (1, 5). The SBs (9, 10) and $t\bar{t}$ CRs (11, 12) are fitted simultaneously and do not follow the κ-parameter categorization. The other channels are somehow simpler, the 1L and MET channel don't have $t\bar{t}$ _CR, and the FH channel doesn't have CR and $t\bar{t}$ _CR.

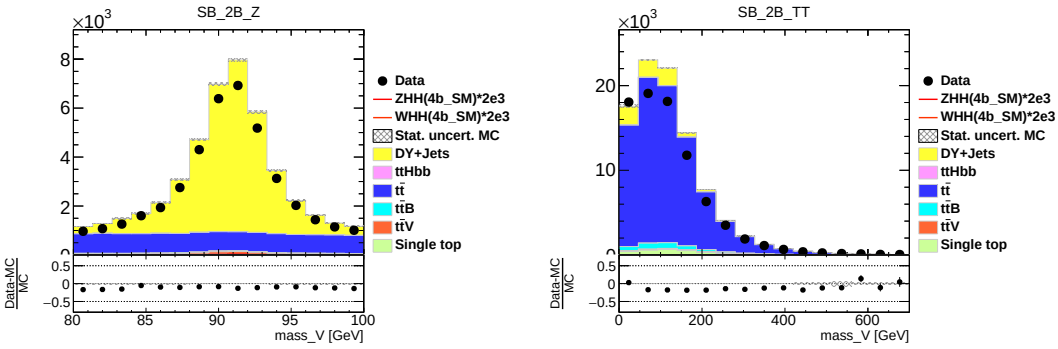

Figure 3.27 Backgrounds in 2b CR inside Z mass window(left) and outside Z mass window($t\bar{t}$ CR)(right).

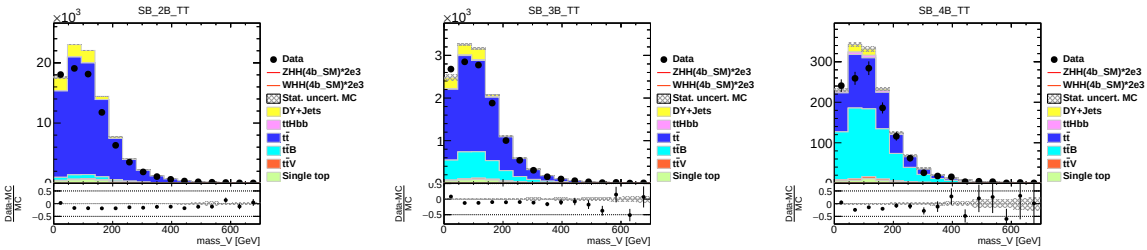

Figure 3.28 Ratio between $t\bar{t}$ and $t\bar{t}+b\bar{b}$ varies when the b-jets multiplicity going higher.

3.4.5 Signal extraction

For signal extraction, we utilize various machine learning techniques to improve sensitivity. In different V-decay channels, we optimize separate machine learning models for signal versus background, notably in both the κ_λ -enriched category and the κ_{VV}-enriched category parallely.

In the leptonic channel, we are adapting BDTs for signal extraction, namely SvB BDTs, and the outputs of these BDTs are used as the observables in the final fit. The training samples consist of MC simulated events of both signals and backgrounds. The backgrounds include the most dominant ones. In the 2L channel, they are $t\bar{t}$, `DY+Jets`, and $t\bar{t}+b\bar{b}$. In the 1L channel and the MET channel, they are $t\bar{t}$, $t\bar{t}+b\bar{b}$, and single-Top events. The signal samples depend on the kappa categories. In the κ_{VV}-enriched category, we are using SM VHH samples, while in the κ_λ -enriched category, we are using $\kappa_\lambda = 20$ VHH samples to maintain higher significance. The variables used in the SvB BDTs are selected from all available kinematics and are chosen to minimize overlap with the categorization BDTs in order to preserve sensitivity. The SvB variables can also be found in the summarizing table 3.16.

In the 2L channel, the signals and backgrounds consist of events from the Signal Regions (SRs) that we defined above, ensuring that the models are optimized in the most sensitive

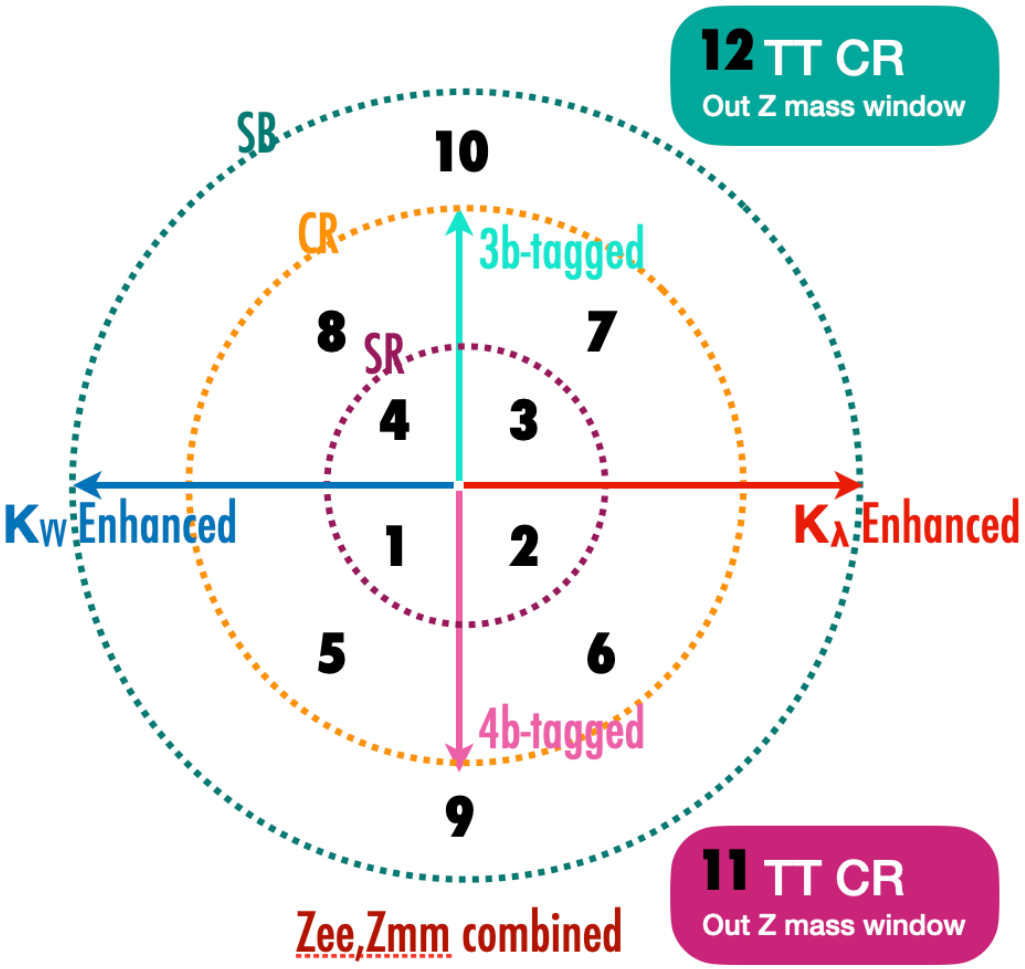

Figure 3.29 The regions that contains in the final template fit in 2L.

regions. The results of the over-training test can be found in Figure 3.30 for two different kappa categories. Additionally, the Boosted Decision Tree (BDT) outputs of the events in the 4b-tagged SRs are shown in Figure 3.31. These output BDT scores will be used as observables for the final fitting.

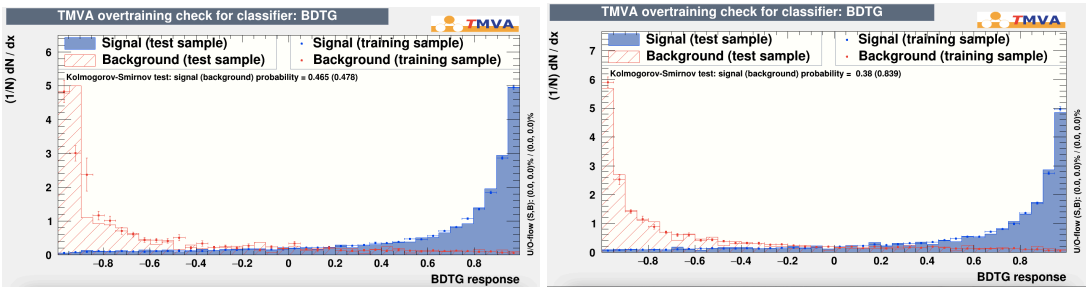

Figure 3.30 Over training test for the SvB BDT in the κ_{VV}-enriched region(right) and κ_λ -enriched region(left).

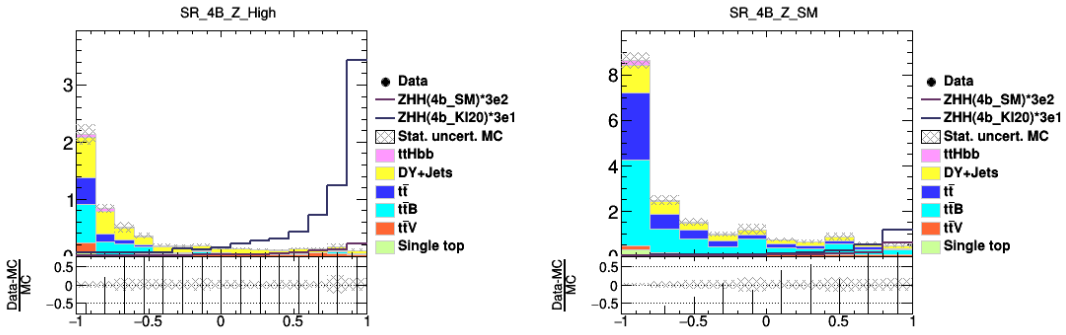

Figure 3.31 Distribution of the SvB BDT output in the κ_λ -enriched region (left) and κ_{VV}-enriched region (right) in signal region with four b-tagged jets.

In the 1L channel, as mentioned earlier, categorization BDTs are utilized to categorize the signal regions. Additionally, two SvB BDTs are further trained to optimize signal extraction within their respective categories, as illustrated in Fig. 3.32. Furthermore, the separation of signal versus background in categorized regions can be examined in Fig. 3.33.

The SvB BDT distribution in the SB3B+SB4B region is depicted in Fig. 3.34. The upper row corresponds to the single lepton channel, while the bottom row represents the single muon channel. The left plots display the κ_λ -enriched BDT, while the right plots depict the κ_{VV}-enriched BDT. The limits shown in Fig. 3.96(a) indicate that a BDT trained for one coupling is not necessarily optimal for another. However, with the current strategy, BDTs can be optimized for both κ_{VV} and κ_λ .

In the MET channel, similar to the single lepton channel, two SvB BDTs are trained

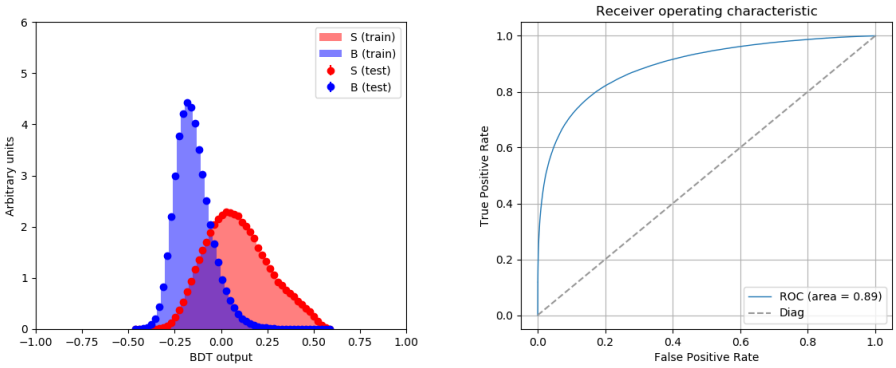

(a) BDT trained in κ_λ-enriched region

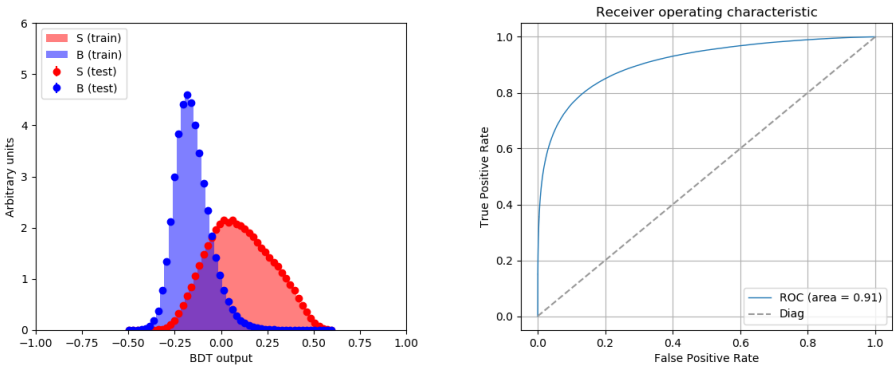

(b) BDT trained in κ_{VV}-enriched region

Figure 3.32 SvB BDTs in 1L channel, resolved topology.

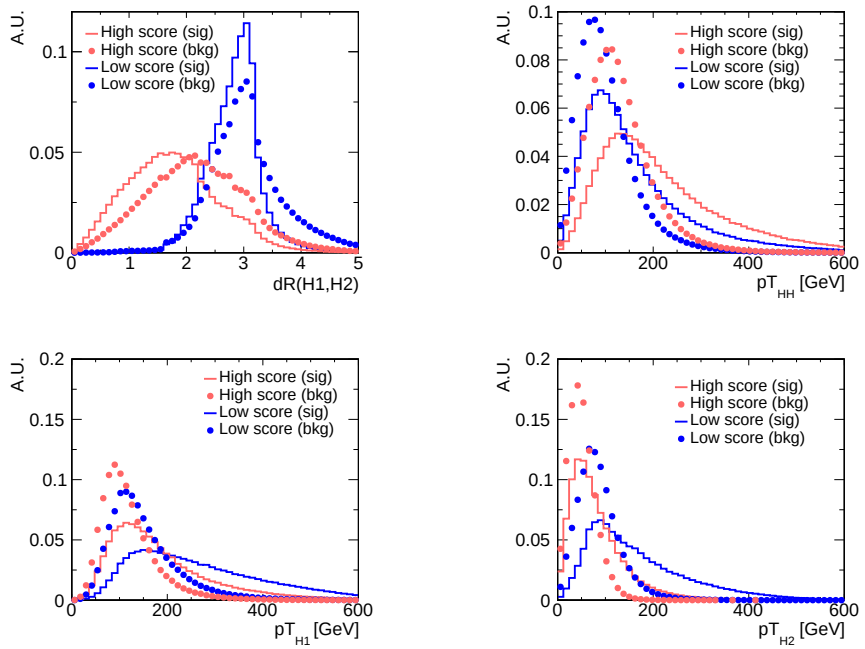

Figure 3.33 Distribution of some input variables of signal/background events in κ_λ -enriched and κ_{VV}-enriched region

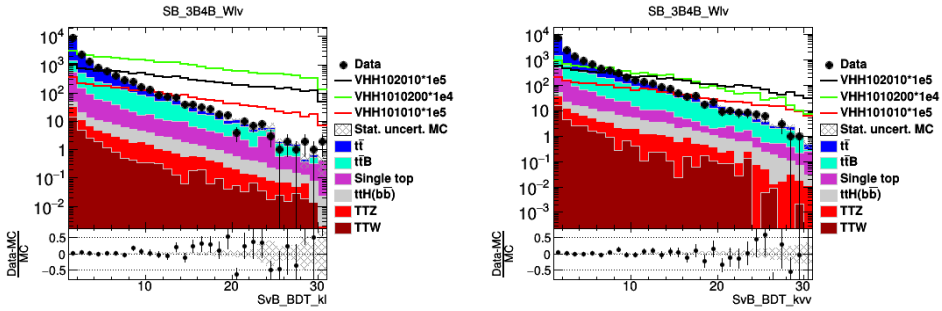

Figure 3.34 The SvB BDT distribution in the SB3B+SB4B region is presented. The left plot corresponds to the κ_λ -enriched BDT, while the right plot depicts the κ_{VV}-enriched BDT. These plots represent prefit distributions with $t\bar{t}$ and $t\bar{t} + b\bar{b}$ scale factors (from final fitting) applied.

in different signal categories. They are illustrated in Fig. 3.35 and will be utilized in their corresponding categorized regions, with their output scores serving as the variables for the final fitting.

The SvB BDT distribution in the SB3B+SB4B region are shown in Fig. 3.36. The left plots are κ_λ -enriched BDT, the right plots are κ_{VV}-enriched BDT.

In the 1L and MET channel, we also consider the boosted topology. As previously mentioned, since AK8 jets are utilized in the boosted topology, there is already an implicit requirement that the two Higgs candidates are not close to each other; otherwise, they would already be merged into the same AK8 jet. Consequently, events with the boosted topology are in a relatively κ_{VV}-enriched region and only one SvB BDT is trained for these regions. The training variables that used in this topology are also listed in the table 3.16.

In the FH channel, the Signal vs Background (SvB) classifier is a neural network discriminator with the architecture described in [80]. The SvB classifier comprises two substructures: a **Hierarchical Combinatoric ResNet (HCR)** that handles the four Higgs candidate jets, and a **Multi-head Attention Block** that manages other jets. The HCR consists of three blocks, as depicted in Figure 3.37, designed to identify the two Higgs dijets. The dijet block takes the kinematics of the four b-tagged jets as input and evaluates all three possible combinations. Subsequently, the quadjet block and the event-level block process the output from their respective former blocks, accompanied by some engineered features, and ultimately yield the probability that an event is signal-like. The Multi-head Attention block corrects the dijet block output based on the kinematics of other jets, including those from the vector boson.

The training dataset comprises both WHH and ZHH signals with all 8 couplings, $t\bar{t}$ Monte Carlo (MC), and the multijet background. The signals from each coupling are scaled to have the same summed weight; otherwise, the training would be dominated by the one with the

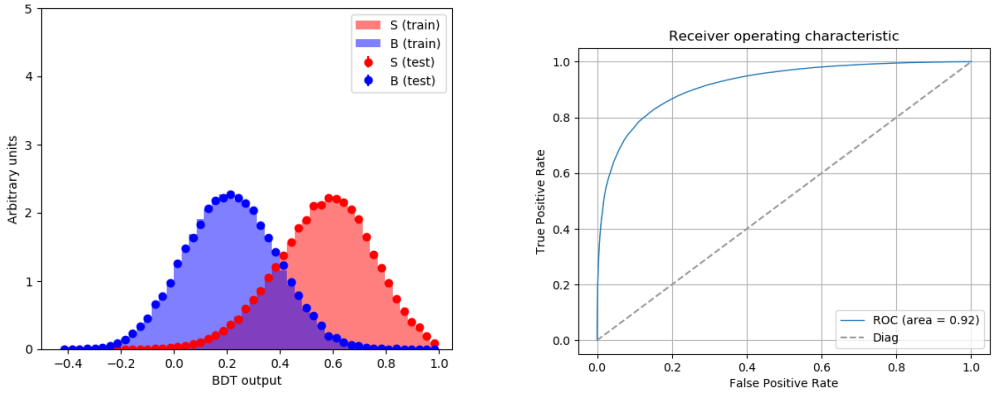

(a) BDT trained in κ_λ -enriched region

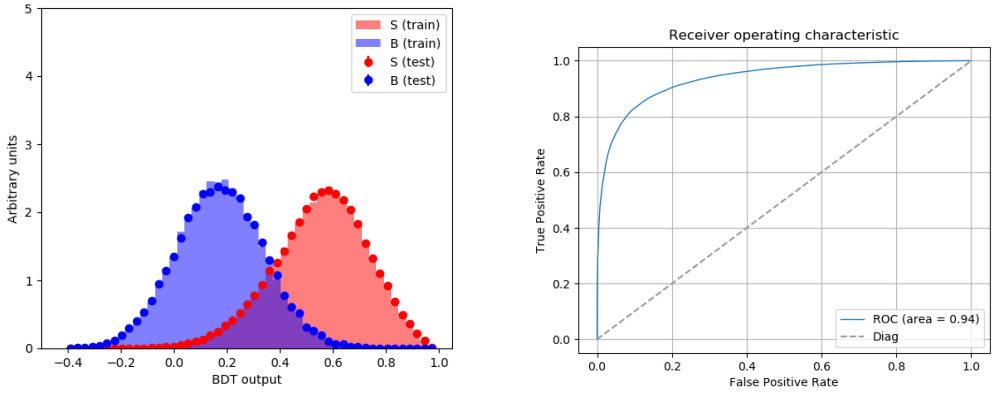

(b) BDT trained in κ_{VV}-enriched region

Figure 3.35 SvB BDTs in 0L channel, resolved topology.

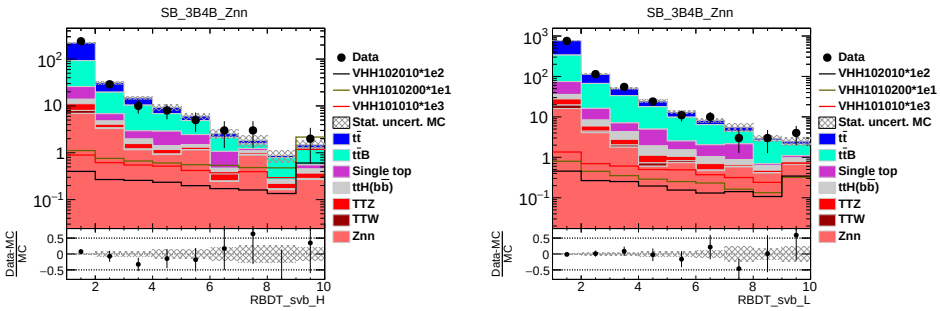

Figure 3.36 The SvB BDT distribution in the SB3B+SB4B region. The left plot is κ_λ -enriched BDT, the right plot is κ_{VV}-enriched BDT. These are prefit plots with $t\bar{t}$ and $t\bar{t}+b\bar{b}$ scale factor (from final fitting) applied.

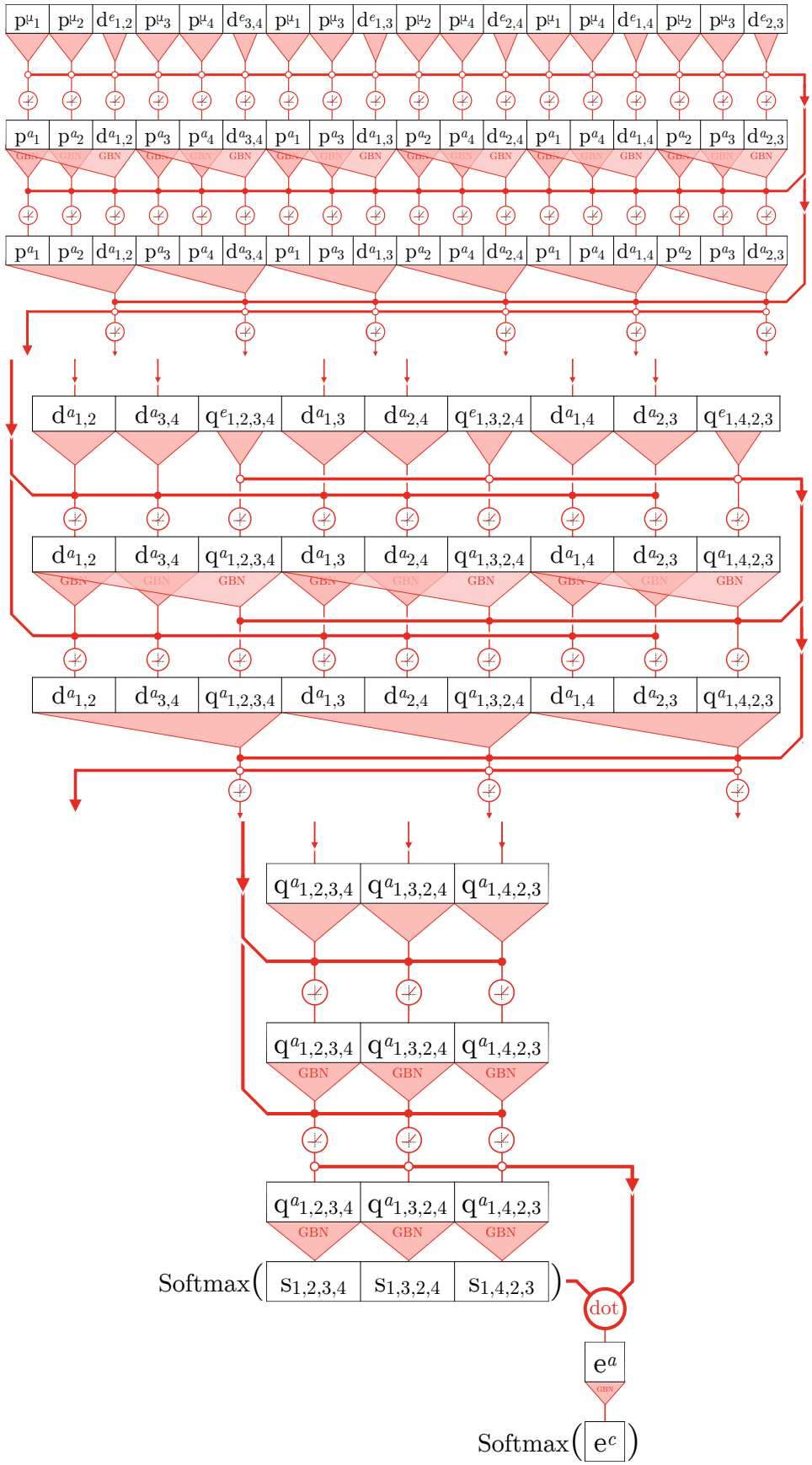

Figure 3.37 The neural network structure: **Top** Dijet block; **Middle** Quadjet block; **Bottom** Event-level block

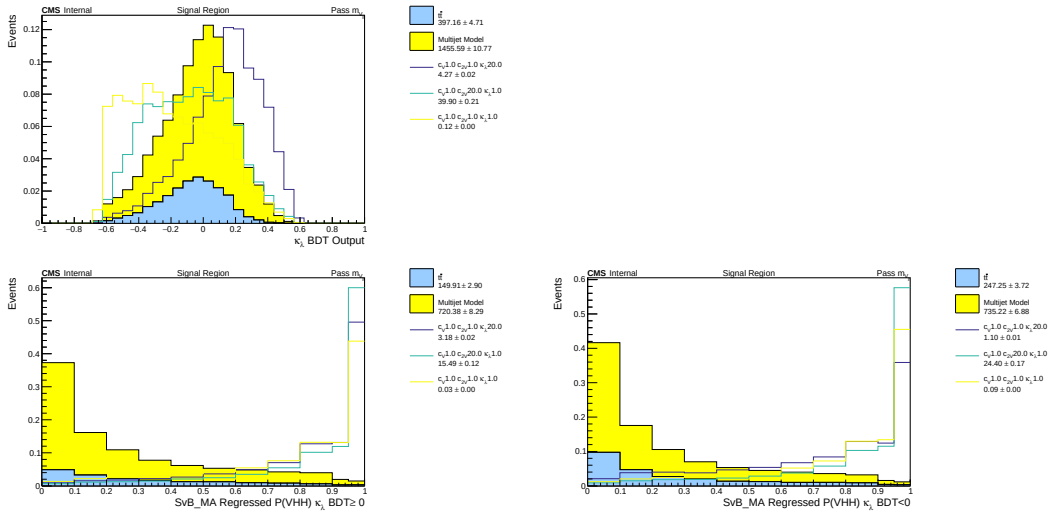

Figure 3.38 **Top** Normalized kinematic categorization BDT distribution **Bottom Left** Normalized SvB distribution in κ_λ -enriched region (BDT score > 0) **Bottom Right** Normalized SvB distribution in κ_{VV}-enriched region (BDT score < 0)

largest cross-section. The target output for each event is a one-hot label.

$$[t\bar{t}, \text{multijet}, \kappa_\lambda \text{ enhanced signal}, \kappa_{VV} \text{ enhanced signal}] \tag{3.9}$$

where the κ_λ -enriched or κ_{VV}-enriched categorization is determined by the kinematic categorization BDT described previously. A k-folding technique is applied by evenly dividing the entire dataset into three training sets, with $2/3$ of events in each set. From these sets, three classifier models are obtained respectively. Each model is then used to predict on the remaining $1/3$ of events not involved in the training to reduce over fitting. Figure 3.38 depicts the distribution of the kinematic categorization BDT output and SvB classifier output.

3.5 Background modeling

The background modeling varies from one topology to another and differs across different channels. Generally speaking, we are using Monte Carlo (MC) simulated events to study the behavior of the backgrounds. In the leptonic channels, the background processes taken into consideration include DY+Jets, Z($\nu\nu$)+Jets, $t\bar{t}$, $t\bar{t}+b\bar{b}$, TTV, TTH, single top, and Multi-Jets. Among these, the DY+Jets, $t\bar{t}$, $t\bar{t}+b\bar{b}$, and the Multi-Jets processes are dominant in certain V-decay channels, and the accuracy and stability of the modeling of these processes are vital for this analysis.

3.5.1 The BDT re-weighting method

In the 2L channel, particularly in the 3b-tagged and 4b-tagged Signal Regions (SRs) and the high-purity (HP) and low-purity (LP) regions in the boosted topology, we encounter a lack of statistics, leading to large statistical uncertainty and difficulties in training the SvB classifier. To address this issue, we opt to estimate the background of the important processes using the following method: **In the 2L channel, we re-weight the 2b-tagged Monte Carlo (MC) events to estimate backgrounds in the 3b-tagged and 4b-tagged SRs. Additionally, we re-weight the failed selection MC events to estimate the backgrounds in the HP and LP regions within the boosted topology.**

In the 2L channel, in order to include the kinematics information as more as possible, BDTs are trained to learn these distributions that can tells the differences between 2b-tagged events and 3 or 4b-tagged events. This re-weighting method is applied to both DY+Jets and $t\bar{t}$ inclusive samples due to the lack of statistics in the 3b-tagged and 4b-tagged regions. Hence, four BDTs have been trained to implement this process, as illustrated in Fig. 3.39.

The training samples are derived from the Sideband (SB) (with r_{HH} greater than 50 GeV and inside the Z mass window), while the validation samples are from the Control Region (CR) and Signal Region (SR). We utilize the same variables as those in the SvB BDT for the training inputs of the re-weighting (RwT) BDT. This is done to maximally reproduce the 3b and 4b final fitting templates using 2b events, aiming to obtain more stable background models with significantly smaller statistical uncertainties.

The number of events should remain unchanged in the re-weighting process. Table 3.17 to 3.19 are used to project the normalization from 2b to 3b and 4b.

To validate the kinematic corrections introduced by the RwT BDTs, key distributions are compared before and after the re-weighting to the real 3b and 4b events. First of all, the p_T

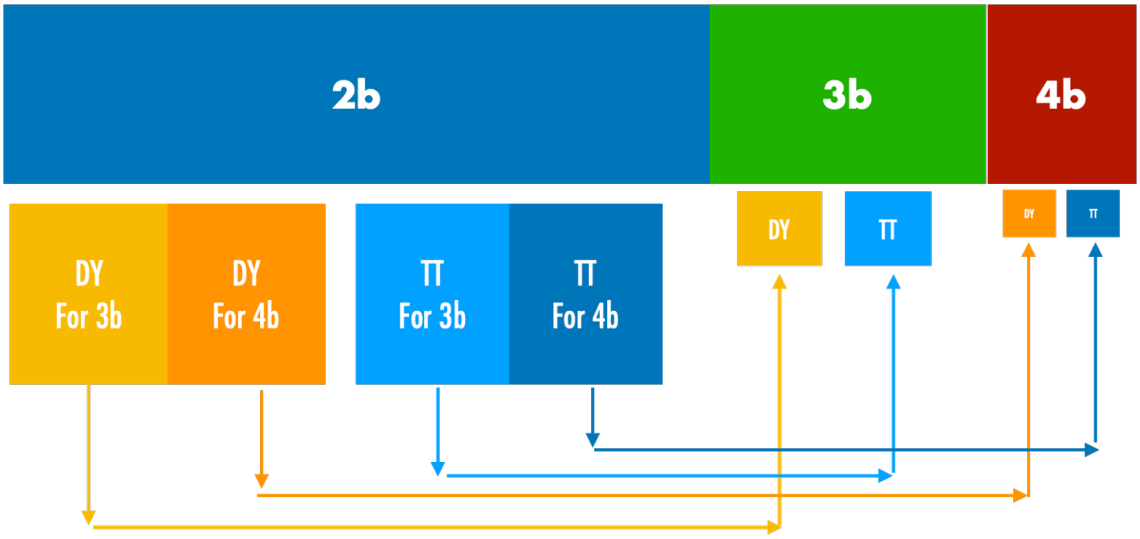

Figure 3.39 4 RwT BDTs trained with SB events.

Table 3.17 Event yield of background MC yield in different rHH regions. (2018)

Background	DY	TT	TTBB
rHH_SB_2B	19569.281	25357.826	818.052
rHH_SB_3B	1949.411	2542.947	723.666
rHH_SB_4B	116.525	135.757	178.626
rHH_CR_2B	4327.48	9021.811	275.45
rHH_CR_3B	505.716	886.676	262.981
rHH_CR_4B	22.809	47.348	64.027
rHH_SR_2B	1740.239	4129.035	125.13
rHH_SR_3B	162.436	410.135	118.88
rHH_SR_4B	7.075	21.334	31.529

distributions of the third and fourth ranked jets using DeepJet score are compared in Fig. 3.40. The original 2b distributions (fail the 3/4b selection, in blue) apparently deviate from 3b and 4b, while the re-weighted distributions (green) match well the real 3b and 4b shapes. Then, the SvB BDT distributions used as the final fitting templates are compared in Figs. 3.41 and 3.42, where the re-weighted distributions reproduce the real 3b and 4b ones decently.

The distributions of the remaining important input variables are also compared between the real 3b and 4b events and re-weighted 2b events, along with the re-weighting uncertainty (which will be introduced in the following texts), in Figures 3.43 to 3.45.

Furthermore, to assess the benefits of using high-statistics 2b events for 3b and 4b, Figure 3.46 provides a direct comparison using the original `DY+Jets` and $t\bar{t}$ Monte Carlo (MC) samples and the re-weighted 2b MC samples. The MC statistical uncertainty is significantly reduced.

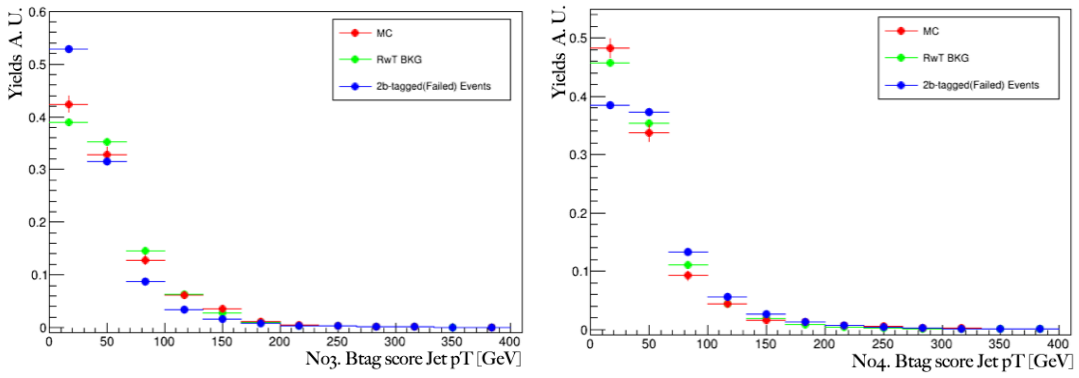

Figure 3.40 The comparison of the original MC events in the signal region(Red) with the MC events in the 2b-tags region(blue) and the same events after re-weighting(green).

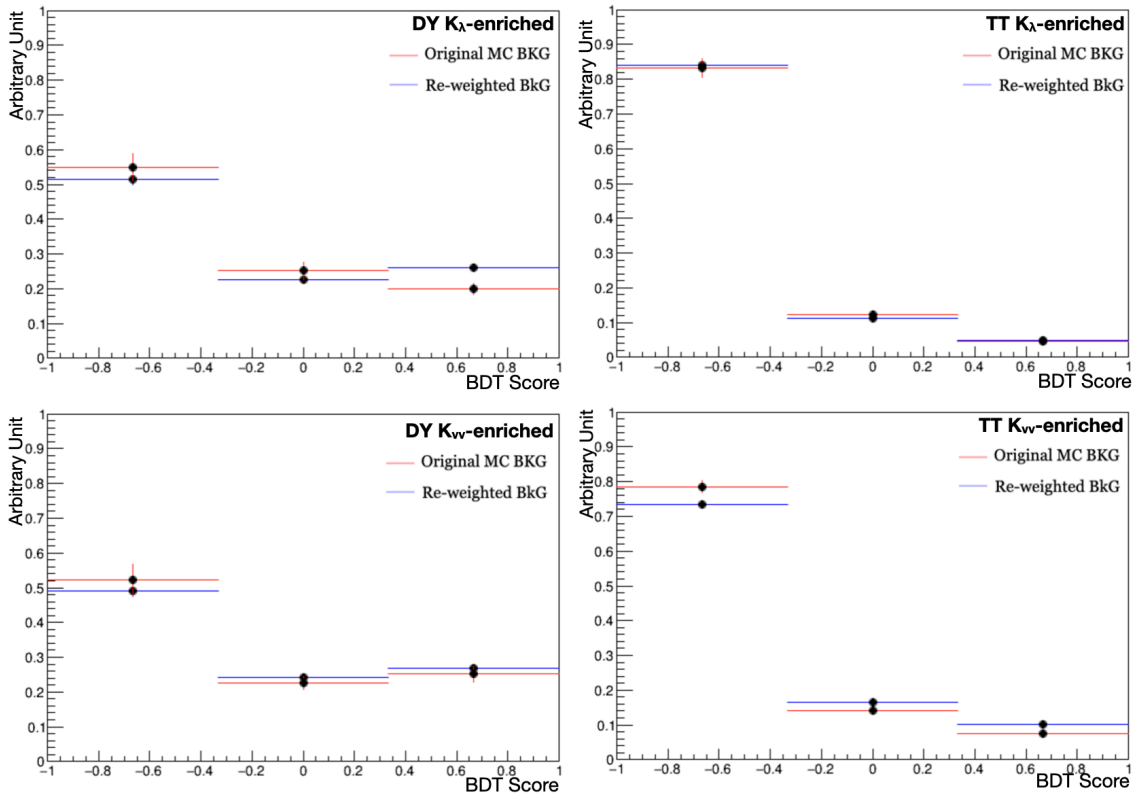

Figure 3.41 The comparison of the original MC events in the signal region(Red) with the MC events in the 2b-tags region(blue) over the SvB BDT output in 3b-tagged signal region.

Table 3.18 Event yield of background MC yield in different rHH regions. (2017)

Background	DY	TT	TTBB
rHH_SB_2B	18581.785	18458.348	606.333
rHH_SB_3B	1155.817	1637.511	510.733
rHH_SB_4B	40.184	78.456	121.898
rHH_CR_2B	3434.052	6587.921	211.26
rHH_CR_3B	232.51	580.235	184.942
rHH_CR_4B	13.095	29.059	45.439
rHH_SR_2B	1394.181	3005.955	94.784
rHH_SR_3B	148.178	261.143	86.075
rHH_SR_4B	4.229	13.52	20.615

Table 3.19 Event yield of background MC yield in different rHH regions. (2016)

Background	DY	TT	TTBB
rHH_SB_2B	10201.914	9027.777	419.792
rHH_SB_3B	760.564	968.877	346.799
rHH_SB_4B	43.513	51.98	87.34
rHH_CR_2B	2105.781	3217.84	142.942
rHH_CR_3B	194.936	334.089	124.165
rHH_CR_4B	9.502	18.771	27.57
rHH_SR_2B	877.797	1476.517	61.984
rHH_SR_3B	80.934	149.144	63.185
rHH_SR_4B	3.597	8.042	14.071

In addition, control plots are provided for additional variables with the re-weighted `DY+Jets` and $t\bar{t}$ using 2b events in Figures 3.47 and 3.60.

Although the statistical uncertainties are reduced, the re-weighting method introduces additional uncertainty to the background models. The re-weighting uncertainties consist of two sources. The first one (Type 1) arises from the fitting uncertainty of the fitting function (polynomial functions, where x represents the RwT BDT score) that re-weights 2b to 3b and 4b events. The function

`ROOT::Fit::FitResult::GetConfidenceIntervals(0.95)`

is used to obtain the 95% confidence intervals of the fitting value variations. The variation is shown in Fig. 3.48 as the dashed yellow curves. This uncertainty is constructed in the likelihood as a nuisance parameter that contains "bkgrwt_t1" in the name (Appx. .3), e.g., "CMS_vhh4b_bkgrwt_t1_2L_tt" for 2L $t\bar{t}$. The second source comes from a bin variation of the weight curve, which contains shifts to one neighboring bin on the left and the right, as shown in Fig. 3.48 as the solid red curve. Its nuisance name contains "bkgrwt_t0", e.g.,

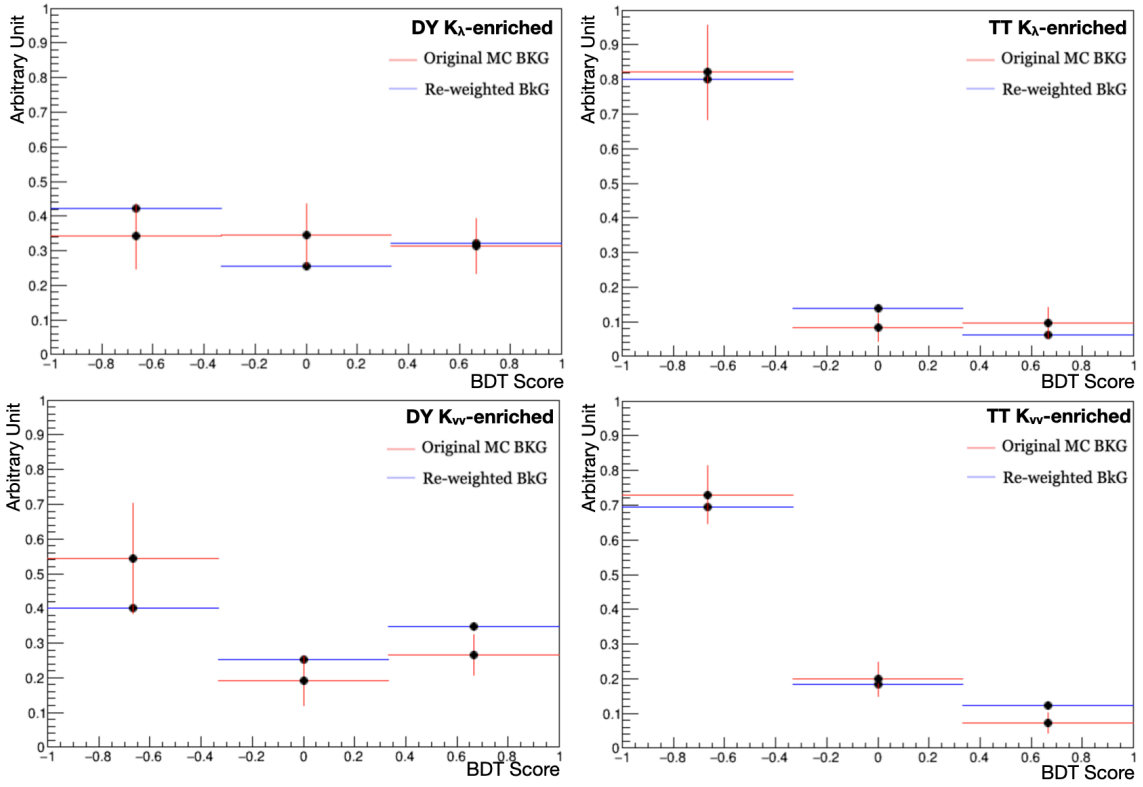

Figure 3.42 The comparison of the original MC events in the signal region(Red) with the MC events in the 2b-tags region(blue) over the SvB BDT output in 4b-tagged signal region.

CMS_vhh4b_bkgrwt_t0_2L_tt for 2L $t\bar{t}$.

We share the same thoughts in the boosted topology, background events ($t\bar{t}$, $t\bar{t} + b\bar{b}$) in the failed region

$!(D_{bb}(H1) >= 0.9 \text{ and } D_{bb}(H2) >= 0.9) \text{ AND } (D_{bb}(H1) >= 0.80||D_{bb}(H2) >= 0.8)$

are well populated. Therefore, we can use these events to mimic the events in the signal region. Two re-weight BDTs are trained to discriminate background events in the failed region and signal regions (LP, HP), as shown in Fig. 3.49 top and bottom left plots. Then we can choose a binning to make the "Passed bkg." distribution flat. This step essentially transforms the original BDT score to a new score, which makes the red distributions flat (Fig. 3.49 top and bottom middle plots). Due to the slight difference in the MC event weight, we can't make it completely flat. The next step is to divide the "Passed bkg." distribution by the "Failed bkg." distribution, and we obtain the weights for "Failed bkg." as shown in Fig. 3.49 top and bottom right plots. In the end the weight is parameterized with a second order polynomial function and the up and down versions are used as the type-1 uncertainty, left and right version are used as the type-2 uncertainty.

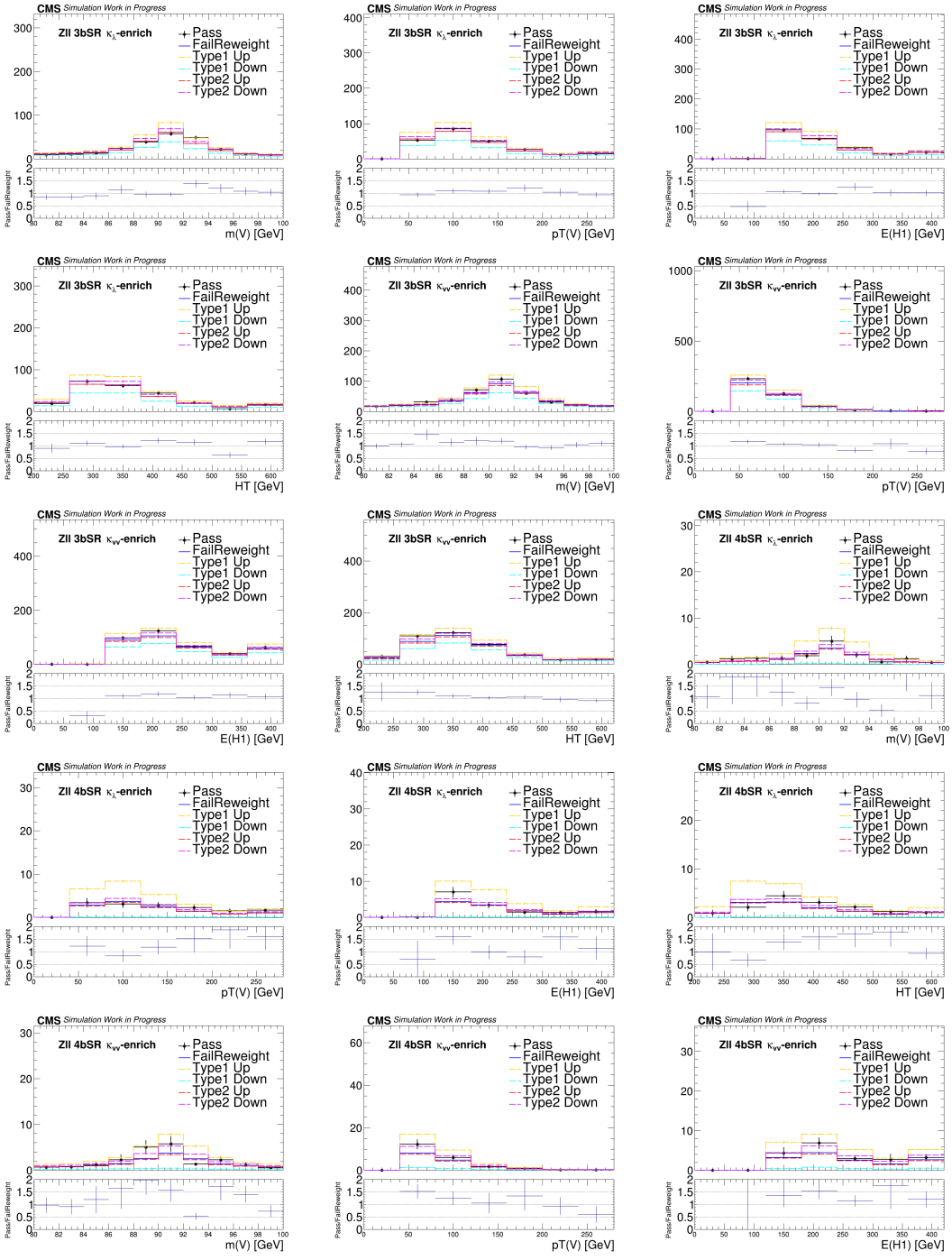

Figure 3.43 The comparison of the original MC events in the signal region (black histogram) with the re-weighted MC events in the 2b-tags region(blue) and the re-weighting uncertainties.

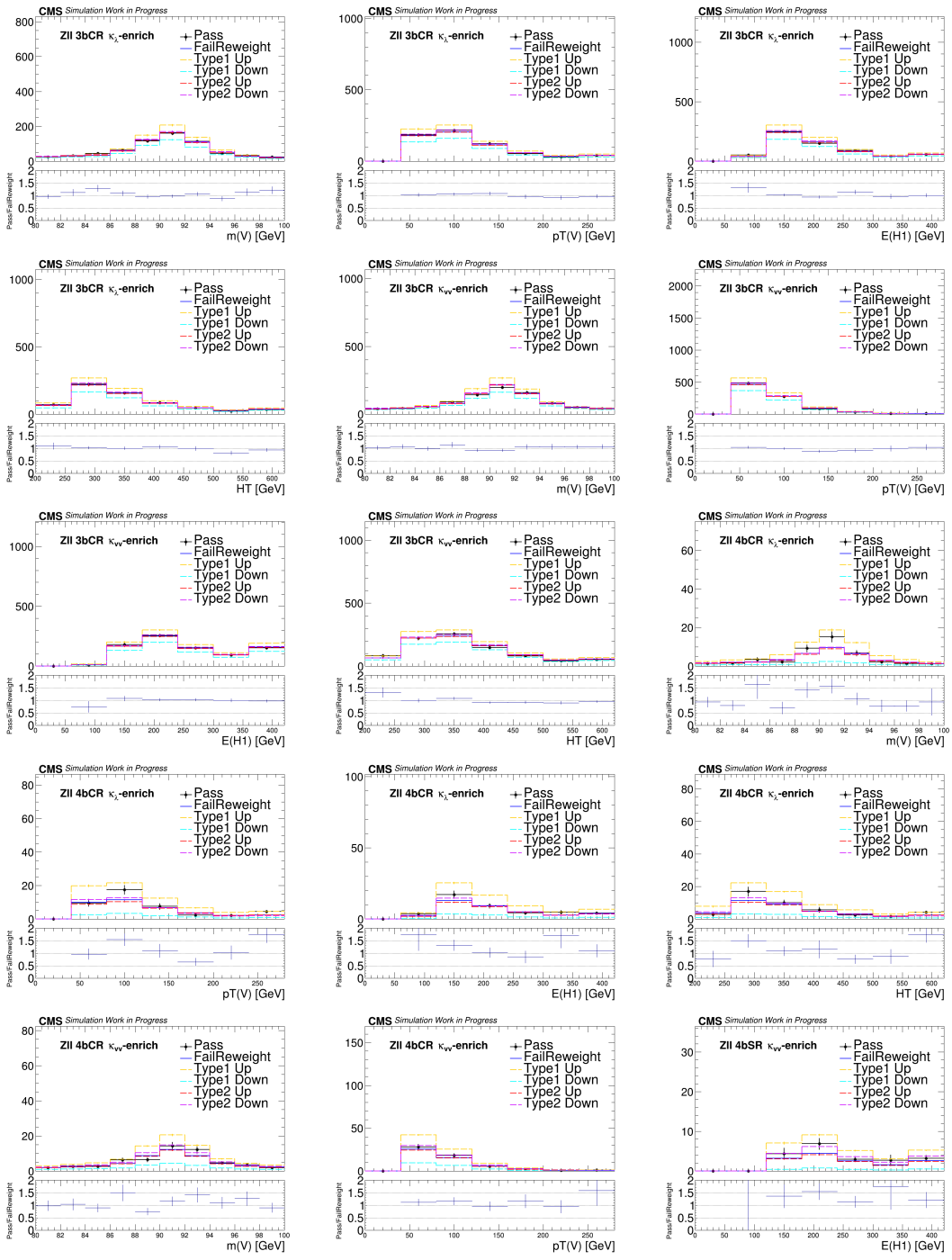

Figure 3.44 The comparison of the original MC events in the control region (black histogram) with the re-weighted MC events in the 2b-tags region(blue) and the re-weighting uncertainties.

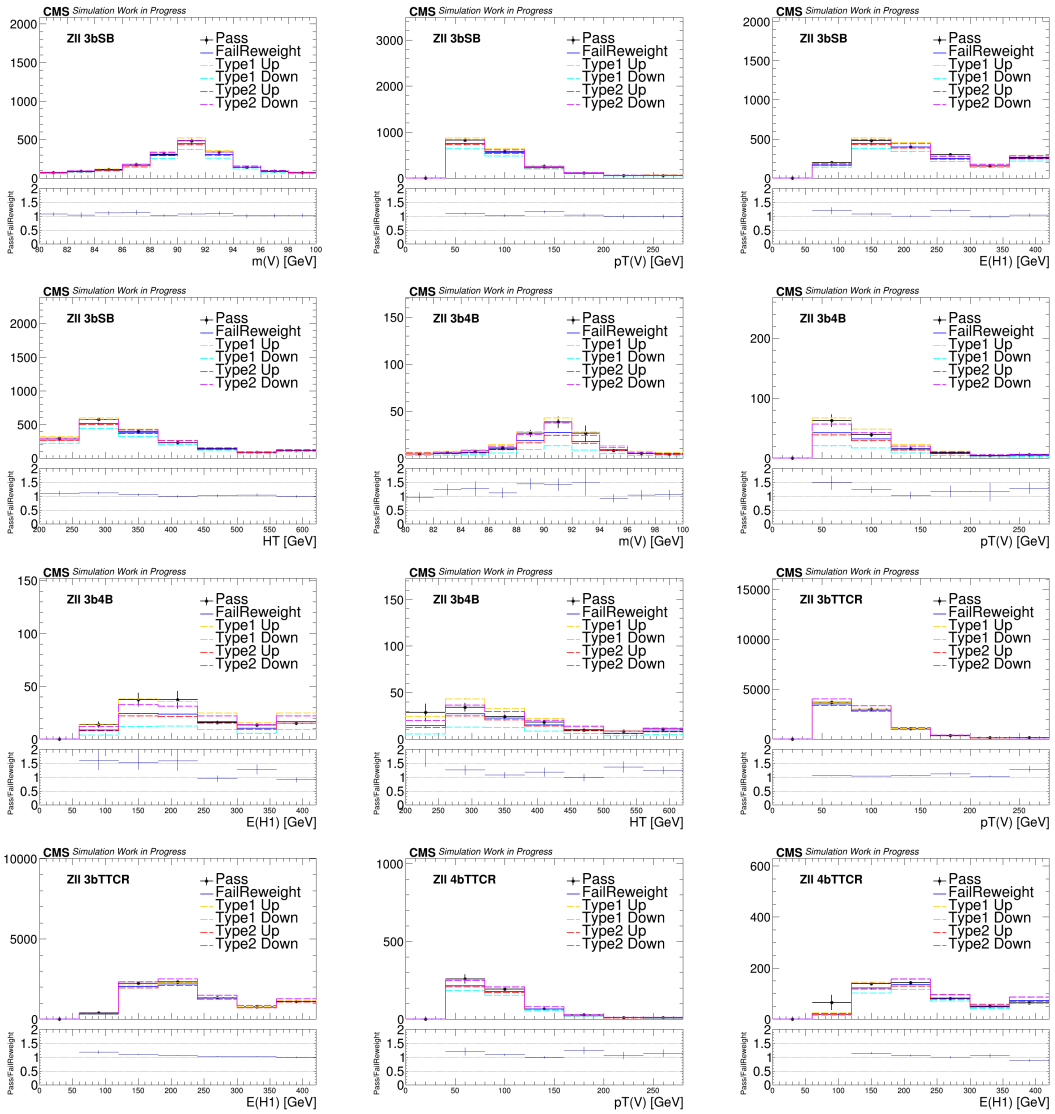

Figure 3.45 The comparison of the original MC events in the sideband region and $t\bar{t}$ CR (black histogram) with the re-weighted MC events in the 2b-tags region(blue) and the re-weighting uncertainties.

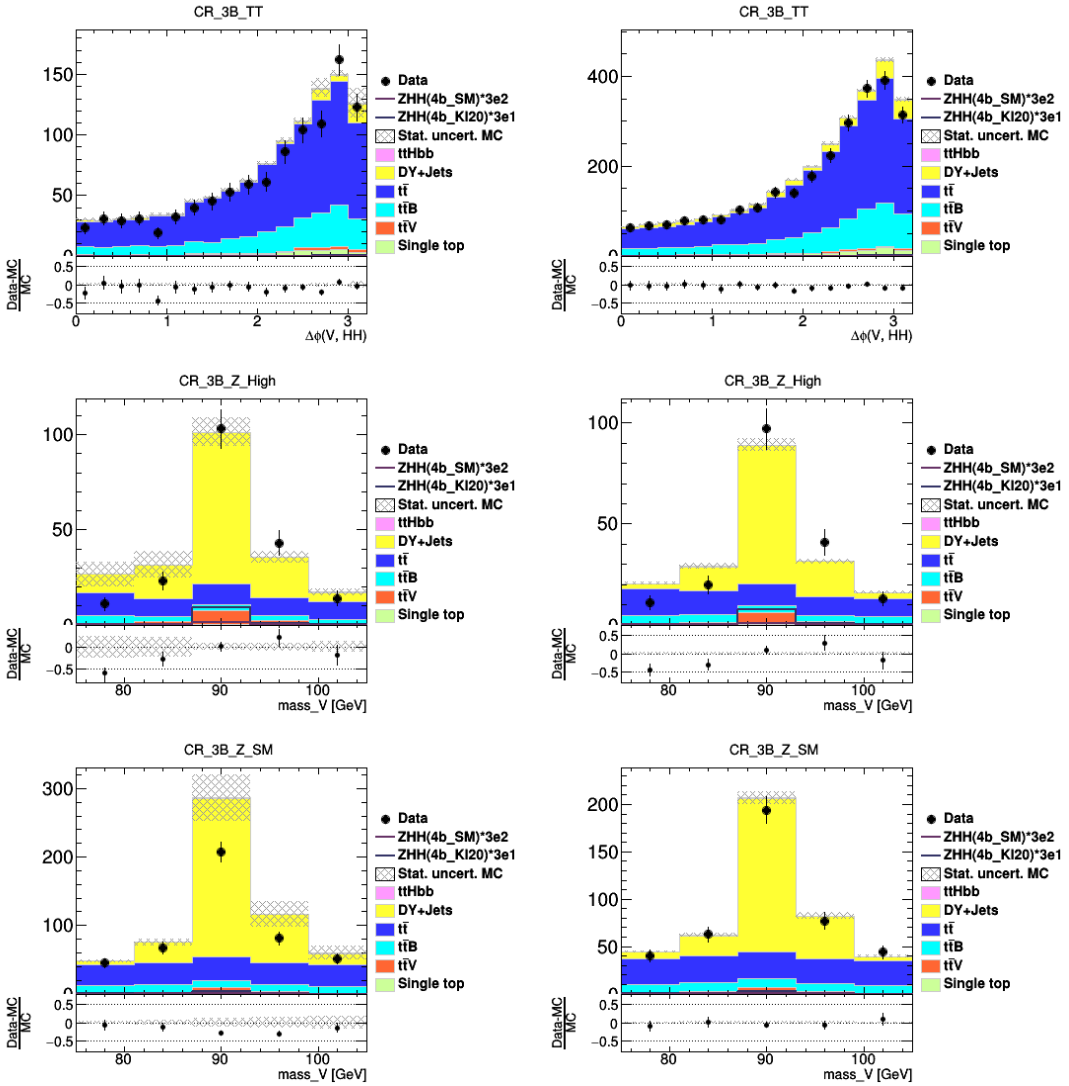

Figure 3.46 Data vs. MC background validation plots from 2018 in different regions. (Left: Original MC estimation; Right: Dominant background estimated using re-weighted 2b-tagged MC events.)

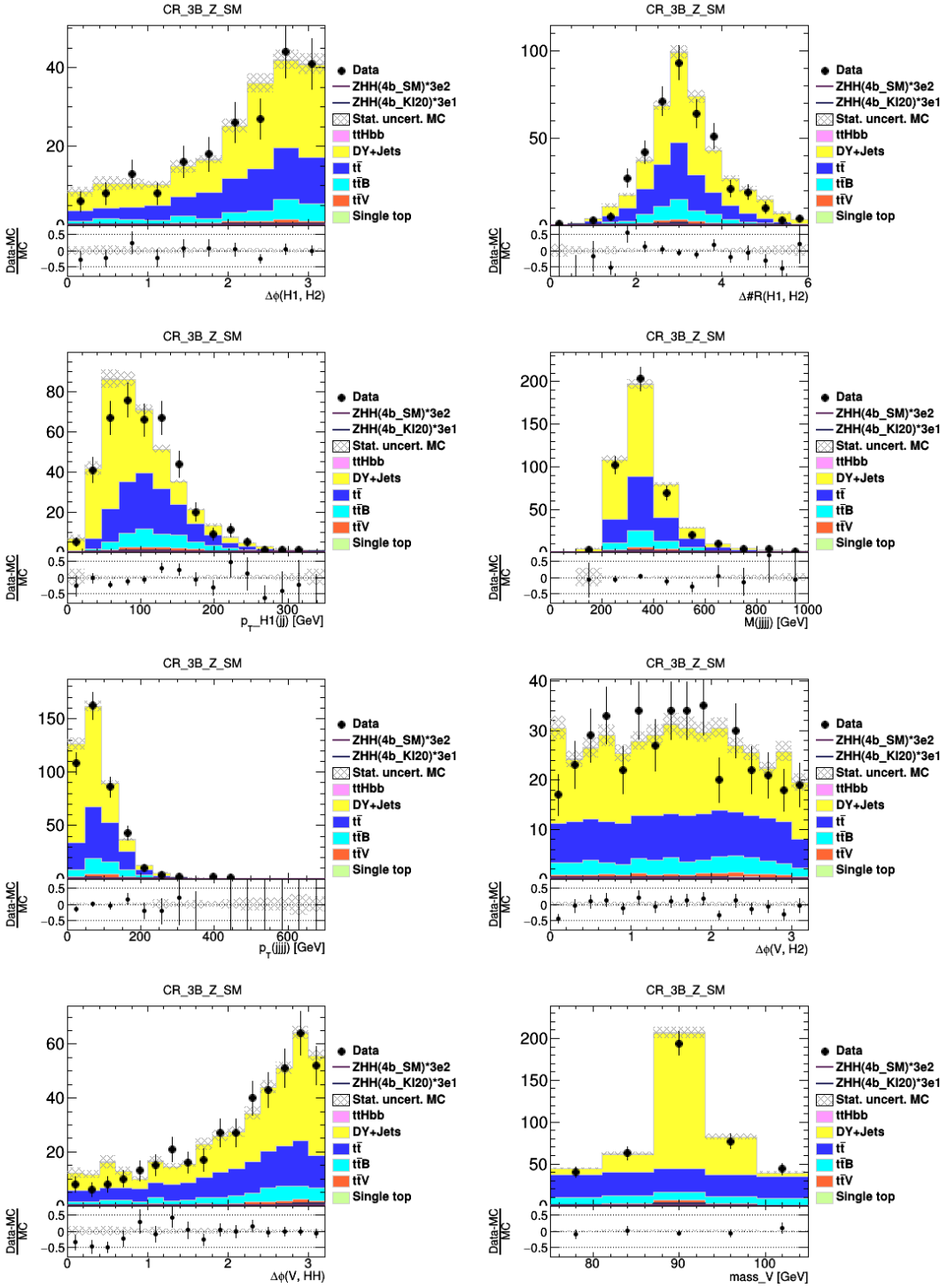

Figure 3.47 Data vs. MC background validation plots from 2018 in Z mass window and SM κ_λ region. (With re-weighted background)

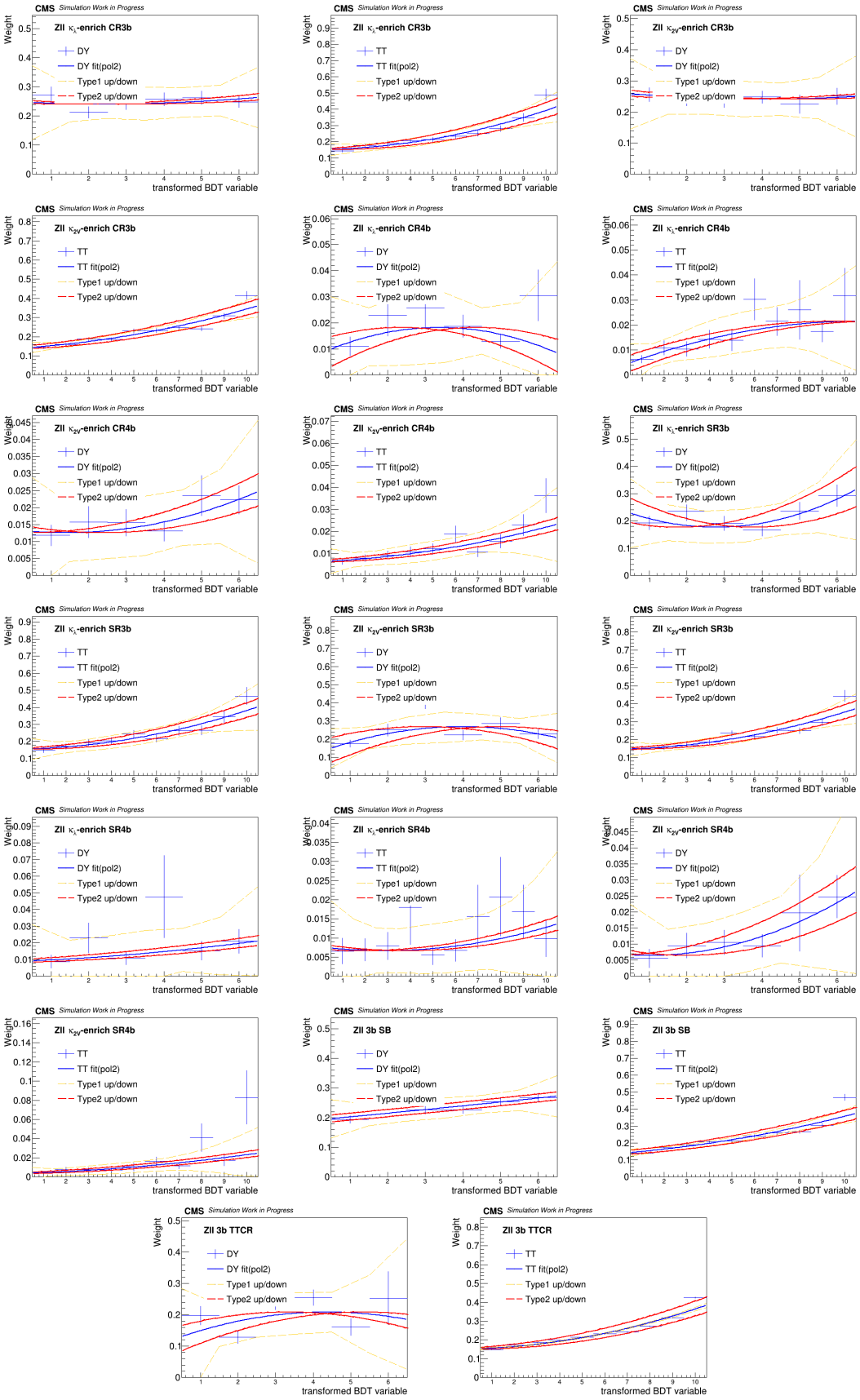

Figure 3.48 The re-shaping histograms for $t\bar{t}$ and DY+Jets background processes and two different types of uncertainty in different regions.

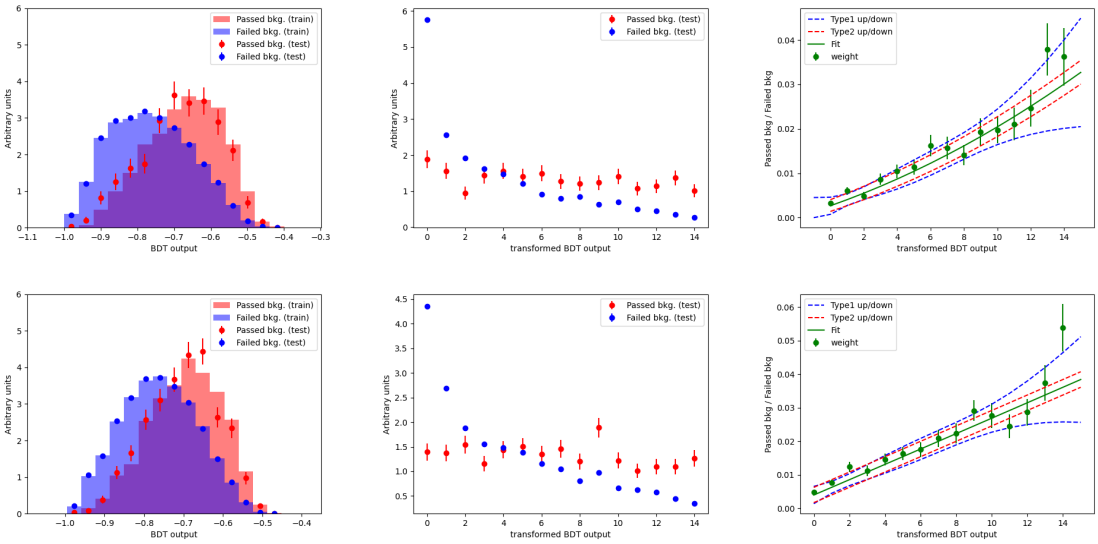

Figure 3.49 Re-weighting BDTs trained with MC events in the HP vs failed region (upper row), and MC events in the LP vs failed region (bottom row) for the single lepton channel. Plot in the middle is the BDT distribution after score transforming. The goal is to make the "Passed bkg." distribution as flat as possible, so even for the high score events, we can still have enough statistical precision.

So all the events in the failed region get a weight according to the re-weighting BDT score, and their kinematics distribution becomes similar to the distribution of real passed events after reweighing. We then use this as the background template in the boosted topology, which provides us with much better statistical precision. During the training of the re-weighting BDT, events in the failed regions are randomly split into two parts, which are used for training the high-purity (HP) and low-purity (LP) regions. A table of input variables is listed in Table 3.20.

Table 3.20 Input variables of Re-weight BDTs in the Boosted Topology.

pT_V	pT_{H1}	pT_{H2}
m_{H1}	m_{H2}	m_{HH}
pT_{HH}	ϕ_V	ϕ_{H1}
ϕ_{H2}	$\tau_{21}(H1)$	$\tau_{21}(H2)$
$\tau_{32}(H1)$	$\tau_{32}(H2)$	

The weights are also parameterized with a linear line as shown with examples in Fig. 3.50 for both 1L and MET channel. Dedicated uncertainty is implemented accounting for small difference between reweighed distribution and real kinematics distribution.

In Fig. 3.51, you can see the distribution of SvB BDTs in the signal region (SR) and the mass of the sub-leading jet in the sideband (SB) region. The BDT distribution of passed events has large statistical uncertainties. In the last several bins, which are our sensitivity

region, usually there are no events from passed events. But the reweighed failed events have much better distributions. In the same figure, we can validate the top background reweighing. Reweighted distributions are compared with the true distribution. The statistical uncertainty is greatly reduced, and the shape is maintained. Additionally, we can see that the type-1 and type-2 variations are able to enclose the "Pass" distributions.

In the LP and HP categories, we use $50 < r_{HH} < 75$ GeV as the validation region to check the MC agreement with data. Figure 3.52 shows some kinematics distributions in this validation region, where the re-weighted failed events are used. We mainly focus on the 1L boosted analysis because the boosted MET analysis shares the same procedure. More validation plots and the handling of uncertainties could be found in the following sections.

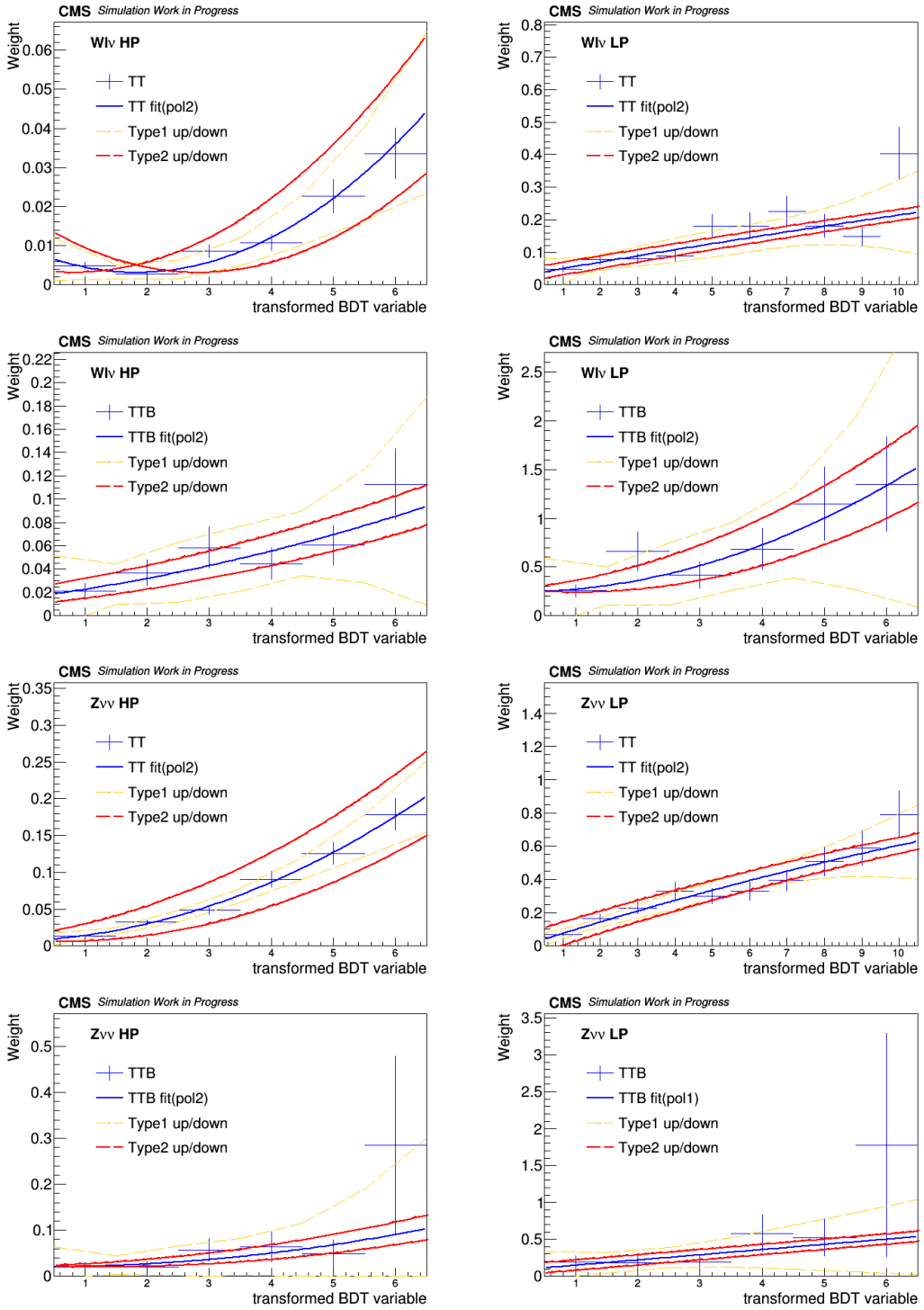

Figure 3.50 Weight parameterization in the boosted 1L channel signal region (Top) and boosted MET channel SB region (Bottom). The solid blue line is a linear fit to the original weight. type-1 Error is from varying the fit value by 95% confidence interval obtained from GetConfidenceIntervals(0.95). type-2 Error comes from shifting the fitted line horizontally by 1 bin.

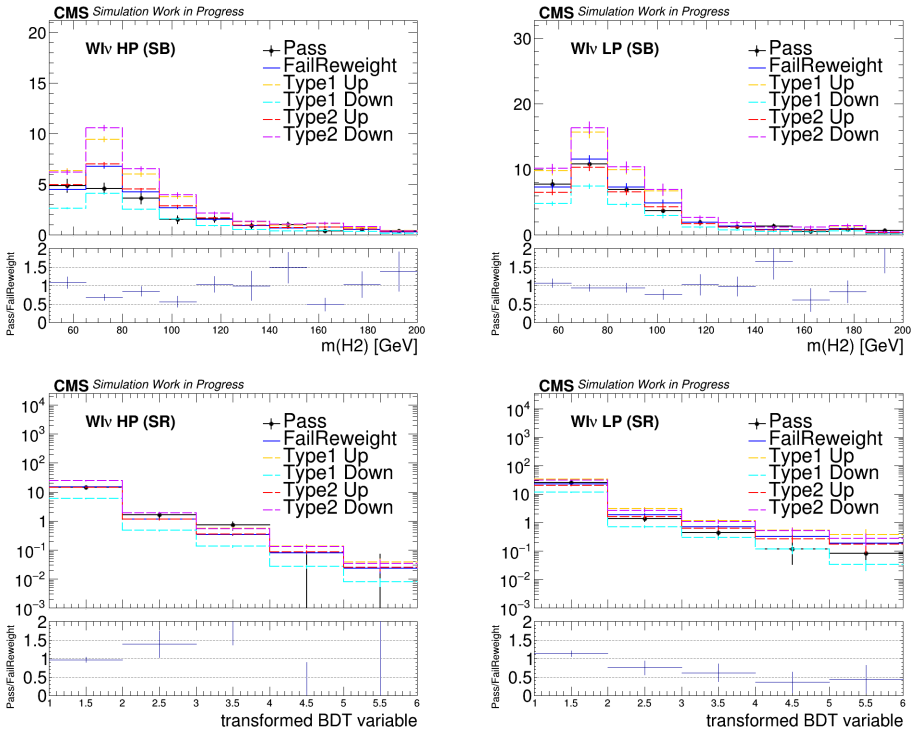

Figure 3.51 [Top] Comparison of "Pass" and "FailReweight" sub-leading Jet mass distribution as well as their up and down variations in $50 < r_{HH} < 75$ GeV for the 1L channel. [Bottom] Comparison of "Pass" and "FailReweight" SvB BDT distribution as well as their up and down variations in $r_{HH} < 50$ GeV for the 1L channel. These are the variable used int the final fitting.

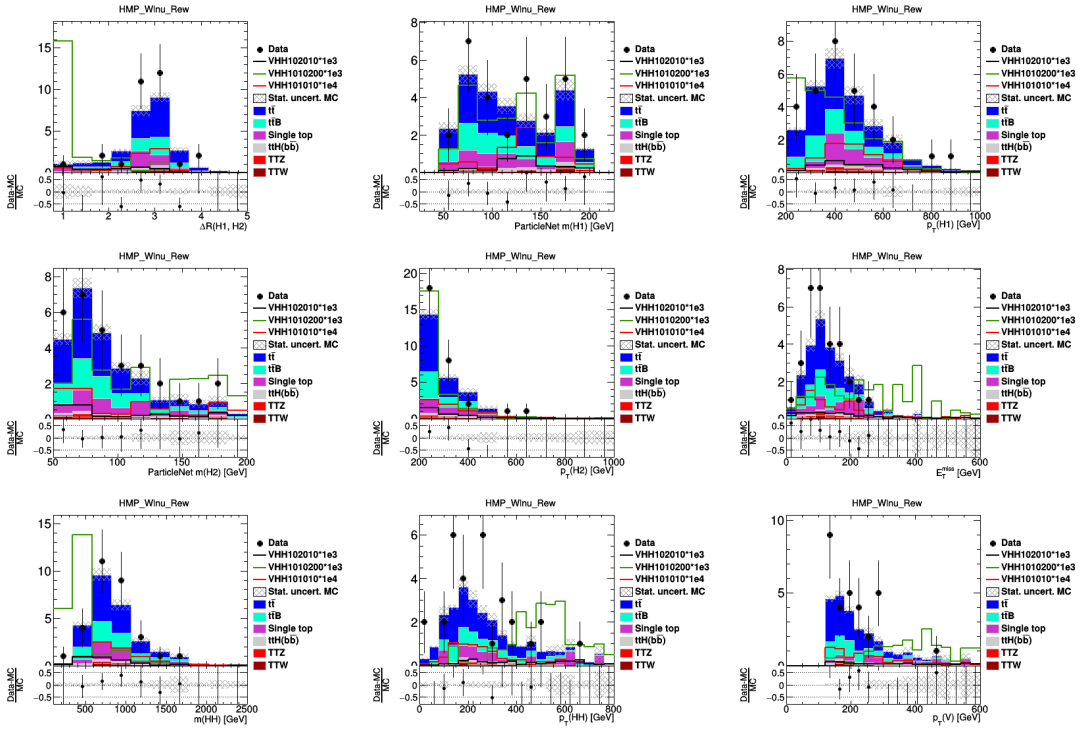

Figure 3.52 $Wl\nu$ channel kinematics distribution (Pre-fit) in 50<r_{HH} <75 GeV in HP category. From left to right, upper to bottom are: $dR(H1, H2)$, $m(H1)$, $p_T(H1)$, $m(H2)$, $p_T(H2)$, MET, m_{HH}, $p_T(HH)$, $p_T(V)$.

3.5.2 The data-driven method

In the FH channel, the background model consists of two parts: $t\bar{t}$ MC simulation and data-driven multijet background. The four-tag multijet background can be approximated by the three-tag data with some higher-order corrections under the assumption that they contain the same processes despite the difference in total event rate, and the signal purity in three-tag events is much smaller. To suppress the signal contamination, we define the **Sideband (SB)** around the SR as follows to derive the corrections on three-tag data. The background model is validated in the closure test with mixed data described in the following sections.

$$\begin{aligned} 52\text{GeV} < &\text{ Leading } S_T \text{ dijet mass} &< 180\text{GeV} \\ 50\text{GeV} < &\text{ Sub-leading } S_T \text{ dijet mass} &< 173\text{GeV} \end{aligned}$$

The first-order correction is from the **Jet Combinatoric Model (JCM)**, accounting for the lower jet multiplicity in the three-tag events. Each untagged jet has the possibility to be b-tagged when it is either a true b-jet or a mis-tagged light or charm jet. By emulating this effect, we can assign each untagged jet a constant **pseudo-tag rate** f, and weight the event with the probability to promote a three-tag event with n untagged jets to a four-tag event:

$$w_{\text{JCM}} = \sum_{i=1}^{n} \begin{pmatrix} n \\ i \end{pmatrix} f^i \times (1-f)^{n-i} \times (1 + e/n^d \times (i \mod 2))$$

where the last factor enhances the condition that b-jets appear in pairs. The parameters are fitted to the jet multiplicity distribution of four-tag data minus $t\bar{t}$ in the SBs.

The higher order kinematic based correction is from the **Fourtag vs Threetag (FvT)** classifier, a neural network which has been introduced in the previous section (signal extraction, Sec. 3.4.5). For each event, the FvT classifier will output the regressed joint probabilities that an event is Four-tag data $\text{P}(\text{D}_{4\text{b}})$, Three-rag data $\text{P}(\text{D}_{3\text{b}})$, Four-tag $t\bar{t}$ $\text{P}(\text{t}\bar{\text{t}}_{4\text{b}})$ and three-tag $t\bar{t}$ $\text{P}(\text{t}\bar{\text{t}}_{3\text{b}})$. So the probability for Four-tag multijet is $\text{P}(\text{M}_{4\text{b}})$:

$$\text{P}(\text{M}_{4\text{b}}) = \text{P}(\text{D}_{4\text{b}}) - \text{P}(\text{t}\bar{\text{t}}_{4\text{b}})$$

and we can re-weight the event with:

$$r_{\text{FvT}} = \frac{\text{P}(\text{M}_{4\text{b}})}{\text{P}(\text{D}_{3\text{b}})}$$

The FvT classifier is trained using both Four-tag and Three-tag data and $t\bar{t}$ MC events in SB with JCM weight applied to Three-tag data. The final multijet background is the Three-tag data weighted by $r_{\mathrm{FvT}} \times w_{\mathrm{JCM}}$. Fig.3.53, 3.54 compare the distributions of boson candidate jets, quadjets kinematics respectively in Four-tag data and background model in Sideband.

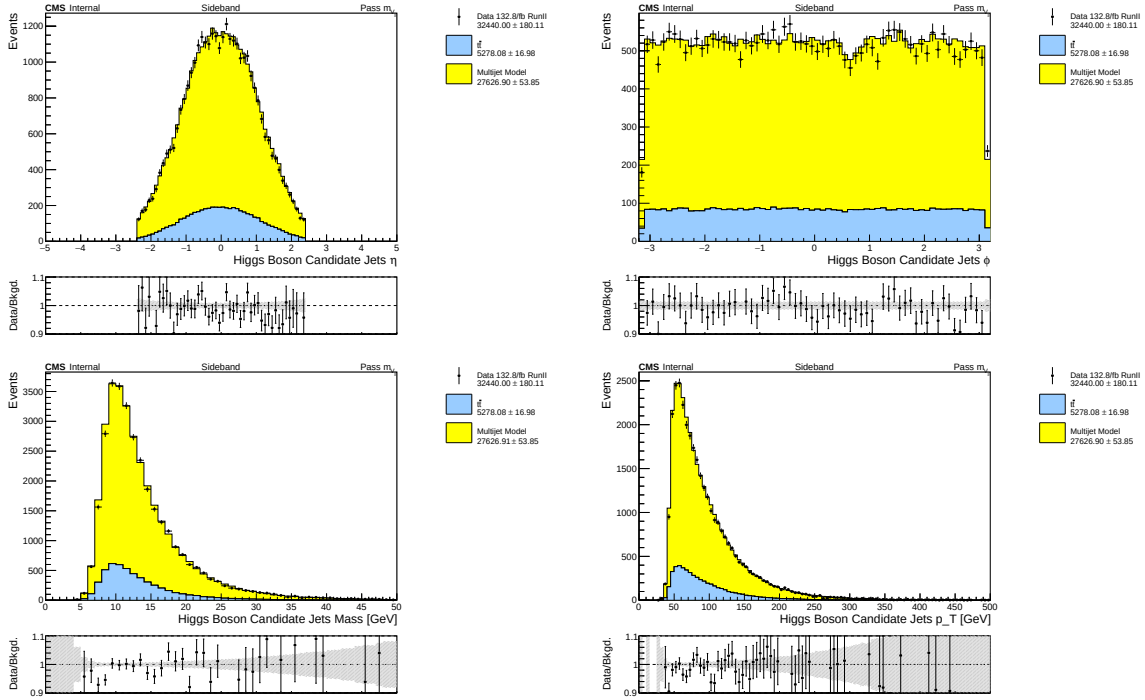

Figure 3.53 Kinematics of Higgs candidate jets in Sideband

We use hemisphere mixing, as described in [80], to generate a sample used for the **closure test of the background method**. The mixed sample provides a signal-free dataset that can be used as a closure test in the SR. The approach involves treating mixed events as '4b-data' and predicting the yield from $3b$ data using the same background procedure as used in the analysis on the non-mixed sample. We then derive a systematic from the comparison of the predicted background to the observed mixed event yield in the SR. In previous iterations of this analysis [81], the modeling in the Control Region (CR) was used to validate – and derive systematic uncertainties on – the background prediction in the SR. Figure 3.55 shows a schematic of this previous background procedure [81].

Kinematic requirements on the di-jet masses suppress signal in the $4b$ SB and CR. The $3b \to 4b$ corrections were derived in the Sideband region and validated in the CR. Testing the background model in the CR validates the $3b \to 4b$ extrapolation in an orthogonal dataset with events that have kinematics similar, but not identical, to those in the SR. Observing closure in the CR is promising, but it validates the extrapolation of the model in a phase space different

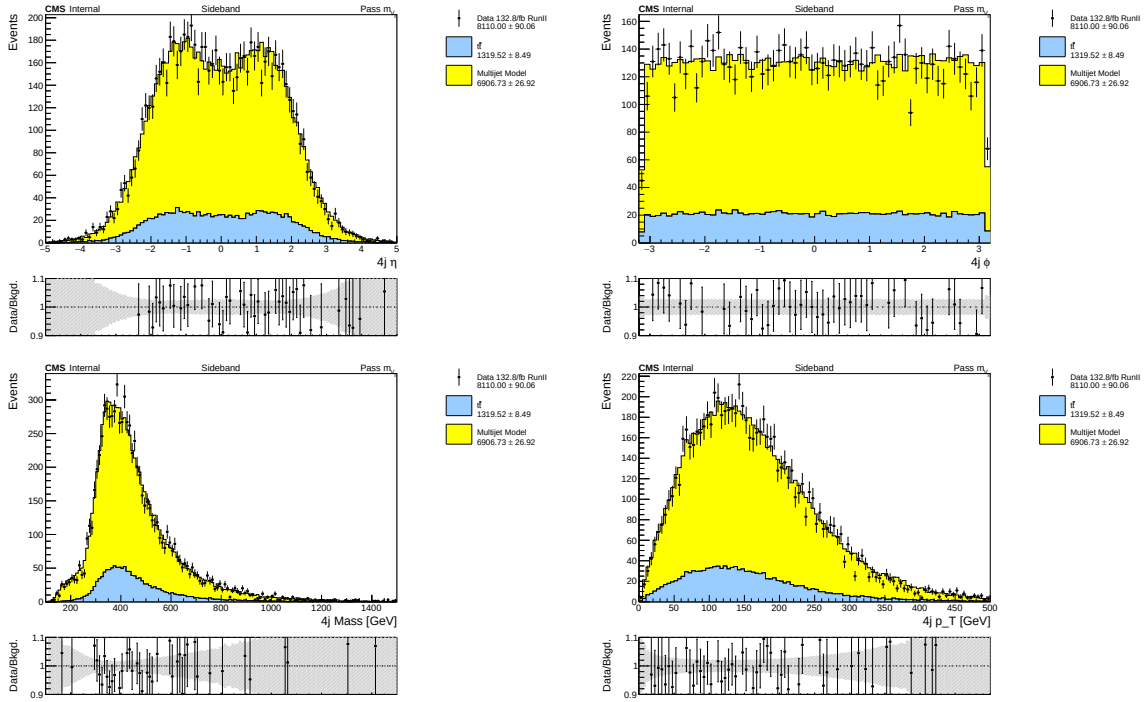

Figure 3.54 Kinematics of quadjets formed by four Higgs candidate jets in Sideband

from the SR and is statistically limited in most relevant regions. The extent to which validating the SB→CR extrapolation validates the background in the most relevant region, the SR, is shown in Figure 3.56. The left-hand plot shows the SvB in the CR, while the right plot shows the SvB in the SR. The high-SvB bins, which are most relevant for signal sensitivity, have negligible yield in the CR. Therefore, testing the background modeling in the CR provides little-to-no insight into how the background extrapolates to the most sensitive phase space in the SR.

Using the mixed sample for closure tests has the advantage of allowing validation of the full SB → SR extrapolation. Figure 3.57 depicts a schematic of the background procedure used in the closure test for this analysis. Here, the $3b \rightarrow 4b$ corrections are again derived in the SB; however, now, because the mixing suppresses signal in the SR, the background model can be validated directly in the SR. This approach follows a similar philosophy to that of using Monte Carlo (MC) in a closure test of a data-driven prediction. Ideally, the synthetic (mixed) dataset should closely resemble the expected background, although perfect consistency with the expected background is not required. What is critical is that the closure test has the same failure modes as the full background prediction.

Using the mixed samples for a closure test requires that mixed events: a) are signal-free and b) approximate the expected $4b$ background. The extent to which these requirements are

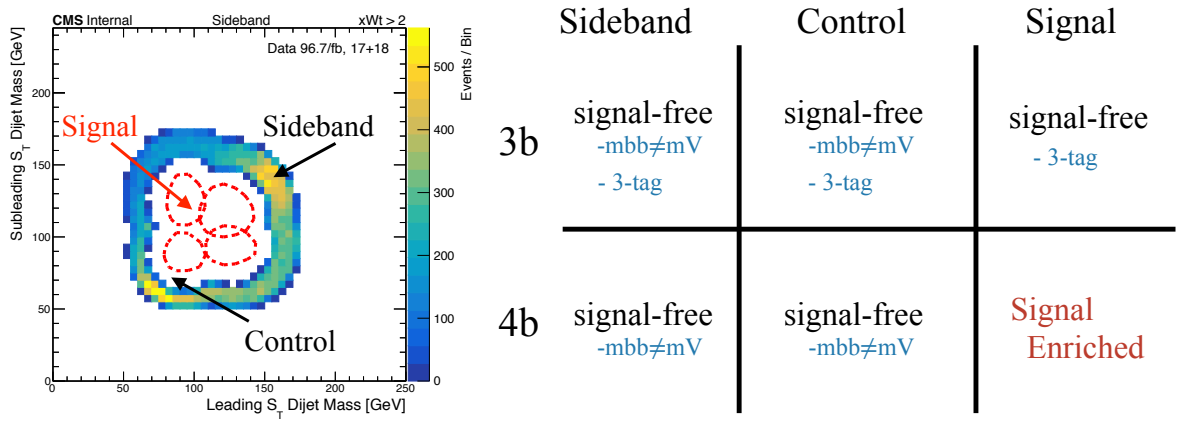

Figure 3.55 Schematic of the datasets used in the previous 4b background procedure.

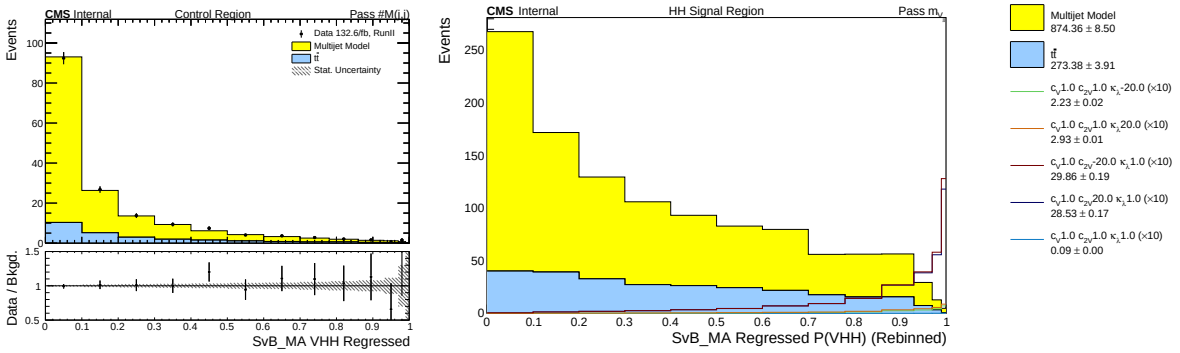

Figure 3.56 Problem with validating the Background estimate using the CR. SvB distribution in the CR is shown on the left. SvB distribution in the SR is shown on the right. The most sensitive SvB bins in the SR have little to no yield in the CR.

met is described in [80].

We use the 3*b* dataset as the input data that is mixed. This 3*b* dataset is a factor of fifteen larger than the 4*b* dataset. For the closure test, it is important that the emulated 4*b* sample has roughly the same statistics as the non-mixed 4*b* sample. The FvT background fit in the Sideband region is limited by the statistics in the 4*b* Sideband data; for the closure test on the mixed sample to be appropriate, we need a similar limitation in the mixed events. The 3*b* dataset is first sub-sampled before mixing to achieve similar statistics in the 4*b* dataset. The sub-sampling is done stochastically using the JCM weights so that the jet multiplicity in the sub-sampled 3*b* data matches that in the 4*b* dataset. The larger 3*b* statistics allow us to create fifteen independent sub-samples which match the 4*b* statistics. The results of the closure test can be run separately on these different sub-samples and combined to improve the systematic uncertainty on the background.

Averaging allows systematic uncertainties to be determined with higher precision than

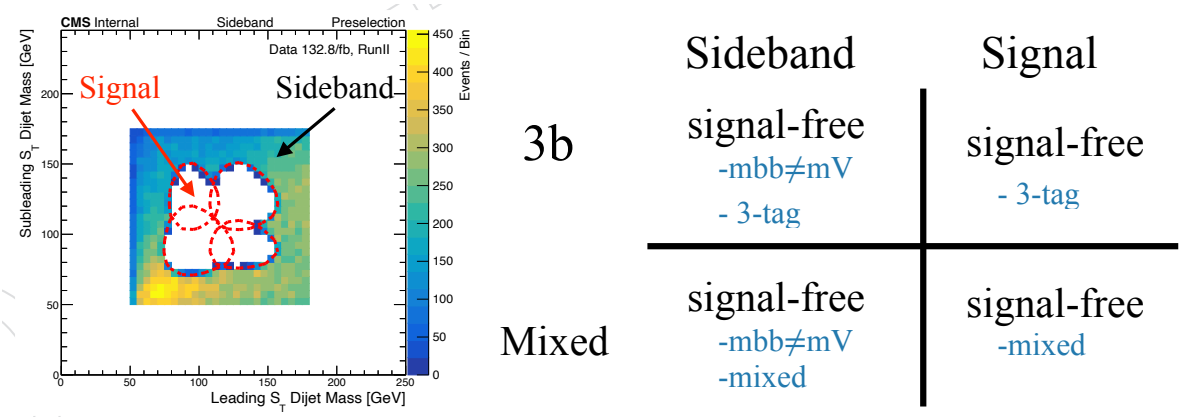

Figure 3.57 Schematic of the datasets used in the background closure test.

statistical uncertainties in the 4*b* data, which was not possible in previous data-driven analyses. Figure 3.58 demonstrates this point, comparing the statistical sensitivity of the Nominal 4*b* sample and a single mixed dataset to the average of the fifteen mixed datasets.

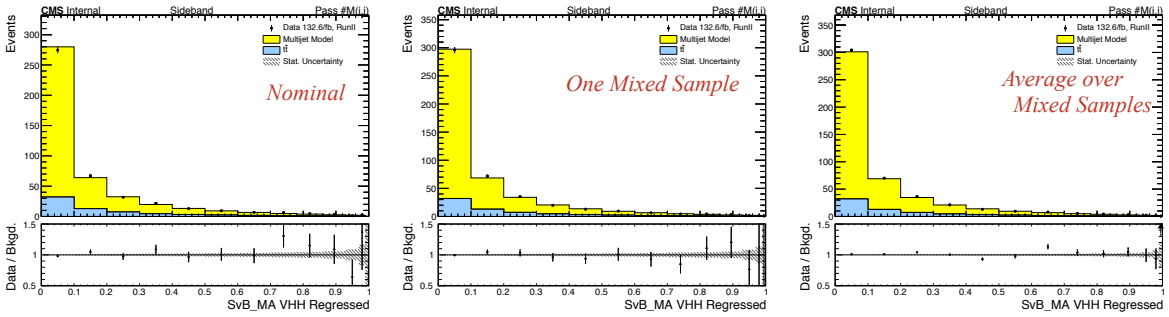

Figure 3.58 Plots of the SvB distribution in the SB for the nominal 4b sample (left) one of the 3b-mixed sub-samples (middle) and after averaging over all fifteen of the 3b sub-samples (right).

Figure 3.59 provides a concise summary of the advantages of using mixed data to perform a closure test. The SvB distribution is displayed in the SB (left) and SR (right). The unmixed 4*b* data is represented by black data points, with the SR blinded. The unmixed 3*b* data, from which the background model will be derived, is shown in yellow before applying the kinematic FvT corrections (stacked with the 4*b* $t\bar{t}$ MC). The mixed data (3bMix4b) is displayed in red. The mixed data serves as a proxy dataset that is well-modeled and can be extrapolated to the SR without signal contamination.

The further results of the closure test and the quantification of the uncertainties brought by this method will be introduced along with the other channels in the next section (background validation, Sec. 3.5.3).

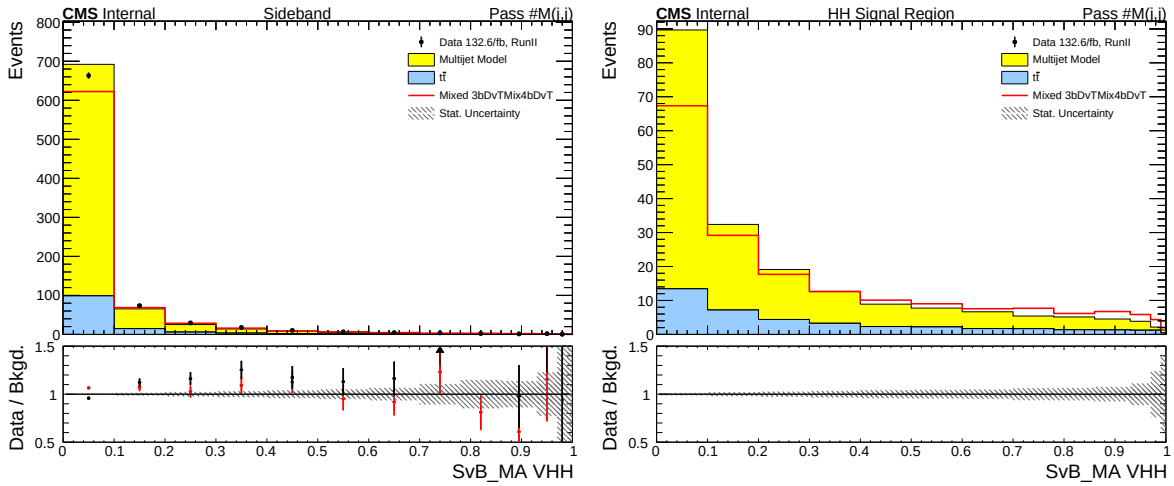

Figure 3.59 Summary of Closure Test. The Mixed data (red) provides a good model of the unmixed 4*b* background (black) and can be extrapolated to the SR without signal contamination.

3.5.3 The background modeling validation

In this section, we present plots testing the consistency between background models and the real experimental data as validation of our background modeling. Any discrepancies observed are rigorously studied, either by making modifications or by introducing modeling uncertainties to ensure the final results are conservative. It is important to note that the discussions in this section are based on the fundamental operations previously introduced in Section 3.2.2 (weighting, scaling, etc.).

The 2L channel

In the 2L channel, validation plots both inside (research region) and outside ($t\bar{t}$ control region) the mass window have already been presented in the previous section on BDT reweighting (Sec. 3.5.1), as shown in Figure 3.46 and Figure 3.47.

As introduced in the previous sections, we are employing a 'stitching' method to replace the $t\bar{t} + b\bar{b}$ events generated alongside the $t\bar{t}$ inclusive sample (5FS) with the $t\bar{t} + b\bar{b}$ events generated separately (4FS) in order to reduce the modeling uncertainty. The generated $t\bar{t} + b\bar{b}$ samples are scaled (Table 3.6) to match the $t\bar{t}$ inclusive samples, as illustrated in Figure 3.5.We validate this method in all the leptonic channels. In the 2L channel, the $t\bar{t}$ control regions (CRs) are used for validation, which can be found in Figures 3.60, 3.61, and 3.62. These plots indicate that the $t\bar{t} + b\bar{b}$ process is well-modeled with MC samples.

Notably, as described in the analysis strategy (Sec. 3.4), the $t\bar{t}$ control regions (CRs) will be used to control the floating of the $t\bar{t}$ fraction as well as the $t\bar{t} + b\bar{b}$ fraction (yield $t\bar{t} + b\bar{b}$ / yield $t\bar{t}$ inclusive) in the final fitting.

The `DY+Jets` $p_{\mathrm{T}}(Z)$ uncertainty

From Figure 3.63, we observe a discrepancy between data and Monte Carlo (MC) simulations in the sideband (SB) region over $p_{\mathrm{T}}(Z)$. To extract the trend of the discrepancy, we relax the $p_{\mathrm{T}}(Z)$> 50 GeV cut for plotting and fitting in this section, although the events will be truncated in the final fit.

We introduce a shape uncertainty on the `DY+Jets` process to account for this discrepancy. The difference, shown in Figs. 3.64 and 3.65 (the black histogram), is calculated as

$$\text{diff} = \frac{\text{Data} - \text{other MC w/o DY+Jets}}{\text{DY+Jets}}$$

We use a linear function to fit the residual difference under $p_{\mathrm{T}}(Z)$at 200 GeV and a constant over 200 GeV to obtain the upper bound, and then symmetrize it. The fitted linear functions and constants are listed in Tab. 3.21. To validate the fitted bounds, they are tested with the data-MC comparison in the CRs. The bounds can generally cover the data-MC difference,

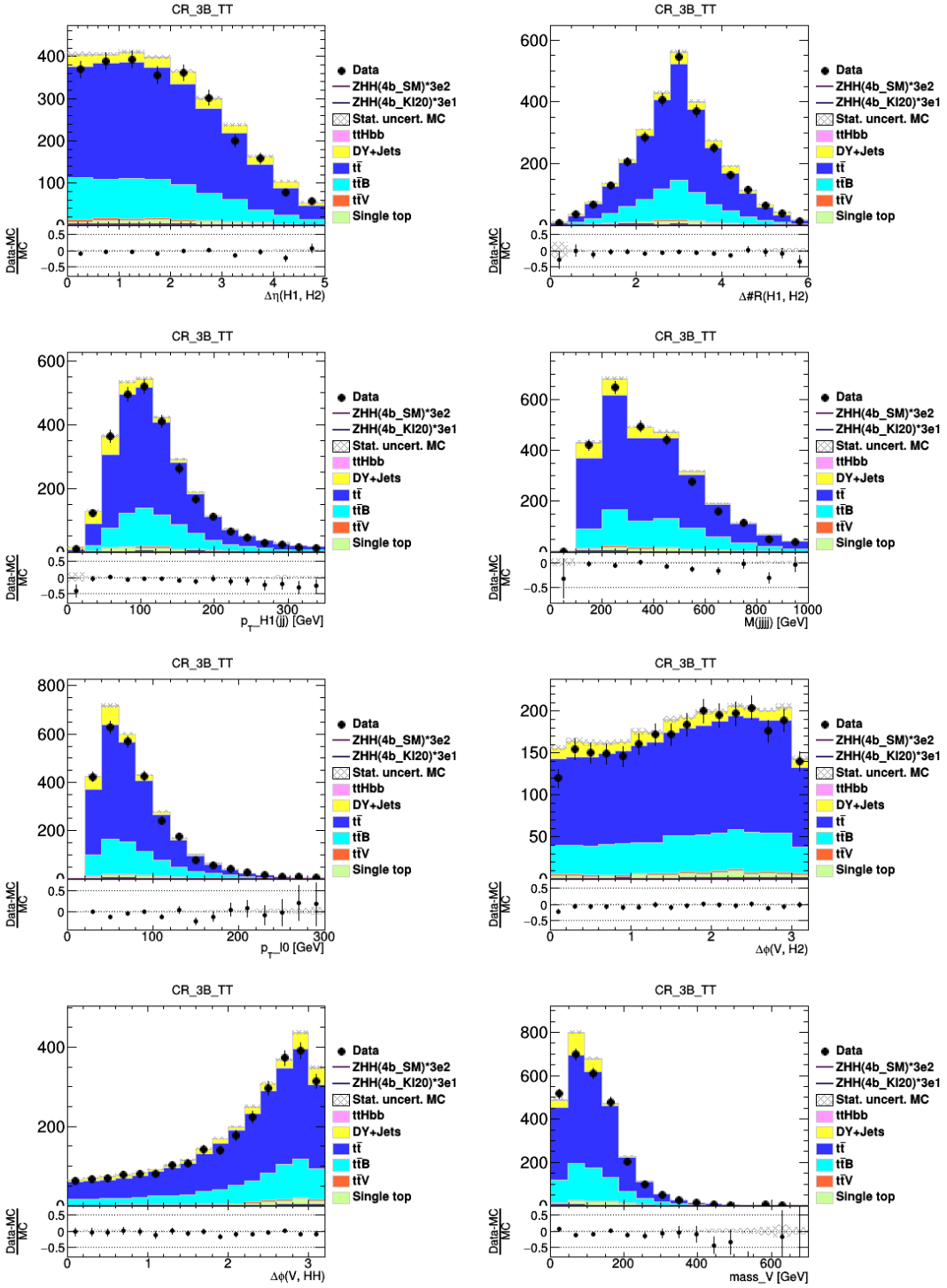

Figure 3.60 Data vs. MC background validation plots from 2018 in $t\bar{t}$ control region (CR). (In r_{HH} signal region with re-weighted background with 3b-tagged)

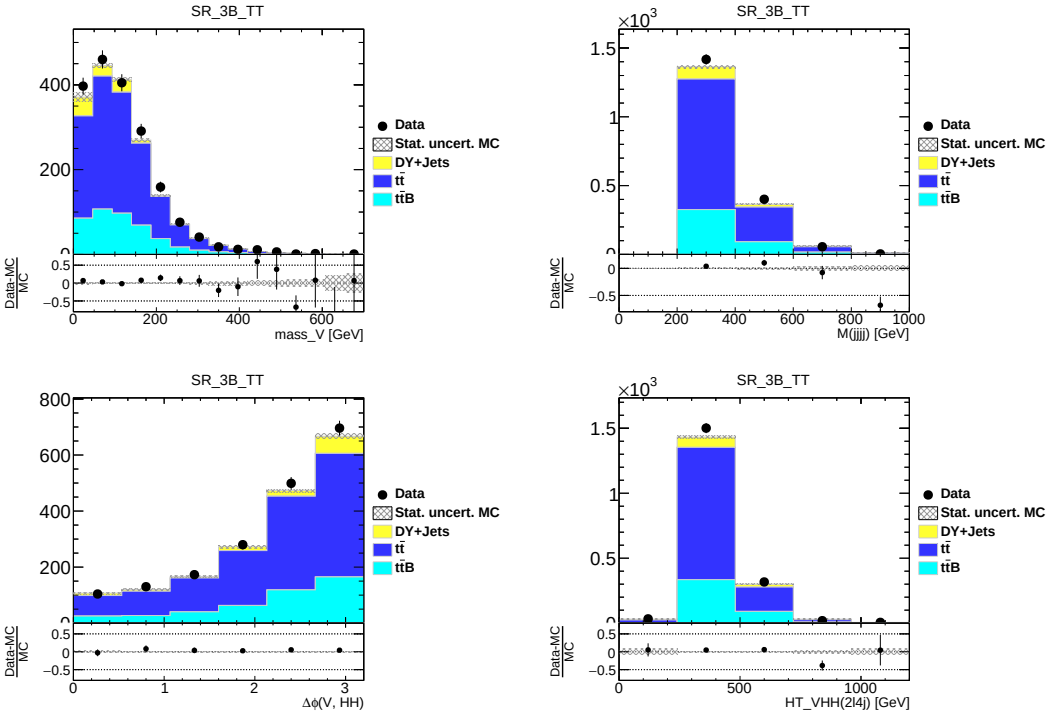

Figure 3.61 Data vs. MC background validation plots from Run-2 in $t\bar{t}$ control region (CR). (In r_{HH} signal region with re-weighted background with 3 b-tagged)

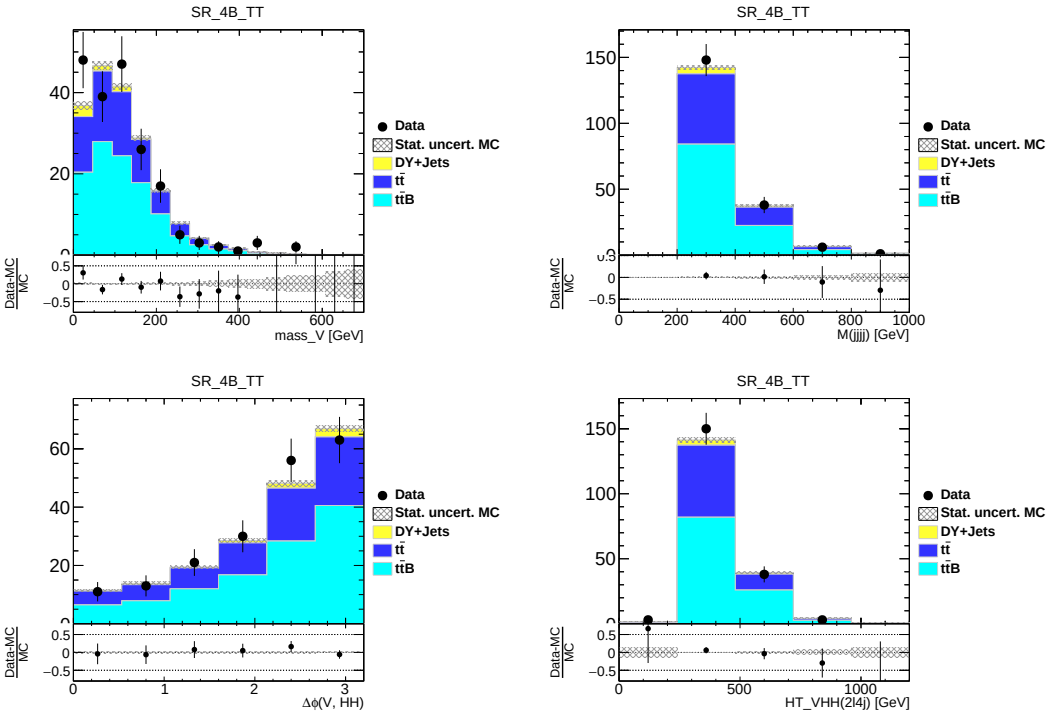

Figure 3.62 Data vs. MC background validation plots with Run-2 data in $t\bar{t}$ control regions (CRs). (In r_{HH} signal regions with re-weighted background with 4 b-tagged)

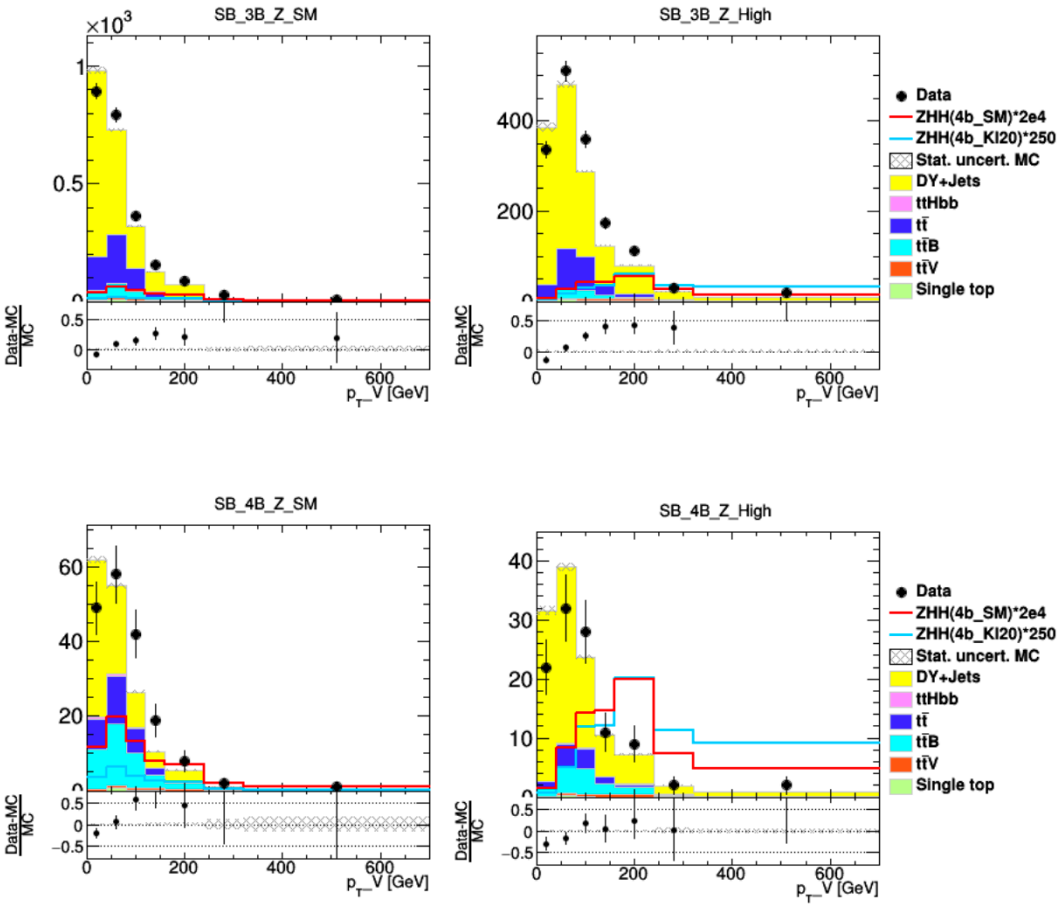

Figure 3.63 Data and MC comparison in DL SB regions over $p_{\mathrm{T}}(Z)$.

as shown in Fig. 3.65. This DY+Jets modeling uncertainty is propagated to the variation in the final fitting variable SvB BDT score, as shown in Figs. 3.66 to 3.68. The corresponding nuisance parameter in the final fit likelihood is named "CMS_vhh4b_DYZptCor".

Table 3.21 DY+Jets $p_{\mathrm{T}}(Z)$correction uncertainty

Region	nB	Function
SB_SM	3	$1.000 + -1.560 \times 10^{-1} + 2.601 \times 10^{-3} pT(\mathrm{Z})$
SB_High	3	$1.000 + -2.667 \times 10^{-1} + 3.446 \times 10^{-3} pT(\mathrm{Z})$
SB_SM	4	$1.000 + -5.592 \times 10^{-1} + 8.612 \times 10^{-3} pT(\mathrm{Z})$
SB_High	4	$1.000 + -3.430 \times 10^{-1} + 4.300 \times 10^{-3} pT(\mathrm{Z})$

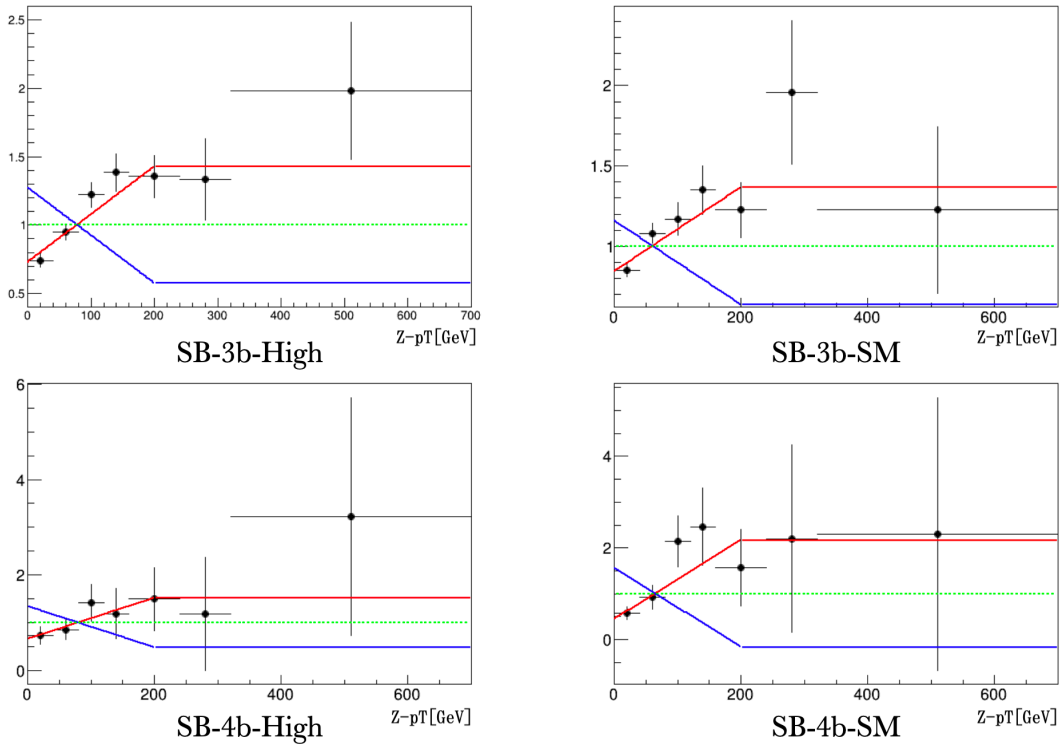

Figure 3.64 Upper(red) and lower(blue) bounds of DY+Jets $p_{\mathrm{T}}(Z)$uncertainty extracted from the SB. The points are the residual difference between DY+Jets MC and Data minus all background MC except DY+Jets in the SB.

The 1L channel

The 1L channel as well as the MET channel are dominated by the $t\bar{t}$ (and $t\bar{t}+b\bar{b}$) events, as is the boosted topology in these two channels.

The Top pT re-weighting

Top pt reweighing is implemented according to the formula:

SF= $exp(-0.202274+1.09734\times10^{-4}\times\mathrm{pT}((\mathrm{top}))-1.30088\times10^{-7}\times\mathrm{pT}((top))^2+(58.3494/(\mathrm{pT}((top))+196.252)))$

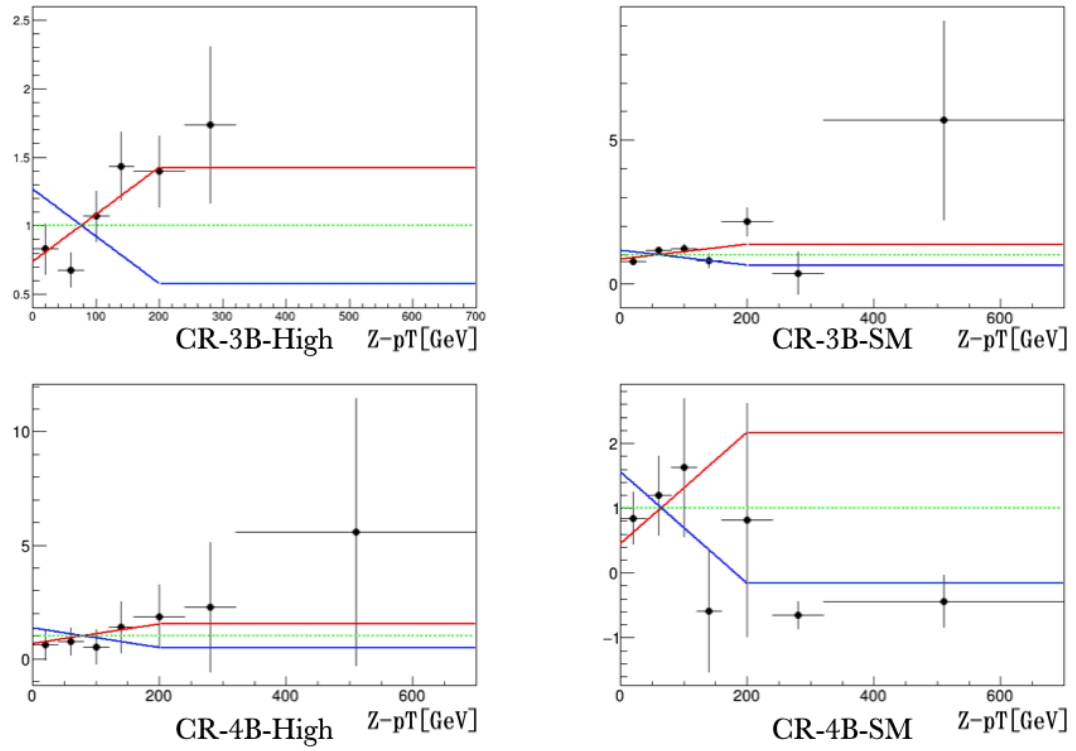

Figure 3.65 Comparison of the upper (red) and lower (blue) bounds extracted from the SB to the data-MC difference in the CR. The points are the residual difference between `DY+Jets` MC and Data minus all background MC except `DY+Jets` in the r_{HH} CR.

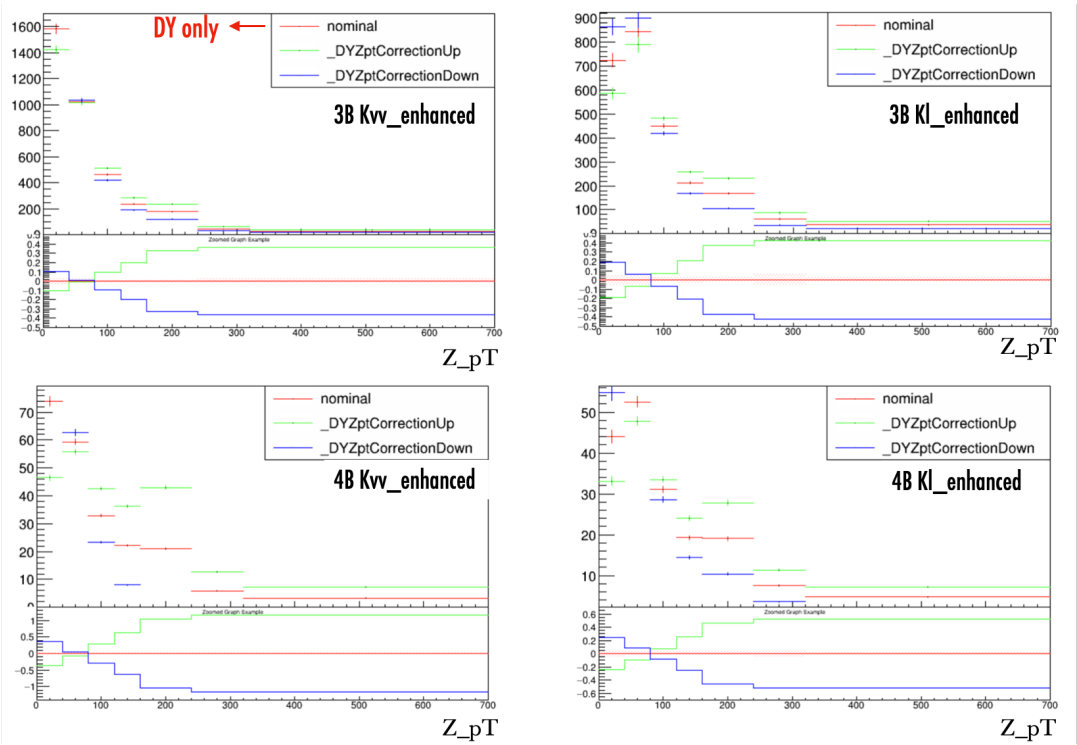

Figure 3.66 The upper and lower bounds of the $p_{\mathrm{T}}(Z)$uncertainty over the nominal `DY+Jets` distribution in r_{HH} SB.

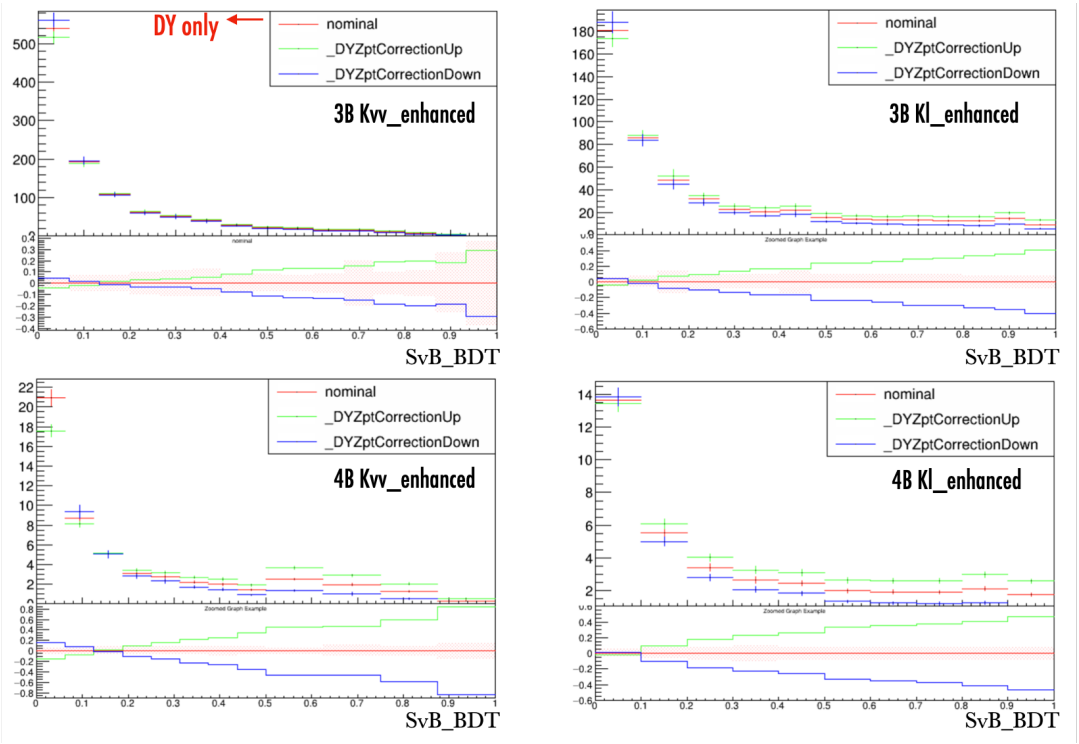

Figure 3.67 The upper and lower bounds of the $p_{\mathrm{T}}(Z)$uncertainty over the nominal `DY+Jets` distribution in r_{HH} CR.

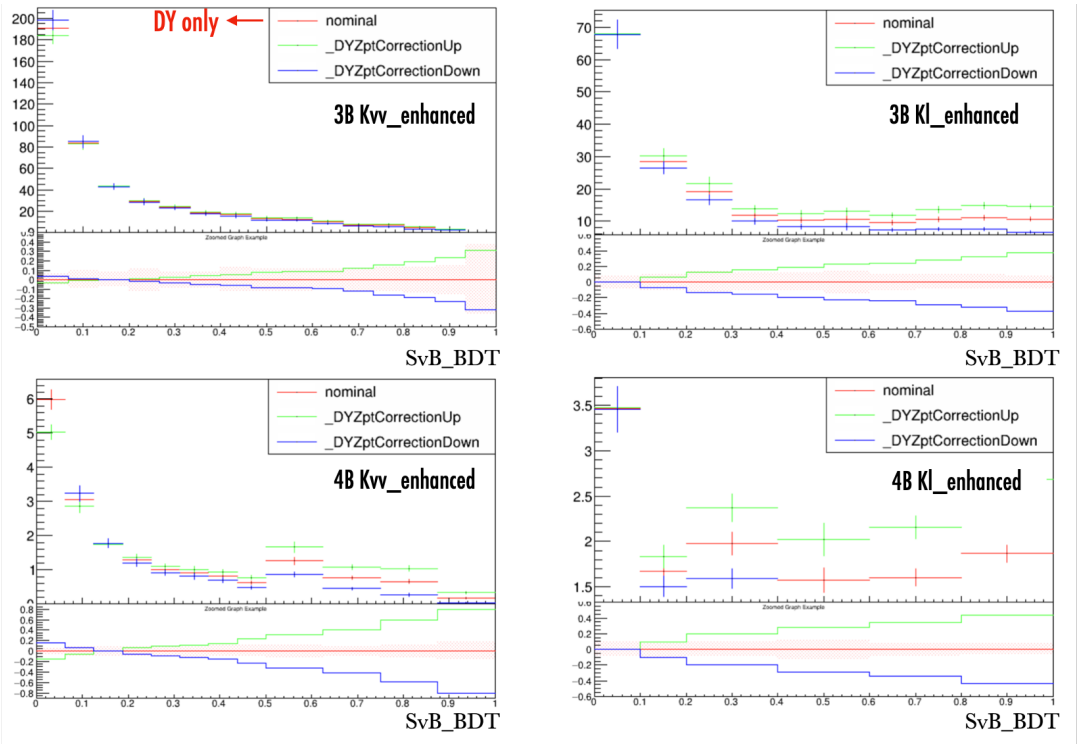

Figure 3.68 The upper and lower bounds of the Z pT uncertainty over the nominal `DY+Jets` distribution in rHH SR.

Where pT((top)) is the Gen level top pt. The distribution of reconstructed vector boson pT distribution in SB3b+SB4b of $We\nu$, $W\mu\nu$, $Z\nu\nu$ are shown in Fig 3.69. The pre and post fit are in Fig 3.70.

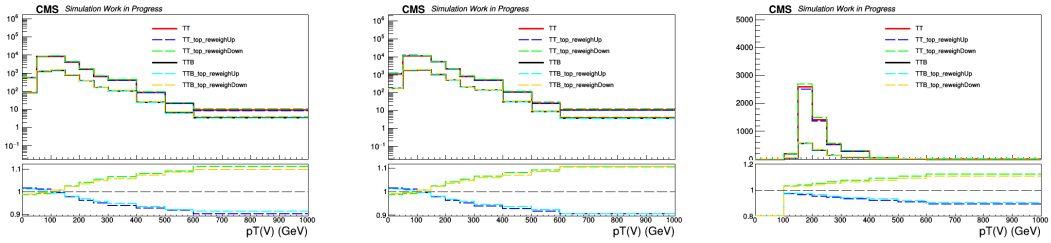

Figure 3.69 Distribution of reconstructed vector boson pT distribution in SB3b+SB4b of $We\nu$, $W\mu\nu$, $Z\nu\nu$(from left to right) channels after top pt reweighing and their up/down version. Up version is applying top pt reweighing twice. Down version is without top pt reweighing.

The shapes of the $t\bar{t}$ and $t\bar{t}+b\bar{b}$ backgrounds are taken directly from MC, but the normalization is left free-floating and constrained in the fit. Except for $t\bar{t}$ and $t\bar{t}+b\bar{b}$, all the other background estimations are directly taken from MC. Top p_T reweighing is also implemented as discussed earlier. Figures 3.71 to 3.72 show the comparison of data and MC in the regions of CR3B and SB3B+4B. These are pre-fit plots with $t\bar{t}$ and $t\bar{t}+b\bar{b}$ normalization applied from the final fitting. In general, we observe good agreement between data and MC, with $t\bar{t}$ and $t\bar{t}+b\bar{b}$ being the main components of the background.

The MET channel

In general, the agreement between data and MC is good in Figures 3.73 to 3.74. It's important to note that $p_{\mathrm{T}}(V)$is reconstructed from MET in this channel, so the plot of $p_{\mathrm{T}}(V)$actually represents the MET object.

The FH channel

Figures 3.75 to 3.78 present the results of applying the nominal background model procedure to the mixed data samples. The $3b \rightarrow 4b$ background procedure, is repeated using mixed samples as a proxy for the $4b$ data. The mixed sample allows the modeling of the background to be tested directly in the Signal region. Non-closure seen in these models is combined to infer a systematic on nominal $3b \rightarrow 4b$ extrapolation. This part describes how these results are used to define a systematic uncertainty on the nominal background prediction.

The plots below show the FvT and SvB distributions before and after the FvT re-weight, but include the 'JCM jet' multiplicity normalization. Figures 3.75 and 3.76 show the distributions in the SB, while Figures 3.77 and 3.78 show the distributions in the SR. These distributions are input to the closure test described above.

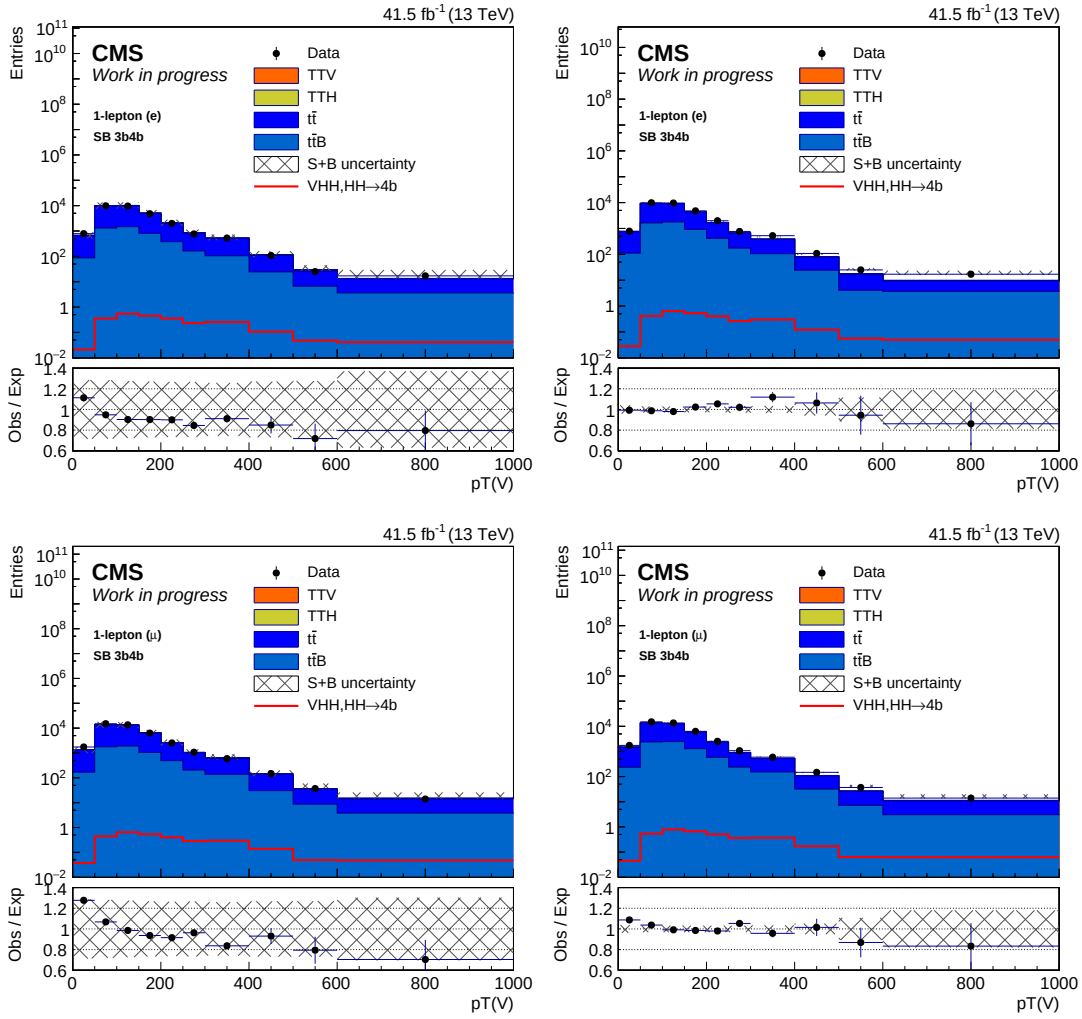

Figure 3.70 Distribution of reconstructed vector boson pT distribution in SB3b+SB4b of $We\nu$(upper row) $W\mu\nu$(bottom row) channels before and after fit.

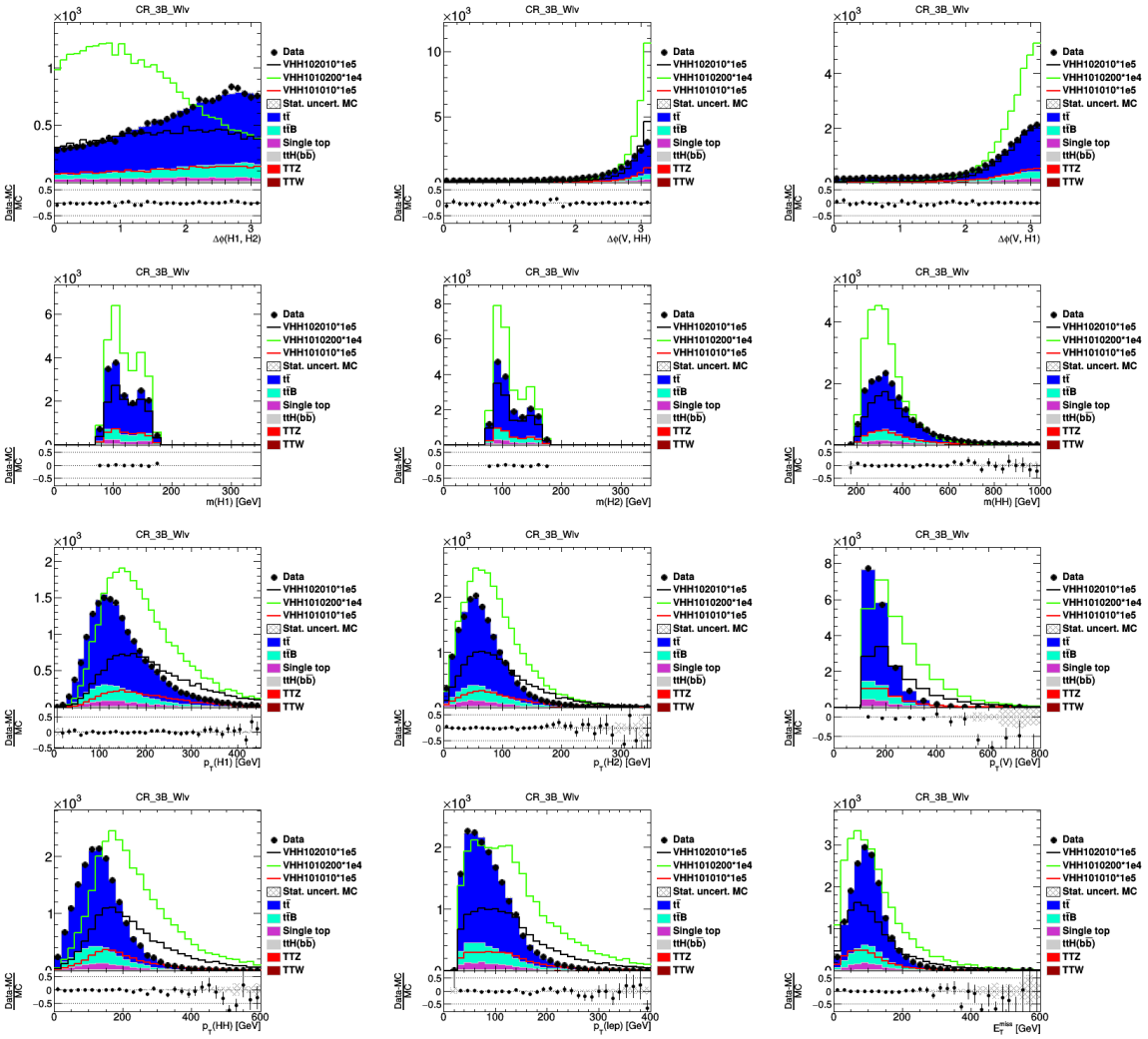

Figure 3.71 1 lepton channel MC validation (CR3B Wlv). Pre-fit plots with $t\bar{t}$ and $t\bar{t}$+$b\bar{b}$ scale factor (from final fitting) applied.

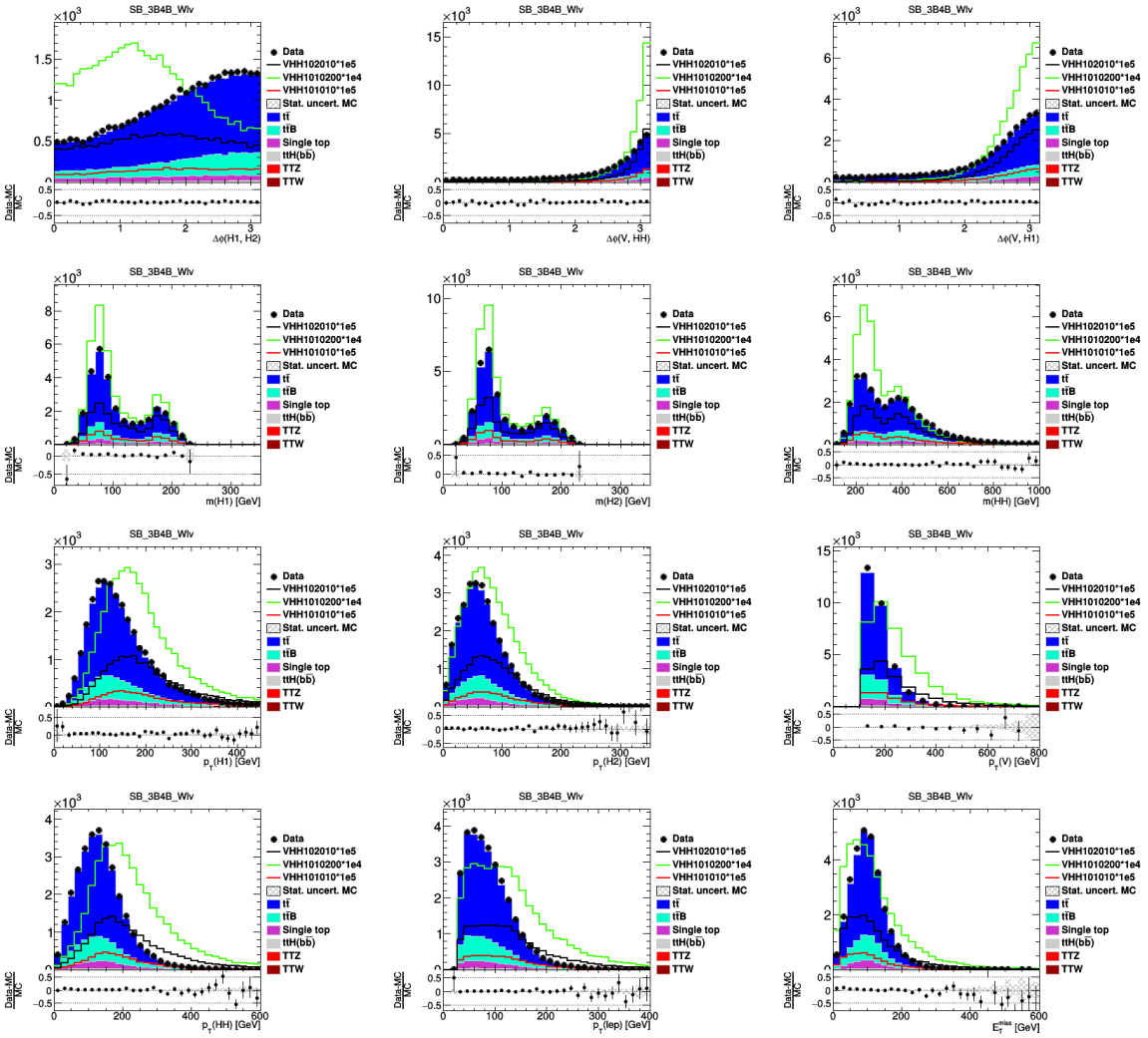

Figure 3.72 1 lepton channel MC validation (SB3B+SB4B $Wl\nu$). Pre-fit plots with $t\bar{t}$ and $t\bar{t}+b\bar{b}$ scale factor (from final fitting) applied.

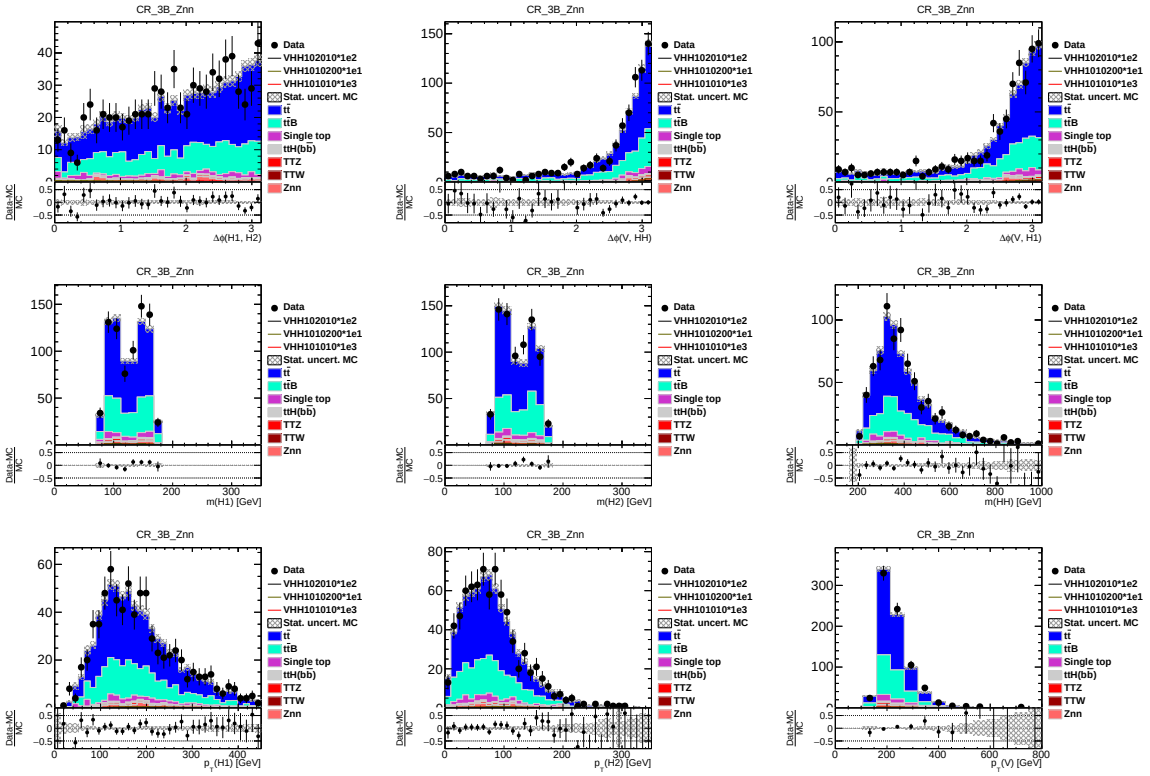

Figure 3.73 MET channel MC validation (CR3B). Prefit plots with $t\bar{t}$ and $t\bar{t}b\bar{b}$ scale factor (from final fitting) applied.

The Data-Driven Uncertainty

To extract quantitative systematic uncertainties from the mixed sample background models, we follow a three-step process: variance, bias, and spurious signal.

1. Estimate the variance among the fifteen mix models by comparing each model to their average. This is achieved by fitting shape basis elements (as described in equation 3.10 and illustrated in figure 3.79) with increasing frequency components until the pulls (defined as the fit value minus the average value, divided by the statistical error of the bin) of adjacent bins of the target distribution are consistent with being uncorrelated. It is important to decorrelate the basis elements from each other with respect to the target distribution so that the fit parameters will be decorrelated, and independent Gaussian priors can be estimated. Decorrelation of the basis is achieved by diagonalizing the initial basis using the Gram-Schmidt process (as described in equation 3.11). The diagonalized basis elements are normalized such that the range from minimum to maximum is 1. This allows the fit coefficients to be easily interpreted in terms of percent variation. Evidence for the remaining correlation in the pulls of adjacent bins is estimated with the p-value of the Pearson correlation coefficient (p-value > 5%). The results of

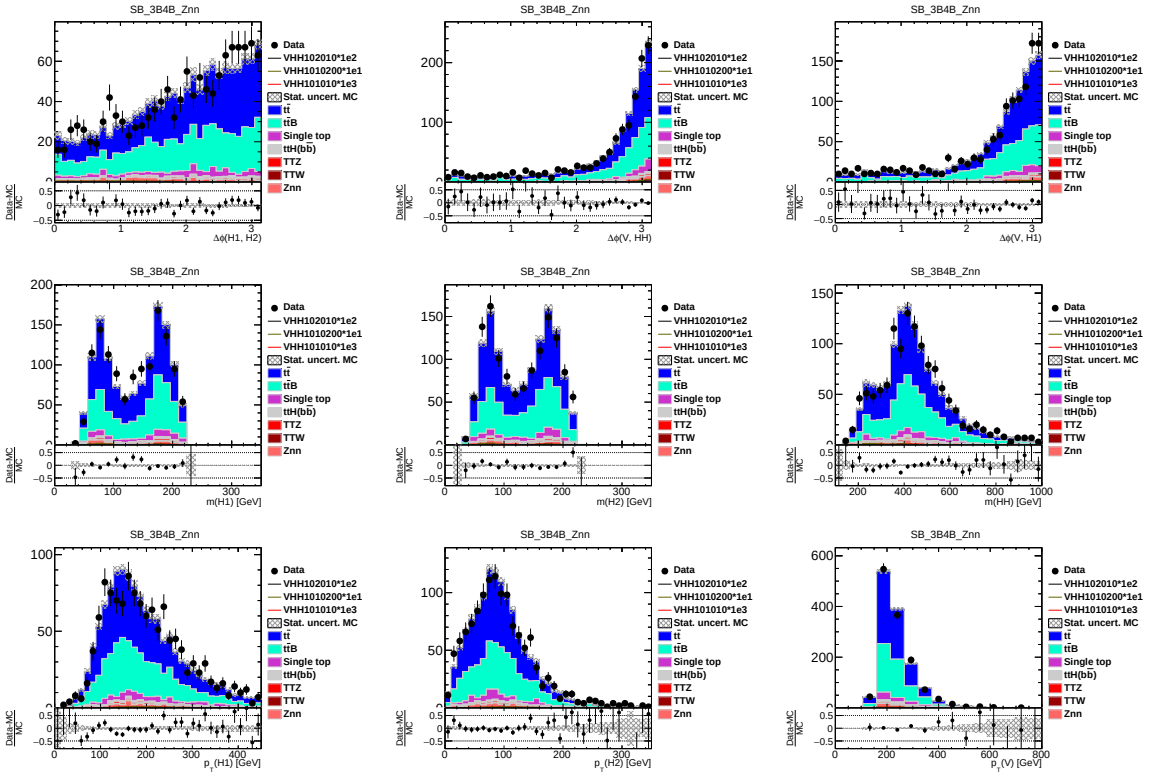

Figure 3.74 MET channel MC validation (SB3B+SB4B). Prefit plots with $t\bar{t}$ and $t\bar{t}b\bar{b}$ scale factor (from final fitting) applied.)

these fits are shown in figures 3.80. Gaussian priors are assigned using the standard deviation over the fifteen fits of the shape basis coefficients.

2. Estimate the bias of the average mix model including the variance priors from the previous step by fitting to the average of the fifteen mix samples. The Gaussian priors are removed sequentially starting with b_0 until the fit is good (p-value > 5%) and an F-test of the nested models does not prefer the next less constrained model by more than 95%. The gaussian priors on the fit parameters are expanded to cover the observed bias (and additional non-closure parameters if required). This is done by adding the observed bias in quadrature with the variance from the previous step and the bias fit uncertainty. The results of these fits are shown in figures 3.81, 3.82.
3. Estimate spurious signal risk by fitting this final average model including variance and bias priors with and without an unconstrained signal template. There is no signal in the average mix sample so the best fit signal residual mismodeling degenerate with the expected signal distribution. If the F-test prefers the model with the unconstrained signal template at greater than 95%, a Gaussian prior will be applied to the spurious signal systematic with one sigma range $\zeta \pm \sigma_\zeta$ where ζ is the best fit spurious signal

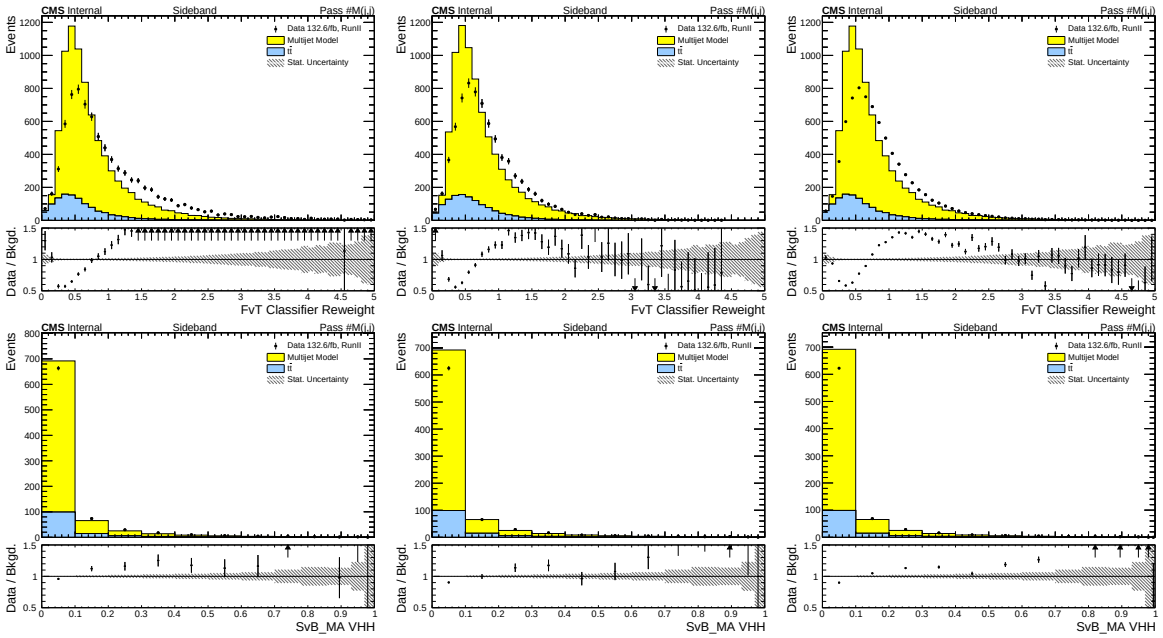

Figure 3.75 Plots of the FvT (upper row) and SvB (lower row) before FvT reweighting in the SB. The left-hand plots show the nominal 4b data; the middle plots show an example of one of the mixed datasets; and the right-hand plots show the average over all mixed datasets samples.

strength and σ_ζ is its uncertainty. The results of these fits are shown in figures 3.81, 3.82.

The variance between the fifteen mix models is due to the finite statistics used in the fitting of the JCM and FvT models. In principle with infinite statistics, these models should converge to a unique best fit, though it is hard to know that for certain with stochastic training methods. The events which are weighted by the JCM and FvT models are the same in all fifteen models, this component of the statistical uncertainty is included as per bin nuisance parameters in the final fits. The difference between the average of the mix models and the average mixed sample is an estimate of the systematic bias of the model procedure relative to the true target distribution. We believe this bias comes primarily from the phase space extrapolation of the model from the Sideband to the Signal Region. There may also be small contributions from the finite dimensionality of the JCM and FvT corrections.

This three-step process is carried out independently for the final signal selection where the regressed signal probability.

$$\mathrm{b}_k = \begin{cases} \sin(\frac{k+1}{2}\pi x) & k \text{ odd} \\ \cos(\frac{k}{2}\pi x) & k \text{ even} \end{cases} \tag{3.10}$$

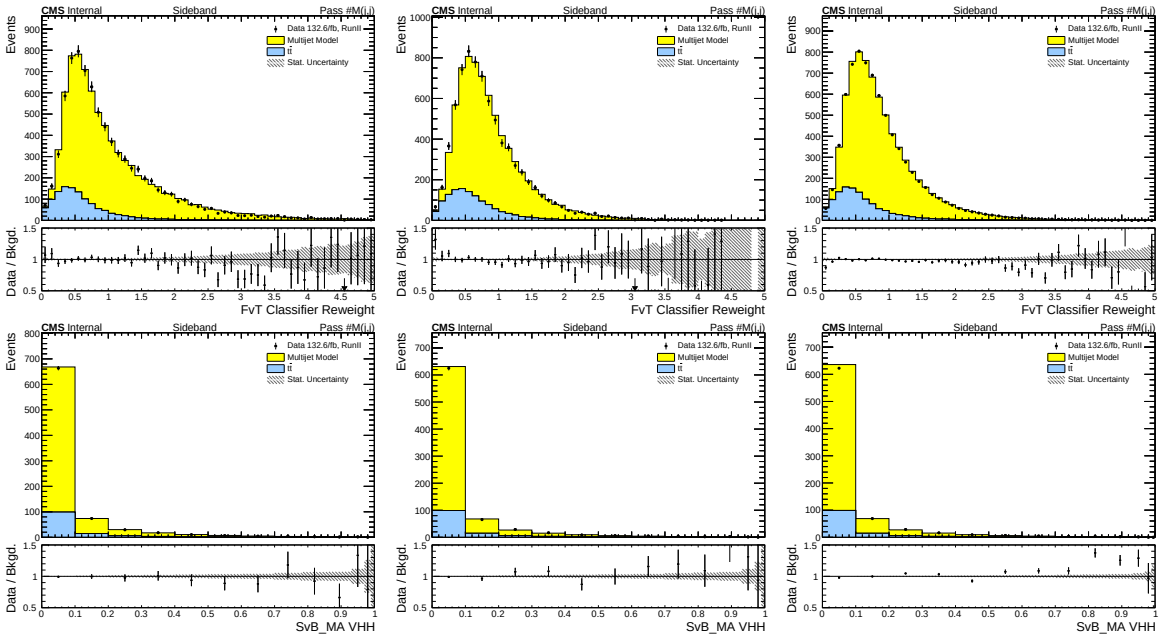

Figure 3.76 Plots of the FvT (upper row) and SvB (lower row) after FvT reweighting in the SB. The left-hand plots show the nominal $4b$ data; the middle plots show an example of one of the mixed datasets; and the right-hand plots show the average over all mixed datasets samples.

$$\mathrm{b}_k \leftarrow \mathrm{b}_k - \sum_{i=0}^{k-1} \frac{\langle \mathrm{b}_i \mathrm{b}_{i+1} \rangle}{\langle \mathrm{b}_i \mathrm{b}_i \rangle} \quad \langle \mathrm{b}_i \mathrm{b}_k \rangle \equiv \int_0^1 \mathrm{b}_i \, h \, \mathrm{b}_k \, dx \quad \text{where } h \text{ is the target histogram} \tag{3.11}$$

$$L(D) = \Big(\prod_{\text{bins } j} \frac{B_j^{D_j}}{D_j!} e^{-B_j} \Big) \Big(\prod_{\text{basis } i} e^{-\frac{1}{2}\left[\mathrm{c}_i^2 / (\sigma_{\mathrm{c},i}^2 + \hat{\mathrm{c}}_i^2 + \sigma_{\hat{\mathrm{c}},i}^2) \right]} \Big) \tag{3.12}$$

$$B_j = t\bar{t}_j + \mathrm{mj}_j (1 + c_i b_{ij})$$

The background model B likelihood of observing data D is given in equation 3.12 where $\sigma_{\mathrm{c},i}$ is the standard deviation of the fit coefficient c_i from the variance fit, $\hat{\mathrm{c}}_i$ is the best fit value from the bias fit, and $\sigma_{\hat{\mathrm{c}},i}$ is the statistical uncertainty from the bias fit. The total expected background depends on the $t\bar{t}$ template, the multijet template, the fit coefficients c_i and the normalized basis elements b_i.

We find two basis elements in addition to a normalization term are needed to appropriately model the expected variance among the multijet models in both the κ_λ and κ_{VV} categories. In both categories none of the fit parameters are needed to be unconstrained in the bias fit to satisfy the goodness of fit or F-test criteria. In neither case, do we find a significant improvement in the model fit when including a spurious signal term.

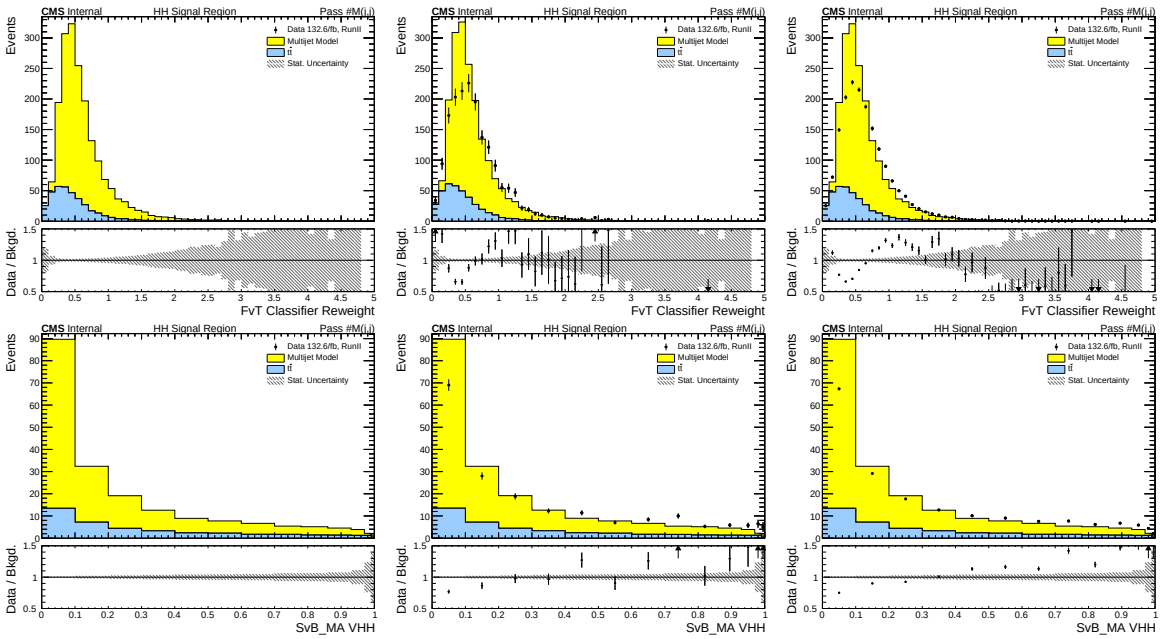

Figure 3.77 Plots of the FvT (upper row) and SvB (lower row) before FvT reweighting in the HHSR. The left-hand plots show the nominal 4*b* data; the middle plots show an example of one of the mixed datasets; and the right-hand plots show the average over all mixed datasets samples.

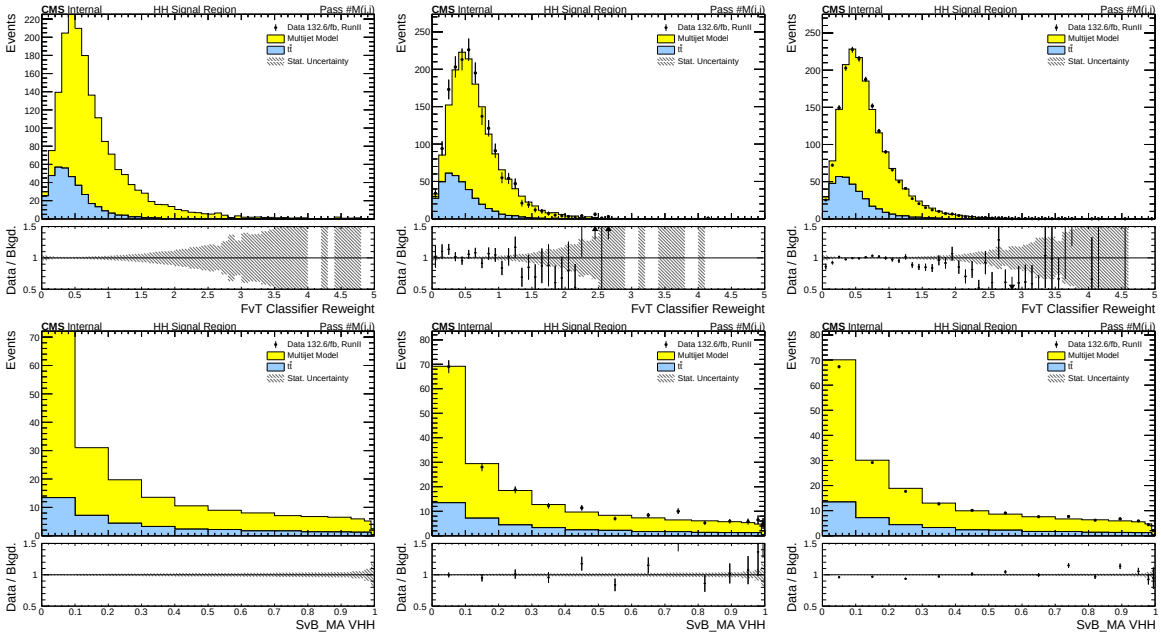

Figure 3.78 Plots of the FvT (upper row) and SvB (lower row) after FvT reweighting in the HHSR. The left-hand plots show the nominal 4*b* data; the middle plots show an example of one of the mixed datasets; and the right-hand plots show the average over all mixed datasets samples.

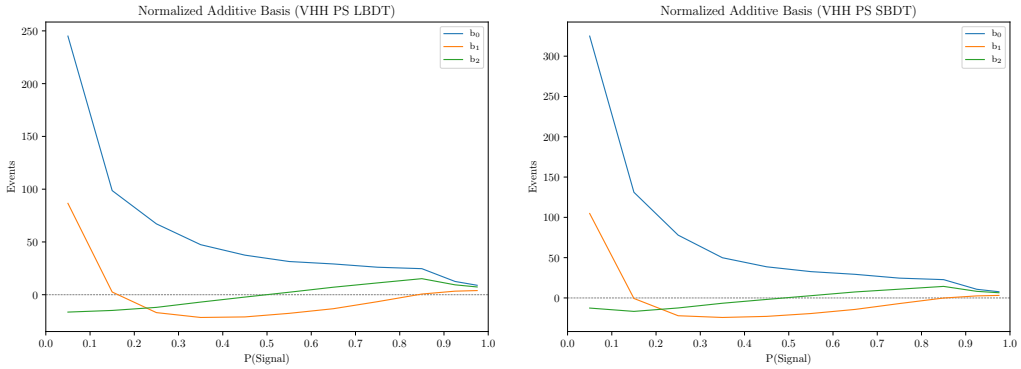

Figure 3.79 Fourier basis after diagonalization and normalization.
Left: κ_λ enhanced categorization
Right: κ_{VV} enhanced categorization

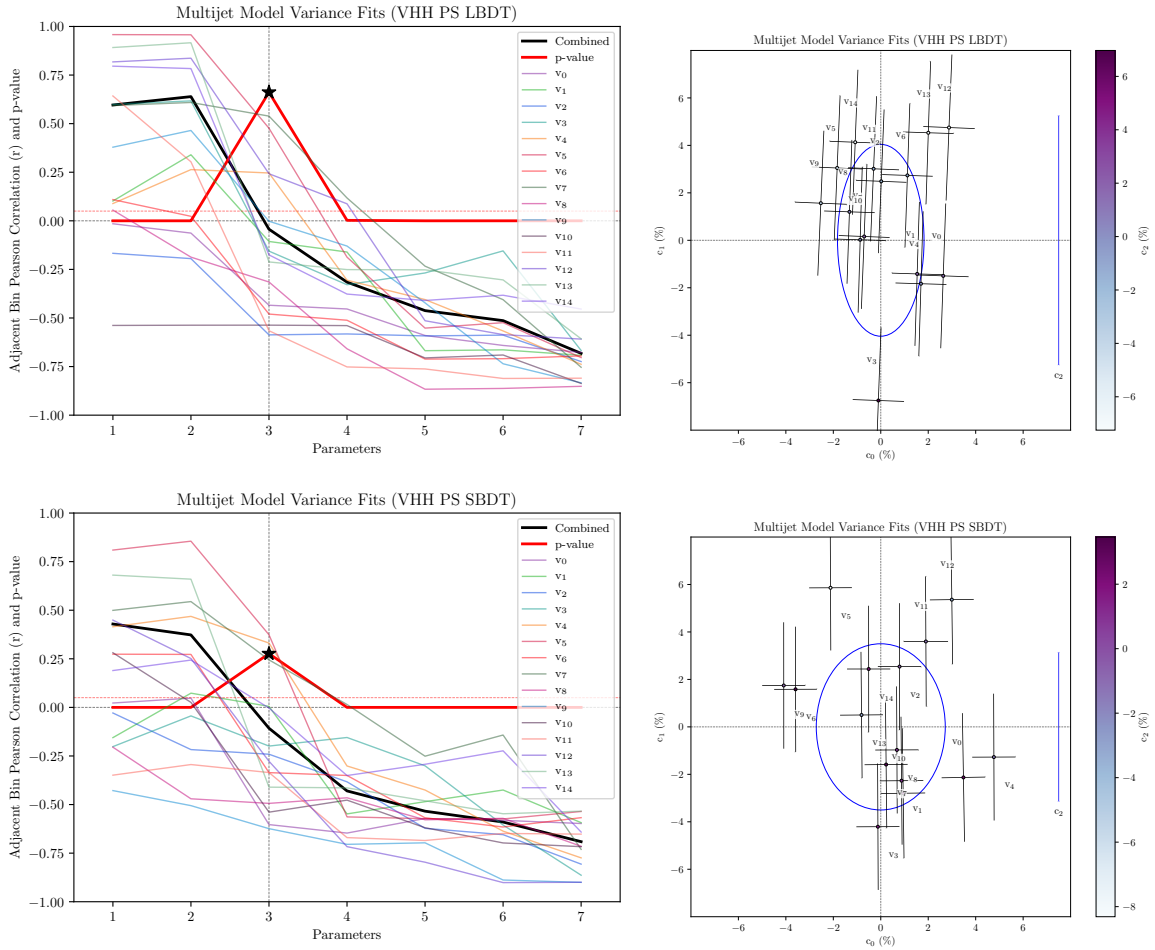

Figure 3.80 The results of step 1 (variance)
Top row: κ_λ enhanced categorization. **Bottom row:** κ_{VV} enhanced categorization.
Left column: The Pearson correlation coefficient r and its corresponding p-value as a function of the number of basis elements. **Right column:** The fit parameters of each mix model and a blue ellipse showing the gaussian priors (projected into the plane) used for the bias fit in the next step.

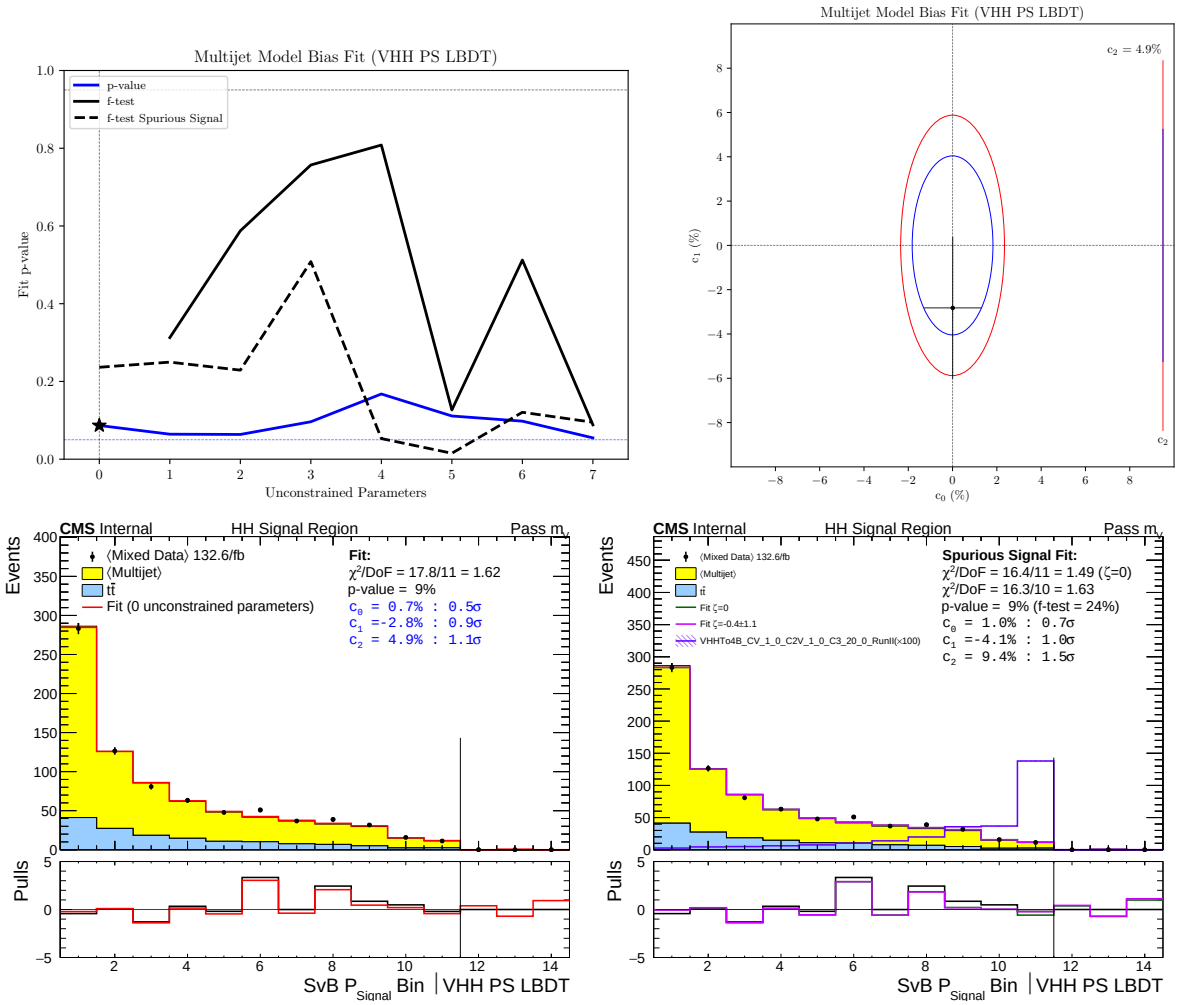

Figure 3.81 The results of step 2 (bias) and step 3 spurious signal in κ_λ enhanced categorization.
Top Left: The fit p-value and f-test as a function of polynomial order. The star denotes the selected order where no unconstrained parameter, additional basis or spurious signal is required.
Top Right: The fit parameters are shown with the blue ellipse being the priors from the previous step and the red ellipse being the updated priors which will be applied for the spurious signal fit in the next step.
Bottom Left: The fit of the average mix model plus the $t\bar{t}$ model to the average mixed data sample. The last couple bins show the pulls of the fit parameters given the gaussian priors from the previous step. The fit parameters are shown with their corresponding statistical significance.
Bottom Right: The fit of the average mix model plus the $t\bar{t}$ model plus Standard Model ZHH + WHH signal to the average mixed data sample.

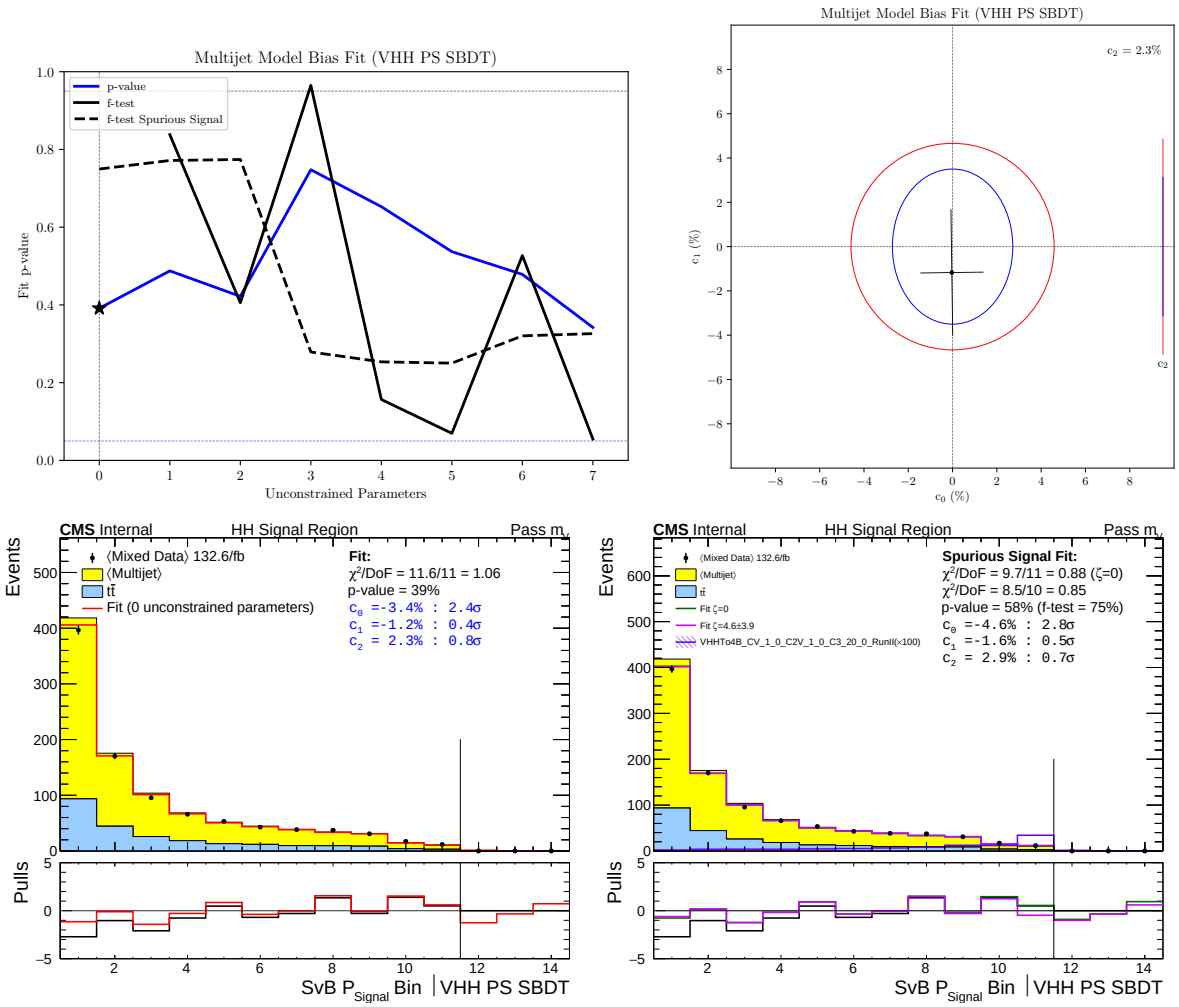

Figure 3.82 The results of step 2 (bias) and step 3 spurious signal in κ_{VV} enhanced categorization.
Top Left: The fit p-value and f-test as a function of polynomial order. The star denotes the selected order where no unconstrained parameter, additional basis or spurious signal is required.
Top Right: The fit parameters are shown with the blue ellipse being the priors from the previous step and the red ellipse being the updated priors which will be applied for the spurious signal fit in the next step.
Bottom Left: The fit of the average mix model plus the $t\bar{t}$ model to the average mixed data sample.
Bottom Right: The fit of the average mix model plus the $t\bar{t}$ model plus Standard Model ZHH + WHH signal to the average mixed data sample.

3.6 Systematic uncertainties

The systematic uncertainties considered in this analysis can either affect the expected signal and background yields or alter the shape of the distribution that enters the template fit to the data. In this section, each source of systematic uncertainty is discussed, providing details of the method of its calculation or its estimated size, and categorized into theoretical or experimental groups based on its source of origin.

3.6.1 Experimental uncertainties

Bin-wise statistical MC uncertainties

Due to statistical fluctuations of Monte Carlo (MC) samples, when the statistics used are finite, the number of selected MC events in a given bin is not always a reliable estimator of expected signal/background events in that bin. This is particularly true for bins with a low number of MC counts. To address this issue, the ”lite” modification of the Barlow-Beston approach was utilized in the analysis. To reduce the number of free parameters in the fit and enhance the robustness of numerical minimization, nuisance parameters corresponding to MC expectations in particular bins were introduced only for bins with at least one MC event. This represents the largest uncertainty in our analysis.

Luminosity

From the recommendations of the CMS luminosity group, a luminosity uncertainty of 1.0% is included for the 2016 dataset, 2.0% for the 2017 dataset, and 1.5% for the 2018 dataset. Additionally, a correlated uncertainty for Run 2 is considered: 0.6% (2016), 0.9% (2017), and 2.0% (2018). Furthermore, a correlated uncertainty for 2017 and 2018 is also included: 0.6% (2017) and 0.2% (2018).

Pile up

The systematic uncertainty on the signal and background shapes introduced by the pile-up re-weighting procedure is quantified by varying the minimum bias cross section within its ±4.6% uncertainty.

L1 prefiring correction

Effects stemming from the uncertainty of the L1 prefiring correction are accommodated by propagating the provided uncertainties on the event weights to the scale factors. The L1 prefiring correction is decorrelated between the 2016 and 2017 datasets and is not applicable for 2018.

Lepton Efficiency

Uncertainty arising from the choice of baseline selections for lepton identification and reconstruction criteria, as well as trigger effects, is incorporated as a nuisance parameter. Scale factors corresponding to these uncertainties are applied to the Monte Carlo samples, and an uncertainty is evaluated from bin-by-bin differences using alternative samples on lepton scale factors by combining all these sources. A separate analysis note for the Lepton Efficiency measurement is available: CMS-AN-21-209.

Jet energy corrections (JER/JES)

To assess the impact on the signal and background shapes resulting from jet energy scale and jet energy resolution, alternative templates of the MVA discriminant were derived by varying the absolute jet energy scale and resolution within their uncertainties and propagating the events through the full reconstruction chain. This source was treated as a shape uncertainty in the fits.

We adopt the "11 scheme" of merged JEC sources as implemented throughout the CMS-HIG-PAG. In this scheme, the sources "FlavorQCD" and "RelativeBal" are fully correlated across all years. The source "RelativeSample" is fully decorrelated across the years. All other sources are divided into a component that is fully correlated across the years and another component per year that is uncorrelated, following the recommendations.

AK4 jet b-tagging

Following the recommendations of the measurements from the CMS-BTV-POG, we apply the efficiency and misidentification scale factors as event weights to the Monte Carlo (MC) and generate alternative up/down shape templates by varying the scale factors by $\pm 1\sigma$ of their uncertainties.

Double b-tagging

ParticleNet uncertainties are incorporated using the uncertainties outlined in Table 19 of CMS-AN-20-231: "Search for non-resonant Higgs boson pair production via vector boson fusion in boosted 4b final state."

Top p_T re-weight uncertainty

It ‘s a known issue that the Top p_T distribution in $t\bar{t}$ MC samples is harder than in data. However the SF provided by Top PAG derived from data is not suitable for analyses using $t\bar{t}$ to model background.

3.6.2 Theoretical uncertainties

Cross section

The total signal cross section has been calculated to next-to-next-to-leading order accuracy, with a total uncertainty of about 3.6% for both ZHH and WHH processes, which includes the effects of scale and PDF variations.

H → bb Branching ratio

The uncertainty for H → bb Branching ratio is -1.26% / +1.24% according to Branching ratios reported in CERN Report 4 [82].

Matrix Element Factorisation and Renormalization scales

The uncertainty arising from the choice of the factorization and renormalization scales in the calculation of the matrix element of the hard-scattering process is estimated by varying each scale by a factor of $1/2$ and 2, excluding nonphysical anticorrelated combinations due to large logarithmic corrections $|\ln(\mu_R/\mu_F)| > 1$, to calculate the envelope around the central value. This is accommodated via weights obtained directly from the generator information. The effects on the signal and background are considered uncorrelated.

PDFs uncertainty

In order to estimate the impact on the limit due to the uncertainty on proton PDFs, event weights corresponding to different sets of NNPDF MC replicas were applied and propagated to the fit template's shape. The total uncertainty is estimated as the envelope of all individual variations at the level of the final discriminant template. For each PDF variation, we first construct the final template distribution, then compute the residual difference between the varied and the nominal template in each bin, and finally compute the envelope of these residuals.

PS scales ISR/FSR

In order to evaluate the impact of the choice of α_s in the parton shower simulation, the scales in the shower simulation are varied by a factor of 0.5 and 2 using weights obtained directly from the generator information. This variation is done independently for the ISR and FSR showers.

3.6.3 Summary of systematic uncertainties

Table 3.22 Systematic uncertainties considered in the analysis. "Type" refers to rate (R) or shape (S) uncertainties. "Correlation" indicates whether the uncertainty is treated as correlated, partially correlated (as detailed further below), or uncorrelated across the years 2016–18.

Source	Type	Correlation	Remarks
Experimental uncertainties			
Norm. scales	R	partially	Scale factors for $t\bar{t}$ (5FS sample), $t\bar{t}$+B (4FS sample) and DY sample
Integrated luminosity	R	partially	Signal and all backgrounds, all channels
Lepton efficiency	S	uncorrelated	1L and 2L channels
MET efficiency	S	uncorrelated	MET channel
L1 prefiring correction	S	uncorrelated	2016 and 2017
Pileup	S	uncorrelated	Signal and all backgrounds
Jet energy scale (11 scheme)	S	partially	Signal and all backgrounds
Jet energy resolution	S	uncorrelated	Signal and all backgrounds
b tag HF/LF fraction	S	partially	Signal and all backgrounds
b tag HF/LF stat (linear)	S	uncorrelated	Signal and all backgrounds
b tag HF/LF stat (quadratic)	S	uncorrelated	Signal and all backgrounds
b tag charm (linear)	S	partially	Signal and all backgrounds
b tag charm (quadratic)	S	partially	Signal and all backgrounds
b regression smear/scale	S	uncorrelated	Signal and all backgrounds
unclusteredEnergy	S	uncorrelated	Signal and all backgrounds
particleNet mass regression	S	uncorrelated	Signal and all backgrounds
b regression smear/scale	S	uncorrelated	Signal and all backgrounds
particleNet tag eff.	S	uncorrelated	Signal
top pt reweighing	S	correlated	$t\bar{t}$, $t\bar{t}$+B
$t\bar{t}$ mis-modeling	S	uncorrelated	$t\bar{t}$, $t\bar{t}$+B
Pileup Jet ID scale factor	S	uncorrelated	FH
Jet trigger emulation	S	uncorrelated	FH
Re-weight DY+Jets	S	uncorrelated	`DY+Jets`
Re-weight TT	S	correlated	$t\bar{t}$ (5FS sample)
`DY+Jets` $p_{\mathrm{T}}(Z)$	S	correlated	`DY+Jets`
Multijet background modeling	S	uncorrelated	multijet
Theoretical uncertainties			
BR_hbb	R	correlated	Signal
ZHH_NNLO	S	correlated	Signal
QCDscale, μ_R, μ_F	S	correlated	Signal, $t\bar{t}$, $t\bar{t}$+B, $t\bar{t}V$, $t\bar{t}H$
PDF+α_s	S	correlated	Signal, $t\bar{t}$, $t\bar{t}$+B, $t\bar{t}V$, $t\bar{t}H$
PS scale ISR/FSR	S	correlated	Signal, $t\bar{t}$, $t\bar{t}$+B, $t\bar{t}V$, $t\bar{t}H$

Table 3.23 Uncertainties from Renormalisation and factorisation, PDF, ISR/FSR, they are correlated across the years 2016–18. In the table, x is the $p_T(V)$, maximum is 525 GeV, minimal is 125 GeV.

Source	Type	size (%)	formula (%)
		μ_R and μ_F	
$t\bar{t}$	Up	0.18 ~ 7.99	-0.061 - 2.30e-3*x +3.36e-5*x*x
	Down	-0.12 ~ -6.10	0.146 + 8.66e-4*x -2.43e-5*x*x
$t\bar{t}$+B	Up	0.3 ~ 14.38	-16.7 + 0.160*x -1.92e-4*x*x
	Down	-0.92 ~ -4.52	3.44 - 0.041*x +4.92e-5*x*x
$t\bar{t}$V	Up	0.55 ~ 5.92	0.171+ 6.06e-4*x + 1.97e-5*x*x
	Down	-0.90 ~ -4.99	-1.02 + 3.67e-3*x -2.14e-5*x*x
$t\bar{t}$H	Up	-0.03 ~ 2.94	-1.40 + 1.18e-2*x - 6.73e-6*x*x
	Down	-0.18 ~ -3.92	1.69 - 1.63e-2*x +1.07e-5*x*x
single top	Up	2.4 ~ 32	0.151 +5.18e-3*x +1.06e-4*x*x
	Down	-1.6 ~ -21.8	0.243 -6.65e-3*x -6.74e-5*x*x
VHH	Up	-0.24 ~ 4.61	-1.47 + 9.27e-3*x + 4.40e-6*x*x
	Down	0.24 ~ -4.61	1.47 - 9.27e-3*x - 4.40e-6*x*x
		PDF	
$t\bar{t}$	lnN	2.45	
$t\bar{t}$+B	Up	0.22 ~ 1.70	0.038 + 9.61e-4*x + 4.19e-6*x*x
	Down	-0.22 ~ -1.70	-0.037 - 9.67e-4*x - 4.18e-6*x*x
$t\bar{t}$V	lnN	1.82	
$t\bar{t}$H	lnN	2.16	
VHH	lnN	1.46	
		ISR	
$t\bar{t}$	lnN	0.77	
$t\bar{t}$+B	lnN	0.30	
$t\bar{t}$V	lnN	0.01	
$t\bar{t}$H	lnN	0.17	
VHH	lnN	1.15	
		FSR	
$t\bar{t}$	lnN	0.79	
$t\bar{t}$+B	lnN	2.46	
$t\bar{t}$V	lnN	1.74	
$t\bar{t}$H	lnN	1.48	
VHH	lnN	1.89	

Table 3.24 The contribution of each group of uncertainties is quantified relative to the total absolute uncertainty in signal strength, which is the final line. To compute these relative contributes, the group of nuisance parameters are fixed to the best fit value while the likelihood is scanned again profiling all other nuisance parameters. The reduction in the up and down bands are shown in each line. The likelihood shape is asymmetric, and so up and down are quantified separately.

Uncertainty sources	2L	1L	MET	FH	Combined
Systematic uncertainty	+54%/−40%	+47%/−40%	+64%/−45%	+51%/−36%	+68%/−49%
Lepton	+2%/−1%	+4%/−1%	+0%/−1%	+0%/−0%	+3%/−4%
MET	+0%/−0%	+1%/−1%	+0%/−1%	+1%/−0%	+0%/−16%
Small-radius jet	+17%/−5%	+15%/−5%	+26%/−23%	+21%/−2%	+26%/−16%
Large-radius jet	+2%/−0%	+12%/−18%	+3%/−3%	+1%/−0%	+5%/−17%
b tagging	+41%/−4%	+35%/−3%	+56%/−29%	+36%/−1%	+62%/−34%
Total modeling	+53%/−38%	+37%/−19%	+54%/−29%	+44%/−19%	+62%/−40%
Normalization	+40%/−12%	+34%/−4%	+52%/−25%	+35%/−0%	+58%/−32%
Re-Weight	+34%/−36%	+13%/−17%	+22%/−13%	+12%/−1%	+25%/−19%
Kinematic	+11%/−10%	+17%/−3%	+13%/−4%	+24%/−24%	+19%/−14%
Luminosity	+6%/−0%	+5%/−1%	+8%/−1%	+4%/−0%	+6%/−4%
Theory	+16%/−3%	+3%/−12%	+23%/−10%	+15%/−2%	+17%/−7%
Others	+3%/−6%	+4%/−2%	+8%/−7%	+3%/−0%	+9%/−14%
Statistical uncertainty	+84%/−91%	+88%/−92%	+77%/−89%	+86%/−93%	+73%/−87%
Total absolute uncertainty	+136/−99	+111/−83	+161/−123	+163/−132	+81/−63

Table 3.25 The contribution of each group of uncertainties is quantified relative to the total absolute uncertainty in signal strength, which is the final line. To compute these relative contributes, the group of nuisance parameters are fixed to the best fit value while the likelihood is scanned again profiling all other nuisance parameters. The reduction in the up and down bands are shown in each line. The likelihood shape is asymmetric, and so up and down are quantified separately.

Uncertainty sources	2L	1L	MET	FH	Combined
Systematic uncertainty	+42%/−39%	+49%/−39%	+43%/−38%	+36%/−42%	+46%/−38%
MET	+0%/−1%	+4%/−1%	+2%/−1%	+1%/−0%	+0%/−0%
Small-radius jet	+8%/−3%	+17%/−10%	+21%/−21%	+3%/−7%	+15%/−10%
Large-radius jet	+0%/−1%	+7%/−10%	+2%/−2%	+0%/−0%	+3%/−3%
b tagging	+10%/−6%	+30%/−5%	+28%/−9%	+0%/−6%	+28%/−4%
Total modeling	+41%/−36%	+32%/−17%	+27%/−16%	+25%/−27%	+37%/−27%
Normalization	+16%/−8%	+26%/−3%	+23%/−5%	+0%/−6%	+26%/−6%
Re-Weight	+37%/−35%	+13%/−13%	+15%/−14%	+0%/−6%	+18%/−24%
Kinematic	+0%/−7%	+15%/−1%	+3%/−1%	+25%/−27%	+15%/−13%
Luminosity	+4%/−1%	+0%/−0%	+2%/−1%	+0%/−1%	+3%/−0%
Theory	+6%/−5%	+11%/−14%	+8%/−8%	+4%/−4%	+0%/−11%
Others	+7%/−6%	+0%/−3%	+7%/−7%	+0%/−1%	+9%/−7%
Statistical uncertainty	+91%/−92%	+87%/−92%	+90%/−93%	+93%/−91%	+89%/−93%
Total absolute uncertainty	+85/−52	+113/−81	+80/−66	+89/−77	+44/−36

3.7 Statistical interpretation

After all the analysis procedures introduced before, including the estimation of backgrounds and the evaluation of systematic uncertainties, a statistical procedure is needed to evaluate the presence or absence of signals in the observed data. The statistical framework used for this search corresponds to the frequentist approach adopted by the ATLAS and CMS collaborations in the context of the Higgs analyses combination [83].

3.7.1 Likelihood function and nuisance parameters

In the forthcoming discussion, we denote the anticipated signal event yield as s, and the aggregate background event yield as b. Since binned distributions are employed in the investigation of HH production outlined herein, s and b are represented as vectors, encompassing the anticipated event yield in all bins across the distributions examined within the three final states and event categories.

In a model-independent search, the signal normalization is arbitrarily fixed ($\sigma \times B = 1$ pb in this case) and is scaled by a signal strength modifier factor μ. The predictions of s and b are affected by systematic uncertainties discussed in Section 3.6. Each of these sources of systematic uncertainties is represented as a "nuisance parameter" θ_i.

The entire set of θ_i considered is collectively denoted as θ, so that $s \equiv s(\theta)$ and $b \equiv b(\theta)$. An example of θ_i is the uncertainty on the integrated luminosity, which is known with a precision of 2.5% and affects the normalization of both the signal and background estimations. The shape uncertainties related to the τ_h and jet energy scales do not impact the total values of s and b but affect their distribution among the considered bins. Generally, nuisance parameters affect the statistical model but do not provide interesting information, unlike the signal strength μ that we are seeking.

From prior considerations or auxiliary measurements, the estimation of nuisance parameters (with events independent from those entering the HH signal regions) is represented by $\hat{\theta}_i$. Our confidence in the true value of θ_i, given its estimation $\hat{\theta}_i$, is conveyed through the Bayesian probability density function $p(\theta_i|\hat{\theta}_i)$. Applying Bayes' theorem transforms this probability into a frequentist probability $p(\hat{\theta}_i|\theta_i)$, utilizing a flat prior elucidated by the functional forms of p later in this section. Assuming uncorrelated systematic uncertainty sources, the combined probability density function $p(\theta|\hat{\theta})$ is the product of individual probabilities p_i, i.e., $p(\theta|\hat{\theta}) = \prod_i p_i(\theta_i|\hat{\theta}_i)$. Given observation n, the likelihood function L is formulated as:

$$L(n, \theta|\mu, \tilde{\theta}) = P(n|\mu s + b) \cdot p(\tilde{\theta}|\theta) \tag{3.13}$$

where P represents the evaluation of the probability density function of the events, dependent on mus and b, given the data n. The latter may refer to either the measured data or the values obtained from a "pseudo-experiment," namely a set of pseudo-random numbers sampled from the expected distributions given mus, b, and $theta$. In the case of binned distributions, P is expressed as the product of Poisson probabilities for every considered bin j:

$$P(n|\mu \cdot s + b) = \prod_j \frac{(\mu s_j + b_j)^{n_j}}{n_j!} e^{-(\mu s_j + b_j)} \tag{3.14}$$

Two cases are considered to select a functional form of $p(\theta_i|\tilde{\theta}_i)$. If the uncertainty arises from an independent measurement, such as those related to the luminosity or trigger efficiencies, the log-normal function is used and defined as:

$$p(\theta_i|\tilde{\theta}_i; \kappa) = \frac{1}{\sqrt{2\pi}\ln(\kappa)\theta} \exp\left(-\frac{(\ln(\theta_i/\tilde{\theta}_i))^2}{2(\ln(\kappa))^2}\right) \tag{3.15}$$

For small uncertainties, the log-normal distribution with $\kappa = 1 + \epsilon$ is asymptotically identical to a Gaussian distribution of width ϵ, but it has the advantage of correctly describing positively defined observables by approaching zero as $\theta_i = 0$.

Uncertainties on the background estimated from the data in control regions or 'failed regions' are handled using a separate approach. This applies to scenarios such as the multijet background estimation with 3-b tagged data or the $t\bar{t}$ estimation with the 2-b tagged MC events. The estimation involves computing the number of events n in the signal regions from the number of events N in the 'failed regions'. A transfer factor α is utilized, resulting in $n = \alpha N$. In this scenario, the uncertainty on n is described by the gamma distribution:

$$\rho(n|N; \alpha) = \frac{1}{\alpha}\left(\frac{n}{\alpha}\right)^N \frac{\exp(-n/\alpha)}{N!} \tag{3.16}$$

that signifies the dissemination of the statistical uncertainties on $N = n/\alpha$ from the control region to the signal region.

3.7.2 Hypothesis testing

The likelihood formalism establishes the foundation for a hypothesis testing procedure used to quantify the presence or absence of a signal in the observed data. This procedure

utilizes two hypotheses: one where a signal contribution is present ($H_{\mu s+b}$) and another where it is absent (H_b). To set a limit on the presence of a signal, it's necessary to determine a value of μ for which the $H_{\mu s+b}$ hypothesis can be excluded in favor of the H_b hypothesis. Conversely, if there is a signal excess that needs quantifying, the compatibility of the observed data with the H_b hypothesis is articulated in terms of a probability or p-value. The hypothesis test is conducted using the "test statistics," a quantity derived from the likelihood of Eq. 3.13.

The test statistic q_μ, utilized for setting exclusion limits (**upper limit**), is computed as:

$$q_\mu = -2 \ln \frac{L(n, \tilde{\theta}_\mu | \mu, \hat{\theta})}{L(n, \hat{\hat{\mu}}, \hat{\theta})}, \quad 0 \leq \hat{\mu} \leq \mu \tag{3.17}$$

The symbol $\hat{\theta}_\mu$ in the numerator represents the conditional maximum likelihood estimator of θ, i.e., the value of θ that maximizes the likelihood of Eq. 3.13 for a fixed μ. Thus, $\hat{\theta}_\mu$ is a function of μ itself. The symbols $\hat{\mu}$ and $\hat{\theta}$ in the denominator, instead, denote the global minimum of the likelihood function, i.e., the values obtained when minimization is performed on both parameters simultaneously. The constraint $\hat{\mu} \geq 0$ indicates that the signal contribution cannot be negative, while the other constraint $\hat{\mu} \leq \mu$ ensures that upward fluctuations of the data, if larger than expected for a signal of strength μ, are not considered evidence against the signal hypothesis itself. This definition implies that larger values of q_μ represent increasing incompatibility between the data n and the hypothesized value of μ. This definition of the q_μ test statistic slightly differs from that used in searches at the LEP or Tevatron colliders. It has been adopted for LHC experiments due to the asymptotic properties of Eq. 3.17, which allow the derivation of the q_μ distribution under the $H_{\mu+s+b}$ and H_b hypotheses with analytical formulas [84] instead of using pseudo-experiments when a large number of background events is expected. This asymptotic approximation is utilized in deriving the results presented in this chapter. It has been verified for a few signal hypotheses that these formulas yield the same result as a complete computation based on pseudo-experiments.

Exclusion limits are calculated using q_μ in the modified frequentist criterion CL_s [85], [86]. Given an observed value of the test statistic q_μ^{obs} (obtained by computing the value of Eq. 3.17 using the data n), the probability for q_μ to be equal to or greater than q_μ^{obs} under the $H_{\mu s+b}$ and H_b hypotheses is defined as:

$$\begin{aligned} \mathrm{CL}_{s+b}(\mu) &= P(q_\mu \geq q_\mu^{obs} | H_{\mu+s+b}) \\ \mathrm{CL}_b(\mu) &= P(q_\mu \geq q_\mu^{obs} | H_b) \end{aligned} \tag{3.18}$$

where the dependence of the two probabilities on the value of μ has been explicitly indi-

cated. The CL_s quantity is defined as:

$$CL_s(\mu) = \frac{CL_{s+b}(\mu)}{CL_b(\mu)} \tag{3.19}$$

A signal of strength μ is considered excluded at a confidence level (CL) of α if $CL_s(\mu) < 1-\alpha$. Exclusion limits are typically computed for $\alpha = 95\%$, with the value of μ being adjusted until the condition is met. Using the CL_s criterion is preferred over an exclusion based on $CL_{s+b}(\mu)$ because the construction in Eq. 3.19 guards against under-fluctuations in the background that could erroneously exclude a signal even if it is absent. Additionally, it's important to note that the CL_s criterion yields a limit on the value of μ, which can be converted into a limit on the signal cross-section by a simple re-scaling of the initially fixed signal normalization.

The test statistics q_0 used to quantify an **event excess** is:

$$q_0 \equiv -2 \ln \frac{\mathcal{L}(n, \tilde{\theta}_0 | 0, \hat{\theta}_0)}{\mathcal{L}(n, \tilde{\theta} | \hat{\mu}, \hat{\theta})}, \quad \hat{\mu} \geq 0 \tag{3.20}$$

a definition corresponding to the test statistics used for upper limits with a signal strength $\mu = 0$.

The significance of an excess is measured as the probability of q_0 to be larger or equal than the observed q_0^{obs} under the assumption that no signal is present:

$$p \equiv P(q_0 \geq q_0^{obs} | H_b) \tag{3.21}$$

This quantity, well known as **p-value**, corresponds to the probability of the background fluctuating and producing an excess at least as large as the one observed in the data. By definition, it is independent of the normalization of the signal, although the value of $\hat{\mu}$ retains information about the magnitude of the excess compared to the expectation. The p-value is typically converted to a Z significance by expressing it as a one-sided Gaussian integral:

$$p = \int_Z^\infty \frac{1}{\sqrt{2\pi}} e^{-x^2/2} dx \tag{3.22}$$

It is customary to consider a significance of 3σ ($Z = 3$, $p = 1.3 \times 10^{-3}$) as "evidence" and a significance of 5σ ($Z = 5$, $p = 2.8 \times 10^{-7}$) as an "observation" of a signal. However, it should be noted that when searches for different signals are conducted simultaneously, such as when examining the presence of a resonance under various m_X mass hypotheses, the p-value underestimates the probability of observing a significant fluctuation for any of the hypothesized

signals. A procedure to correct for the combined probability associated with this multiple testing and to compute a "global" p-value, as opposed to the "local" p-value introduced above, is outlined in Ref. [83].

3.7.3 Validation of the statistical model

The statistical methodology outlined above provides an objective means to quantify the presence of a signal or to determine an upper limit on its magnitude using the collected data. Both the CL_s and p-value quantities are formulated within a frequentist framework, allowing them to be interpreted as probabilities of an observed outcome under well-defined hypotheses. Still, a danger lurks beneath the method and can distort the inference that we draw from the data: the bias from the analysts. If the selection is made based on the observed data, the probability of observing an excess cannot be calculated a priori using the methods discussed in the preceding sections, as it becomes contingent on the data themselves. A common scenario is fine-tuning the kinematic selections to maximize the number of observed signal-like events in real data: in such cases, the likelihood of observing an excess of events is artificially heightened during the selection process. Put differently, an analysis strategy defined based on the observed data introduces a bias that cannot be addressed within the statistical procedure outlined above.

To prevent this scenario, high-energy physics collaborations typically adhere to the "blind analysis" procedure. This involves defining, developing, and validating the analysis strategy using only Monte Carlo (MC) simulation or data from signal-free control regions. Only after the procedure is established is it permissible to examine the data in the signal region (the "unblinding" procedure) and ascertain if a signal is present. Blind analyses are standard practice in searches conducted by the CMS Collaboration, and the one outlined in this thesis is no exception. Each time a new dataset became available, the search was developed and optimized in a blinded manner, with the unblinding process being preceded by thorough checks of the quality of the physics modeling.

Significant checks involve controlling the impacts of nuisance parameters and their **'pulls'**. These pulls are the disparity between the $\hat{\theta}$ estimate derived from likelihood maximization and the initial value of the nuisance parameter, normalized to the uncertainty value.

For our VHH analysis, this validation is depicted in Figure 3.83 (based on the fit during the blinded procedure) using the non-resonant signal in a combined likelihood maximization simultaneously conducted on the four decaying channels and two event categories in each channel. Only the top 30 significant nuisance parameters are shown in this figure. The 'unblinded'

impact plots can be find in the appendix .3.

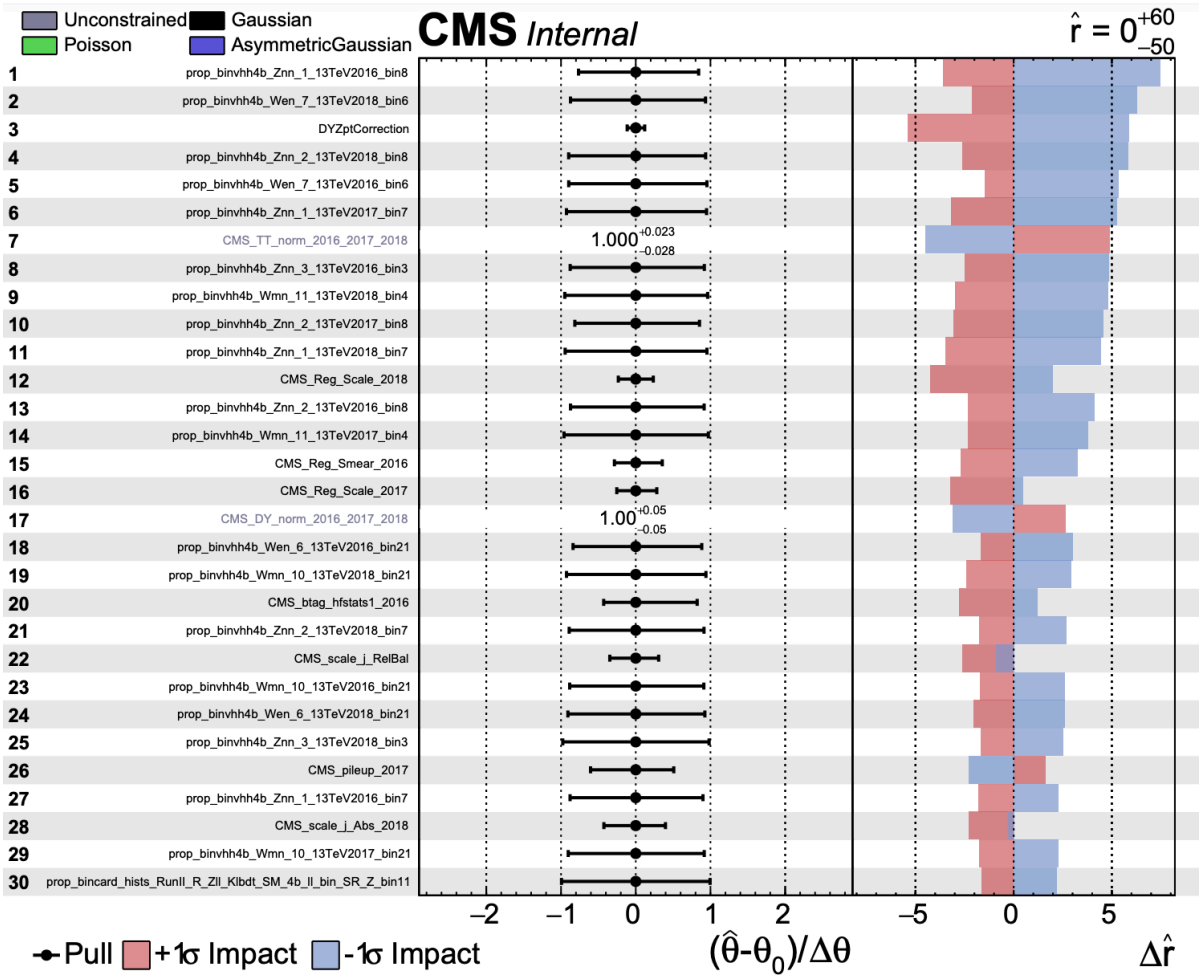

Figure 3.83 The pull-impact summary plot from the `HHCombine` tool, the data is blinded.

Further confirmation of the accurate modeling of the data is furnished by the goodness-of-fit assessment using the ”saturated” method [87]. It is an extension of the χ^2 method designed for data that deviate from normal distribution, such as the event counts in the binned distributions utilized in this study. This test is structured as a likelihood ratio, with the alternative hypothesis aligning precisely with the data. The distribution of this test statistic is derived from pseudo-experiments generated based on the modeled background, then compared to that computed using the observed data. The findings are elaborated in Figure 3.84. The observed value is situated within the central region of the anticipated distribution, indicating that the background accurately models the data.

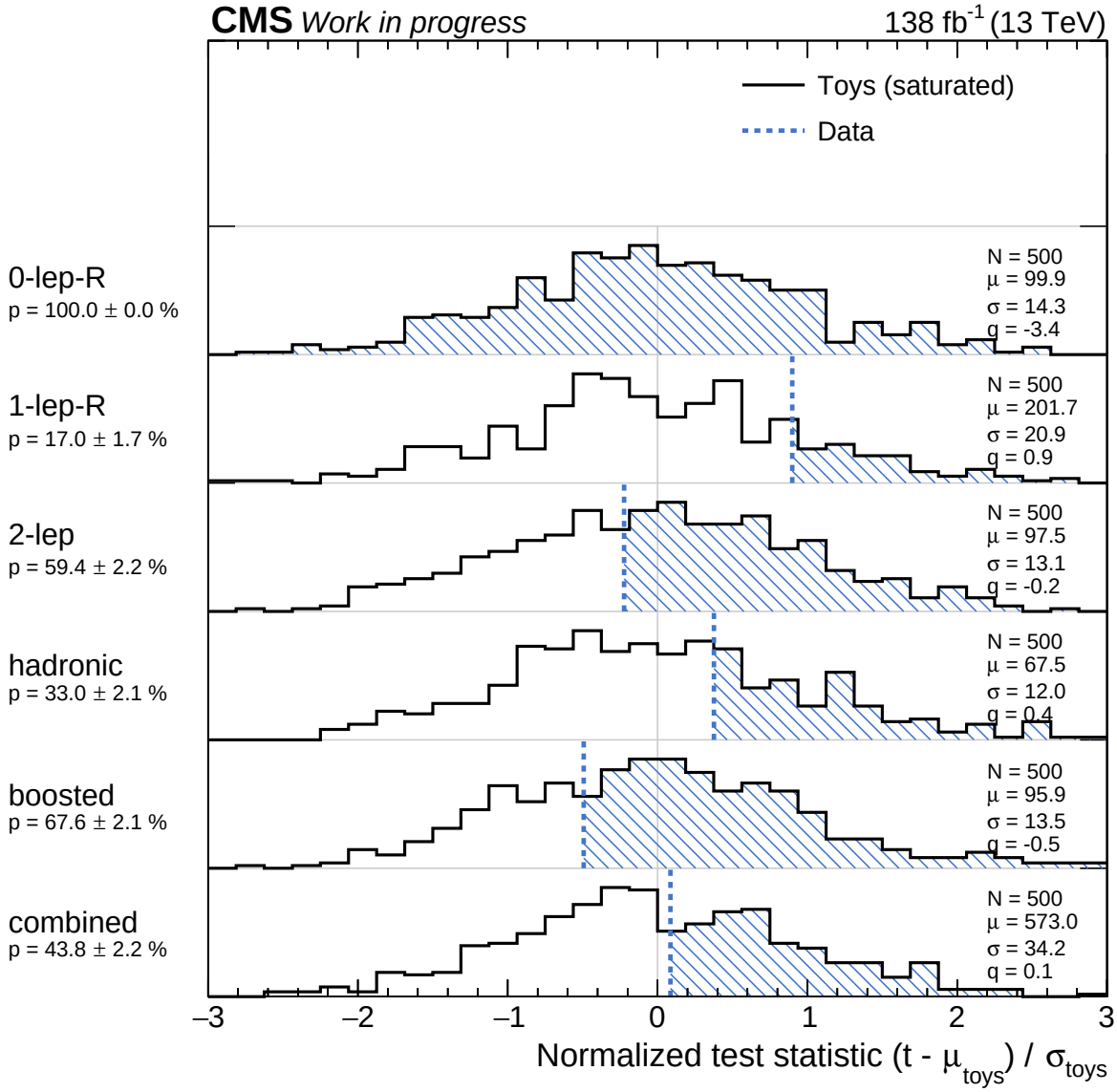

Figure 3.84 Unblinded Goodness-of-Fit test in all the channels

3.8 Result

Given the Feynman diagrams in Figure 3.1, this process depends on four couplings: κ_V, κ_{WW}, κ_{ZZ}, and κ_λ . The HH inference tool [61] developed in the HH group is the natural tool to implement interpolations and extrapolations of cross sections and kinematics with different coupling schemes, and so the following results have been obtained using it.

The VHH analysis has implemented an eight-LO-sample basis. All of the LO cross sections for each coupling sample, listed in Table 3.3, are derived from MadGraph. In addition, considering known NLO (and NNLO for ZHH) effects, we have scaled all of these LO cross sections by the ratio of NLO/LO (NNLO/LO for ZHH) assuming standard model couplings. For WHH, this effectively corresponds to a scale of 1.2 across the p_T of the W boson at the generator level, while the scale of ZHH varies across the p_T of the Z boson up to 1.5, as mentioned in Section 3.2.1.

3.8.1 `HHinference` Validation

For each of the 8 signal samples, the expected upper limit extracted directly from the Higgs Combine tool is compared with its counterpart using the `HHinference` tool and shown in Table 3.26, utilizing datacards combining all channels.

Table 3.26 Expected upper limits for each signal sample from Combine and `HHinference`, using datacards combining all channels.

Signal point	Higgs Combine tool	`HHinference`
CV_0_5_C2V_1_0_C3_1_0	$80.63^{+35.67}_{-23.91}$	$81.75^{+36.17}_{-24.24}$
CV_1_0_C2V_0_0_C3_1_0	$89.38^{+42.39}_{-27.71}$	$89.75^{+42.57}_{-27.83}$
CV_1_0_C2V_1_0_C3_0_0	$163.75^{+73.76}_{-48.95}$	$165.50^{+74.55}_{-49.48}$
CV_1_0_C2V_1_0_C3_1_0	$124.69^{+54.17}_{-36.97}$	$125.00^{+54.31}_{-37.07}$
CV_1_0_C2V_1_0_C3_2_0	$78.44^{+34.08}_{-23.07}$	$78.75^{+34.22}_{-23.16}$
CV_1_0_C2V_2_0_C3_1_0	$29.45^{+12.91}_{-8.67}$	$29.38^{+12.88}_{-8.71}$
CV_1_5_C2V_1_0_C3_1_0	$32.66^{+14.97}_{-10.05}$	$32.50^{+15.16}_{-9.87}$
CV_1_0_C2V_1_0_C3_20_0	$1.71^{+0.76}_{-0.51}$	$1.70^{+0.76}_{-0.51}$

3.8.2 Stacked background templates + signal templates

The post-fit distributions with the signal+background hypotheses are depicted in Figs. 3.85 to 3.86.

For a comprehensive and simultaneous representation, the signal regions (SRs) are amalgamated by binning all discriminant outputs into bins of escalating signal purity, expressed as

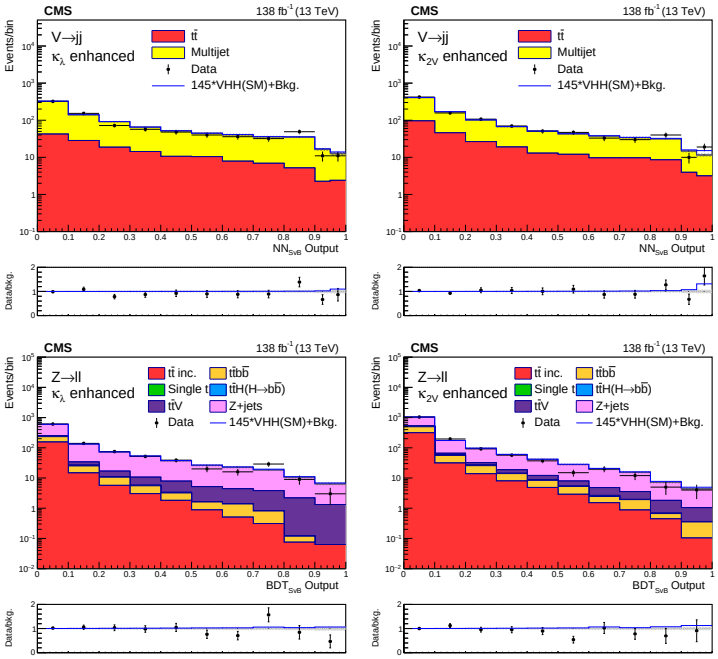

Figure 3.85 Postfit BDT distributions with the signal-plus-background hypotheses of the FH and 2L channels.

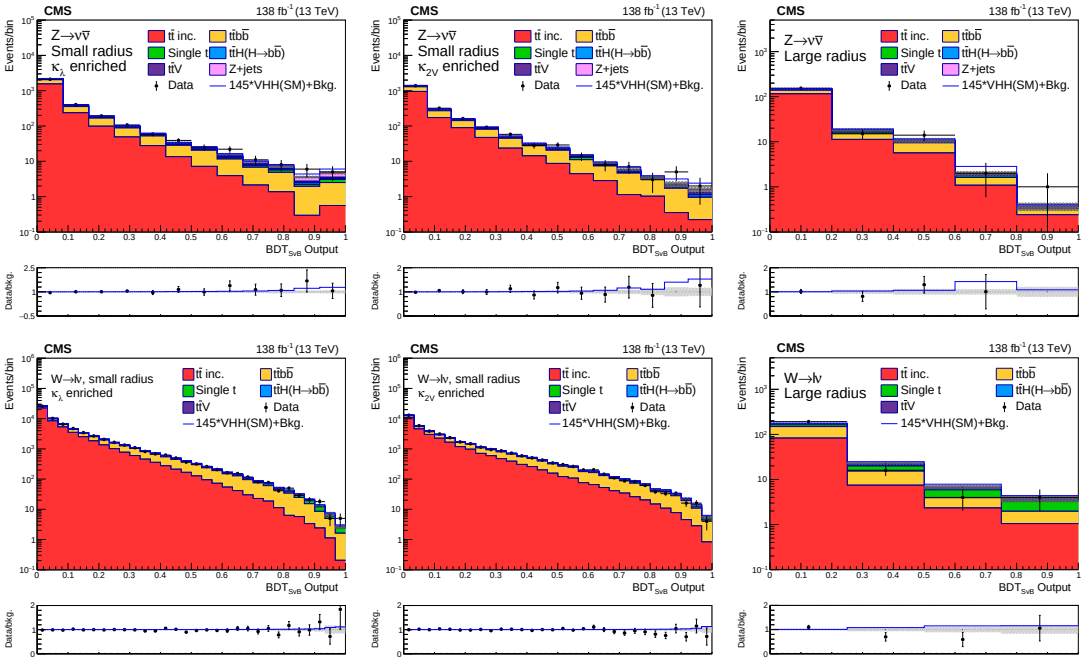

Figure 3.86 Postfit BDT distributions with the signal-plus-background hypotheses of the MET and 1L channels.

$\log_{10}\left(100(S_{SM}/B)\right)$, where S_{SM} signifies the signal anticipated by the Standard Model, and B denotes the estimated background. These bin sums are computed separately for each enrichment type. In Fig.3.87, these aggregated distributions are depicted, superimposed with data

and signal models falling within the sensitivity of this analysis. For clarity, the Single-Top, $t\bar{t}H$, and $t\bar{t}V$ backgrounds are amalgamated and denoted as "Other" in Fig.3.87.

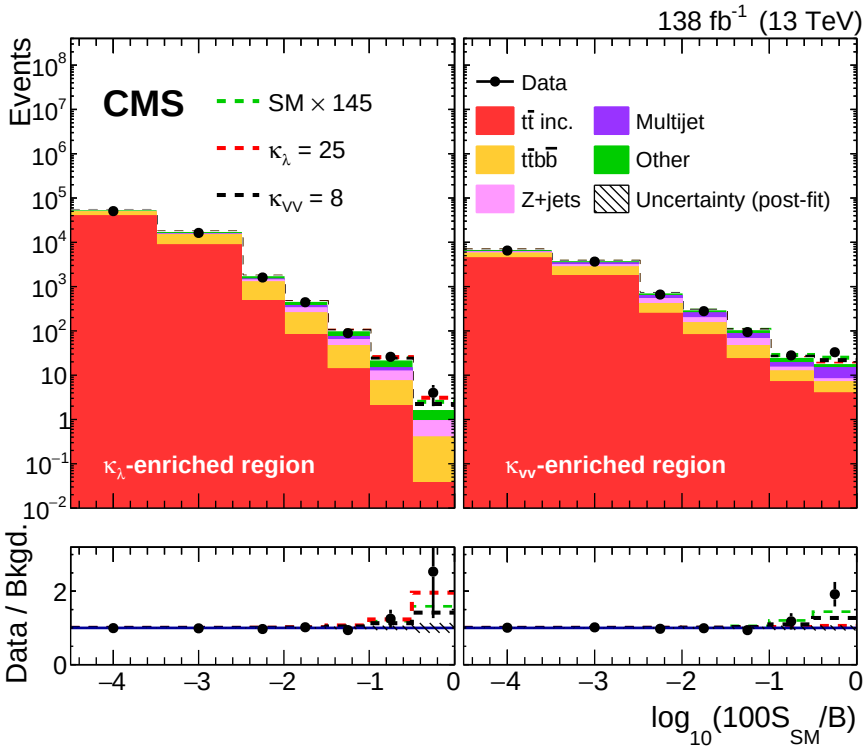

Figure 3.87 Machine learning output distributions are transformed to $\log_{10}\left(100(S_{SM}/B)\right)$ and summed for κ_λ - and κ_{VV}-enriched SR samples separately. The filled histograms represent the postfit simulation. The total postfit uncertainty is represented by the hatched band. The SM contribution and two signal models near expected exclusion at the 95% CL are shown with the dashed lines.

3.8.3 Scans on signal strength and cross sections

A test statistic derived from the profile likelihood ratio [88] is employed to ascertain the signal strength, with the combined signal strength serving as the parameter of interest (POI). Systematic uncertainties are integrated as supplementary nuisance parameters. In the likelihood computations, each of these parameters contributes an extra multiplicative factor to the total likelihood. Alternatively, four signal strengths are designated as POI for each channel and compared to the combined signal strength. Figure 3.88 illustrates the signal strengths per analysis channel, along with the combined signal strengths.

In Fig. 3.87, an excess of data compared to the background-only anticipation is observable in the most signal-enriched bins across both enrichment regions. In the κ_λ -enriched region,

the excess is roughly consistent with background expectations within approximately one standard deviation in the most sensitive bin. However, in the MET channel κ_{VV}-enriched region, the excess is more pronounced. For a signal resembling the SM, the observed local significance, discounting any look-elsewhere effect [89], stands at 2.6 standard deviations. The signal strength determined is 145 times the SM signal when all coupling modifiers are set to 1. [79] The observed excess requires further investigation with additional data. Results from two fits are illustrated in Figure 3.88: an inclusive fit employing a single signal strength modifier, and a second fit with distinct signal strength modifiers per channel. In the latter fit, the excess is predominantly observed in the MET channel, accompanied by some additional excess in the FH and 2L channels.

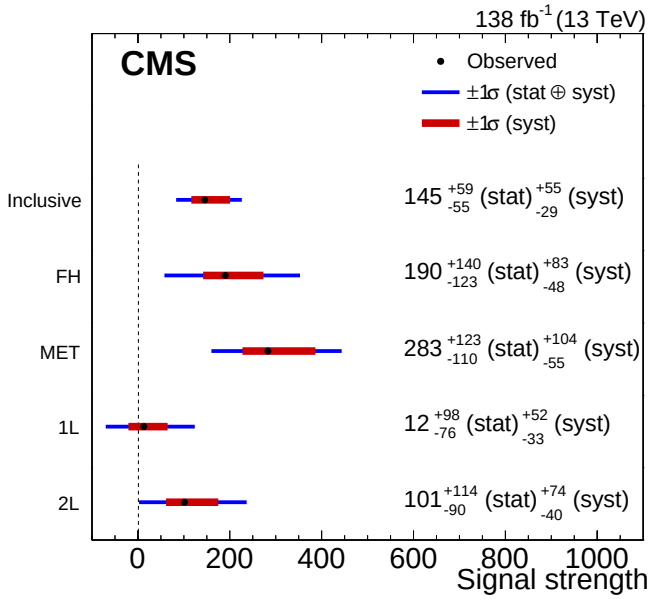

Figure 3.88 Results from two maximum likelihood fits are presented. The first entry, labeled "Inclusive," represents the outcome of a single signal strength fit across all channels. The remaining four entries stem from a fit of identical regions but with separate signal strengths allocated to each channel. Thinner blue bands denote one standard deviation from the full likelihood scan in that parameter, while thicker red bands represent one standard deviation bands of the systematic uncertainties exclusively.

Two-dimensional likelihood scans of κ_λ versus κ_{VV} and κ_{ZZ} versus κ_{WW} are shown in Fig. 3.89 and 3.90, respectively. Other couplings are fixed to their SM values.

Using the CLs criterion [85, 86] and asymptotic formulas [84], we establish the upper limits on the VHH cross section at a confidence level of 95%. These limits are obtained under two scenarios: with the SM couplings and through scans on the coupling modifiers. The upper limit at 95% CL of the VHH production cross section is observed (expected) to be at 294 (124)

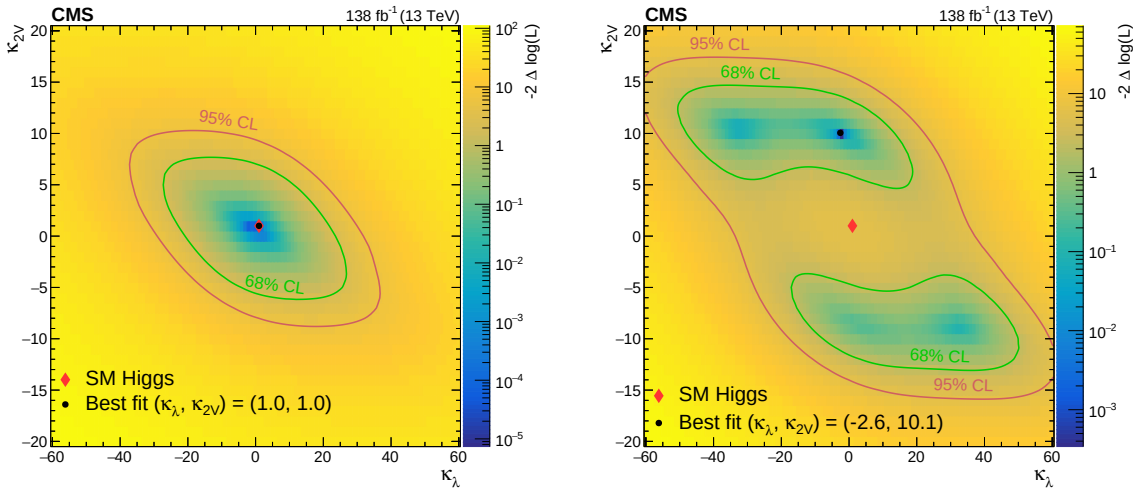

Figure 3.89 Expected (left) and observed (right) likelihood scans in κ_λ versus κ_{VV} are displayed, with other couplings fixed to the SM predicted strength. The excess is most prominent in the κ_{VV}-enriched region, and thus the most likely point of the scan at κ_{VV} = 10.1 and κ_λ = -2.6 is shifted from the SM mostly in the κ_{VV} dimension.

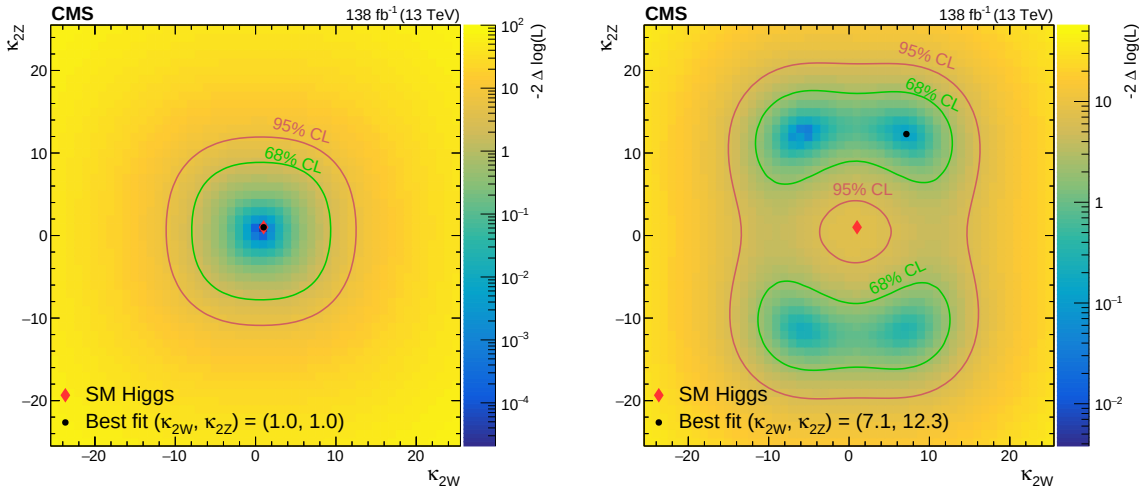

Figure 3.90 Expected (left) and observed (right) likelihood scans of κ_{WW} versus κ_{ZZ} are shown, with other couplings fixed to the SM predicted strength. The excess is most prominent in the MET channel, and so the most likely point of the scan at κ_{WW} = 7.1 and κ_{ZZ} = 12.3 is pulled from the SM mostly in the κ_{ZZ} dimension, to which the signal in the MET channel is solely sensitive.

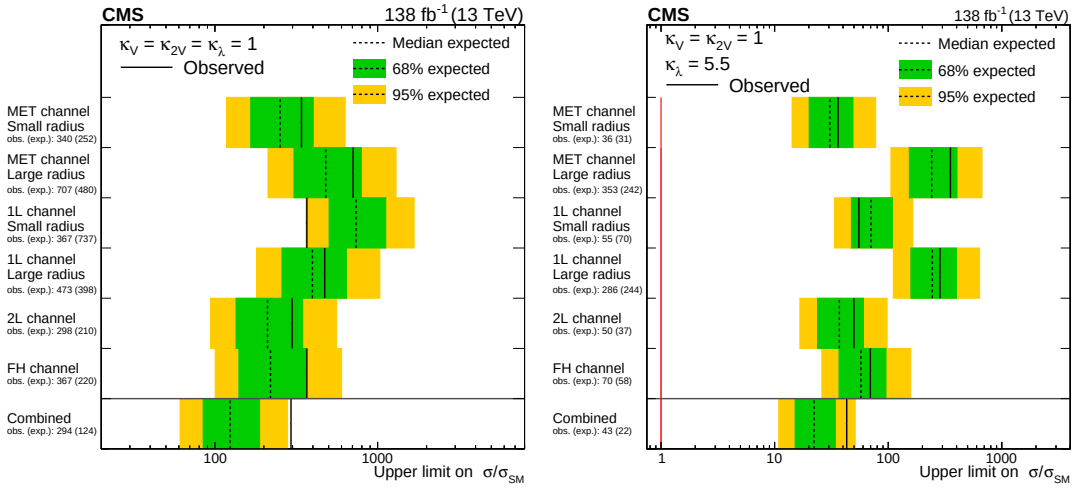

Figure 3.91 The left plot shows the VHH cross section limits per channel and combined for SM value couplings, while results with $\kappa_\lambda = 5.5$ and $\kappa_{VV} = \kappa_V = 1.0$ are shown on the right.

times the SM prediction. Because of destructive interference with positive κ_λ in leading HH production modes (ggF and VBF), VHH searches can significantly contribute to the overall HH program near the corresponding minimum in HH sensitivity. Particularly, in the range of $4 < \kappa_\lambda < 7$, this search exhibits sensitivity comparable to other HH searches. For instance, the $pp \rightarrow HH$ cross-section 95% CL expected limit from this VHH search is approximately 3–4 times the $b\bar{b}\tau^+\tau^-$ cross-section in this range on the equivalent dataset [90]. Figure 3.91 illustrates the SM 95% CL cross-section limits, as well as those for $\kappa_\lambda = 5.5$, positioned in the middle of the highlighted region, with other coupling modifiers set to unity. The upper limits on VHH and total HH cross-section as functions of κ_λ , κ_{VV}, and κ_V are depicted in Figures 3.92, 3.93, and 3.94. The 95% CL limits are summarized in Table 3.27.

Table 3.27 Observed and expected 95% CL upper limits on the coupling modifiers.

	κ_λ	κ_{VV}	κ_V	κ_{ZZ}	κ_{WW}
Observed	(−37.7, 37.2)	(−12.2, 13.5)	(−3.7, 3.8)	(−17.4, 18.5)	(−14.0, 15.4)
Expected	(−30.1, 28.9)	(−7.2, 8.9)	(−3.1, 3.1)	(−10.5, 11.6)	(−10.2, 11.6)

One of our motivation to explore the VHH production mode is because of it's constructive interference as explained in Section. 1.3. We can find the comparison of the κ_λ scan at Fig. 3.95 to see that VHH has a very hard distribution at around $\kappa_\lambda = 5$ and around, only weaker than the well known channel like $bbbb$, $bb\gamma\gamma$and shows no destructive interference.

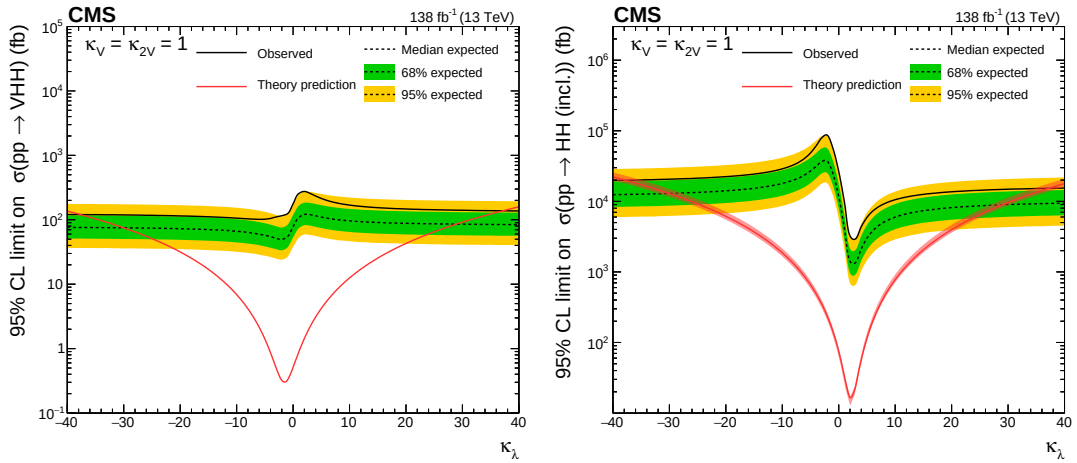

Figure 3.92 Upper 95% CL limits on VHH (left) and HH (right) signal cross section scanned over the κ_λ parameter while fixing the κ_{VV} and κ_V to their SM-predicted values. The independent axis is the scanned κ_λ parameter, and the dependent axis is the 95% CL upper limit on signal cross section.

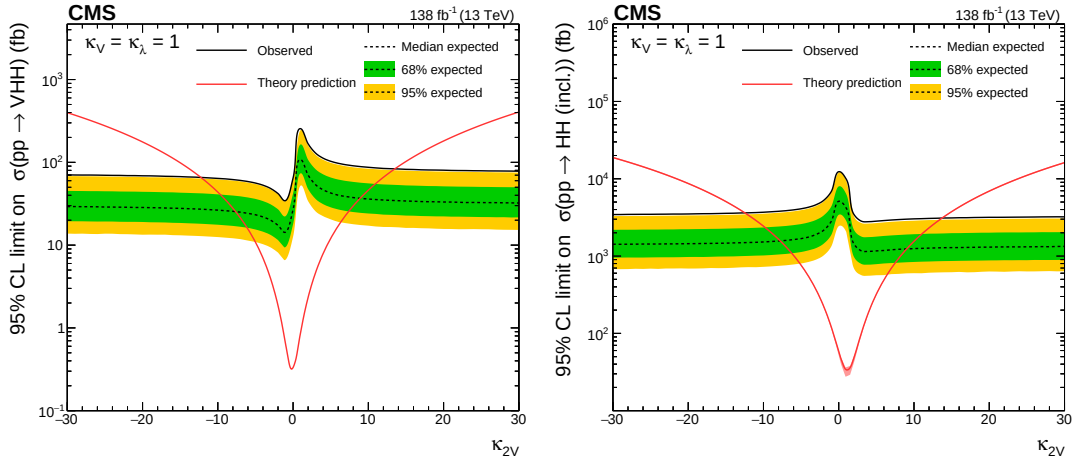

Figure 3.93 Upper 95% CL limits on VHH (left) and HH (right) signal cross section scanned over the κ_{VV} parameter while fixing the κ_λ and κ_V to their SM-predicted values. The independent axis is the scanned κ_{VV} parameter, and the dependent axis is the 95% CL upper limit on signal cross section.

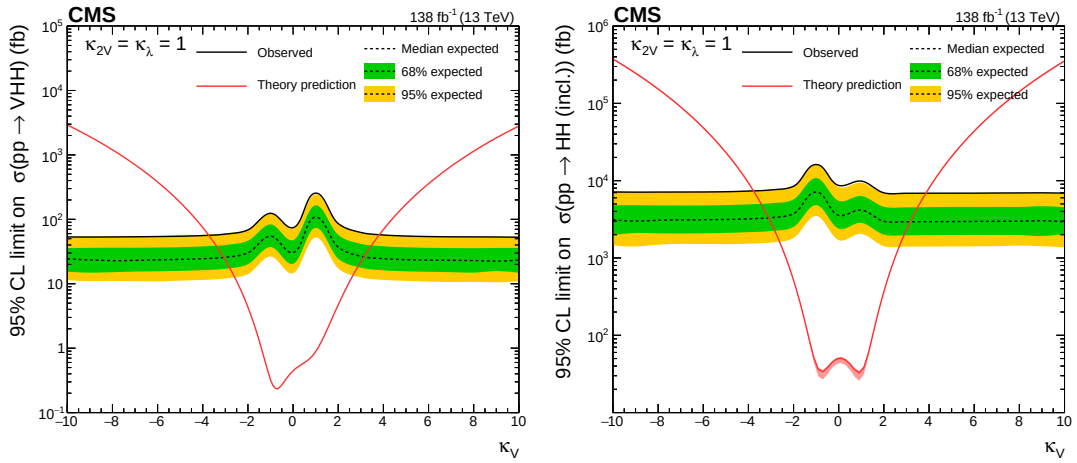

Figure 3.94 Upper 95% CL limits on VHH (left) and HH (right) signal cross section scanned over the κ_V parameter while fixing the κ_{VV} and κ_λ to their SM-predicted values. The independent axis is the scanned κ_V parameter, and the dependent axis is the 95% CL upper limit on signal cross section.

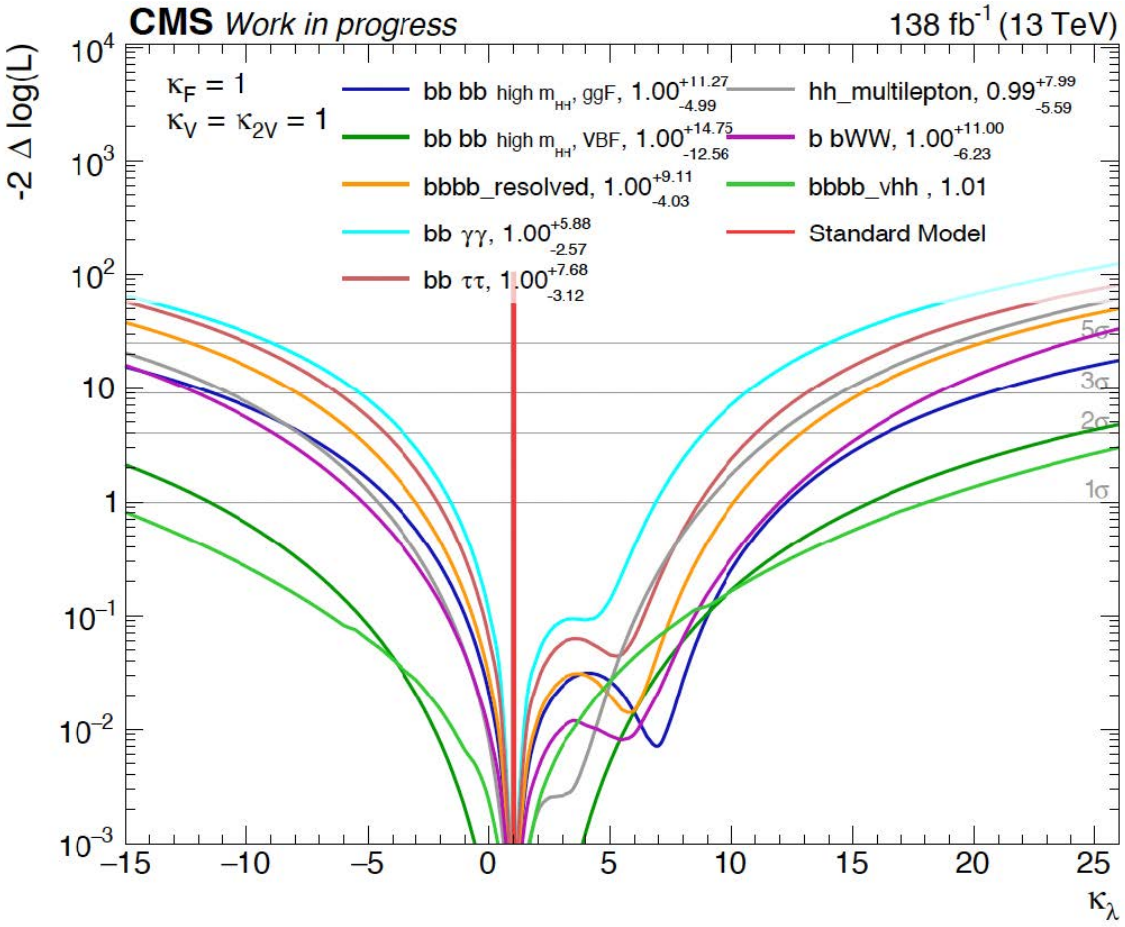

Figure 3.95 The upper limit scan for multiple published HH channel, we can find VHH have a very hard distribution at around $\kappa_\lambda = 5$ and around, only weaker than the well known channel like $bbbb$, $bb\gamma\gamma$and shows no distructive interference.

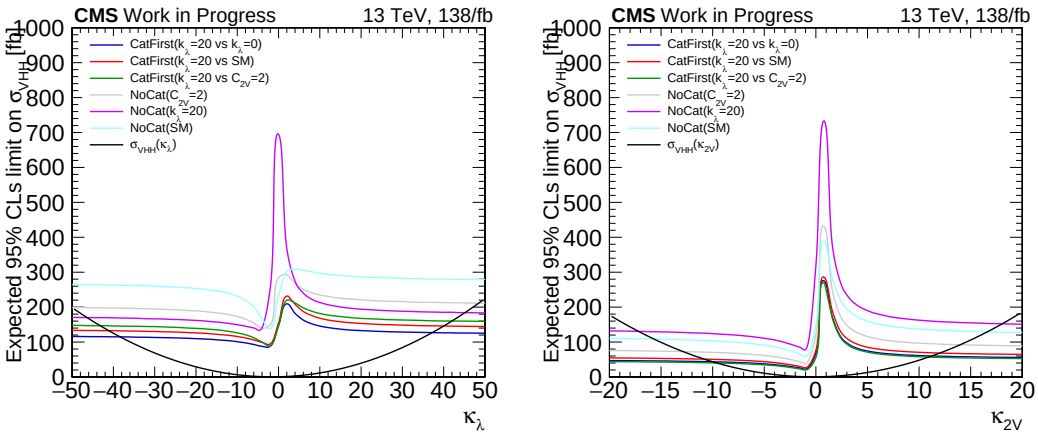

(a) Resolved

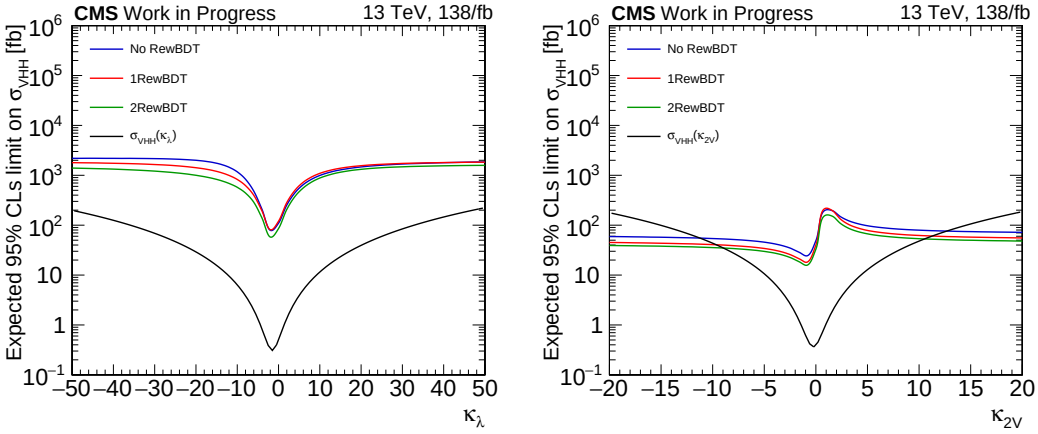

(b) Boosted

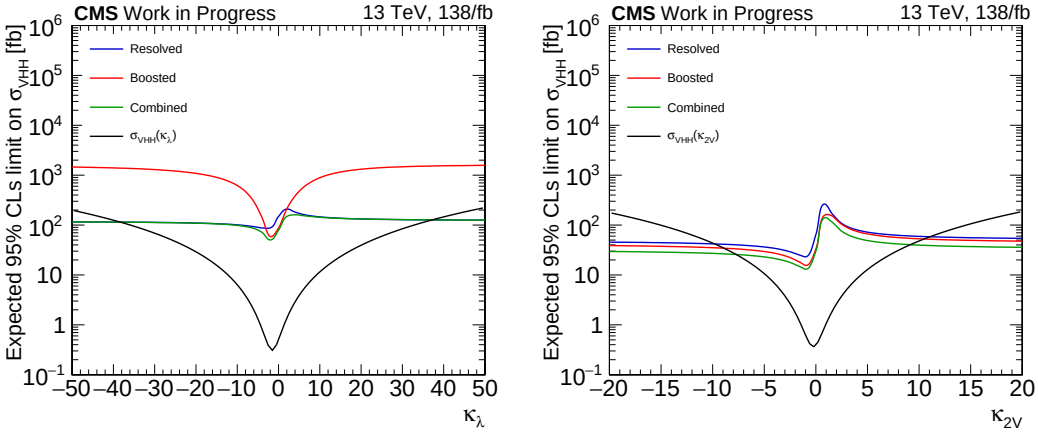

(c) Combined

Figure 3.96 Limit scans to compare different strategies in the (a) resolved (b) boosted topologies. The two topologies are combined in (c), which also shows the sensitivity of boosted topology is enhanced around the SM coupling.

Chapter 4 Future Prospects for HH searches

THE discussion in the previous chapters emphasized the rarity of HH production signals and the challenges inherent in physics analysis due to limited statistics. To improve physics performance or even directly detect these signals, one straightforward approach is to increase data accumulation under higher luminosity or upgrade detectors to expand acceptances or enhance precision. However, upgrading experimental instruments, particularly for large experiments like CMS or those conducted at the LHC, poses significant challenges. This will be further explored in Chapter 5.

In the context of utilizing current data, there are still two aspects to consider for future HH research.

If we examine the typical analysis process, we can conclude that the efficiency of detecting a signal amidst the backgrounds primarily relies on effectively identifying fundamental objects such as leptons, jets, etc. Additionally, the efficiency depends on extracting the signal from the background, involving processes like selection and categorization. By employing more robust algorithms or dedicated analysis strategies, we can significantly enhance physics performance. In this chapter, we will explore the potential of the data using HH decays into the $b\bar{b}\tau^+\tau^-$ and $b\bar{b}\mu^+\mu^-$ channels as example.

4.1 The HH decay to $b\bar{b}\tau^+\tau^-$ final states study in Boosted topology

Both CMS and ATLAS Run-2 have observed a sensitive channel for probing HH [17, 18]. Referring to Figure 1.10, we observe that the $b\bar{b}\tau^+\tau^-$ decay mode has the third-largest branching ratio, approximately 7.3%, which is less than a quarter of the largest 4b decay mode. However, due to its relatively cleaner backgrounds, the sensitivity is comparable to the 4b mode, setting the second most stringent limit on the cross-section upper limit as well as the allowed interval of the kappa parameters of interest.

If we look back into the CMS Run-2 HH to $b\bar{b}\tau^+\tau^-$ search, we can find a certain amount of points that could further improve the results. According to the Run-2 analysis flow chart(Fig. 4.1), we could point out some measurements that could potentially improve the result in Run-3 or even with Run-2 data.

Exploring the usage of cutting-edge machine learning techniques for jet tagging, we delve into ParticleNet, a model already instrumental in the VHH analysis (detailed in Sec. 3.3.3) and

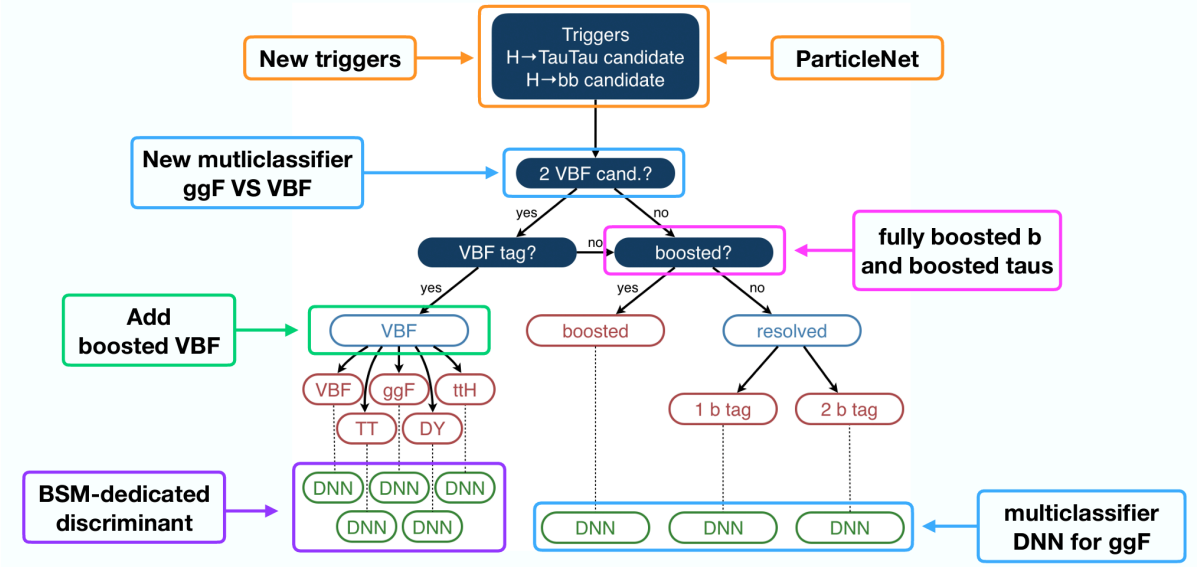

Figure 4.1 Potential improvement point based on CMS Run-2 $b\bar{b}\tau^{+}\tau^{-}$ analysis.(The DNNs are also potential measurements.)

numerous other studies. Its standout deployment includes a double-b large radius jet tagger in the boosted HH to 4b analysis [91], significantly tightening constraints on the kappa parameters, particularly κ_{VV}. This analysis was pivotal in ruling out the $\kappa_{VV} = 1$ scenario with over six standard deviations at the 95% CLs level. Among the channels probing κ_{VV}, the $b\bar{b}\tau^{+}\tau^{-}$ decay emerges as notably sensitive, especially at elevated energies. Another motivating factor for adopting ParticleNet is its recent enhancement to effectively tag double tau large radius jets, enabling consistent tagging of both Higgs to 2b and Higgs to 2tau decays with a singular framework. This advancement simplifies the analysis of HH to $b\bar{b}\tau^{+}\tau^{-}$ decays in the boosted regime by focusing on a single entity: the large radius jets (AK8 jets, per CMS's official reconstruction methodology).

We conduct a Monte Carlo-based preliminary study to investigate the potential of this channel (HH to $b\bar{b}\tau^{+}\tau^{-}$ in the double boosted topology). Given that the only object used for the reconstruction of Higgs bosons is the AK8 Jet, we commence with an AK8 Jet-based analysis to assess the potential enhancements achievable through the utilization of ParticleNet. The analyses presented in this section are grounded on simulated events from CMS Run-2. Our objectives include evaluating the performance of the mass regression generated by the ParticleNet model and comparing this new tagger with the current tagger, DEEPTAU [92].

We utilize the ggFHH sample generated for the CMS 2018 study as the signal sample, along with the main background processes consisting of DY+Jets and $t\bar{t}$ inclusive samples, all of which are officially generated by CMS for Run-2 study. Initially, we focus on events

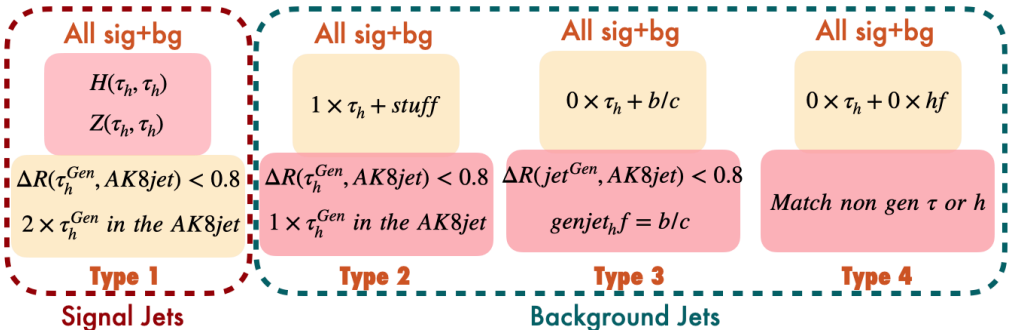

Figure 4.2 Cartoon of the categorization of the AK8 jets, only type1 is signal jets.

containing at least 1 AK8 jet with p_T higher than the 200 GeV threshold, as our interest lies primarily in the boosted topology. Subsequently, we analyze all AK8 jets from the events to conduct the jet-based study, considering these AK8 jets as potential Higgs candidates.

For the reason of comparing the mass distribution and the performances of the taggers, all the AK8 jets are categorized into 4 different types based on the matching results referring to the generator level information, as illustrated in the cartoon Fig. 4.2. Type1 jets match with 2 generator level hadronic decay taus, which are the only kind that been considered as signal jets but will not only contains di-tau decay from Higgs but also di-tau decay from the Z boson. Since we are comparing the power of the di-tau jet taggers, we define type1 as the signal category. There are also type2, in which jets match with only 1 hadronic decayed tau. Type 3 match 0 hadronic taus but match with heavy flavor generator level jets, so it would contains the H decay to bb candidates. Type4 jets match neither hadronic tau nor heavy flavor jets.

The mass distribution can be found in Fig. 4.3. In the left panel, the mass spectrum of the type 1 jets is displayed. Due to the missing energy during tau decay, the mass peak of the Higgs boson or Z boson is smaller than their theoretical value. Comparing the solid line with the dashed lines, which represent the distribution of jet mass after the mass regression provided by the ParticleNet model, reveals that both the HH and DY+Jets processes exhibit improved mass resolution. However, the background $t\bar{t}$ process does not show the expected improvement. Nevertheless, this enhanced resolution will provide additional sensitivity in the full analysis.

The subsequent step involves comparing ParticleNet with DEEPTAU in terms of their ability to suppress backgrounds while maintaining signal acceptance efficiencies. We aim to conduct a direct comparison between these two taggers, which is not very easy. DEEPTAU scores can only be evaluated when the objects are recognized as taus, meaning that only AK8 jets containing two tau objects can yield two DEEPTAU scores to determine whether they are

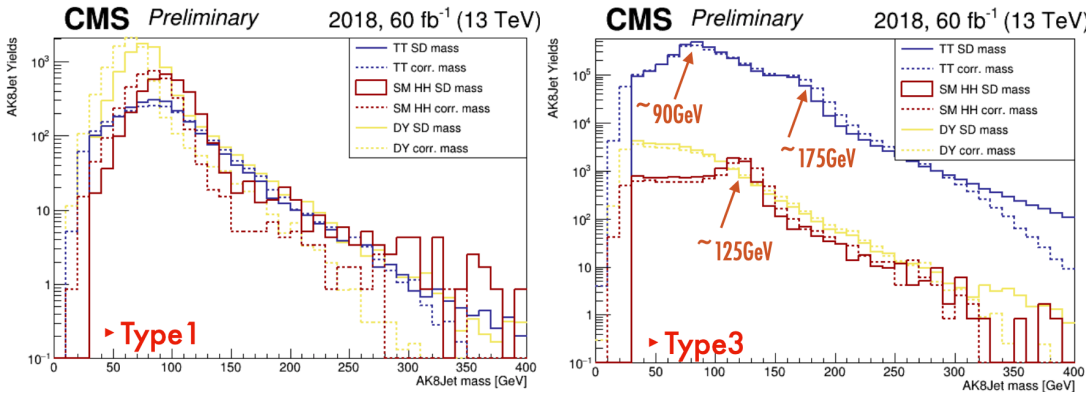

Figure 4.3 Jet mass distribution of type1(left) and type3(right) jets. The solid lines are the soft-drop mass and the dashed lines are the mass after PNet regression.

X($\tau\tau$) jets. Conversely, ParticleNet scores can be assessed for any AK8 jets, ensuring that each jet is associated with a PNet score. Our initial task is to assess the impact of this difference on the number of affected jets and how these jets may influence the overall physics performance.

In CMS, the τ is reconstructed using an algorithm known as the Hadron Plus Strips (HPS) algorithm [93], which achieves approximately 90% efficiency under the typically recommended working point for reconstructing single τ objects. In Fig. 4.4(left), the matching efficiencies of the HPS tau pair with type 1 AK8 jets are illustrated. The first data point is calculated based on all type 1 jets, and from left to right, the evaluation is performed on jet sets with higher p_T ranges. The purple and red dots represent the results for jets with or without a loose Higgs mass window limitation between 60 to 150 TeV. From the initial data point, the overall matching efficiency is approximately 80%, comparable to the single HPS reconstruction efficiency. However, as the p_T increases, the efficiencies drop significantly, attributed to the increasing merging of the two τ's inside one jet due to higher energy. This figure suggests that the 20% of lost jets could be reintroduced into the analysis by employing ParticleNet as the jet tagger, with the potential to recover even more jets in higher p_T ranges. These jets are all type 1 jets and are those matched with two generator-level taus. In Figure 4.4(right), the ROC curve of the ParticleNet model is depicted, dividing signal jets (type 1) and background jets (types 2 to 4). Different colors represent the ROC curves of type 1 jets against different backgrounds, where dashed lines represent results from the jets set without HPS matching, while solid lines depict those with matching. This panel indicates that the classification power of ParticleNet remains unaffected even when all jets that cannot be analyzed using DEEPTAU are reintroduced and more statistics is almost always an advantage.

Jets that fail to match are selectively excluded from the comparative jet collections to en-

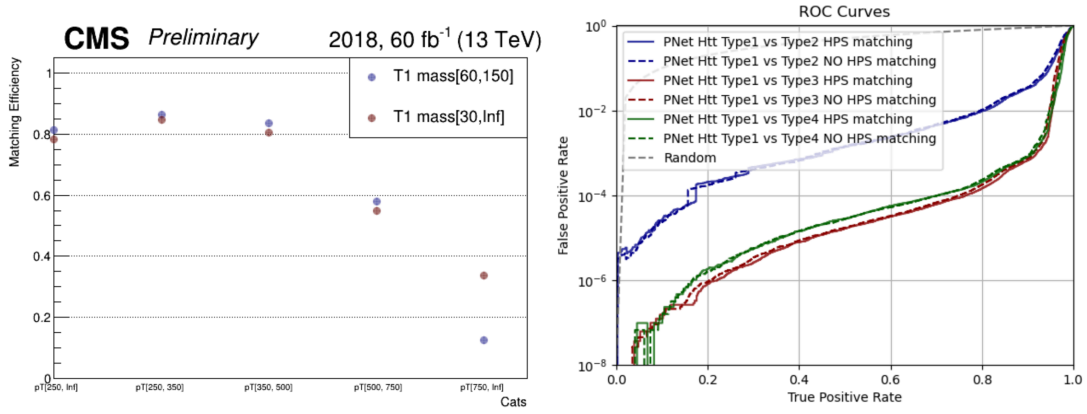

Figure 4.4 The HPS matching efficiency of the type 1 AK8 jets in different p_T ranges. The purple dots are the jets within the Higgs mass window, the red dots are all the jets. Within all the type 1 jets, around 20% of them failed to be matched by the HPS tau reconstruction algorithm.(left) The ROC curve of the ParticleNet model divide signal jets and background jets. Different colors represent the ROC curves of type 1 jets against different backgrounds, dashed lines are the results from the jets set without HPS matching while the solid lines are with matching.(right)

sure a balanced evaluation. Currently, DEEPTAU offers solely a single tau tagger, prompting a synchronization of dual objects within AK8 jets, where both must exceed a specified threshold to qualify as X($\tau\tau$) jets. Figure 4.5 illustrates the comparative analysis. The Receiver Operating Characteristic (ROC) curves, differentiated by color, display the discriminatory capability of type 1 jets against types 2 to 4 jets for both ParticleNet and DEEPTAU taggers, utilizing an identical jet set. ParticleNet's efficacy is depicted by solid lines, whereas DEEPTAU's performance is delineated by dashed lines. The horizontal axis measures the signal jets' efficiency, and the vertical axis gauges the background jets' acceptance, positioning curves towards the lower right as indicative of superior performance. This visual comparison underscores ParticleNet's consistent outperformance over DEEPTAU in segregating type 1 from other background jets. Table 4.1 further clarifies these findings, detailing background survival rates at signal acceptance benchmarks of 80%, 50%, and 20%. ParticleNet exhibits enhanced effectiveness, particularly against types 3 and 4, with certain rejection rates surpassing those of DEEPTAU by one to three orders of magnitude. Regarding type 2 jets, which inherently contain a genuine tau, DEEPTAU's tagging efficiency is naturally higher. However, ParticleNet's AK8 jet tagger, not specifically trained for this scenario, faces challenges. Moreover, type 2 jets exert minimal impact on the overall background due to their scarce prevalence.

Conclusively, employing the cutting-edge machine learning tagger, ParticleNet, is anticipated to significantly enhance the search for the HH process in the $b\bar{b}\tau^+\tau^-$ final state within

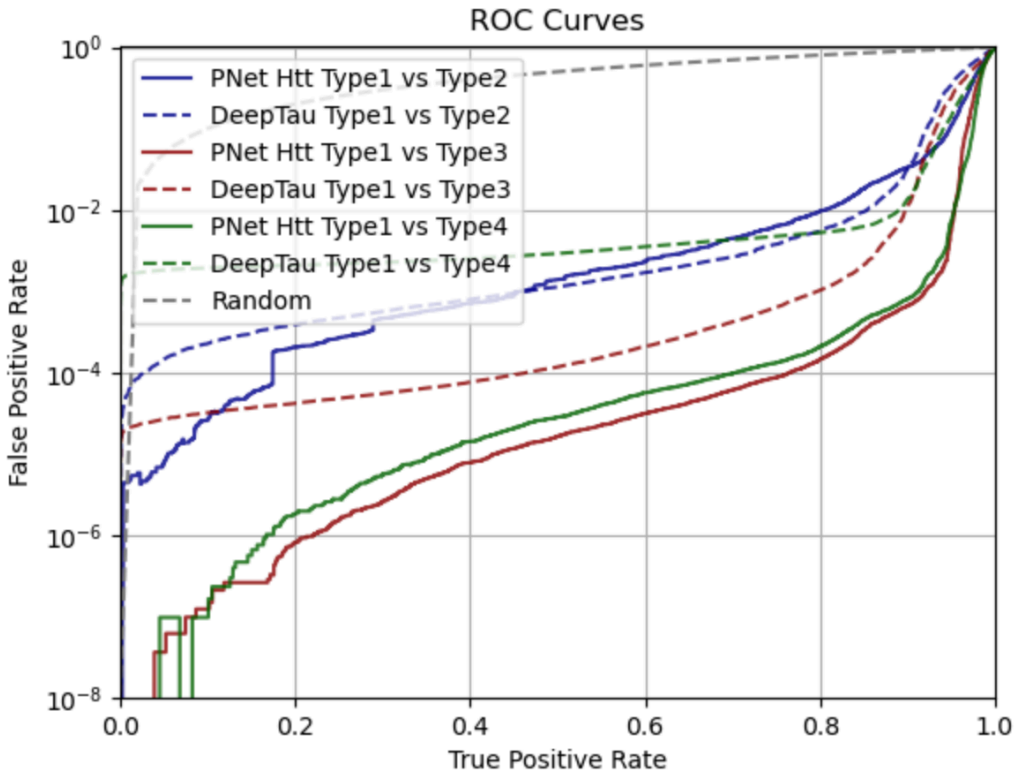

Figure 4.5 The ROC curve comparing the performance of ParticleNet and DEEPTAU tagger in the same jets set. The solid lines represent the PNet performance while the dashed lines are DEEPTAU. The horizental axis equal to the efficiency of the accepting of the signal jets and the vertical axis represent the acceptance of the background jets. So the curves at the right bottom side indicating a better performance.

Table 4.1 The comparison between ParticleNet and DEEPTAU of the background acceptance rate($\times 10^{-3}$)under the same signal acceptance. Smaller the number, better the backgrounds rejection performance.

DEEPTAU	**T1 vs. T2**	**T1 vs. T3**	**T1 vs. T4**
80%	5.45	1.02	5.26
50%	1.13	1.17×10^{-1}	2.91
20%	3.89	4.20×10^{-2}	2.09
ParticleNet	**T1 vs. T2**	**T1 vs. T3**	**T1 vs. T4**
80%	9.65	1.46×10^{-1}	2.11×10^{-1}
50%	1.39	1.65×10^{-2}	2.84×10^{-2}
20%	2.07×10^{-1}	8.09×10^{-4}	1.82×10^{-3}

a boosted topology. This approach is expected to reintroduce at least 20% more statistics into the analysis pool without compromising the signal extraction capability. Moreover, ParticleNet demonstrates formidable background suppression efficiency, particularly against heavy flavor and light jets, in comparison to the currently utilized DEEPTAU tagger. The deployment of a meticulously optimized and calibrated tagger like ParticleNet promises substantial improvements in physics performance.

4.2 The HH decay to $b\bar{b}\mu^+\mu^-$ final states study on HL-LHC

In the previous section about the $b\bar{b}\tau^+\tau^-$ final state, we discussed about how the ML algorithm adapted in the object tagging level can potentially boosted our physics performance. In this section, we discuss about another decay mode to see how the algorithms adapted in the event level can effect the final result.

To date, investigations into Higgs boson pair (HH) production have predominantly focused on decays to bosons and third-generation fermions, leveraging their substantial branching ratios. Conversely, decays to second-generation fermions, such as $HH \rightarrow bb\mu^+\mu^-$, remain underexplored despite their rarity, owing to the exceptional dimuon invariant mass ($m_{\mu\mu}$) resolution of 1-2 GeV at the LHC, mirroring the precision achieved with $m_{\gamma\gamma}$ [94]. CMS has substantiated evidence of $H \rightarrow \mu\mu$ [94], with ATLAS reporting significant findings in the same decay channel [95], rendering this avenue experimentally viable.

This study delves into the $HH \rightarrow bb\mu^+\mu^-$ channel, scrutinizing both the gluon-gluon fusion (ggF) and vector boson fusion (VBF) production mechanisms, with particular attention to the Higgs self-coupling (κ_λ) and the HHVV coupling (κ_{2V}). The analysis adheres to the precedent set by recent ATLAS and CMS research, fixing other couplings like κ_V and κ_t, pivotal to the primary HH diagrams, to their Standard Model (SM) values. Discussions on κ_V and κ_t, typically grounded in single Higgs phenomena, fall beyond this paper's ambit. Both cut-based and boosted decision tree (BDT) methodologies were employed to refine event selection strategies. The evaluation hinges on kinematic distributions, specifically $m_{\mu\mu}$ and the dijet invariant mass (m_{bb}), contrasting with existing studies such as Ref. [96], which contemplated $HH \rightarrow bb\mu^+\mu^-$ through a cut-based approach for SM ggF HH production, and Ref. [97], which applied a BDT analysis for $HH \rightarrow bb\mu^+\mu^-$ in the context of the high-energy LHC.

In our simulated event-based analysis, gluon-gluon fusion (ggF) HH processes are produced at next-to-leading order (NLO) in QCD using `POWHEG-BOX-V2` [98, 99], whereas vector boson fusion (VBF) HH processes are generated at leading order (LO) in QCD with `MG5_aMC@NLO2.6.5`.

We created a total of seven ggF HH Monte Carlo (MC) samples with varied κ_λ values of -5, 0, 1, 2.4, 5, 10, and 20, alongside seven VBF HH MC samples featuring different κ_{VV} values of -10, -5, 0, 1, 2, 5, and 10. The selection of other coupling values for subsequent analysis relies on merging these generated samples, as the differential cross-section undergoes modification by a second-order polynomial in κ_λ and κ_{VV}, aligning with leading-order electroweak precision. This methodology of blending samples across diverse coupling scenarios adheres to practices outlined in Ref. [79, 100].

In our analytical approach, events are classified into four distinct categories based on their originating processes and kinematic characteristics: ggF SM, ggF BSM, VBF SM, and VBF BSM. The differentiation between ggF and VBF processes hinges on the kinematic profile of the two VBF jets, identified by selecting the jet pair with the highest dijet mass, m_{jj}^{VBF}. This selection criterion and the contrasting kinematics of the jet pair are depicted in Figure 4.6, upper panel. Within both ggF and VBF categories, events are further divided into SM and BSM groups based on variations in the critical kinematic parameter, m_{HH}. For enhanced accuracy, we utilize a corrected version of this parameter, detailed in Equation 4.1:

$$m_{\mathrm{HH}^{\mathrm{corr}}} = m_{\mathrm{HH}} - (m_{\mu\mu} - 125) - (m_{bb} - 125) \tag{4.1}$$

The corrected di-Higgs mass distribution, $m_{\mathrm{HH}}^{\mathrm{corr}}$, is depicted in Figure 4.6, with the lower panel distinctly showcasing the categorization: the left segment for the ggF HH processes and the right for the VBF HH processes. This parameter demonstrates sensitivity to variations in coupling, leading to the higher energy side representing the SM domain of the ggF category, while the lower end signifies the SM domain of the VBF category. The demarcations for these regions are detailed in Table 4.2.

Table 4.2 Summary of the event categorization[101].

Category	m_{jj}^{VBF} (GeV)	$m_{\mathrm{HH}}^{\mathrm{corr}}$ (GeV)
ggF SM	<880	>400
ggF BSM	<880	<400
VBF SM	>880	<680
VBF BSM	>880	>680

A cut-based analysis has been conducted, meticulously examining each parameter involved in distinguishing signal events from background noise. Synchronized cuts, applied across multiple dimensions, were optimized to enhance sensitivity to the utmost degree. The variables selected for background filtration are comprehensively listed in Table 4.3.

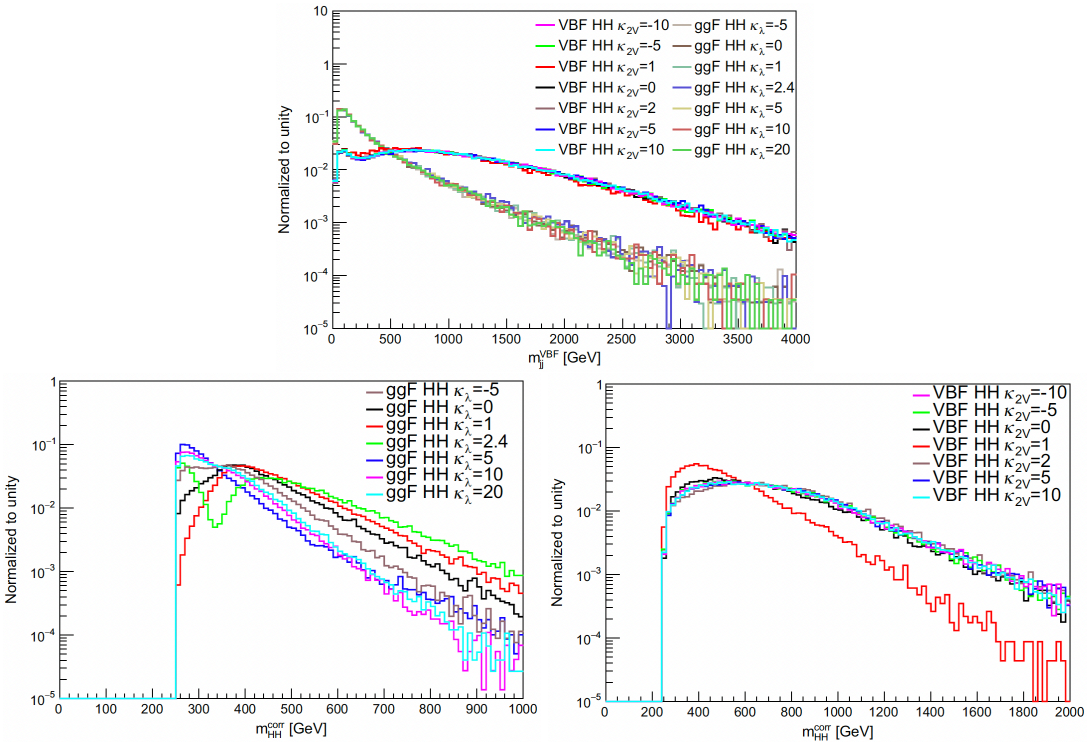

Figure 4.6 Kinematic distributions utilized for categorization in the HH to $b\bar{b}\mu^{+}\mu^{-}$ analysis are depicted. Top: m_{jj}^{VBF} is utilized to distinguish between the ggF and VBF enriched categories. Bottom: $m_{\mathrm{HH}}^{\mathrm{corr}}$ is employed to differentiate between the SM and BSM regions, with the left side representing the ggF process and the right side depicting the VBF process. [101]

Table 4.3 Summary of the optimized cuts for background suppression and the corresponding efficiencies ϵ in all the four categories. The efficiencies are calculated with the number of events passing the full set of cuts over the number of events that enter the category. For the signal efficiencies, only the relevant signals in the corresponding categories are listed.[101]

Category	Variable cut	ϵ_{Signal}	$\epsilon_{\text{DY+tt}}$
ggF SM	$\lvert\Delta\eta_{\text{HH}}\rvert < 1.9$ $p_T^{bb}/m_{bb} > 1.1$ $p_T^{\mu\mu}/m_{\mu\mu} > 1.1$ $p_T^{bb}/m_{\text{HH}} > 0.3$ $H_T > 320$ GeV	53% ($\kappa_\lambda = 1$)	11%
ggF BSM	$\lvert\Delta\eta_{\mu b}^{\text{max}}\rvert < 2.3$ $\lvert\Delta\eta_{bb}\rvert < 1.6$ $E_T^{\text{miss}} < 40$ GeV	55% ($\kappa_\lambda = 5$)	13%
VBF SM	$m_{\text{HH}}^{\text{corr}} > 370$ GeV $\lvert\Delta\eta_{\text{HH}}\rvert < 1.5$ $\lvert\Delta\eta_{bb}\rvert < 1.7$ $\lvert\Delta\eta_{\mu b}\rvert > 0.7$	39% ($\kappa_{2V} = 1$)	3%
VBF BSM	$C_{\mu\mu} > 0.8$	69% ($\kappa_{2V} = 10$)	15%

The variables selected for analysis derive from fundamental kinematics, with their respective thresholds finely tuned to maximize overall sensitivities. Notably, the variable $C_{\mu\mu}$, as defined in Eq. 4.2 and referenced from [102], was included. Signal events typically exhibit a greater η separation between the two VBF jets, leading to values of $C_{\mu\mu}$ closer to 1 compared to those of background events.

$$C_{\mu\mu} = \exp[-\frac{4}{(\eta_1^{\text{VBF}} - \eta_1^{\text{VBF}})^2} \times (\eta^{\mu\mu} - \frac{\eta_1^{\text{VBF}} + \eta_1^{\text{VBF}}}{2})^2] \tag{4.2}$$

In the boosted scenario, where the two b quarks are indistinguishable as separate small-R jets, merged jets are instead reconstructed with R = 0.8. Consequently, the final state is characterized by a large-R jet accompanied by two muons. Nonetheless, this region exhibits limited statistical significance, ultimately rendering its contribution to the overall analysis, which primarily relies on resolved b quarks, as minimal.

In the ggF SM and BSM categories, the availability of sufficient statistics permits the use of machine learning algorithms to enhance sensitivity further. The BDT algorithm, utilizing the `XGBoost` package [103], is selected for this purpose. This approach involves training a substantial number of shallow decision trees to achieve robust discriminatory capabilities through the collective strength of the tree ensemble. The training configuration comprises 2,500 trees, with a tree depth set to 3 and a learning rate of 0.08 for the ggF SM category and 0.1 for the

BSM category. Limiting the tree depth to 3 is a strategic choice to prevent overfitting. The MC samples are divided into 64% for training, 16% for validation, and 20% for application, equating to event counts of 101,000 (335,000) for training, 25,000 (84,000) for testing, and 32,000 (104,000) for application within the ggF SM (BSM) categories. The signal to background ratio, including DY+Jets and $t\bar{t}$ events, is adjusted to 40:60:1 (4:7:1) for the ggF SM (BSM) categories, respectively, reflecting the lesser significance of $t\bar{t}$ in the ggF SM category. The variables selected for model training are detailed in Table 4.4, with training processes tailored separately for the ggF SM and BSM categories. For the ggF SM category, the signal sample produced with $\kappa_\lambda = 1$ is employed in the training, whereas signal samples with κ_λ values of 5, 10, and 20 are used for the BSM category training. Both DY+Jets and $t\bar{t}$ backgrounds are incorporated in the training across both categories.

Table 4.4 Summary of input variables for the BDT training in the two ggF categories. Besides the variables that are already explained in the texts, $|\Delta\eta_{\mu b}^{\text{max}}|$ is the maximal $|\Delta\eta|$ between muons and bjets, while $|\Delta\eta_{\mu b}^{\text{other}}|$ is for the other muon and bjet. $|\Delta R_{\mu b}^{\text{min}}|$ and $|\Delta R_{\mu b}^{\text{other}}|$ are defined accordingly. [101]

Input variable	ggF SM	ggF BSM
$p_T^{\mu 1}$, $p_T^{\mu 2}$, p_T^{b1}, p_T^{b2}	✓	✓
$E_{\mu 1}$, $E_{\mu 2}$, E_{b1}, E_{b2}	✓	
$\eta^{\mu 1}$, $\eta^{\mu 2}$	✓	
η^{b1}, η^{b2}	✓	✓
η_{j1}^{VBF}		✓
$E_{\mu\mu}$, E_{bb}, $\eta_{\mu\mu}$, η_{bb}, $\cos\theta_{\mu\mu}$, $\cos\theta_{bb}$	✓	
$p_T^{\mu\mu}$, p_T^{bb}, $m_{\mu\mu}$, m_{bb}	✓	✓
m_{HH}^{corr}, m_{HH}	✓	
p_T^{b1}/m_{bb}, p_T^{b2}/m_{bb}, p_T^{bb}/m_{bb}, $p_T^{\mu 1}/m_{\mu\mu}$, $p_T^{\mu 2}/m_{\mu\mu}$	✓	
p_T^{bb}/m_{bb}, p_T^{bb}/m_{HH}, $p_T^{\mu\mu}/m_{\mu\mu}$, $p_T^{\mu\mu}/m_{HH}$	✓	✓
H_T, p_T^{HH}, $p_T^{\mu\mu}/m_{bb}$	✓	✓
E_T^{miss}, η^{miss}	✓	✓
$\lvert\Delta\eta_{HH}\rvert$, $\lvert\Delta\eta_{\mu b}^{\text{max}}\rvert$, $\lvert\Delta\eta_{\mu b}^{\text{other}}\rvert$, $\lvert\Delta\eta_{\mu b}\rvert$	✓	✓
$\lvert\Delta\eta_{bb}\rvert$, $\lvert\Delta\eta_{\mu\mu}\rvert$	✓	✓
$\lvert\Delta R_{HH}\rvert$, $\lvert\Delta R_{\mu b}\rvert$, $\lvert\Delta R_{bb}\rvert$, $\lvert\Delta R_{\mu\mu}\rvert$	✓	✓
$\lvert\Delta R_{\mu b}^{\text{min}}\rvert$, $\lvert\Delta R_{\mu b}^{\text{other}}\rvert$, $\lvert\Delta R_{jj}^{VBF}\rvert$	✓	
$\lvert\lvert\Delta\phi_{HH}\rvert\rvert$, $\lvert\Delta\phi_{\mu b}\rvert$, $\lvert\Delta\phi_{bb}\rvert$, $\lvert\Delta\phi_{jj}^{VBF}\rvert$	✓	✓
$\lvert\Delta\phi_{j\mu\mu}\rvert$	✓	

To enhance signal purity, a threshold on the BDT score is established, aiming to match the signal efficiency observed in the cut-based analysis, approximately 50%, as detailed in Table 4.3. Setting the threshold at this level significantly reduces background efficiency to 0.85% and 0.94% for the ggF SM and BSM categories, respectively—representing a tenfold

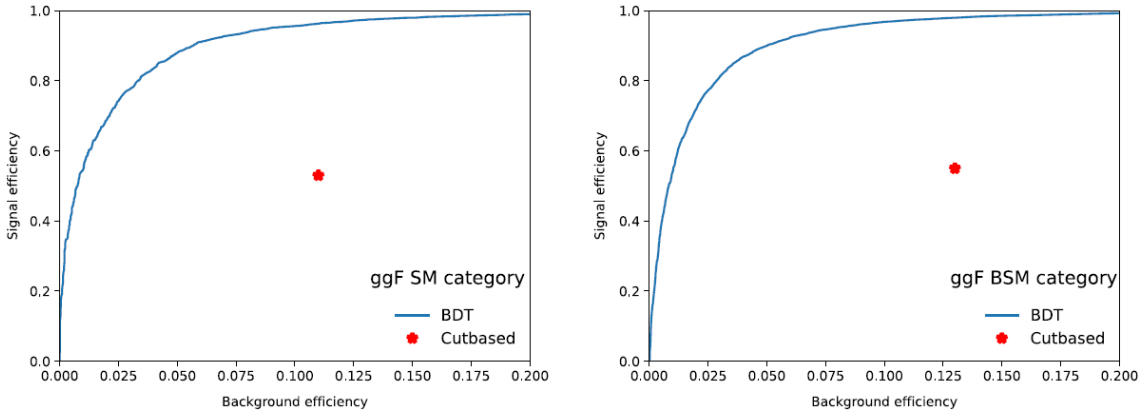

Figure 4.7 The ROC curve in the training of the ggF SM and BSM categories. The red dots present the performance of the cut-based approach. [101]

decrease compared to the efficiency rates yielded by the cut-based method, also documented in Table 4.3. The efficacy of the BDT approach is further illustrated in the ROC curves, displayed in Figs. 4.7(left) and **??**(right), with the cut-based analysis outcomes marked by red stars for comparison. Events scoring above this BDT threshold are subsequently incorporated into the final analyses.

Table 4.5 The upper limits at 95% CL of the ggF and VBF HH cross section in the cut-based and BDT analyses. [101]

Analysis type	300 fb^{-1}	450 fb^{-1}	3000 fb^{-1}
ggF HH ($\sigma/\sigma_{\mathrm{SM}}$)			
Cut based	152^{+87}_{-46}	123^{+70}_{-37}	$47^{+26.1}_{-14.1}$
BDT	$96^{+56}_{-29.8}$	$77^{+45}_{-23.9}$	$28^{+16.3}_{-8.8}$
ggF + VBF HH ($\sigma/\sigma_{\mathrm{SM(ggF+VBF)}}$)			
Cut based	152^{+86}_{-46}	122^{+70}_{-37}	$46^{+26.1}_{-13.9}$
BDT	$96^{+56}_{-29.7}$	$77^{+45}_{-23.9}$	$28^{+16.2}_{-8.8}$
VBF HH ($\sigma/\sigma_{\mathrm{SM}}$)			
Cut based	3195^{+1440}_{-960}	2555^{+1130}_{-760}	928^{+380}_{-265}

With an integrated luminosity of 3000 fb^{-1}, the search for HH decay into $b\bar{b}\mu^{+}\mu^{-}$ does not achieve the threshold for discovery. Upper limits on the cross sections at a 95% confidence level (CL) are determined using the modified frequentist CLs method, applying the asymptotic approximation. For the SM ggF and VBF HH cross sections, their 95% CL upper limits are expressed in terms of their SM cross section values, as detailed in Table 4.5. These limits are given for integrated luminosities of 300 fb^{-1}(corresponding to LHC Run 3), 450 fb^{-1}(combining Runs 2 and 3), and 3000 fb^{-1}(encompassing all LHC and HL-LHC runs). The expected 95% CL upper limit on the ggF HH cross section is calculated to be 47 (28) times its

Table 4.6 The 95% CL constraints on κ_λ and κ_{VV} in the cut-based and BDT analyses. [101]

Analysis type	300 fb^{-1}	450 fb^{-1}	3000 fb^{-1}
	κ_λ constraints		
Cut based	$(-26.9, 32.2)$	$(-24.0, 29.3)$	$(-13.8, 19.1)$
BDT	$(-20.7, 26.2)$	$(-18.3, 23.8)$	$(-10.0, 15.5)$
	κ_{VV} constraints		
Cut based	$(-7.6, 9.8)$	$(-6.6, 8.8)$	$(-3.4, 5.5)$

SM prediction using the cut-based (BDT) analysis with the total integrated luminosity. Similarly, the expected 95% CL upper limit on the VBF HH cross section is 928 times its SM prediction using the cut-based method with the complete luminosity. Expected upper limits are also established for the combined ggF and VBF HH processes, assuming their SM cross sections. Given the relatively low VBF rate, its influence on the combined ggF and VBF HH upper limits is considered marginal. All results are extracted assuming the Higgs mass equals 125 GeV, closely matching the most precise measurement of the Higgs boson mass to date, $m_H = 125.38 \pm 0.14$ GeV [104].

Additionally, constraints on κ_λ and κ_{VV} are determined for lower integrated luminosities, specifically 300 fb^{-1} from LHC Run 3 and 450 fb^{-1} from the combined Runs 2 and 3, as summarized in Table 4.6. The 95% confidence level constraints are $-13.8 < \kappa_\lambda < 19.1$ ($-10.0 < \kappa_\lambda < 15.5$) and $-3.4 < \kappa_{VV} < 5.5$, using the cut-based (BDT) approach, respectively.

Recent experimental outcomes for $HH \rightarrow b\bar{b}\tau^+\tau^-$, leading in HH sensitivity, are extended to projections at the HL-LHC with an integrated luminosity of 3000 fb^{-1} and $\sqrt{s} = 14$ TeV [105]. For an equitable comparison, only projections incorporating statistical uncertainties are discussed. The anticipated 95% confidence level constraints on κ_λ are $1.2 < \kappa_\lambda < 4.2$ for $HH \rightarrow b\bar{b}\gamma\gamma$ and $2.4 < \kappa_\lambda < 4.5$ for $HH \rightarrow b\bar{b}\tau^+\tau^-$. The expected 95% CL upper limits on the cross section are 0.86 and 0.49 times the SM predictions for $HH \rightarrow b\bar{b}\gamma\gamma$ and $HH \rightarrow b\bar{b}\tau^+\tau^-$, respectively.

In summary, while the $HH \rightarrow b\bar{b}\mu^+\mu^-$ decay channel may not independently lead to observation up to the HL-LHC with the methodologies described herein, it holds potential for a significant contribution to the combined HH search efforts and exhibits sensitivity to BSM enhancements due to its low occurrence rate and the precise dimuon mass resolution.

From the forward-looking study on HH searches utilizing both existing and anticipated CMS experimental data for HH decays into $b\bar{b}\tau^+\tau^-$ and $b\bar{b}\mu^+\mu^-$ final states, the advantages of incorporating machine learning algorithms are evident. These algorithms not only facilitate the tagging of basic physical objects, thereby amplifying our analysis capabilities, but also

significantly improve categorization and signal extraction processes. The integration of such cutting-edge tools can streamline analytical procedures and bolster final outcomes. Concurrently, the ”black box” nature of machine learning, alongside the selection and refinement of machine learning models, will continue to pose significant challenges in future physics research endeavors.

Chapter 5 Upgrading CMS: Muon and Timing Detectors for HL-LHC

Other than the new approaches with cautious adoption of machine learning techniques and the dedicated design of analysis algorithms, there is a more straightforward way to achieve additional opportunities in physics or enhance the current analysis performance. This approach involves upgrading the experimental instruments: increasing the experimental data statistics, enhancing detection performance, and adding measurement dimensions.

The High-Luminosity LHC (HL-LHC) is anticipated to commence operations by the end of 2027. Engineered to achieve a peak instantaneous luminosity of $5 \times 10^{34} \mathrm{cm}^{-2}\mathrm{s}^{-1}$, it will facilitate access to a total integrated luminosity of 3000 fb^{-1}, thereby augmenting the discovery potential of the LHC. The HL-LHC promises to enable more precise measurements of Standard Model (SM) properties and enhance sensitivity to rare processes, potentially revealing the existence of previously unknown particles and Beyond Standard Model (BSM) scenarios.

The increased luminosities anticipated at the HL-LHC will lead to significantly higher pile-up rates, with approximately $\mathcal{O}(200)$ events per bunch crossing, and unprecedented radiation levels, with fluences reaching up to $10^{16} \mathrm{n_{eq}}/\mathrm{cm}^2$ and doses of approximately 2 MGy. Consequently, several technical challenges will arise for the operation of the detectors and the overall infrastructure. For instance, the LHC tunnel will necessitate the deployment of the most advanced superconducting magnets, vacuum pipes, cryogenic systems, and superconducting radio-frequency cavities.

The CMS Collaboration, along with other LHC experiments, is embarking on a series of significant upgrades to the sub-detectors. These upgrades are anticipated to be commissioned during the second and third long shutdowns, aiming to uphold the current physics performance in the challenging environment of the HL-LHC.

Section 5.1 provides a concise overview of the CMS upgrade plans, while Section 5.2 and 5.3 delves into the specifics of the **Endcap Muon GEM detector (ME)** and **Barrel Timing Layer (BTL) of the MIP Timing Detector (MTD)** respectively.

5.1 The CMS Phase-II upgrade

The HL-LHC project imposes greater demands on the detectors of the experiments, prompting the upgrading projects of the CMS [106, 107].

There are two main aspects that determine the content of this upgrading program. Firstly, from a technical perspective, the upgrade of the existing detectors as well as the newly proposed detector systems should be carefully designed to tolerate the high radiation doses resulting from the HL-LHC collisions. Secondly, from a physics standpoint, the higher integrated luminosity is intended for direct research into rare processes, potential hints of BSM physics, and higher precision measurements. However, the higher instantaneous luminosity will lead to increased pile-up, which may degrade the performance of data analysis.

As a brief summary, these two aspects directly pose two challenges for the new CMS detectors:

- **The unprecedented radiation doses:**
  Necessitate a complete replacement of the tracker and the endcap calorimeter systems, as well as the adoption of new technologies for the electrical boards (EB). Additionally, substantial improvements in the electronics systems of the barrel calorimeters and the muon detectors are required.
- **The increase in the pileup rate:**
  Mandates highly granular readouts wherever feasible within the detector, the incorporation of precision timing detectors, and the development of novel approaches to pileup mitigation.

Fig. 5.1 illustrates a cross section of the CMS detector, along with the various upgrades planned for the HL-LHC. Some detectors will undergo complete replacement, while others indicate new detector systems not included in the current CMS design that will be installed. The blue boxes represent the sub-detectors involved in the work of this thesis.

The tracking system will undergo complete replacement to increase the granularity of the detector, thereby enhancing reconstruction performance, while simultaneously reducing the overall material budget. The inner tracking system will consist of pixel detectors of smaller size compared to the current ones, while the outer tracking stations will incorporate strips and macro-pixel sensors, extending the coverage up to $|\eta| = 3.8$ [108]. This design choice will improve longitudinal and transverse resolutions, and it will lead to lower fake rates, thereby enabling the reconstruction of L1 trigger tracks up to $|\eta| = 2.4$.

The endcap calorimeters will be replaced with the HGCAL, a high granularity sampling

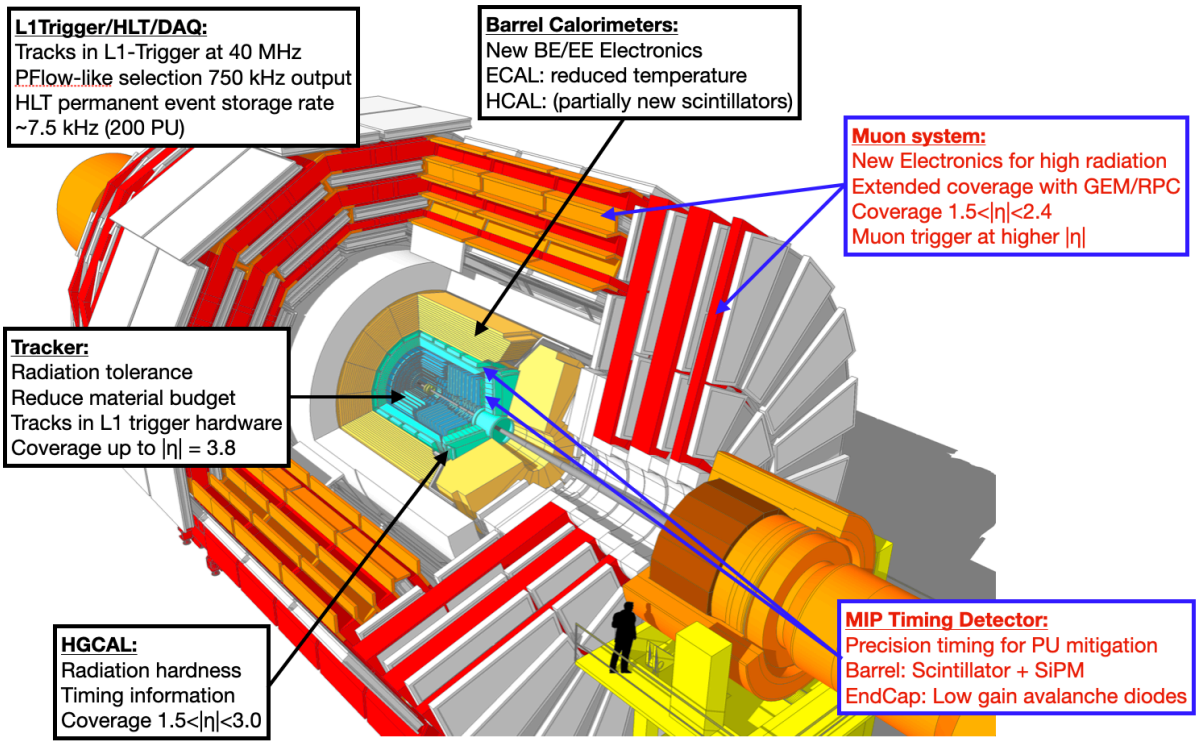

Figure 5.1 Cross section of the CMS detector with the indicated upgrades planned for the HL-LHC. Blue boxes represent the sub-detectors that are involved in the work of this thesis.

calorimeter that will provide, thanks to its features, enhanced shower separation and particle identification, as well as additional precise timing information [109].

With a similar goal of increasing the overall granularity and providing additional timing measurements, an upgrade of the ECAL and HCAL barrel electronic readout is foreseen [110].

The complex of the current **muon detection system** featuring **Drift Tubes (DTs), Resistive Plate Chambers (RPCs), and Cathode Strip Chambers (CSCs)**, will be increased with the installation of Gas Electron Multiplier(GEM) chambers and a new generation of RPCs [111], which will also extend the coverage up to $|\eta| = 2.8$ and $|\eta| = 2.4$, respectively.

MTD [112] will be placed in front of the barrel and endcap calorimeters to increase the available timing information on physics objects.

The works represented in this thesis will focus on the GEM detectors in the endcap muon system and the barrel MTD.

5.2 The endcap Muon detector upgrade

Originally designed for high hermeticity and redundancy, the CMS muon sub-detector incorporates three distinct detection technologies. Drift tubes (DT) in the barrel enable precision measurements and Level 1 (L1) triggering, effective up to an acceptance of $|\eta| < 1.2$. In contrast, the endcaps employ cathode strip chambers (CSC) for coverage in the $1.0 < |\eta| < 2.4$ range. Furthermore, resistive plate chambers (RPC) offer additional trigger capabilities and coarse localization within both the barrel and endcap areas, although their deployment was limited to $|\eta| \leq 1.6$, stemming from performance concerns under high background particle flux. [113]

Investigations into muon triggers for the CMS Phase 1 Upgrade, as detailed in Ref. [114], indicate that post-LS2, securing an acceptable L1 trigger rate for muons with pT below 25 GeV necessitates notable efficiency sacrifices in the endcap areas, which account for more than half of the total CMS muon coverage. To preserve muon trigger and reconstruction performance amidst high background levels, the CMS experiment's Muon Spectrometer's forward section will undergo enhancements, incorporating Gas Electron Multipliers (GEM) and the advanced Resistive Plate Chambers(iRPC) technology [111].

The CMS GEM upgrade plan involves installing three detector stations, namely GE1/1, GE2/1, and ME0 (as illustrated in Fig. 5.2), in the endcap region. This addition aims to supplement the current CSCs located in the high pseudorapidity region and broaden the geometric acceptance of the muon system to encompass the very forward region. During the Long Shutdown 2 (LS2, 2019–2021), the initial GEM station (GE1/1) was installed, followed by the installation of a second station (GE2/1) in the winters of 2023–24 and 2024–25, and a novel 6-layer station (ME0) is planned for the third Long Shutdown (LS3, 2026–2028). The GE1/1 installation marks a precursor to the Phase-2 upgrades, enhancing the p_T threshold efficiency by integrating GEM with CSC readings in the forward muon system, doubling the expected LHC luminosity ($\mathcal{L} = 2 \times 10^{34} \text{cm}^{-2} s^{-1}$, 50 PU). Following Run-3's outset in 2022, which garnered nearly 40 fb^{-1}, GE1/1's commissioning is on the verge of completion [115], with most chambers maintaining over 95% efficiency, paving the way for the 2023 CSC-GEM trigger integration demonstration. Insights from GE1/1's deployment have propelled enhancements in both detector and electronic designs for GE2/1 and ME0 Phase 2 detectors.

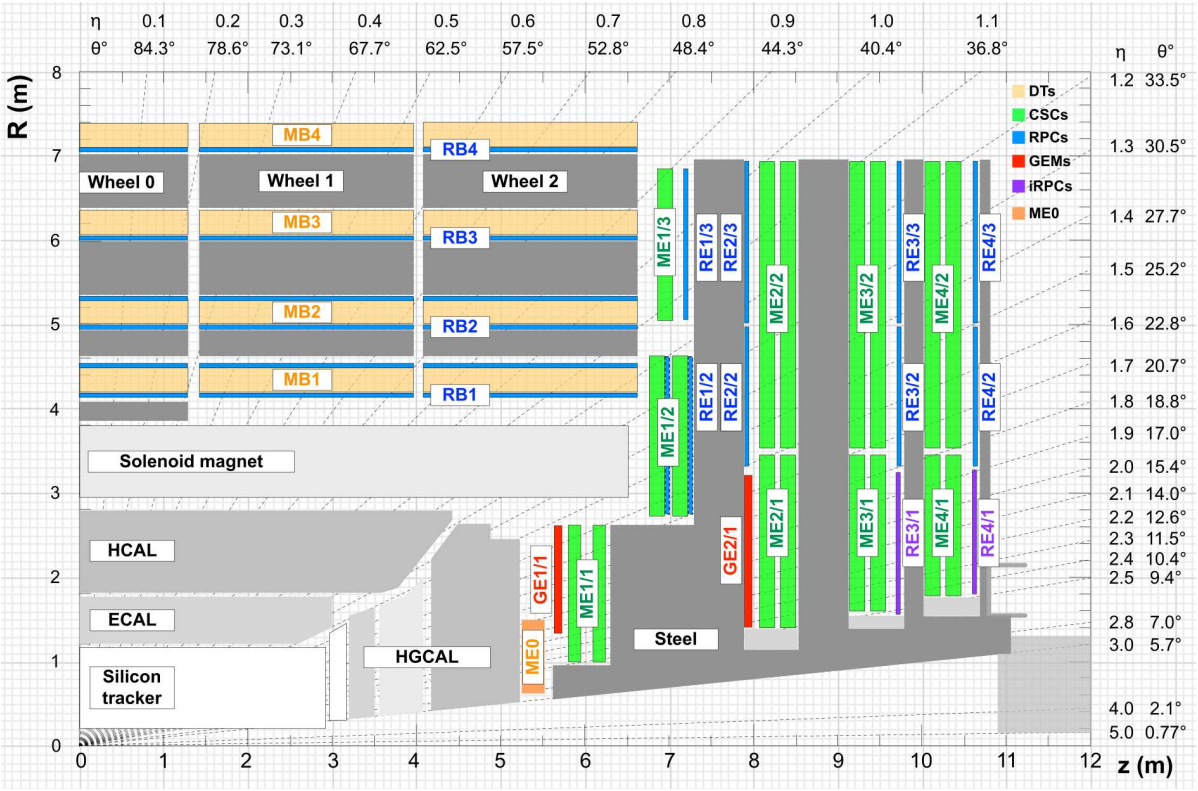

Figure 5.2 Quadrant of a section of the CMS muon spectrometer, showing the Phase-1 muon stations and the new stations after the Phase-2 upgrade (in red and orange)

5.2.1 Assembly and quality control of the GEM detector

A Gas Electron Multiplier (GEM), as detailed in [116], consists of a metal-clad polymer foil with numerous microscopic holes. The material, typically 50μm thick polyimide (e.g., Kapton by DuPont or Apical by Kaneka), has a dielectric constant of 3.5 and is copper-clad on both sides to 5μm . These holes, as depicted in Fig. 5.3, are double-conical with diameters of about 70μm and 50μm for the outer and inner parts, respectively, arranged hexagonally at 140μm pitch distances.

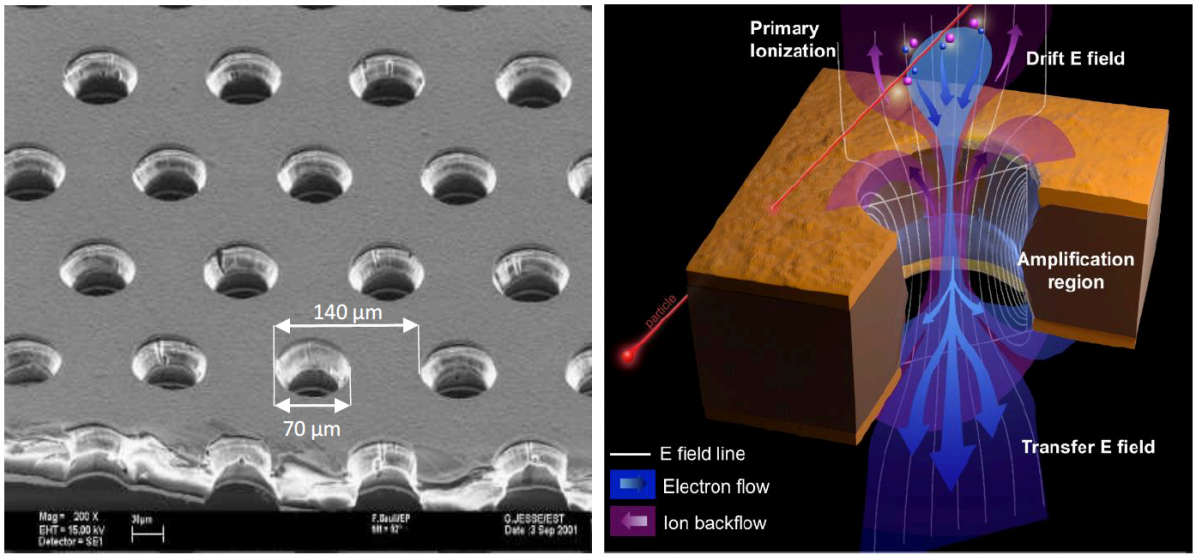

Figure 5.3 A Scanning Electron Microscope (SEM) image displays a GEM foil (left), while a schematic depiction (right) illustrates the electric field lines (white), electron flow (blue), and ion flow (purple) passing through a bi-conical GEM hole. The hole has an outer diameter of 70μm and an inner diameter of 50μm , with a pitch of 140μm .

Basic design

The trapezoidal GEM foils employed in a specific CMS triple-GEM module are essentially identical, requiring only one type of GEM foil per module. The surfaces of the GEM foils facing the readout board form a single contiguous conductor, while those facing the drift board are divided into multiple high-voltage (HV) sectors. The sectors traverse the width of the trapezoid (see Fig. 5.4). Their width decreases from the narrow end to the wide end, ensuring each strip covers approximately 100 cm^2. This segmentation restricts charge flow during a discharge to about 2 mC per foil, limiting the total discharge energy to less than 0.5 mJ. Thus, the GEM foil is safeguarded against damage from discharges, which may occur even at low rates under normal operating conditions. In the worst-case scenario, a destructive discharge

in an HV sector would permanently disable only that specific sector, rather than rendering the entire chamber unusable. To minimize the dead area resulting from the 200 micron thick separation lines between HV sectors, a left/right partition is added for the wide GE2/1 foils, reducing the total number of separation lines by half.

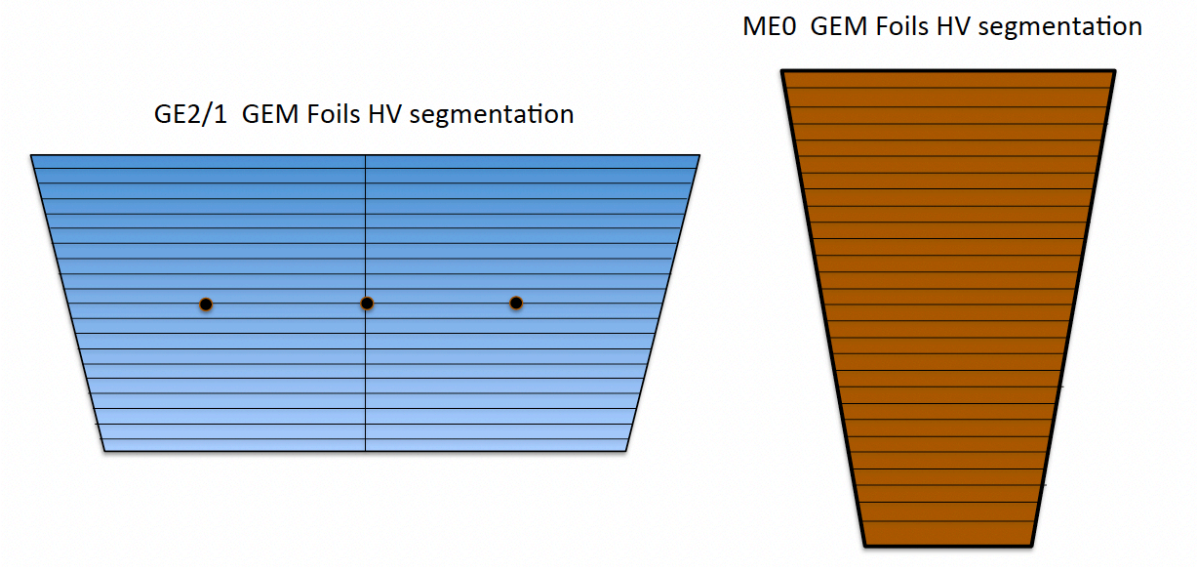

Figure 5.4 Schematic high-voltage (HV) segmentation of GE2/1 (M4 module) and ME0 GEM foils into strips on the sides facing the drift board. It is worth noting that only the largest module, M4, of GE2/1 requires division into left and right segments. Segments in modules M1-3 remain undivided.

Each HV segment is individually powered through a trace that encircles the GEM foil, originating from a unified connection point where it receives its external HV supply. This circuitry, connected to 10 MW protection resistors, ensures each segment's isolation. The foil's opposite side is energized via a singular contact point, positioned at its broader end, as illustrated in Fig. 5.5.

GEM foil production utilizes photolithography, a standard in the printed circuit sector. This process, mirroring the GE1/1 foil production approach, is detailed further in the GE1/1 TDR [117].

A triple-GEM chamber is formed by aligning three GEM foils a few millimeters apart within a counting gas environment. An electric field of approximately 80 kV/cm is generated across the foil's copper surfaces, intensifying within the GEM holes as illustrated in Fig. 5.3(right). Electrons, ionized by a passing charged particle, are drawn towards these holes. Here, the elevated electric field grants them the kinetic energy necessary for further ionization, leading to a cascade of electron multiplication. This avalanche effect results in a detectable

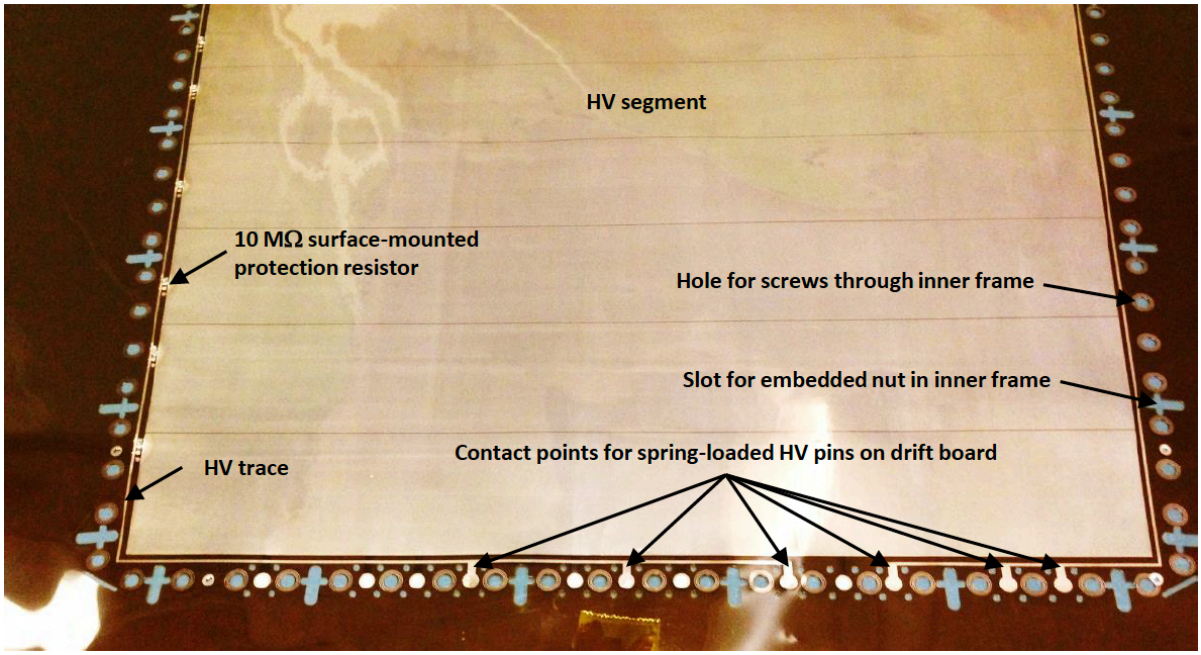

Figure 5.5 The GEM foil features traces along the active area, routing high voltage (HV) to the HV segments through 10 MW protection resistors.

signal on the readout strips. Fig. 5.6 schematically outlines the operational framework of the chamber, highlighting the drift, transfer, and induction regions in the triple-GEM setup.

In CMS triple-GEM detectors, the dimensions are as follows: a 3 mm drift region between the drift cathode and the first GEM, with electron transfer gaps of 1 mm and 2 mm between the GEM foils, and a 1 mm gap in the induction region, as illustrated in Fig. 5.6. The detectors operate on an Ar/$CO_2$70:30 gas mixture.

The triple-GEM stack foils are tensioned against stainless steel pull-outs attached to the drift and readout PCBs to ensure uniform tautness (refer to Fig. 5.7, left). The tension is applied by tightening screws that pass through the pull-outs, countered by nuts within the frame encasing the GEM stack (see Fig. 5.7, right), with a minimum torque of 7 cNm, securing the foils snugly within the gas frame.

Materials for the GE2/1 and ME0 chambers replicate those in GE1/1, having undergone rigorous testing against harmful outgassing as detailed in [117]. This precludes the necessity for additional material validation. The trio of GEM foils is encased along its periphery by quadruple strata of slender internal framing, as depicted in Fig. 5.8, utilizing halogen-free glass epoxy (ISOLA DE156), segmented into eight discrete parts for each layer. The layer thicknesses delineate spacings within the assembly, specifically: a 3 mm drift gap, 1 mm and 2 mm transfer gaps between sequential GEM foils, and a 1 mm induction gap, as detailed: Drift

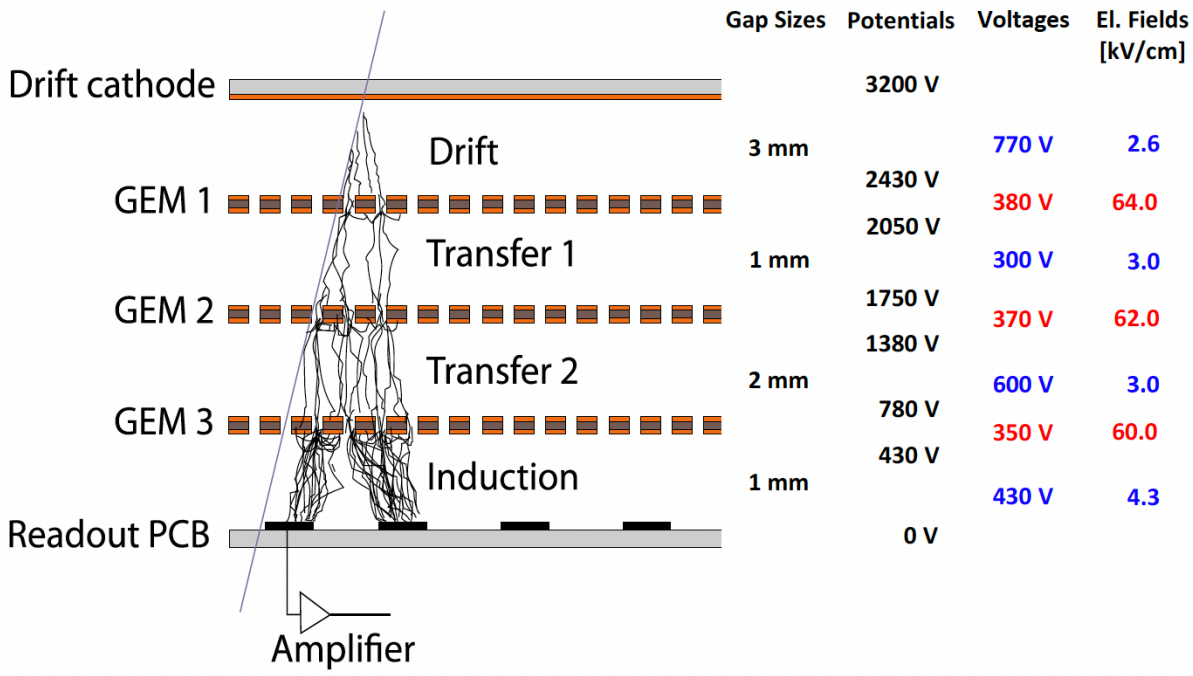

Figure 5.6 Principle of operation of a generic triple-GEM chamber and definition of drift, transfer, and signal induction gap regions within the detector [116]. The columns on the right provide the actual gap sizes in the detector, along with typical values for electric potentials on the seven electrodes and typical values for voltages and electric fields across the four gaps (blue) and the three foils (red) when the nominal potential of 3200 V in Ar/$CO_2$70:30 is applied to the drift cathode, i.e., for operation at the beginning of the efficiency plateau.

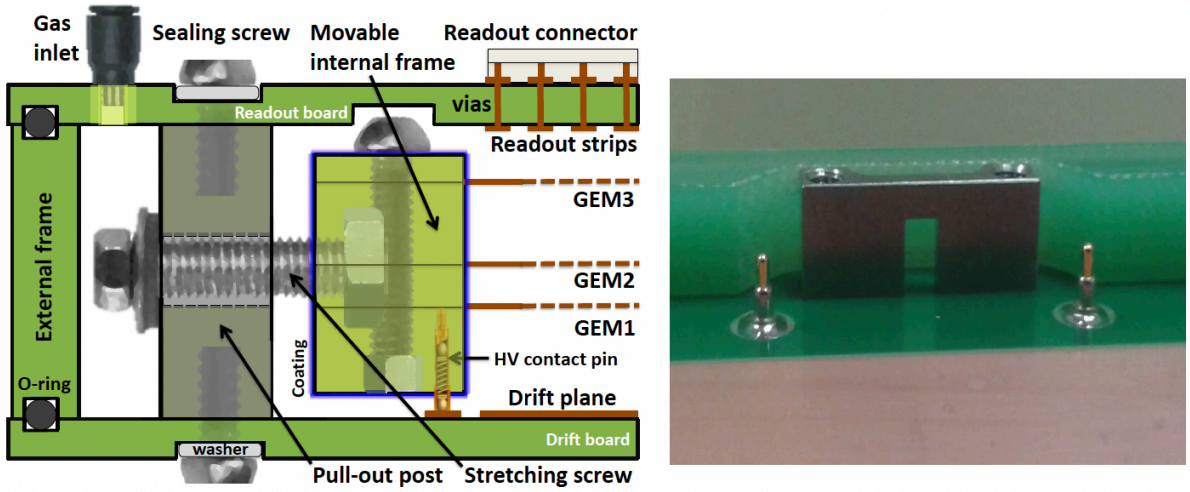

Figure 5.7 Left: Cross-section through inner and outer module frames and GEM foils illustrating how the GEM foils are positioned within a CMS triple-GEM module, enabling them to be mechanically tensioned against the pull-out posts without distorting the drift or readout boards. Right: Stainless steel pull-out posts and spring-loaded pins soldered to the drift board to establish electrical HV connections with corresponding contact pads on the GEM foils.

gap / GEM1-GEM2 transfer gap / GEM2-GEM3 transfer gap / induction gap: 3/1/2/1 mm. The stack is assembled using multiple small M2 × 6 stainless steel screws with T6 Torx heads, which penetrate all frame layers and foils approximately every centimeter. These screws are tightened against small threaded M2 brass inserts (see Fig. 5.8 right center). Employing inserts to counter the screws prevents the loosening of macroscopic and microscopic glass epoxy particulates from the frames, a phenomenon observed in earlier prototypes where screws were threaded directly into the frame material. Before assembly, frame components are treated with a coating of Nuvovern polyurethane varnish. This practice, along with other precautions, prevents the detachment and subsequent fall of glass epoxy particulates from the frame onto the GEM foils, mitigating the risk of electrical shorts within the GEM holes. The design incorporates conical screw heads with flat exteriors, which are embedded into the frame counterbores encircling the through-holes as they are tightened, as depicted in Fig. 5.8 (top right). In a similar way, the nuts are recessed into counterbores on the frames, as shown in Fig. 5.8 (center right), ensuring that both screws and nuts align seamlessly with the inner frame's top and bottom surfaces upon completing the stack assembly.

Incorporated at intervals of a few centimeters into the frames are additional square stainless steel nuts, with the orientation of their threaded holes perpendicular to both the inner frame and the surfaces of the GEM foils, as illustrated in Fig. 5.8 (bottom right). These nuts are designed to interact with M2.5 × 8 stainless steel screws featuring T8 Torx heads, which engage with small stainless steel supports, referred to as 'pull-outs', situated within the gas volume. Manually tightening these 'pull-out' screws applies tension to the GEM foils in the stack, pulling the inner frame outward toward these supports. The abundance of screws facilitates precise manual adjustment of the GEM foil tension, aiming for the most uniform tension distribution achievable. The substantial size and quantity of the square nuts play a critical role in minimizing the force exerted on the frame at each pull-out point, thereby reducing the risk of long-term localized frame deformation from stress. The 'pull-outs' themselves are securely fastened to the PCB, which acts as the drift cathode, using two stainless steel M3 × 6 screws with T10 Torx heads. These screws are further sealed with polyamide washers against the drift board to ensure integrity.

Surrounding the tensioned GEM stack and the brass 'pull-outs', a substantial outer frame crafted from a single piece of glass-epoxy provides the perimeter of the gas chamber, as illustrated in Fig. 5.8 (left). This frame features several broad indentations to accommodate the brass 'pull-outs' and receives a protective coating of Nuvovern polyurethane varnish prior to

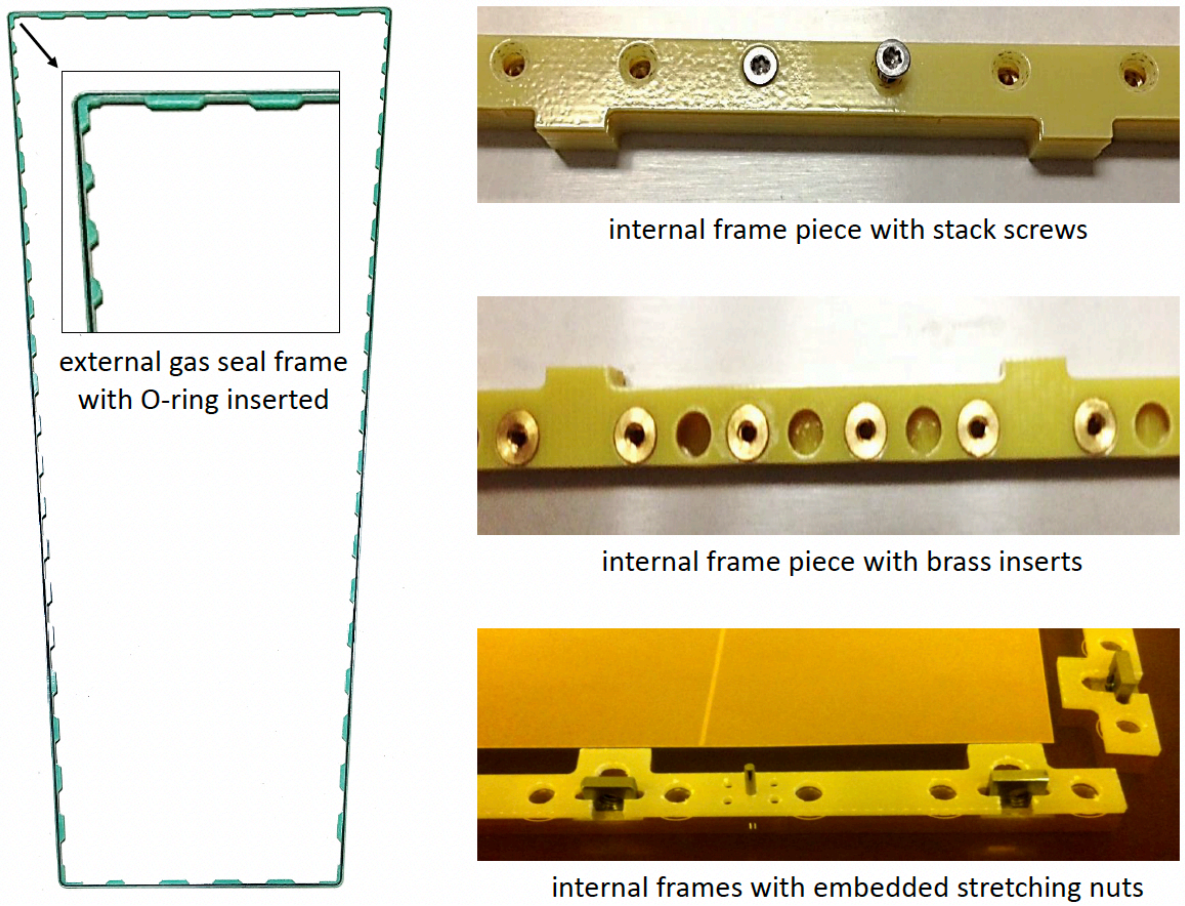

Figure 5.8 Frames utilized in the assembly of a CMS triple-GEM module. On the left, an external gas frame crafted from a single solid piece of halogen-free glass epoxy (ISOLA DE156) with an inserted O-ring. On the right, a segment of the internal frame of a GEM stack featuring stainless steel screws and counterbores on one side (top) and embedded countering brass nuts on the other (center). The shiny surface of the frame (top) results from its coating with Nuvovern polyurethane varnish, which prevents fiberglass dust accumulation. Square nuts are incorporated into the tabs on the frame (bottom) to facilitate tensioning the GEM stack against pull-outs using tensioning screws.

assembly, effectively encapsulating any particulates. To ensure a hermetic seal, a Viton O-ring is nestled into a continuous groove along both sides of the outer frame. Atop this frame, the anode readout board is positioned and secured to the stainless steel 'pull-outs' using A4 stainless steel M3 $\times$ 6/ $\times$ 10 screws, complemented by polyamide washers to seal against the readout board, mirroring the assembly technique used for the drift board screws. This arrangement clamps the outer frame firmly between the drift and readout boards, relying predominantly on friction to maintain its position, thereby creating a robust barrier against gas leakage. The design incorporates merely two slender openings at opposite corners of the readout PCB to facilitate gas flow into and out of the chamber.

Electrical connections to the GEM foils are established through spring-loaded pins depicted in Fig. 5.7, which are affixed to the drift board and press against designated pads on the GEM foils. To enable the HV pins to contact GEM foils 2 and 3, areas on GEM foils 1 and 2 are precisely removed during the assembly process. The drift electrode directly receives its power from the HV supply entering the drift board, with the required voltages supplied via individual HV lines to the drift board and then distributed to the GEM foils through the pins.

Addressing an HV short within a GEM foil necessitates removing the affected module from the CMS, disassembling the module, and substituting the faulty GEM foil. For GE2/1 and the new calorimeter endcap (ME0), this involves extensive procedures such as opening CMS or uninstalling the endcap. Consequently, the HV supply system is designed with two critical functionalities. Firstly, in the event of a short within an HV segment of a GEM foil, it must maintain the voltage across the foil while managing the current flow through a 10 MW protection resistor in the impacted HV sector, thus ensuring the chamber's operational continuity. Secondly, the system is engineered to synchronize the adjustment of voltages on either side of the GEM foils, provided by separate HV channels, with stringent monitoring and protective measures to prevent voltage spikes beyond a predefined limit (approximately 500V). This precaution is essential to avert transient overvoltages that could induce sparking and potentially ruin the GEM foils.

Efforts to ensure uniform gas circulation within the detector aim to prevent the formation of regions characterized by minimal gas movement, where hazardous gas impurities might collect. Finite-element analysis conducted on the GE1/1 model confirmed the efficacy of a straightforward gas circulation strategy, involving a single gas inlet and outlet situated at two opposite corners of the chamber [117], a method that has been extended to both GE2/1 and ME0 configurations.

Despite the distinct geometries of GE2/1 and ME0 modules, their dimensions are sufficiently similar to warrant identical assembly and quality assurance practices. These practices are in line with those developed during the mass production of GE1/1 units across various manufacturing locations.

Assembly

An overview of the mechanical structure of a single trapezoidal CMS triple-GEM module is depicted in Fig. 5.9. The primary constituents and materials of a single CMS triple-GEM module are outlined in Table 5.1. The construction and sealing of the detector are entirely mechanical. No adhesive is utilized during assembly, enabling the detector to be reopened for repairs if necessary. Moreover, this approach accelerates the assembly process of the module as there are no delays associated with the curing of adhesive.

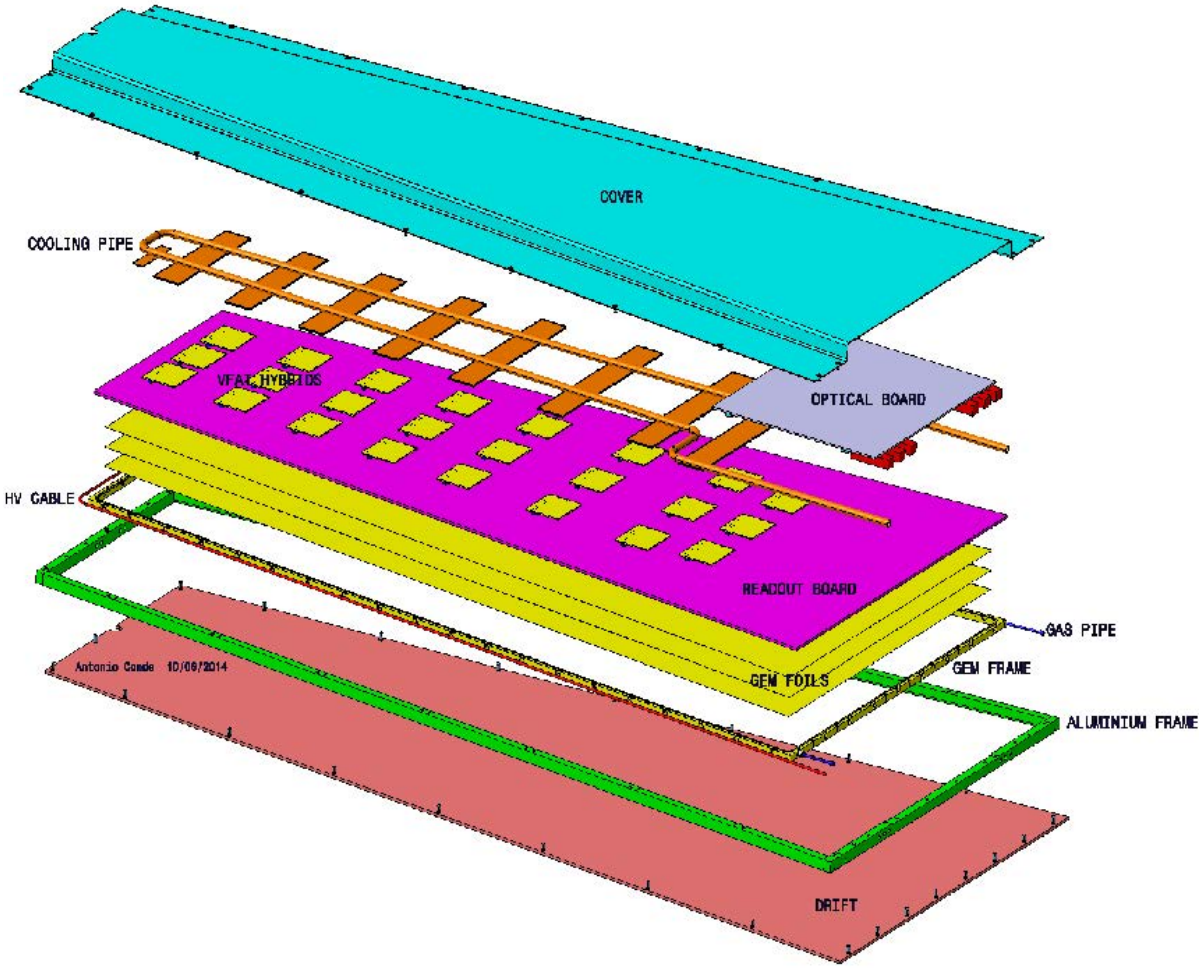

Figure 5.9 Exploded view of the mechanical design of a single CMS triple-GEM module.

Table 5.1 Summary of layer structure and materials of a single CMS triple-GEM module.

Layer	**Material**	**Thickness [mm]**
Protective cover	Al	1.0
Cooling pipe	Cu (filled with H_2O)	8 external Ø, 6 inner Ø
Cooling pads	Cu	1.0
GEB board	Cu/FR4	0.140/0.856
Readout board	Cu/FR4/Cu	0.035/3.2/0.035
Induction gap	Ar/CO_2	1.0
GEM 3	Cu/polyimide/Cu	0.005/0.050/0.005
Transfer gap 2	Ar/CO_2	2.0
GEM 2	Cu/polyimide/Cu	0.005/0.050/0.005
Transfer gap 1	Ar/CO_2	1.0
GEM 1	Cu/polyimide/Cu	0.005/0.050/0.005
Drift gap	Ar/CO_2	3.0
Drift board	Cu/FR4/Cu	0.035/3.2/0.035

The drift board is equipped with a drift cathode on its inner surface and a solid ground layer on the exterior for RF shielding. It incorporates high voltage noise filtering circuitry to connect with external power supplies, distributing seven distinct voltages to the GEM electrodes and the drift cathode.

On its external side, the readout board features high-density header connectors to link the internal radial readout strips to the external VFAT3 hybrids via vias covered by an insulating coverlay (manufactured by Krempel corporation under the name AKAFLEX KDF HT 0/25/25).

These VFAT3 hybrids are also connected to another large PCB, the GEM Electronics Board (GEB), positioned directly atop the readout PCB. The GEB facilitates the transfer of digital signals from the VFAT3 hybrids to the module's broader end for further processing and integration into the Trigger/DAQ system, as extensively discussed in the electronics and DAQ chapter. It includes openings for readout board connectors and is outfitted with copper tubes overhead for cooling the VFAT3 components.

An aluminum perimeter frame is installed around the drift board's edge, complemented by an aluminum shield featuring a slender central vent along the module's length, affixed atop this frame (refer to Fig. 5.9). This combination of frame and cover offers robust shielding for the module's electronic components and auxiliary systems.

Quality control

Within the operational framework of detector production, it is imperative that both the

GEM foils and the fully assembled GEM detectors undergo rigorous quality assessments post-manufacture and prior to their dispatch to the CERN assembly facility. The responsibility of evaluating the integrity of GEM foils and the construction of detector chambers falls upon the assembly sites. A schematic of the quality assurance protocol, exemplified by GE1/1 procedures, is depicted in Fig. 5.10 [118]. Notably, QC2 tests are mandated at both CERN and the manufacturing sites, whereas tests from QC3 through QC5 are exclusive to the manufacturing locations. QC2 at the manufacturing site entails a swift cleaning and evaluation of the GEM foils to ascertain their condition following transit from CERN. Subsequent to QC2, the assembly phase commences. Post-assembly, QC3, a gas leak examination, is conducted to ensure the gaseous environment's stability, crucial for the functioning of this MPGD. Following QC3, the detectors undergo a high voltage (HV) scrutiny under QC4 to verify the integrity of the resistance chain and the proper connectivity of the GEM foils. The final phase, QC5, involves testing for effective gain and its uniformity using an external X-ray source to evaluate the detectors' effective gain across different HV settings and to assess noise levels.

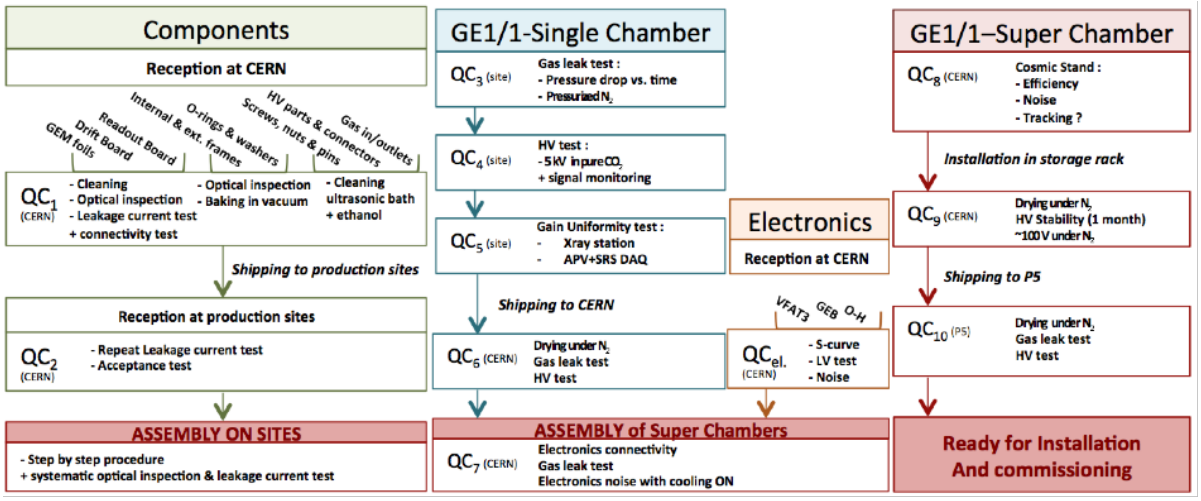

Figure 5.10 The quality control(QC) flow of the triple-GEM detectors, using GE1/1 as an example. Among which, the QC2 need to be performed at both CERN and production centers and QC3 to QC5 need to be performed at the procution centers.

`QC3: Gas leak test`

Due to the operating principle of the detector, which relies on the deposition of particle energy to excite atoms in the working gas, leading to the generation of electron-ion pairs, and as elucidated above, it is evident that the magnitude and speed of the signal are correlated with the purity and composition of the gas. Moreover, the ingress of interfering substances such as oxygen and dust from the air into the detector's gas chamber can potentially cause GEM

foils arcing or gas breakdown. These occurrences could affect the application of high voltage or the magnitude of partial pressure, subsequently influencing the effective gain and thereby impacting the quality of the detector. In summary, ensuring the gas-tightness of the detector is crucial for guaranteeing the quality of gas detectors.

Typically, a mixture of argon and carbon dioxide gas is used as the working gas medium in GEM detector experiments. However, during gas-tightness tests, pure carbon dioxide gas is employed as the testing gas. When the internal pressure exceeds atmospheric pressure by 25 mbar, the entire gas chamber is sealed. The pressure inside the chamber is continuously monitored for one hour. If the pressure decreases at a rate of less than 1 mbar/hour within one hour or longer, the detector chamber is considered to have passed the gas-tightness test. If the above requirements are not met, the detector needs to be repaired. A gas leak detector sensitive to carbon dioxide gas is used to determine the location of the gas leak. The detector is then sealed by reassembling it and using polymeric substances until it meets the required standards.

Initially, we designed a testing platform for sealing the detector chamber and testing internal and external air pressures. The external supply of test gas is provided by an overpressure-adjustable carbon dioxide cylinder. First, the gas passes through a pressure regulator valve to control the overpressure, ensuring that the testing conditions meet the requirements without damaging the detector chamber or GEM foils. Next, it flows through an adjustable flow meter and a ball valve, with the ball valve leading to the interior of the detector chamber. Another set of ball valves and flow meters are installed downstream of the detector's exhaust port to prevent gas leakage. Adjacent to the detector chamber, there is a sealed chamber connected to the same Arduino microcontroller, ensuring the same temperature and pressure conditions as the detector chamber. Temperature and gas pressure sensors are placed inside this chamber to measure the pressure and temperature of the detector chamber. Both the detector inside the chamber and the pressure sensors outside are connected to the same Arduino microcontroller for data collection during experiments. Refer to Fig.5.11(left) for the specific gas flow diagram. It can be seen that besides the input and output ports of the detector, there are also circuits for sensors and multiple valves that may cause gas leaks and interfere with experimental results. Therefore, a control group must be set up. To further address this, the gas circuit diagram shown in Fig.5.11(right) was established, where the input and output ports of the detector gas were connected end-to-end. This configuration allows the test results to reflect the leakage status of the test circuit, eliminating interference from the equipment. This completes the design of the detector gas tightness test.

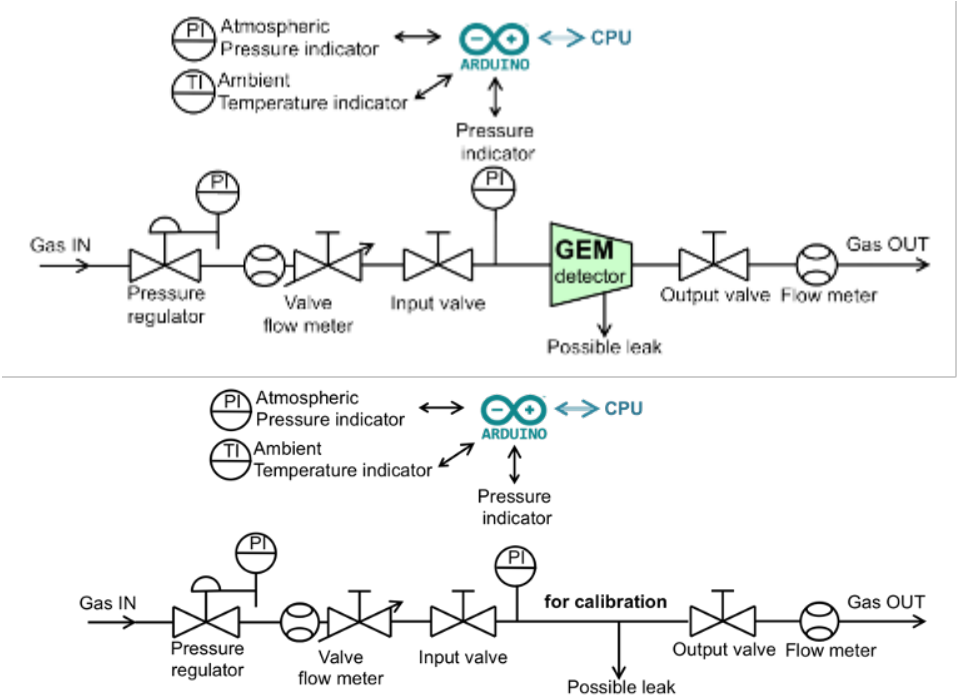

Figure 5.11 Left: Gas leak test circuit for the detector chamber. Right: Control gas leak test circuit for the reference group.

The gas circuit is constructed using stainless steel pipes combined with valves and easy-to-connect fittings. During the experiment, we utilized an aluminum plate to construct a simple test stand model as a base, designed to fit into a NIM cabinet according to its dimensions. The front and back views of the test stand are shown in the upper left and right images of Fig. 5.12, respectively. The detector is connected to the microcontroller via metal connectors, extending data lines from the metal enclosure. Preliminary pressure control is performed at the valve of the carbon dioxide cylinder, and the pure carbon dioxide gas passes through a pressure controller before entering the test circuit. The dual pressure control aims to ensure that the detector is not damaged by excessive pressure. Upon entering the test circuit, the carbon dioxide gas first passes through a flow meter, then through a needle valve, before reaching the detector chamber. Along this section of the circuit, a metal chamber branches off, housing the sensors described below. After passing through the detector chamber and exiting from port B, the gas passes through a ball valve and then another flow meter before leaving the test platform. Refer to the schematic diagram in Fig. 5.12 lower panel for details.

We designed the core of the data acquisition system to consist of a microcontroller and a computer. The microcontroller controls and collects data from sensors, which is then transmitted to the PC for data acquisition and subsequent processing either via data cables or a Wi-Fi

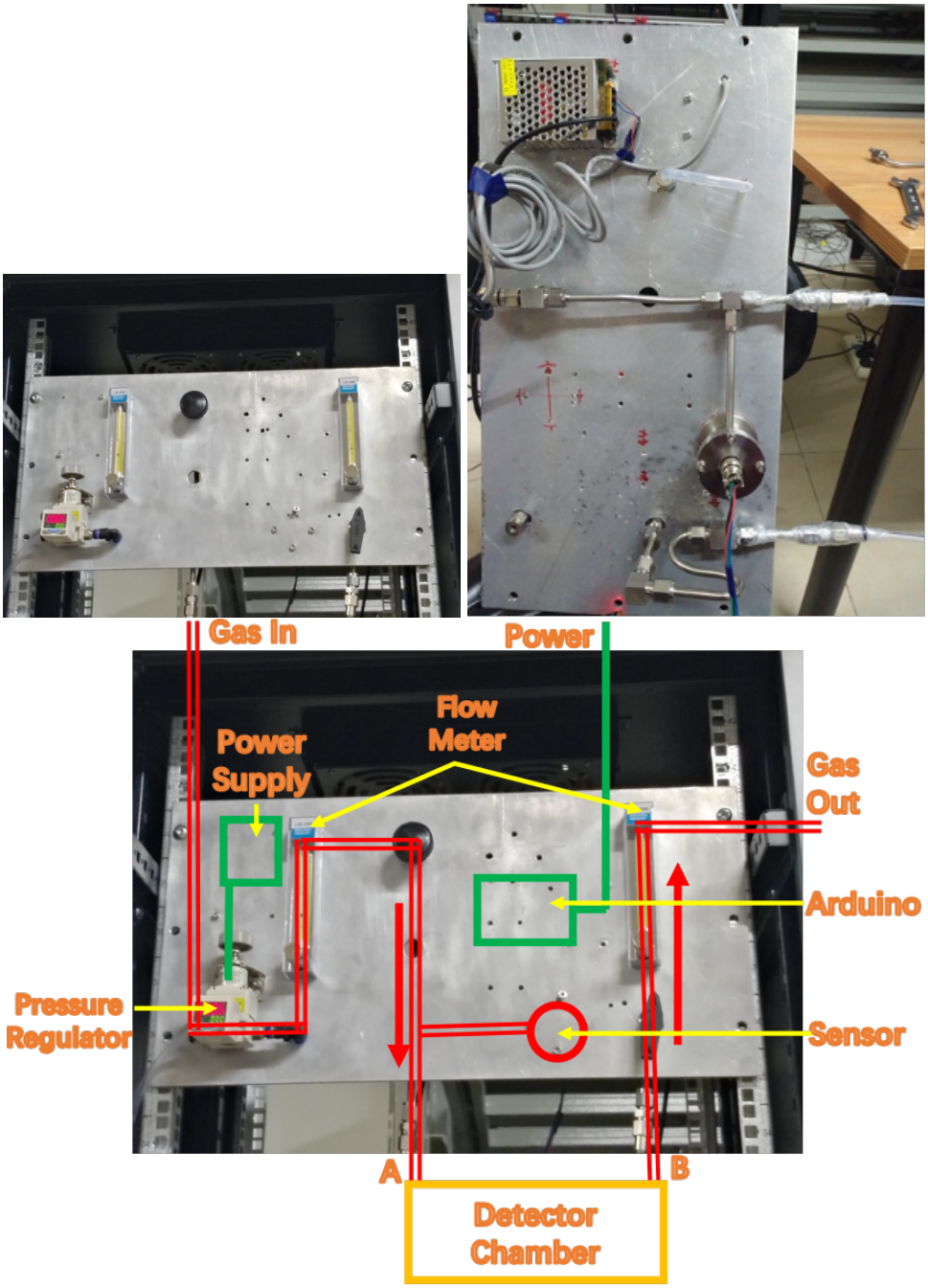

Figure 5.12 Upper: Photographs of the gas test stand model. (Left) Front view. (Right) Back view. Lower: Schematic diagram of the gas leakage test platform.

module. The flowchart of the electronic platform process is shown in Fig. 5.13.

As mentioned earlier, the role of the microcontroller in the gas leakage test is relatively straightforward. It powers the sensors, collects instructions, and transmits data to the PC via data cables or a Wi-Fi module. Therefore, we chose to use an Arduino microcontroller. Arduino is a flexible open-source platform developed by a European team in 2005, comprising both hardware (development boards) and software (Arduino IDE). Developers build the Processing/Wiring development environment on their computers and use a high-level language between C and Java to write programs in the IDE. These programs are then burned into various models of development boards via data cables, and the microprocessor on the development board compiles them into binary files. These files control electronic components through various interfaces to achieve desired functionality. On the other end, the computer triggers certain functions of the development board and obtains feedback signals by sending simple strings via data cables or wireless signals, thereby achieving data acquisition.

Additionally, the limited length of data cables may pose various challenges during testing, especially when encountering complex laboratory setups or sensor requirements. Relying solely on data cables can lead to unnecessary complications. Therefore, we opted to build a wireless reading and writing platform using an Arduino-based Wi-Fi expansion board. For our experiments, we employed the Wi-Fi SHIELD V3 expansion board, which offers three operating modes: ”AP+STA” mode for TCP-Client or TCP-Server mode, and AP mode. We selected the TCP-Client mode, which allows us to establish an AP network. This network can be accessed via a computer for configuration, enabling the module to join other Wi-Fi AP networks. In this mode, the Wi-Fi expansion board's IP address remains fixed, and the computer can control it as long as they are on the same Wi-Fi network, eliminating the need for repeated configuration. To collect data, we simply open the data acquisition software on the computer, input the corresponding IP address and port number, and proceed with data collection smoothly.

Due to the limited number of interfaces on the development board, it cannot accommodate more than two sensors simultaneously, and using two identical sensors concurrently is also not feasible. Therefore, we opted for two different integrated sensors.

The `BME280` sensor can simultaneously measure temperature, humidity, and pressure, offering the advantages of multifunctionality, compact size, and high precision. It is designed with a Gravity-I2C interface and includes a reserved SPI interface, allowing for the rapid prototyping of products for applications such as environmental monitoring and IoT control. The

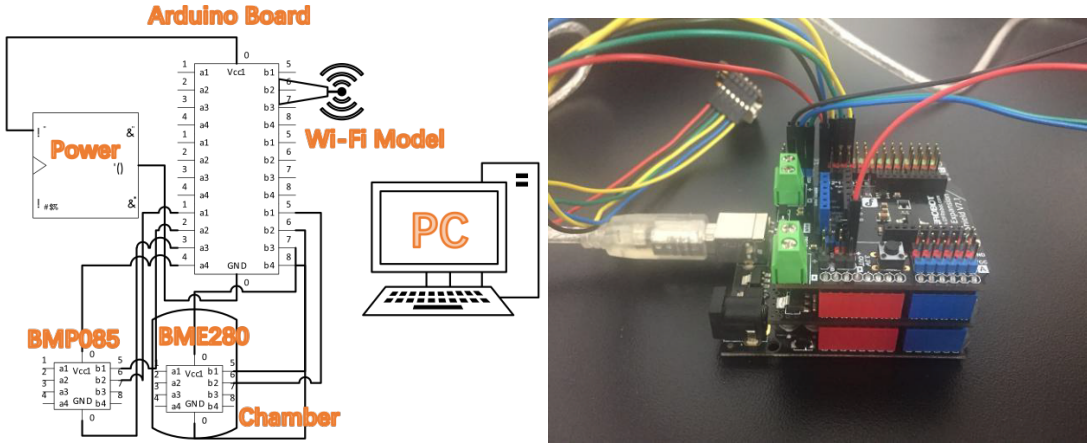

Figure 5.13 Left: Gas leak test DAQ flow chart. Right: The Wi-Fi SHIELD V3 board.

sensor is responsible for conducting internal pressure tests within the detector or gas circuit.

The BMP085 is a small-sized, low-power, and high-precision atmospheric pressure sensor. It can also be connected to Arduino via the I2C bus to obtain real-time pressure data. Commonly enclosed within instruments, it is used for precise applications such as GPS navigation, vertical velocity indication, and floor altitude measurement. In our setup, the BMP085 sensor is employed as the external atmospheric pressure sensor.

A typical test result shown in Fig. 5.14, where the pressure drop can be compared with the reference group and the leaking ratio pass the requirement which means the detector chamber can operate normally under standard gas flow.

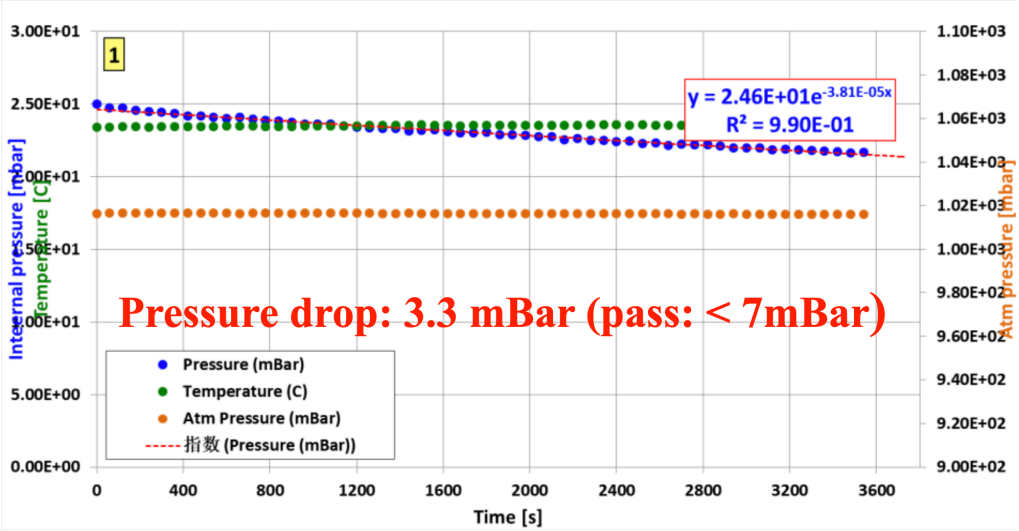

Figure 5.14 A typical result of the gas leak test.

QC4: High voltage test

The QC4 phase aims to assess the quality of the detector's high-voltage divider circuit and

the extent of noise impact. To prevent potential damage to detector components, especially the GEM foil, resulting from faults in the voltage divider circuit, it is necessary to measure the classical I-V curves and monitor the frequency of noise signals.

QC4 analysis is divided into two main sections. The first part involves testing the IV curve of the voltage divider circuit, wherein different voltages are applied to the drift electrode of the Triple-GEM detector, and the resulting currents are measured. By analyzing the IV curve, the actual total resistance of the circuit can be determined. This value is then compared to the design resistance to assess whether the circuit exhibits leakage currents, dark currents, or non-standard resistance values. The second part focuses on measuring the frequency of noise signals, also known as spurious signals. The detector is placed in its operational environment, with no incident particles, and the frequency of signal occurrences is measured. Despite efforts to minimize electronic noise and the presence of cosmic rays, some signal frequency persists. A detector is considered to pass the quality control test if the frequency of spurious signals does not exceed 10 Hz under operational voltage.

As analyzed in the previous section, the testing protocol revolves around the voltage divider circuit and noise, with the primary focus on drift current and noise frequency. Consequently, our hardware and software platform design is centered on these aspects. The design of a suitable voltage divider circuit involves two key considerations. Firstly, the resistors must be appropriately sized to meet the operational requirements of the detector. Secondly, the layout should be conducive to effective wiring, facilitating the connection of the voltage divider circuit to the surfaces of each GEM foil in the Triple-GEM detector, as well as to the drift and readout electrodes. In accordance with the design schematics of the voltage divider circuit outlined in the CMS upgrade TDR [117], the complete voltage divider circuit and its connectivity are illustrated in Fig. 5.15.

The second part involves setting up the testing platform, which will evidently involve a considerable number of electronic components. The determination of the current-voltage (IV) characteristics is relatively straightforward, as it simply entails applying high voltages across the voltage divider circuit using a specialized high-voltage power supply while measuring the corresponding current values. However, measuring noise is more complex. Firstly, it requires arranging experimental conditions identical to those during detector operation to discern false signals caused by factors unrelated to the experiment. Secondly, the amplified signals from the detector need to undergo preprocessing before being directed to the computer. The flowchart for this part is as shown in Fig. 5.16, the signal will be extracted from the bottom of GEM3

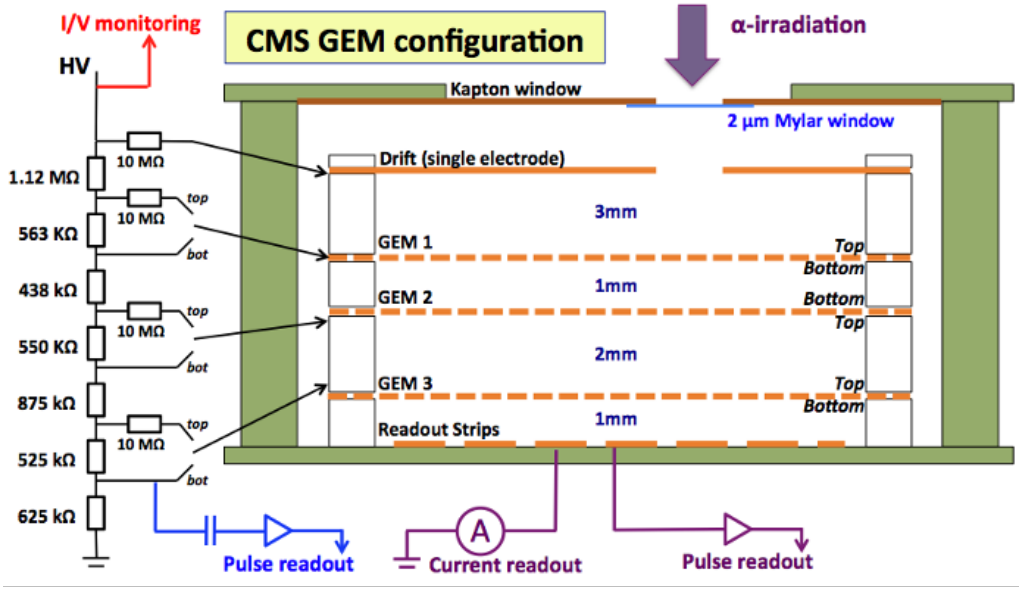

Figure 5.15 The connection of the high voltage divider and the values of the resistances.

foil, first pass through the primary amplification of the preamplifier, then enter the resistor amplifier for further amplification and shaping, and then flow through the signal discriminator to remove spurious signals and integrate larger pulse signals into standard signals input to the counter for signal counting. On the software side, it is designed to complement the hardware design, requiring software control for both the voltage and current testing of the high-voltage power supply, and another software for controlling the counter.

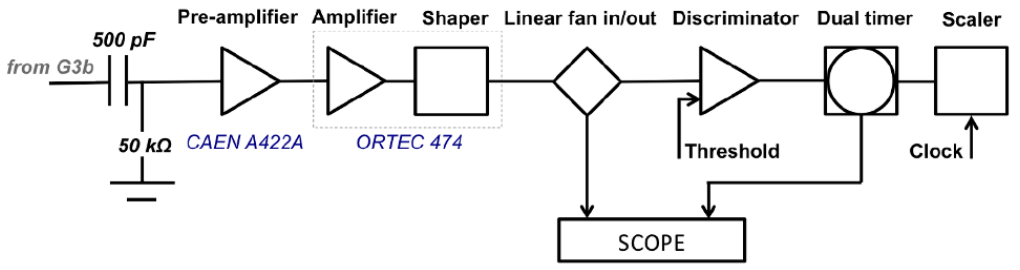

Figure 5.16 The flowchart of the signal counting electronic platform.

The power supply and working gas in the laboratory are centrally managed. The laboratory's high-voltage power supply is uniformly provided by the CAEN-SY5527 high-voltage power supply, which features 6 interfaces for 10,000V and 10 interfaces for 6,000V, connected to the computer via Ethernet cable. It can be controlled using dedicated software developed by CAEN or other computer programs. The entire laboratory, including the high-voltage power supply in the cleanroom, is controlled by this power supply unit. The laboratory houses several

types of gases, including nitrogen, argon, and carbon dioxide. Nitrogen is used for purging the gas lines, while argon and carbon dioxide serve as the working gases for the Triple-GEM detector. The gases are extracted from steel cylinders and fed into the SY-9506 gas mixer through metal conduits. The gas mixer can output either pure gas with a certain flow rate or mixed gases with specific compositions. Similar to the high-voltage power supply, the laboratory's gas supply is centralized and controlled by one or several gas mixers.

The ORTEC 142PC interfaces with input and output signals through a radio frequency (RF) interface and provides power to the preamplifier via an RS232 interface. This interface can be connected to the ORTEC 474 amplifier for power supply, as it is a compatible product. The ORTEC 474, also interfacing with input and output signals through a radio frequency (RF) interface, allows for adjustment of amplification factor, time differentiation, and delay on the front panel. Its RS232 interface on the rear panel can supply power to the preamplifier. The CAEN Mod.N843 signal discriminator is a standard NIM module with 16 channel inputs and 48 channel outputs. Each input corresponds to two discriminated signal outputs and one reverse output after internal settings. The threshold can be set on the front panel to isolate signals below this threshold. Additionally, the occurrence time of signals above the threshold is determined using a ratio method, and a fixed-width narrow pulse signal is output at that time. The ORTEC974A pulse counter, with appropriate internal configuration, counts pulses of a certain size and width. The front panel allows for a range of settings including time regions, which can also be configured through computer programs. Communication with a computer is facilitated through the RS232C interface.

Once the Ethernet port of the high-voltage power supply and the RS232C serial port of the ORTEC974A are connected to the computer terminal, the electronic test platform is essentially set up. A typical QC4 test result is shown in Fig. 5.17, we can find a linear IV curve and a reasonable level of noise.

`QC5: Effective gain and uniformity test`

QC5 testing involves evaluating the detector's effective gain and uniformity. Similar to QC4, it entails performance testing of fully assembled detectors and comprises two parts: the first part involves assessing the effective gain, while the second part focuses on evaluating the uniformity of detector gain. The effective gain refers to the ratio at which the triple-GEM foils multiply the number of electrons during actual detection operations. Let Q denote the number of primary electrons generated by a certain particle entering the detector within a certain period of time t, and N represent the number of particles entering the window. Consequently,

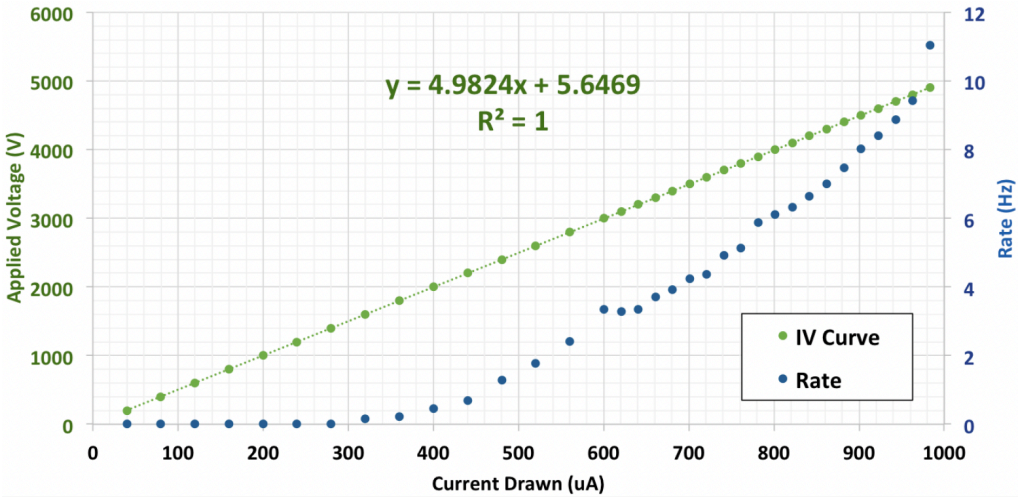

Figure 5.17 QC4 typical results with GE1/1.

the number of primary electrons should be the product of the two. Similarly, based on the principle, it can be inferred that the amplified electrons will generate an equivalent amount of induced charge at the readout electrode and be directed to ground, thus the number of amplified electrons is given by $I \times t$. According to the principle, the effective gain of the triple-GEM detector can be expressed as equation 5.1.

$$G = \frac{It}{QN} \tag{5.1}$$

We found that, for practical measurements, it is necessary to determine four physical quantities: the time duration t, the continuous readout current $I(t)$ during this period, the number of incident particles N, and the number of electrons excited by a single particle Q. While the measurement duration can be arbitrarily defined, the current magnitude can be read using a current meter. The more challenging aspects are the two parameters in the denominator. After conducting research, we have chosen the following approach for measurement. The number of electrons excited by a single particle can be calculated using theory. The total ionization can be described by the following formula [119](Eq. 5.2).

$$n_T = \frac{\Delta E}{W_i} \tag{5.2}$$

In the above equation, ΔE represents the total energy lost by the incident particle in the medium, and W_i represents the energy required for the gas to ionize and produce one electron-ion pair on average (also known as the average ionization energy in pure substances). At standard temperature and pressure, the ionization energy of most working gases ranges from 20 eV

to 40 eV or the same order of magnitude citehohlmann2009geant4. During the testing, we irradiate the detector with X-rays to generate electron-ion pairs, so the energy source for primary ionization is the incident X-rays. The working gas used is a mixture of CO_2:Ar = 30:70, which has been tested to achieve good results. It can both excite free electrons from argon atoms and utilize the greater molecular degrees of freedom in carbon dioxide molecules to consume excess energy without sufficiently exciting new electrons, thus maintaining system stability. The ionization energy of this mixture is 26.4 eV. Then we derive from equation 5.1 the following equation(Eq. 5.3).

$$G = \frac{I}{eR\Delta E/26.4\text{eV}} \tag{5.3}$$

Where G, I, and ΔE retain their meanings unchanged, R represents the frequency of incident particles, and e is the electric charge constant. Referring to relevant literature, we can approximate ΔE as the energy of X-rays. Therefore, the final physical quantities that need to be measured are only I(t) and R. In addition to measuring the effective gain, another part of the QC5 process is to determine the uniformity of the effective gain. The detector is divided into different regions, and the effective gain of these regions is tested separately to assess whether all positions of the detector are in good working condition.

The hardware platform needs to achieve the following functions: stable supply of working gas, stable supply of operating voltage, stable supply of X-rays (with limited irradiation area), testing of pulse frequency on the bottom surface of GEM3, and testing of real-time current signals from the readout circuit board. In Chapter Four, during the introduction of QC4, some laboratory environments were described, and thus will not be repeated here. Only a brief explanation of the above five objectives will be provided.

Stable working gas: As mentioned earlier, the working gas is supplied uniformly by the gas distributor, providing a mixture of CO_2 : Ar = 30 : 70, which is then piped into and out of the X-ray shielding box.

Stable operating voltage: The SY5527 integrated high-voltage power supply is employed to provide power. The power is fed into the X-ray shielding box via high-voltage RF cables.

Stable X-ray: A stable silver-target X-ray source is used to irradiate the detector inside the shielding box. The emission aperture is equipped with a specially designed collimator, providing an emission area of one square millimeter, which perfectly meets the positional accuracy requirements of this experiment. A temperature sensor is installed on the X-ray tube to

monitor temperature data, which can be read by the computer. This allows for timely experiment termination in case of overheating. Additionally, a cooling fan is installed at the bottom of the X-ray tube to reduce its temperature. Furthermore, to test the uniformity of the gain, the position of the X-ray tube will be frequently adjusted during the experiment. Therefore, it is mounted on metal rails, allowing for three-dimensional free movement within the X-ray shielding box.

Testing Pulse Frequency: The procedure and equipment for testing pulse frequency are identical to the testing of false signals in QC4, and thus, will not be reiterated here.

Testing Real-Time Current Signal of the Readout Circuit Board: The current flowing from the readout board is routed through an adapter interface into the coaxial cable and directly connected to a sensitive microammeter. The microammeter used in the experiment is the KEITHLEY Model 6482, which can be connected to a computer via an RS232 serial port for control and data retrieval.

The electronic equipment for data collection has been fully assembled after the preparation of the five aforementioned hardware components. Considering the specific locations of laboratory items, the number of computer serial ports, and operational feasibility, we layout the setup as shown in Figure 5.18. Pulse counting, readout current, and operating voltage are controlled by one computer, while X-rays are controlled by another dedicated computer. If the performance status of PC1 permits, it can also control all components.

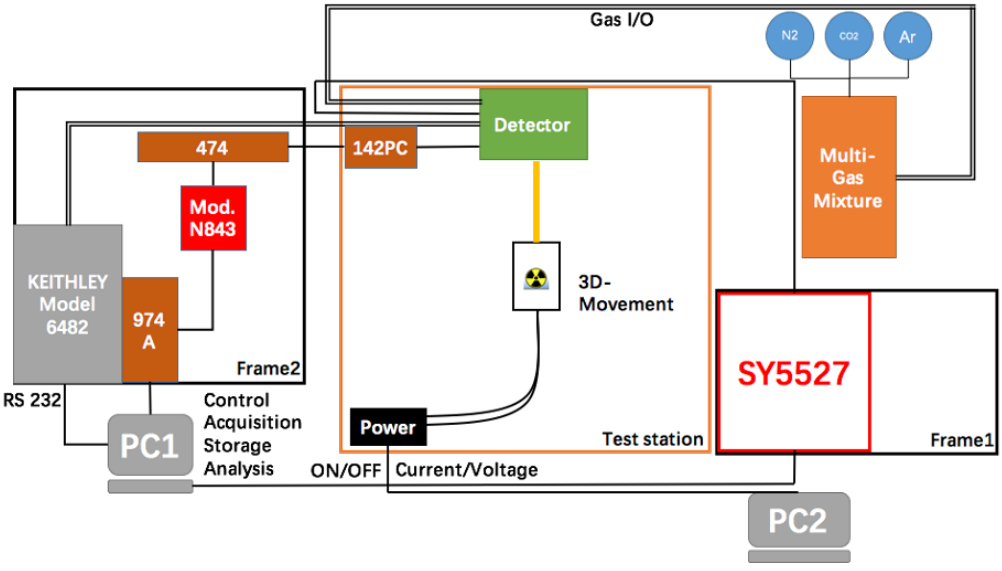

Figure 5.18 Layout of hardware setup for complete QC5 experiment..

And the typical result of QC5 can be found in Figure 5.19, the upper panel shows the IV curve and the level of noise under the X-ray source, and the lower panel shows the distribution

of the effective gain at different locations on the board, which indicates the uniformity of the effective gain.

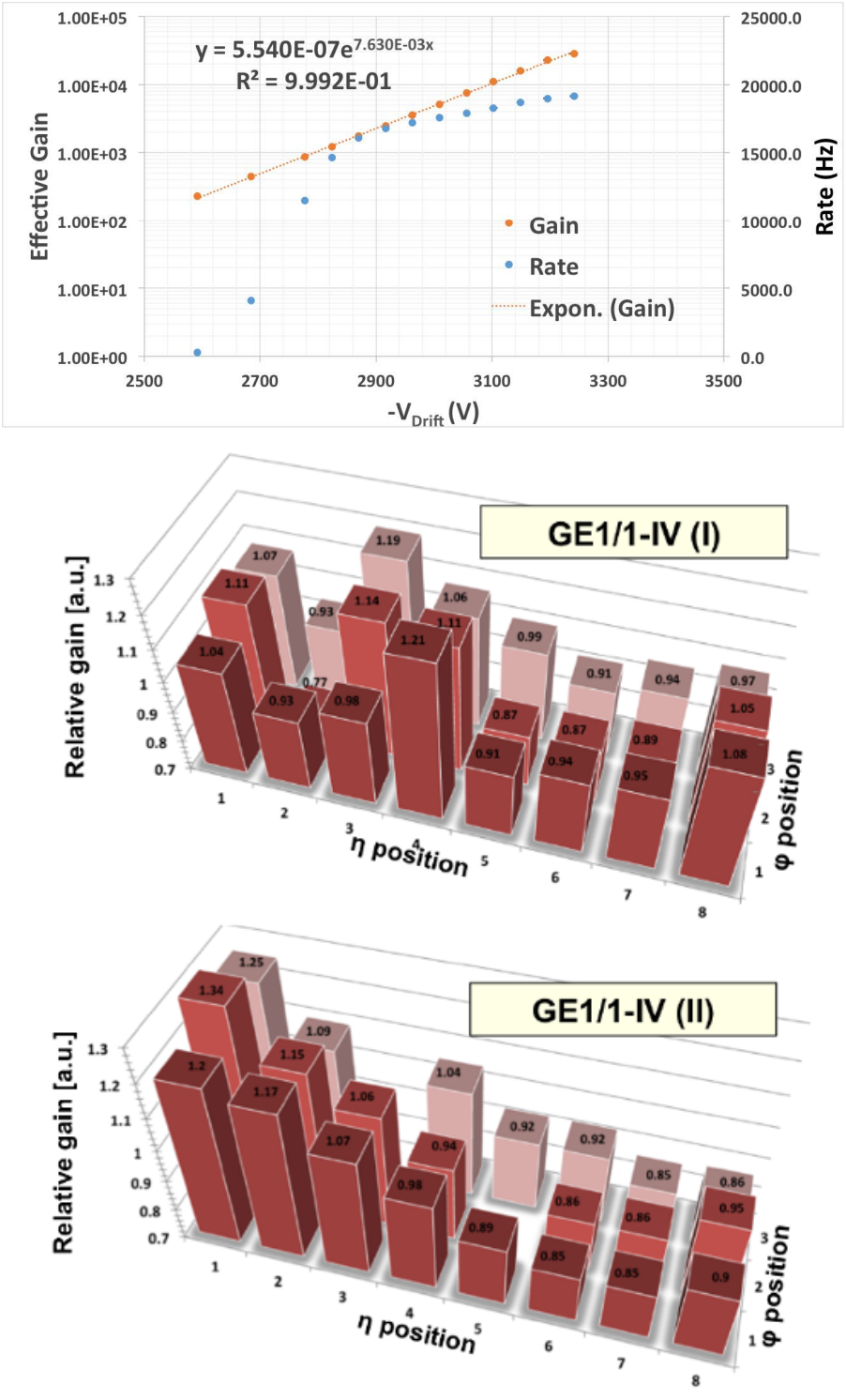

Figure 5.19 The typical result from the QC5. Upper: The IV curve under X-Ray source and the level of noise. Lower: The distribution of the effective gain.

5.2.2 Simulation study of multi-layer GEM detector

As discussed in the previous section, the triple GEM detector is selected to be the detectors in CMS phase-II operation for its good performance under high radiation environments. Multi-GEM detectors are effective at reducing the discharge probability and Ion Back Flow (IBF) [120]. They can operate at lower voltages, while maintaining a high effective gain. They are widely used for the high-energy experiments in the high luminosity environment. For instance, a triple-GEMdetector is adopted as the baseline solution for the CMS muon system upgrade as introduced, and a quadruple-GEM detector is a candidate for the upgrade of the ALICE Time Projection Chamber (TPC) [121].

A gas discharge is initiated when the gain surpasses a critical threshold, identified as the Raether limit [122]. Experimental observations have shown that the discharge likelihood for a triple-GEM detector subjected to α-particle exposure is significantly high once the effective gain exceeds 4×10^5 [123]. Conversely, a quadruple-GEM detector can achieve equivalent gains at reduced, safer operational voltages, thereby diminishing the probability of discharge. Moreover, the space charge effect is mitigated due to a decrease in the IBF [124]. Given these advantageous performance traits, a thorough investigation through simulation of the physical principles governing quadruple-GEM technology is warranted.

`Configurations`

The comprehensive simulation workflow is depicted in Fig. 5.20, utilizing software suites such as Garfield++ [125], ANSYS, and ROOT. ANSYS is employed to construct the three-dimensional GEM detector unit model and to calculate the field map at specific voltage settings, serving as inputs for Garfield++. Garfield++ then develops the full model, sets up various physical conditions, and simulates intricate physical processes via the Monte Carlo method. ROOT facilitates data processing and analysis. To align simulations more closely with experimental outcomes and enhance understanding of multi-GEM detectors, a parametrization approach is applied in gain studies.

Signal simulation involves computing induced currents through the Shockley–Ramo theorem [125, 127], with algorithms for charge integration and signal amplification mimicking those of a pre-amplifier [128]. These induced signals are then processed with the VFAT3 transfer function [117] to produce voltage pulses for signal shaping, with a shaping time set at 100 ns. The signal's amplitude, reflecting the total induced charge, benefits from an optimized shaping time [117]. The simulation outcomes presented derive from these induced signals.

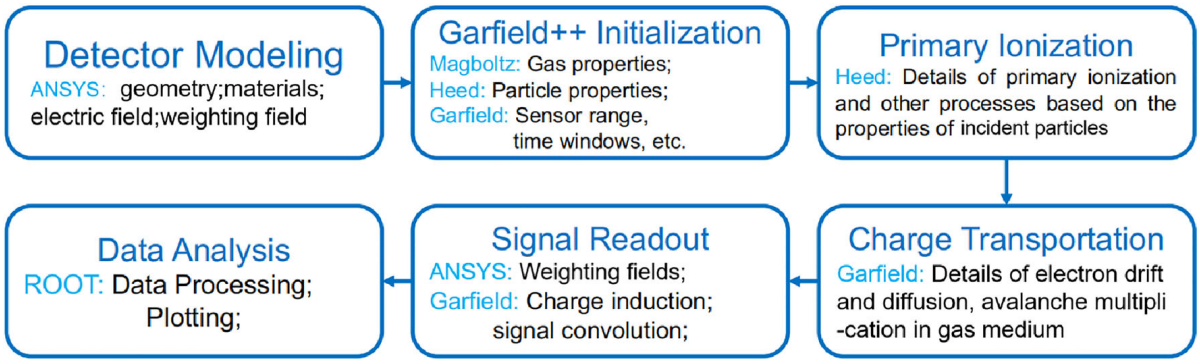

Figure 5.20 The flow chart of the full simulation [126].

To facilitate comparisons with existing experimental data, we model a quadruple-GEM detector akin to the design implemented for the ALICE TPC upgrade [129, 130]. Figure 5.21 illustrates the schematic design of the quadruple-GEM detector, featuring a GEM foil composed of a 50μm thick Kapton layer with 5μm copper cladding on each side. Utilizing photolithography, biconical holes are etched into the foil in a regular hexagonal pattern, with inner and outer hole radii of 50μm and 70μm, respectively, and a hole pitch of 140μm. The drift, three transfer, and induction regions have thicknesses of 4.8-2-2-2-2mm, with a readout strip pitch of 210μm and a width of 150μm. For comparison with the CMS triple-GEM detector, which features 3-1-2-1mm thick regions [117, 131], we also designed a quadruple-GEM detector with 3-1-1-1-1mm thicknesses, referred to as the 'CMS quadruple-GEM' detector.

The high voltage (HV) divider circuit diagrams for the ALICE quadruple-GEM detector in simulation are presented in Fig. 5.21, mirroring those used in experimental setups [129, 130]. Voltage distribution across each region can be adjusted proportionally using a conventional HV divider, while a non-conventional HV divider allows for independent modification of the electric field strength in the drift region. The CMS triple-GEM and 'CMS quadruple-GEM' detectors utilize other conventional HV dividers [117]. Figure 5.22 displays the unit models, typical electric field distributions, and the voltage applied across each GEM foil. The electric field in each region facilitates electron drift, with the fields inside the GEM holes reaching up to ~60 kV/cm, leading to electron avalanche multiplication. Electrons traversing the induction region induce currents on the readout strips lasting tens of ns. Gas mixtures of Ar/CO_2 in ratios of 70:30 (70% Ar, 30% CO_2) and 90:10 (90% Ar, 10% CO_2) are evaluated to assess gas composition effects. Simulated particle beams are directed perpendicularly onto a rectangular area on the cathode plane, encompassing all possible alignments with the first GEM foil. The simulation involves four different particles:

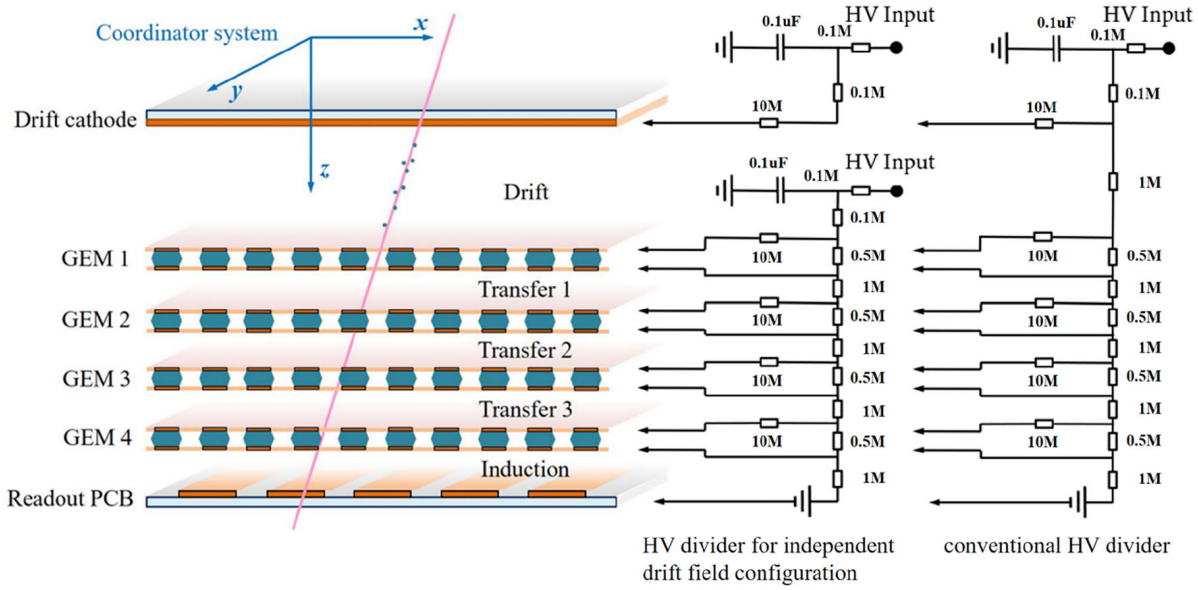

Figure 5.21 The schematic design of a quadruple-GEM detector (left); two types of high voltage dividers (right). [126]

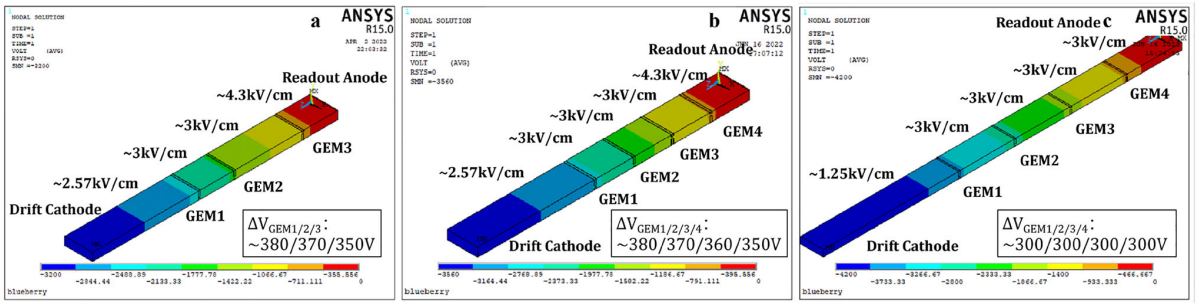

Figure 5.22 The unit models, typical electric field distributions, and voltage drop applied on each GEM foil for these detectors calculated with ANSYS. a) CMS triple-GEM detector; b) 'CMS quadruple-GEM' detector; c) ALICE quadruple-GEM detector. [126]

- 5.89 keV X-ray produced by ^{55}Fe source.
- β^- electrons produced by ^{106}Ru-Rh source, with the maximum energy of 3.54 MeV.
- Free electrons around 10 eV (similar to the low-energy ionized electrons), used in the electron transparency and effective gain studies, especially for the parametrization method.
- 150 GeV μ^- beam, studied in a series of beam tests at CERN [131].

Results

The quadruple-GEM detector simulation results encompass various parameters, including time resolution, spatial resolution, electron transparency, effective gain, and detection efficiency. These parameters significantly influence particle identification, energy measurement,

trigger efficiency, and track reconstruction.

`Time resolution`

The time resolution is influenced by the location of electron ion clusters, the drift and diffusion of electrons, and electronic noise. To evaluate timing performance, the pulse signal from the strip with the highest amplitude is considered. The Amplitude and Rise time Compensated (ARC) timing method [132], which utilizes only the signal's rising edge, is employed to determine the timing point. This technique negates the effects of pulse amplitude and rise time, indicating that the drift time of the primary electron cluster nearest to the first GEM foil primarily triggers and substantially influences time resolution. Electron diffusion, both transverse and longitudinal, also impacts this drift process [133].

The drift time distribution closely resembles an exponential function $f(t) = n\nu_d e^{-n\nu_d t}$, with a standard deviation of $1/n\nu_d$, where n represents the average number of primary electrons per unit length (approximately linearly proportional to the gas's average atomic number), and ν_d denotes the drift velocity [134]. The time distribution is simulated analogously to experimental procedures, defining the signal time as the moment the pulse signal's rising edge crosses a predetermined 80 mV threshold.

The results for the simulated time resolution of both triple-GEM and quadruple-GEM detectors are depicted in Fig. 5.23(a). A positive correlation exists between the drift velocity and the electric field strength in the drift region [135], leading to improved time resolution as the field strength increases. A gas mixture of Ar/CO_2 at 70:30 enhances time performance due to a higher average number of primary electrons per unit length [134]. With identical cathode voltage settings, the triple-GEM detector exhibits a higher drift electric field strength, attributable to its unique voltage distribution and a narrower drift region, explaining its superior time resolution compared to the quadruple-GEM detector under these conditions. Optimal time resolution is achieved through careful adjustment of the drift electric field strength and gas mixture.

Figure 5.23(b) explores time resolution with varied drift field strengths, showing improvements with increasing field strength and achieving optimal resolution near 3 kV/cm due to the saturation effect on electron drift velocity [134]. When simulating according to experimental procedures, including the time-walk effect [128], results align more closely with experimental data. Conversely, the ARC timing method incorporates time-walk corrections [132], enhancing time performance. However, these simulations do not fully account for the actual electronic noise encountered in experimental setups.

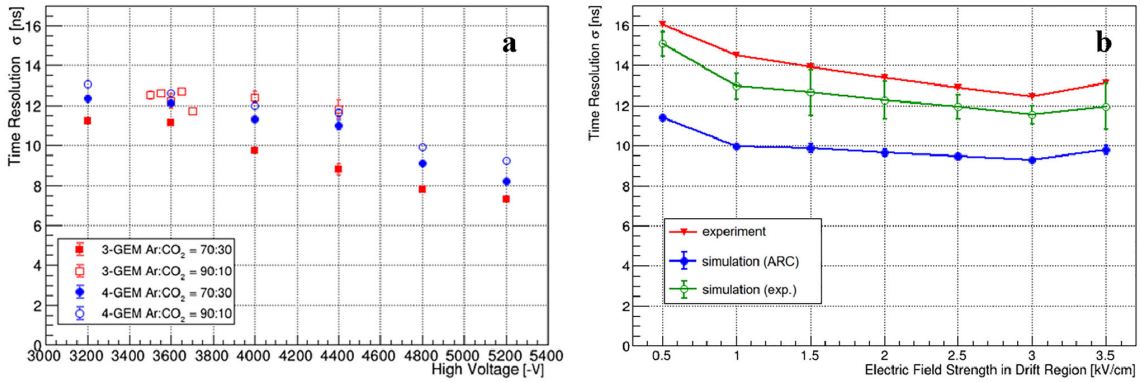

Figure 5.23 The β^--source is adopted. **a** Simulated time resolution as a function of the drift cathode voltage for the ALICE quadruple-GEM and CMS triple-GEM detectors operated with Ar/CO_2 70:30 and 90:10, by the conventional HV dividers. The ARC timing method is used. The relationships between the drift electric field strengths and the cathode voltage for the triple-GEM and quadruple-GEM detectors are as follows: $E_{3,\text{drift}} \approx 8 \times 10^{-4} V_{\text{cathode}}$ kV/cm, $E_{4,\text{drift}} \approx 3 \times 10^{-4} V_{\text{cathode}}$ kV/cm. **b** Simulated and measured time resolution as functions of the drift electric field strength for the ALICE quadruple-GEM detector with Ar/CO_2 70:30. The ARC timing method and the experimental method are used, respectively. The total voltage drop applied on the GEM foils is kept at 1400 V for the independent drift field study. [126]

`Space resolution`

The coordinate system is shown before. By the center of gravity method, the hit position is reconstructed as:

$$\bar{x} = \frac{\sum_{i=1}^{n} A_i(x_i) x_i}{\sum_{i=1}^{n} A_i(x_i)}, \tag{5.4}$$

where x_i is the center position of the ith readout strip, A_i is the corresponding signal amplitude, and n is the total number of the readout strips. The spatial resolution is defined as the standard deviation of the Gaussian fit for the differences between the reconstructed and real hit positions.

The spatial resolution mainly depends on the transverse diffusion of electrons, and the density of readout strips. The x positions of electrons in the drift process basically obey the Gaussian distribution:

$$g(x) = \frac{N_0}{\sqrt{4\pi D t}} e^{-\frac{(x-x_0)^2}{4Dt}}, \tag{5.5}$$

with the standard deviation $\sqrt{2Dt}$, where D is the diffusion coefficient (determined by the electric field distribution and the electron energy) and t is the drift time [129, 135]. x_0 is the incident position of the particle beam, and N_0 is the total number of ionized electrons.

The spatial resolution performance of the quadruple-GEM detector subjected to a 150 GeV μ^- beam, utilizing a conventional HV divider, is presented in Fig. 5.24a. The resolution enhances as the drift field strength increases, leading to a substantial rise in drift velocity [129] and a consequent reduction in drift time. This effect significantly suppresses the transverse diffusion of electrons. Spatial resolution in relation to independent drift field configurations is explored in Fig. 5.24b, where the transverse diffusion coefficient markedly increases with the drift field strength within the 1.5–2kV/cm range [129], thereby intensifying charge dispersion. As the drift velocity escalates, it becomes the predominant factor influencing the results. This behavior mirrors the trends observed in spatial resolution simulations for the triple-GEM setup [136].

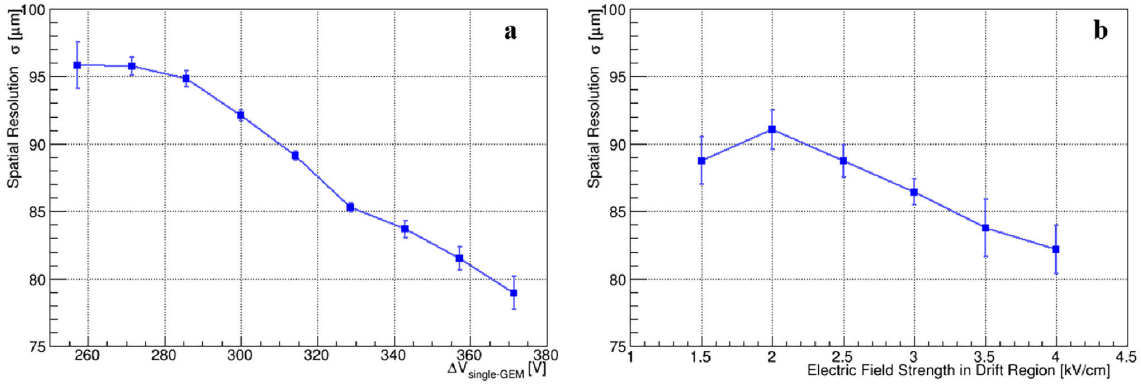

Figure 5.24 The μ^- beam is adopted for the ALICE quadruple-GEM detector operated with Ar/CO_2 70:30. **a** Simulated spatial resolution as a function of the voltage drop applied on one single GEM foil, by the conventional HV divider. The relationships between the electric field strength for the drift region, three transfer regions and induction region and the voltage drop on single GEM foil are as follows: $E_{\text{drift}} = \frac{\Delta V_{\text{single-GEM}}}{240}$ kV/cm, $E_{\text{transfer}} = \frac{\Delta V_{\text{single-GEM}}}{100}$ kV/cm, $E_{\text{induction}} = \frac{\Delta V_{\text{single-GEM}}}{100}$ kV/cm. **b** Simulated spatial resolution as a function of the drift electric field strength, by the HV divider for the independent drift field study. The total voltage drop applied on the GEM foils is kept at 1400 V. The electric field strengths for the three transfer regions and induction region are fixed at 3.5 kV/cm. [126]

`Electron transparency`

Electron transparency, defined as the ratio of ionized electrons collected in the GEM holes from the drift region, is primarily influenced by the electric field distribution and electron diffusion. Through simulation, each electron originating from primary or secondary ionization is microscopically tracked. After normalizing to the maximum, the transparency outcomes for the quadruple-GEM detector, when exposed to X-ray, are depicted in Fig. 5.25, showing quantitative alignment with experimental findings [137, 138].

Initially, electron transparency remains constant but begins to decline as the drift field

strength is elevated. Initially, the drift electric field lines directly enter the holes of the first GEM foil. With an increase in drift field strength, an increasing number of lines end on the copper layer of the GEM foil, thereby capturing some of the ionized electrons. Enhanced voltage drop across the first GEM foil enables more electric field lines to reach the holes, thus augmenting electron transparency. However, due to transverse diffusion [130], these electrons do not strictly follow the electric field lines, resulting in a marginal reduction in transparency.

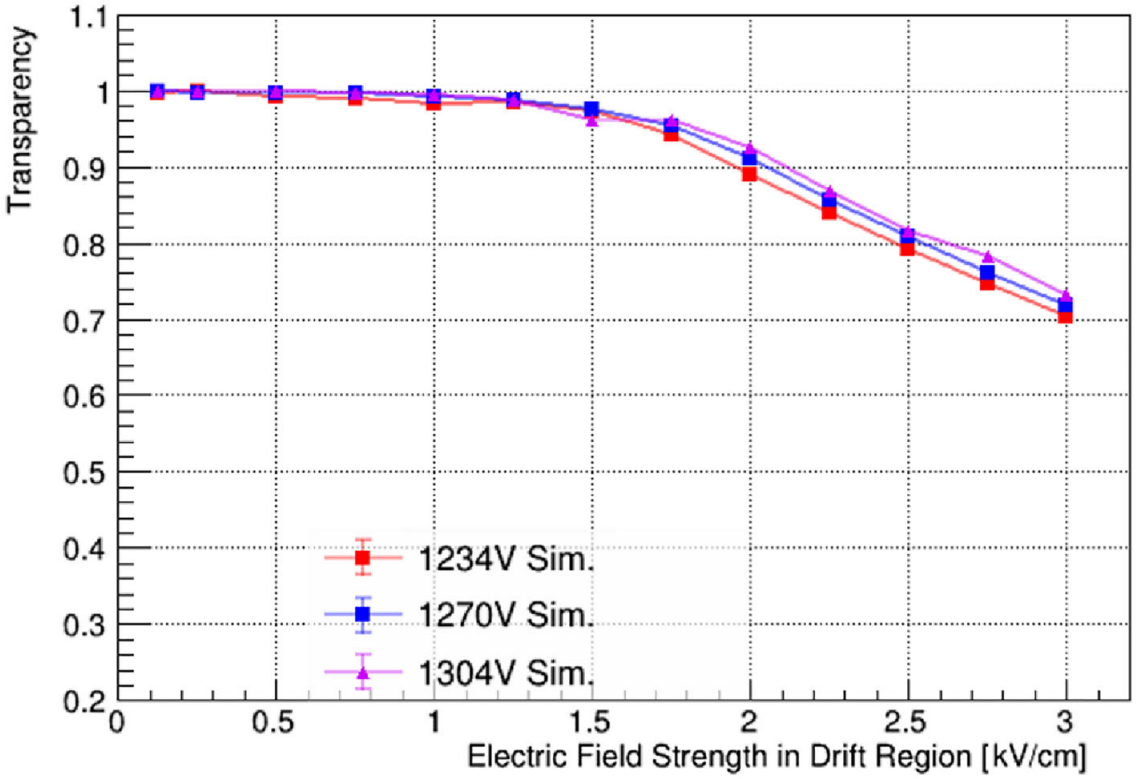

Figure 5.25 Simulated electron transparency as functions of the drift electric field strength under different total voltage drops applied on the GEM foils. The ALICE quadruple-GEM detector is studied with Ar/$CO_2$70:30, by the HV divider for independent drift field configuration. The X-ray is adopted. The true values of the maximum points are 0.897, 0.910 and 0.918 respectively for the 1234 V, 1270 V and 1304 V total voltage drops applied on the GEM foils. [126]

`Effective gain`

The effective gain is defined as:

$$G_{\text{eff}} = \frac{N_f}{N_d}, \tag{5.6}$$

where N_d is the total number of ionized electrons generated inside the drift region, and N_f is the number of the final electrons derived from the complete avalanche multiplication process, passing through the induction region and reaching the anode. It characterizes the level

of signal amplification of a GEM detector and plays a decisive role in the detection efficiency. The formula is adopted to calculate the effective gain in the full simulation. The corresponding results for the ALICE quadruple-GEM detector with different incident particles are shown in Fig. 5.26a.

The amplification factor for every electron from the primary or secondary ionization is obtained by the following formula:

$$M = e^{\int_{r_1}^{r_2} \alpha(r)dr}, \tag{5.7}$$

where α represents the first Townsend coefficient, positively correlated with the electric field strength, and r_1 and r_2 denote the starting and ending positions of the electron's trajectory [139]. An increase in the voltage applied across each GEM foil intensifies the electric field within the holes, exponentially boosting the resulting effective gain.

In our simulations, attention is confined to ionized electrons originating from the drift region, leading to electron avalanche multiplication occurring sequentially through the holes of the four GEM foils. The energy distributions and diffusion characteristics of these ionized electrons remain consistent across various types of incident particles, rendering the simulated gains nearly identical. Notably, at lower voltages, gains for β^- particles are significantly reduced, a phenomenon warranting further examination.

It is important to note that simulated gain results are lower than experimental outcomes. This discrepancy could be attributed to the simulation's minimum time step being too small to accurately replicate real-life scenarios. Additionally, the default Penning factor [140] used in the simulation may not align with experimental conditions. These factors contributing to the difference in gain results will be explored in greater detail in subsequent sections.

The **parameterization method**, derived from Monte Carlo simulations initially applied in the triple-GEM detector study for the BES-III experiment [127], is detailed through a flow chart in Fig. 5.27. This approach mirrors the geometric modeling and conditions of the comprehensive simulation. Physical phenomena such as primary and secondary ionization, electron transport, and avalanche multiplication are individually simulated using Garfield++. Statistical distributions of key physical metrics are generated from these simulations and subsequently fitted with theoretical models to extract crucial statistical parameters (mean, variance, etc.). These parameters are amalgamated to assess the GEM detector's overall efficacy, with adjustment factors introduced to align simulation outcomes with experimental observations [127].

This method is particularly designed to elucidate the intricate physical mechanisms within

the GEM detector, a task unachievable through full simulations alone. Thus, the effective gain for the quadruple-GEM detector is also conceptualized via this approach:

$$G_{\text{eff}} = \prod_{i=1}^{4} G^i_{\text{intr}} \cdot \epsilon^i_{\text{coll}} \cdot \epsilon^i_{\text{extr}}, \tag{5.8}$$

where G^i_{intr} is the intrinsic gain [127], ϵ^i_{coll} and ϵ^i_{extr} are the collection extraction efficiencies [138] of the ith GEM foil. The parametric simulation steps for the effective gain calculation are listed as below:

- **Step I** Simulate the ionization and drift processes under the given conditions. Get the number, position and energy distributions of the ionized electrons.
- **Step II** Simulate the electron multiplication process inside each GEM foil, and calculate the fractions of the electrons collected into and extracted from the foil. Obtain the distributions of the intrinsic gain, the collection and extraction efficiencies for each GEM foil. Fit the gains with the Polya distribution 5.9 [125] and the efficiencies with two Gaussian functions. $\bar{n}$ is the average intrinsic gain, and θ is the factor controlling the distribution shape.
- **Step III** Generate the characteristic statistical parameters, especially the mean values and integrate them together to obtain the simulated effective gain. Compare these results with the experimental data.
- **Step IV** Tune these physical parameters by correcting the internal factors (the θ factor, Penning factor, and minimum time step, etc) in Garfield++. Make the simulation results more approach to the realistic scenarios.

$$P(n) = \frac{(1+\theta)^{(1+\theta)}}{n^{\bar{n}}\Gamma(1+\theta)} \left(\frac{n}{\bar{n}}\right)^n e^{-(1+\theta)n/\bar{n}}, \tag{5.9}$$

The effective gain results for the ALICE quadruple-GEM detector with X-ray exposure are depicted in Fig. 7b. For these parametric simulations, both the Penning factor and the minimum time step are finely adjusted. The gains obtained from this approach, particularly the slope of the gain versus voltage curve, align more closely with experimental observations [130] than those derived from full simulations. Prior analyses indicate that simulations tend to underestimate effective gains compared to experimental results, attributed to overly small time steps and inaccurately chosen Penning factors [140]. Further exploration into the ionization and amplification dynamics within GEM detectors is warranted.

Figure 5.28 illustrates the effective gains ascertained through parametric simulations for

both the CMS triple-GEM and 'CMS quadruple-GEM' detectors, alongside experimental results for the triple-GEM detector for comparative analysis. Initial adjustments are made to the Penning factor and the minimum time step in tandem to align the triple-GEM detector's simulated outcomes with experimental data. Subsequently, simulations for the quadruple-GEM detector proceed with these parameters fixed. The quadruple-GEM detector demonstrates superior effective gain compared to the triple-GEM under identical total voltage conditions. For example, achieving an effective gain of 4000 necessitates operating the triple-GEM detector at a -3200 V negative high voltage, whereas approximately -2960 V suffices for the quadruple-GEM. Thus, the 'CMS quadruple-GEM' detector presents a viable solution for mitigating discharge risks amidst the high-luminosity conditions prevalent in LHC experiments.

We have evaluated the quadruple-GEM detectors' performance through comprehensive and parametric simulations. The outcomes concerning spatial and time resolution, electron transparency, effective gain, and detection efficiency are documented and scrutinized alongside available experimental findings and the simulation insights of the triple-GEM detector across a spectrum of operational settings. Discrepancies between simulated and experimental results are elucidated, with subsequent optimization of key parameters ensuring simulated outcomes closely match experimental data.

Quadruple-GEM detectors emerge as promising candidates for minimizing discharge risks and ion backflow (IBF), all while sustaining high counting capabilities. Our simulations indicate that a quadruple-GEM detector, mirroring the triple-GEM's total thickness for the CMS upgrade, can attain comparable effective gains at significantly reduced operational voltages. These simulation endeavors offer valuable insights for future detector designs, optimization of operational conditions, and the selection of technological approaches. Prospective simulation studies, encompassing effects such as charging-up [141], discharge probabilities, and IBF, warrant further exploration and enhancement.

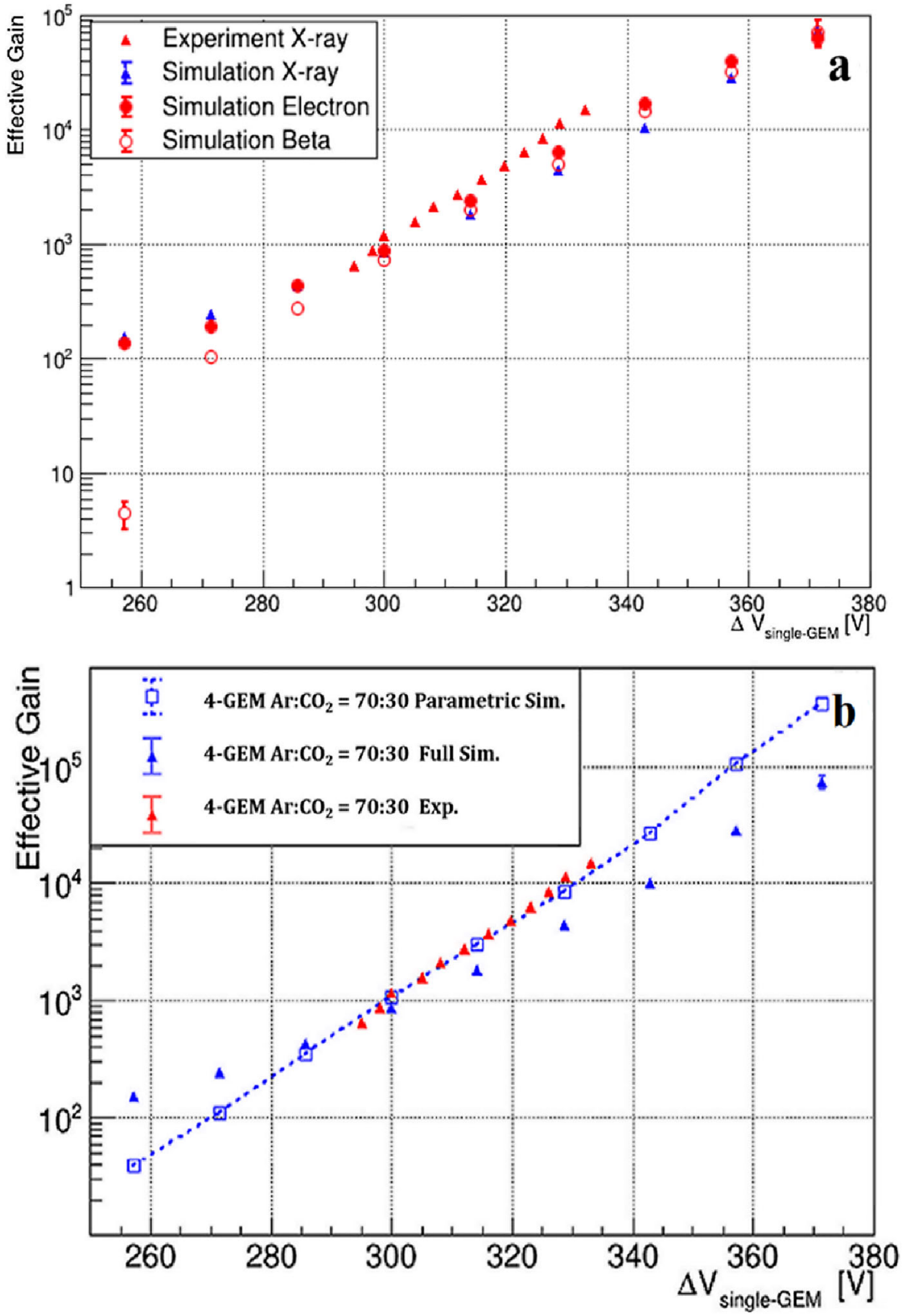

Figure 5.26 Simulated and measured effective gain as functions of the voltage drop applied on one single GEM foil for the ALICE quadruple-GEM detector operated with Ar/$CO_2$70:30, by the conventional HV divider. a Theβ^- beam, the X-ray and the free electron are adopted, respectively. The full simulation is used. b The comparison among the full simulation, parametric simulation results and the experimental data with the X-ray incident. [126]

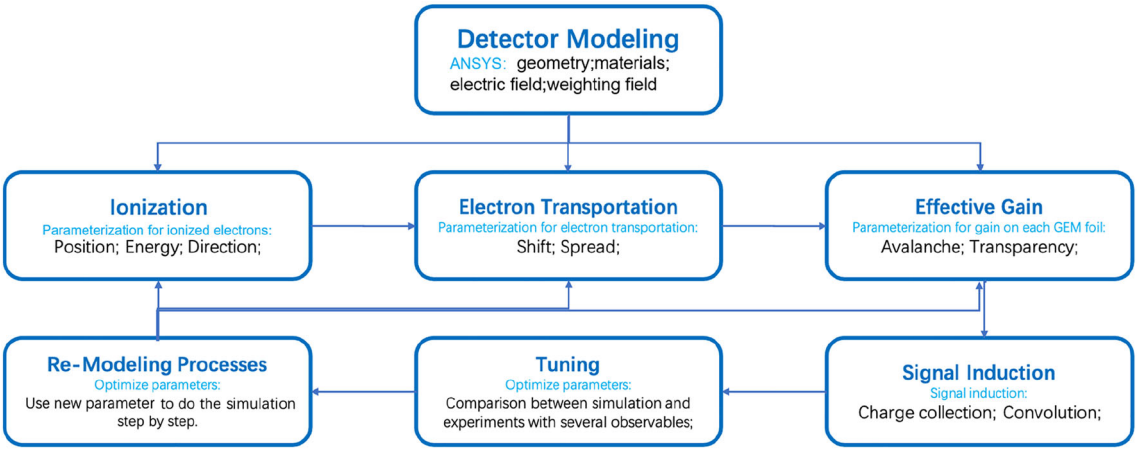

Figure 5.27 The flow chart of the parametric simulation. [126]

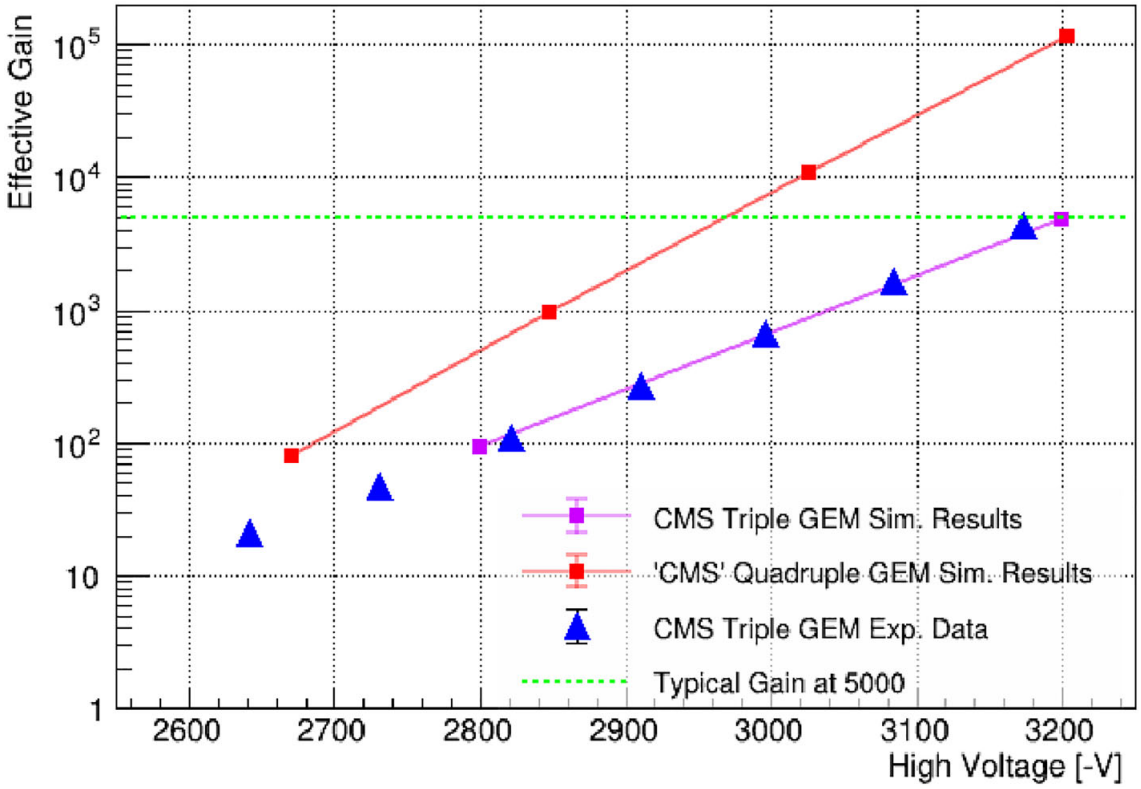

Figure 5.28 Simulated and measured effective gain as functions of the drift cathode voltage for the CMS triple-GEM and 'CMS quadruple-GEM' detectors operated with Ar/CO_2 70:30 and the X-ray, by the conventional HV dividers. The parameterization method is adopted. The relationships between the cathode voltage and the voltage drop applied on the first GEM foil for the triple-GEM and quadruple-GEM detectors are as follows: $\Delta V_{\text{First-GEM}} \approx 0.12 V_{\text{cathode}}$, $\Delta V_{\text{First-GEM}} \approx 0.11 V_{\text{cathode}}$. [126]

5.3 The barrel MIP timing detector upgrade

The MIP Timing Detector (MTD) is designed to precisely measure the arrival times of minimum ionizing particles (MIPs) with a resolution of about 30 ps and hermetic coverage up to a pseudorapidity $|\eta| = 3$. With this level of precision, the MTD will help to disentangle different interactions that occur in the same LHC bunch crossing that are distributed over time with an RMS of 180-200 ps, improving the event reconstruction and pileup mitigation of the CMS experiment during the High Luminosity LHC phase (HL-LHC). The benefits in terms of physics performance and an overview of the detector design are documented in the Technical Design Report [142]. Figure 5.29 shows a schematic view of the proposed MTD layout, comprising both BTL and ETL sections, as implemented in the GEANT simulation of the CMS detector.

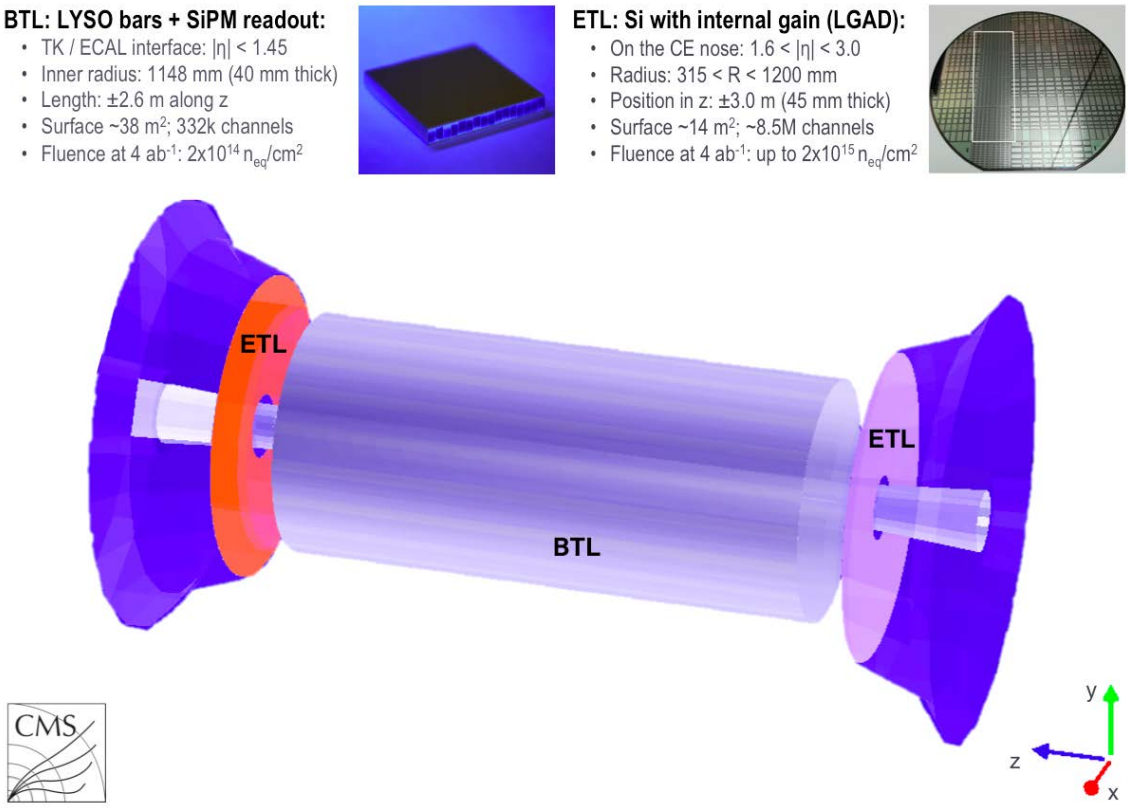

Figure 5.29 A schematic view of the GEANT geometry of the timing layers implemented in CMSSW [143] for simulation studies comprising a barrel layer (grey cylinder), at the interface between the tracker and the ECAL, and two silicon endcap (orange and light violet discs) timing layers in front of the endcap calorimeter. [142]

`Physics potential`

The physics potential offered by the MTD is derived principally from two key areas.

Firstly, pileup mitigation leverages the particle-flow event reconstruction framework outlined in preceding chapters. This process enhances the fidelity of objects associated with the vertex of interest by excluding charged tracks not emanating from that vertex and neutral calorimeter deposits likely belonging to an alternate interaction, employing statistical inference methods [144].

Fig. 5.30 vividly showcases the efficacy of space-time reconstruction amidst 200 pileup collisions, utilizing a 4D extension of the deterministic annealing approach for vertex reconstruction employed by CMS [48]. Simulations indicate a reduction in vertex merging occurrences from 15% in spatial analysis alone to merely 1% when incorporating space-time dimensions. Integrating timing data for each track, along with its z position projection onto the beam line, significantly diminishes the mis-assignment of tracks from pileup vertices to the primary interaction vertex.

Secondly, the MTD introduces additional timing data for all physics objects utilized in analyses, such as photons, MET, and others referenced in preceding chapters, enhancing sensitivity in searches and measurements. For instance, in Long-Lived Particle (LLP) searches, precise timing information can significantly boost performance.

The removal of pileup near signal candidate particles, like in b-jet identification, enhances performance notably in di-Higgs production searches, given the complex combinations of physics objects from Higgs decay modes. This improvement directly benefits the measurement of the Higgs boson's self-coupling, a top priority in the HL-LHC physics agenda. Precision timing can increase signal yields for a constant background in the HH $\rightarrow b\bar{b}\gamma\gamma$ process by 17% with barrel coverage and 22% with endcap coverage (Fig. 5.31 left). Furthermore, track-time reconstruction introduces a novel approach in neutral LLP searches, relevant in various SM extensions like Split-SUSY, GMSB, RPV SUSY, and Stealth SUSY, among others discussed in Ref. [145]. This method significantly enhances search sensitivities, even when decays are partially invisible, and provides a unique strategy for characterizing any future discoveries. Space-time data from displaced decay vertices, derived from detectable decay daughters, furnish the kinematic constraints necessary for direct LLP mass measurement, as demonstrated for a 700 GeV neutralino, χ_1^0, in Fig. 5.31 as an example.

`Technical design`

The sensor technology used to instrument the central part (up to $|\eta| = 1.48$) of the MTD, the Barrel Timing Layer (BTL), consists of Lutetium Yttrium Orthosilicate crystal bars doped with Cerium ($Lu_{1-x}Y_xSiO_5 : Ce$), abbreviated as LYSO:Ce, with dimensions of about $3 \times 3 \times$

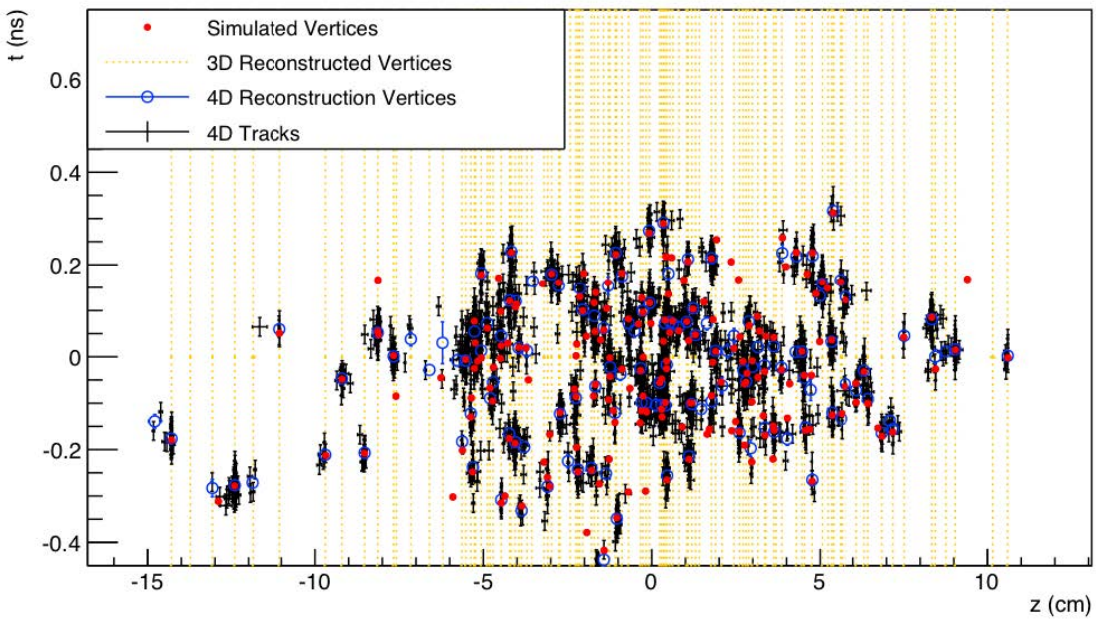

Figure 5.30 Simulated and reconstructed vertices in a bunch crossing with 200 pileup interactions are presented, assuming a MTD with approximately 30 ps time resolution covering both the barrel and endcaps. The z position along the beam line is depicted on the horizontal axis, with '0' marking the center of the interaction region (IR). The vertical axis represents time, with '0' indicating the moment when the beams fully overlap in the z dimension. Simulated vertices are shown as red dots. Vertical yellow lines delineate 3D-reconstructed vertices, which do not utilize timing information, highlighting occurrences of vertex merging across the display. Black crosses and blue open circles illustrate tracks and vertices reconstructed with a methodology that incorporates time information, hence termed '4D'. This inclusion of timing allows for the distinct separation of many vertices that, in the spatial domain alone, would seem merged. [142]

57mm^3. An overview of the detector layout is shown in figure 5.32. Crystal bars are oriented with their long axis along the ϕ direction in the CMS coordinate system, where the z axis runs along the beam line and ϕ is the azimuthal angle measured in the plane perpendicular to the beam line. The crystal width in the z direction is 3 mm, the radial thickness is varied along the same direction (3.75 mm for $|\eta| < 0.7$, 3.0 mm for $0.7 \leq |\eta| < 1.1$, 2.4 mm for $|\eta| \geq 1.1$) to maintain an approximately constant slant thickness crossed by the particles and to limit the amount of material in front of the CMS electromagnetic calorimeter. The scintillation light is measured with a pair of Silicon-Photo-Multipliers (SiPMs), one at each end of the crystal bar, matching the size of the crystal end face for optimal light collection. This layout provides the advantage of minimizing the SiPM active area per crystal surface and is thus suitable for instrumenting the large area ($38m^2$) of the MTD barrel detector with a limited

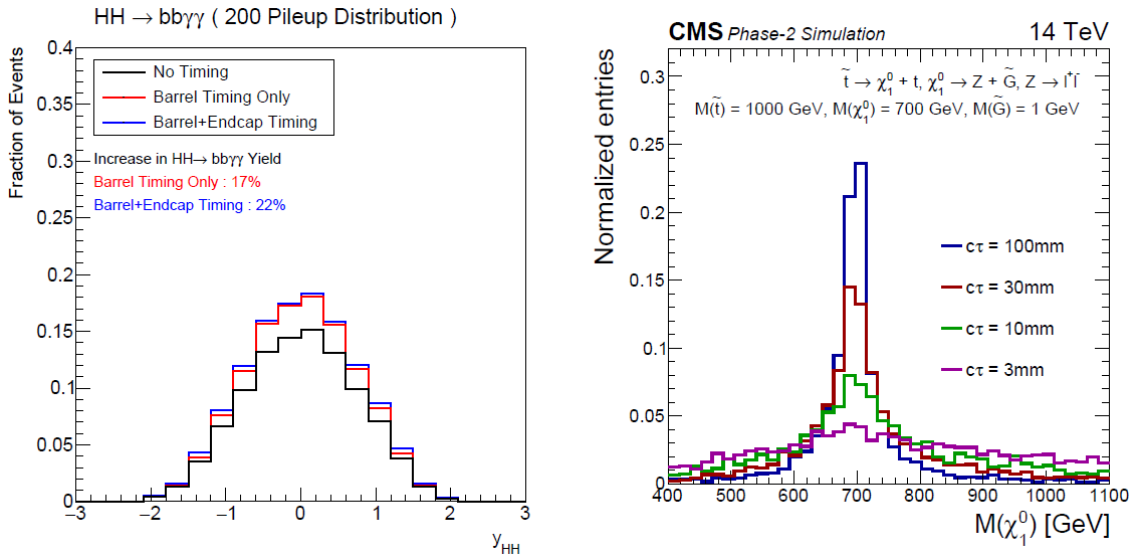

Figure 5.31 Left: Impact on signal efficiency for $HH \to b\bar{b}\gamma\gamma$ process with no-timing, barrel only timing, and barrel plus endcap timing scenarios. The quantity y_{HH} is the rapidity of the Higgs boson pair system. Right: Mass peak of a 700 GeV neutralino, $\tilde{\chi}_1^0$, with three different lifetimes reconstructed from the kinematic closure of the secondary vertex using time information with 30 ps resolution. [142]

number of channels and constrained power budget. Since the time resolution strongly depends on the thermal noise in the SiPM (dark counts), which is proportional to the active area, small area SiPMs are preferred for optimal performance. In addition, the use of two independent SiPMs for the readout of the light and the combination of their time measurements offer the dual advantage of providing a uniform spatial response of the sensor and an improvement of the time resolution by a factor of $\sqrt{2}$ with respect to a single readout per crystal. Both LYSO:Ce crystals and SiPMs were shown to be capable of withstanding the integrated radiation levels foreseen for the BTL at the end of the detector operation, amounting to a nominal fluence of about 1.9×10^{14} MeV neutron equivalent and a dose of about 32 kGy at 3000fb^{-1}.

`Test Beam experiments`

Prior to the massive production and assembly of the detector and its integration into the CMS detector, beam tests are essential for characterizing the modules' properties. These evaluations will inform subsequent adjustments and software development efforts.

The experiments which data of this presented work were conducted at the Fermilab Test Beam Facility (FTBF), utilizing 120 GeV protons sourced from the Fermilab Main Injector accelerator. Proton batches, comprising approximately 20k-50k particles per burst, were delivered over durations of about 4 seconds, termed spills. Typically, the accelerator schedule allows for a spill frequency of about once every minute. The experimental setup, positioned

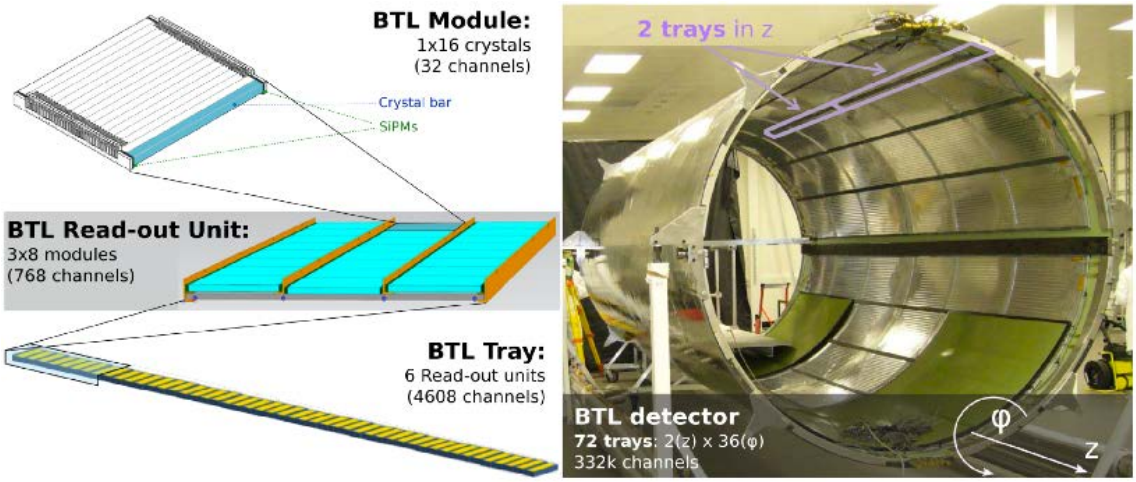

Figure 5.32 Overview of the CMS Barrel Timing Layer layout. Left: view of a BTL module, BTL Read-out Unit and BTL tray. Right: the support cylindrical structure that will host the 72 BTL trays. [142]

a few meters upstream, incorporated a 10cm^2 scintillation counter for triggering purposes, as depicted in figure 5.33. A silicon tracker telescope, consisting of twelve strip modules with a 60 μm pitch in alternating orientations along orthogonal axes, was situated ahead of the crystals and SiPMs under examination. This setup ascertained the beam particles' impact points with a precision of approximately 0.2 mm. The tested crystals and SiPMs were housed within a dark box, where the temperature was consistently maintained at approximately 12 ± 1 °C via a thermo-electric cooler, with temperature monitoring conducted by a thermistor positioned near the SiPMs. This assembly was supported by a structure that facilitated sensor rotation relative to the beam direction.

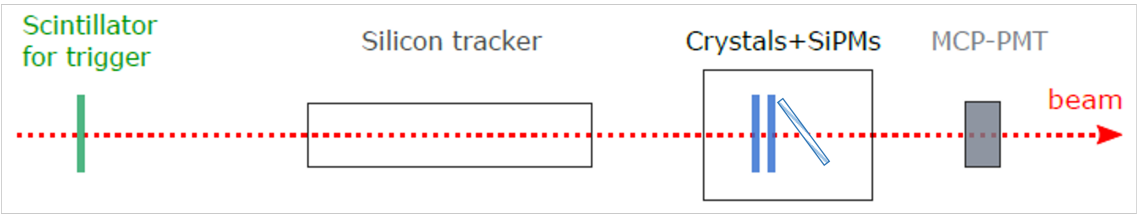

Figure 5.33 Schematic view of the beam line. From left to right, the scintillator is used for the trigger, the silicon tracker defines the MIP impinging position in theX-Y plane, the Micro Channel Plate-PMT (MCP-PMT) is used to define the reference time. The two crystal+SiPMs test setups, one for test and the other for the reference usage, the dashed one is the spined version for the energy sharing test, are positioned along the beamline. [146]

`Energy sharing`

Numerous data analyses are concurrently underway to assess varying performance metrics under different conditions, such as alterations in the cross-sectional area of the crystal bars

or the cell sizes of the SiPMs. The aim is to identify an optimal combination that balances efficiency and performance effectively. Within this scope, we present a preliminary study on energy sharing, leveraging test beam data.

In actual operational conditions at the CMS, particles emanate from the primary vertices and traverse toward the timing layer in various directions, resulting in a broad distribution of incident angles. This scenario may lead to particles depositing energy across multiple crystal bars rather than being confined to a single one. Such occurrences introduce significant challenges and uncertainties in reconstructing the correct time information.

As depicted in the sketch in Fig. 5.34 on the right, incident particles have the capability to deposit energy across multiple crystal scintillator bars when their entry is not perpendicular to the detector. Specifically, they can traverse more than 2 bars if their incident angles exceed 45 degrees. To model situations that could occur at the limits of the barrel's coverage in the test beam experiments, an incident angle of 53 degrees is chosen. This angle is representative of conditions near the edge of the barrel's coverage range. The orientation of a single crystal bar is shown in Fig. 5.34 on the left, where trajectory lengths can be determined through geometric relationships. Given the static positioning of the beam and the modules during test beam activities, our analysis will concentrate on the central bars, namely numbers 7, 8 and 9, to ensure optimal acceptance.

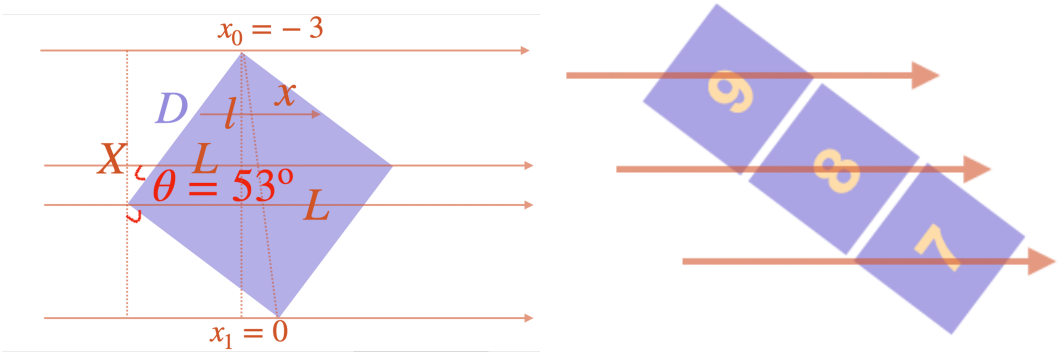

Figure 5.34 The cartoons of how the incident particles can go across more than one even three crystal bars.

Events traversing more than one LYSO bar, which are of particular interest, can be identified as follows: An event passing through a scintillator crystal results in energy deposition recorded by the Data Acquisition (DAQ) system, thus each SiPM registers an energy spectrum. By aggregating the spectra from all SiPMs involved, such as two on LYSO 7 and two on LYSO 8, a distinctive Minimum Ionizing Particle (MIP) peak becomes evident, as illustrated in Fig. 5.35 on the left. The peak region predominantly contains events passing through both

LYSO 7 and 8. Additional plots represent spectra involving LYSO 8 and 9, with the rightmost displaying events traversing LYSO 7+8+9. For research purposes, the selected energy-sharing events are those with definitive MCP recordings, exceeding a specific MCP energy threshold, and surpassing 0.7 times the MIP peak position.

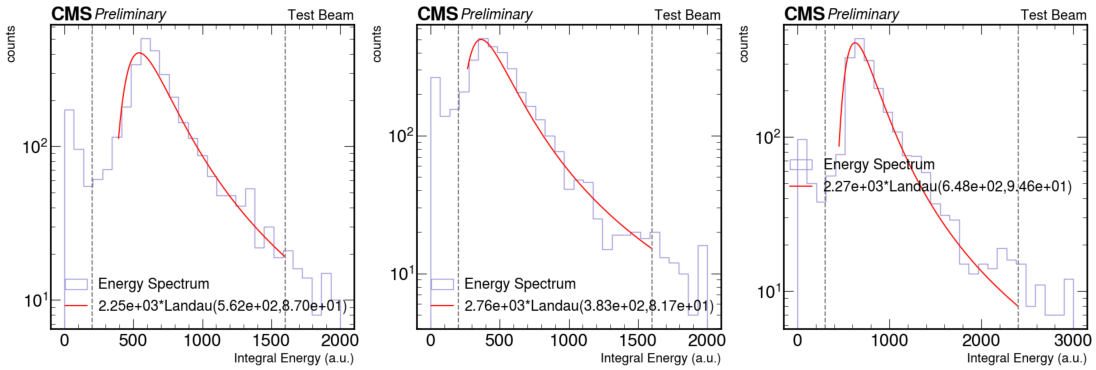

Figure 5.35 The energy spectrum get from the summation of two or three bars, on which the MIP energy peaks can easily been found. From left to right are the combinitions of LYS 7+LYSO 8, LYSO 8+LYSO 9 and LYS 7+LYSO 8+LYSO 9, respectively. The areas limited by the dashed lines are only for the fit, not data filters.

During test beam experiments analysis, two methods are utilized to ascertain time resolution when a particle traverses a single LYSO crystal, generating timing records from the SiPMs positioned at both ends of the bar. The first approach involves calculating the time difference between the records of these two SiPMs, denoted as the time of left minus right ($\Delta t = t_L - t_R$). Alternatively, the MCP timestamp can serve as a reference to determine $time = 1/2(t_L + t_R) - t_{\text{MCP}}$. Based on error propagation principles, the time resolution for $t_L - t_R$ is expressed as $\sigma(t_{\text{L-R}}) = \sqrt{\sigma(t_L)^2 + \sigma(t_R)^2}$, whereas the resolution for the second method is $\sigma(t_{\text{ave -MCP}}) = 1/2\sqrt{\sigma(t_L)^2 + \sigma(t_R)^2} = 1/2\sigma(t_{\text{L-R}})$. And our purpose is to find a way to reconstruct a time information that could bring a better resolution based on this $1/2\sigma(t_{\text{L-R}})$.

Firstly, we can compare the $1/2\sigma(t_{\text{L-R}})$ and $\sigma(t_{\text{ave -MCP}})$, which can be find in figure 5.36, where ϕ is defined as a normalized time. The upper row figures are the distribution fit by a gaussian function based on $1/2\sigma(t_{\text{L-R}})$ and the lower figures are $\sigma(t_{\text{ave -MCP}})$, from left to right are the result of bar 7, bar 8 and bar 9. The $1/2\sigma(t_{\text{L-R}})$ of the three bars are 43.4 ps, 37.5 ps, 34.7 ps, and the $\sigma(t_{\text{ave -MCP}})$ resolutions are 45.6 ps, 36.6 ps and 33.7 ps, respectively. Which are highly consistant with each other. Notablly, both results are the times after certain corrections.

For the method utilizing $1/2\sigma(t_{\text{L-R}})$, a position correction is implemented to account for the finite speed at which the light signal propagates through the LYSO bar. Given that the beam impact points are unlikely to be consistently central, the arrival times of signals at the

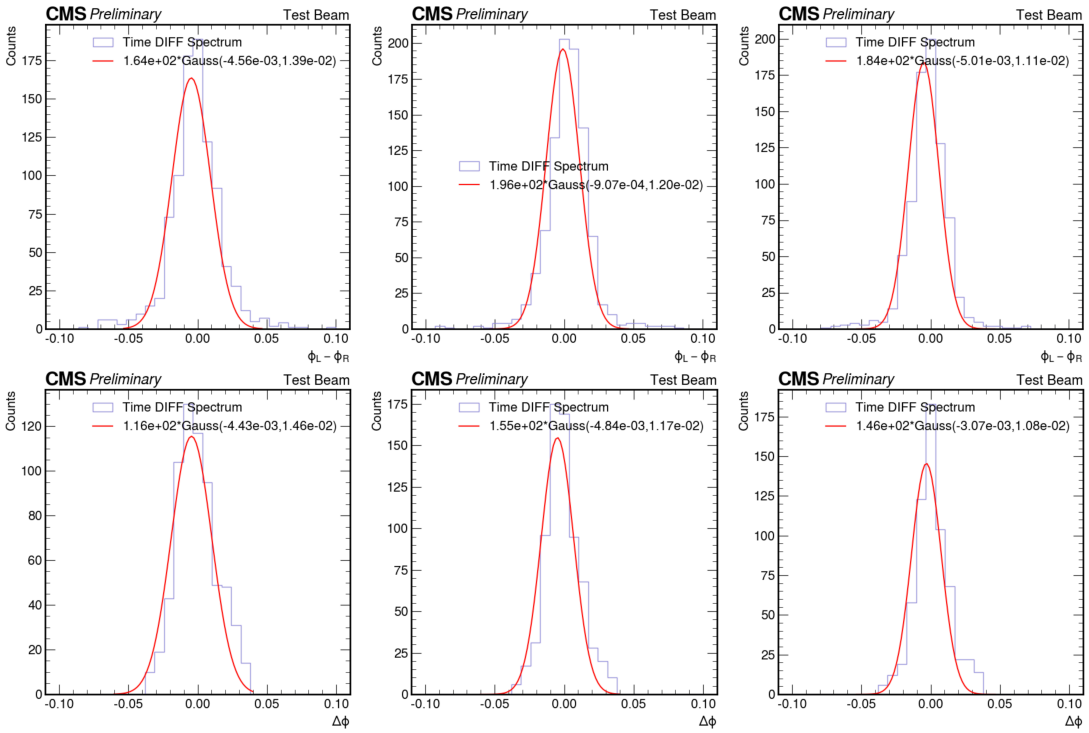

Figure 5.36 The time resolution of the single LYSO bars, the upper line are the distribution fit by a gaussian function based on $1/2\sigma(t_{\text{L-R}})$ and the lower figures are $\sigma(t_{\text{ave -MCP}})$, from left to right are the result of bar 7, bar 8 and bar 9.

SiPMs at opposing ends differ significantly. As depicted in Fig. 5.37 on the top left, the original distribution is shown with the horizontal axis representing the impact position and the vertical axis indicating the normalized $\Delta t = t_L - t_R$. A linear function is applied to model this trend, attributing its simplicity to a slope that corresponds closely with the speed of light. After applying the position correction, a more focused timing distribution is observed in the top right plot.

Regarding the $\sigma(t_{\text{ave -MCP}})$ method, an energy correction is deemed crucial. Interestingly, the position correction becomes redundant here since the $t_L + t_R$ term inherently neutralizes position-related effects. The bottom left plot of Fig. 5.37 illustrates the normalized $t_{\text{ave -MCP}}$ on the vertical axis against normalized energy on the horizontal axis. A polynomial function fits this relationship to effectuate the correction, resulting in a more focused timing distribution showcased in the bottom right plot following the energy correction.

As for the combination, we will model the process under two key assumptions. The first assumption posits that the energy deposit is proportional to the length of the particle trajectories within the crystal. Utilizing previously outlined geometrical considerations, we can develop a model for events with normalized energy deposition. The second assumption holds that the

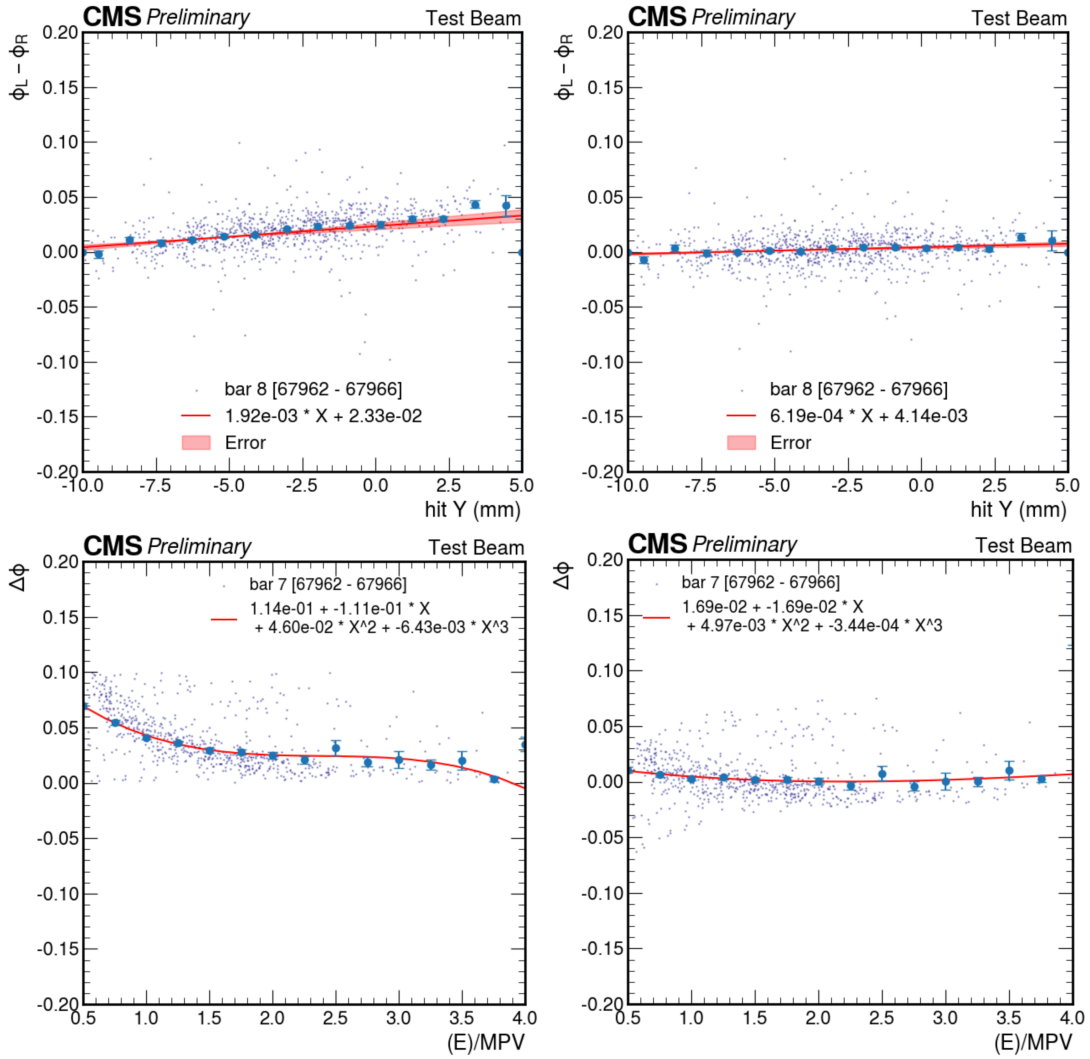

Figure 5.37 The effects of the position correction(on the top) and the energy correction(on the bottom), the left column represent the pre-correction ones and the right column is the post-correction ones.

time resolution adheres to a model contingent upon the energy deposition. The relationship with the signal amplitude, A, is characterized using two types of functional forms: a power law supplemented by a constant term:

$$f_1(A) = \frac{a}{A^\alpha} \oplus c \tag{5.10}$$

and the second model is the sum in quadrature of a stochastic s, noise n and constant term c in the form:

$$f_2(A) = \frac{s}{\sqrt{A}} \oplus \frac{n}{A} \oplus c \tag{5.11}$$

The fitting result can be find in the Fig. 5.38, since the statistic collected in this test is not sufficient, we only have several data points and only $f_2(A)$ is used for the fit.

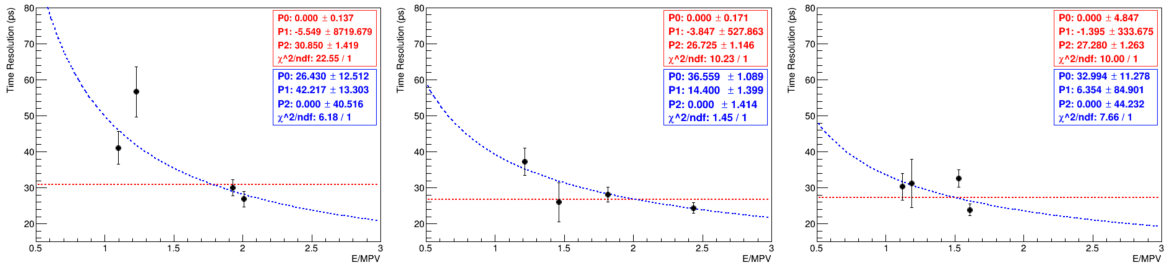

Figure 5.38 The fitting result of the correlation between the time resolution against energy deposition of bar 7, bar 8 and bar 9.

Integrating the fitting function with the geometry and based on the two foundational assumptions, we are able to compute the expected time resolution for each bar, as depicted by the colored curves in Fig. 5.39. It's observable that the time resolution significantly deteriorates for events impacting at the borders of the bars. To address this issue, we devised a composite model that combines the time resolution of the individual bars:

$$t_{\text{comb}} = \frac{\sum w_i t_i}{\sum w_i} \tag{5.12}$$

with weights $w_i = 1/\sigma_i^2$, where σ_i represents the anticipated time resolution for each bar. Here, σ_i is presumed to be inversely proportional to A_i^{α}, with A_i denoting the energy detected in the i-th bar. Employing this combined model allows for the determination of the time distribution for events intersecting more than one bar. As illustrated in Fig. 5.39 with the black curves, this method effectively rectifies the issue, yielding significantly enhanced time resolution, particularly around the bar boundaries.

Real data, filtered to include events within the MIP peak, is depicted as dots in the corresponding plot. While statistical limitations are evident, there is a discernible trend suggesting the viability of the proposed model. To validate and refine this model, it is necessary to accumulate more test beam data and develop an enhanced timing reconstruction methodology.

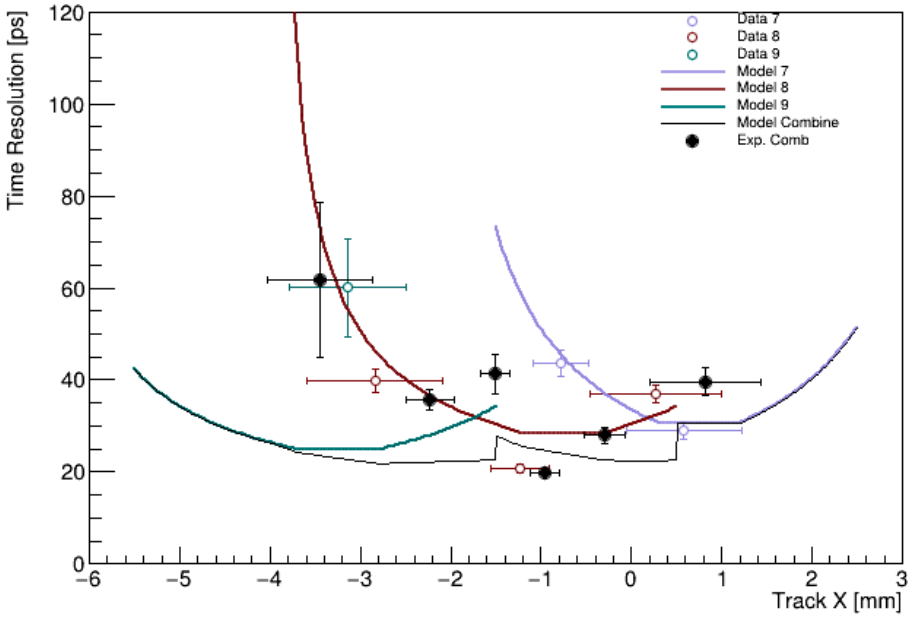

Figure 5.39 The prediction model of the time resolution of the three bars and the black curve is the prediction combined model, the black dots are the real test beam data.

Chapter 6 Conclusion

Given the accurate determination of the Higgs boson's mass and the concurrence of its observed properties with theoretical predictions, the production of Higgs boson pairs (HH) is emerging as a critical avenue for exploring the scalar sector of the SM. Such searches allow for the concurrent investigation of new resonances, anomalous couplings, and crucially, the Higgs boson self-coupling.

Utilizing the complete Run-2 proton-proton collision dataset amassed by the CMS detector from 2016 to 2018 at a center-of-mass energy of 13 TeV, we embarked on the inaugural search at the CMS experiment for the HH production process in association with a vector boson (Z/W). This analysis encompasses all decay channels of the vector boson, concentrating on the HH decay into a 4b final state. The leptonic decay channels of the vector boson facilitate the independent assessment of HHZZ and HHWW couplings.

The study notably includes a boosted topology for both one-lepton and zero-lepton channels, employing Boosted Decision Trees (BDTs) to identify regions enriched with κ_λ (HHH coupling modifier) and κ_{VV} (HHVV coupling modifier), thus optimizing sensitivity across a broad spectrum of kappa parameters. A key feature of this analysis is the strategic categorization and application of machine learning algorithms. Rather than excluding events that fail selection criteria, these are repurposed for background modeling and controlling specific background processes in the fitting procedure. Furthermore, categorization based on BDT outputs, sensitive to variations in coupling strengths, enables enhanced sensitivity throughout the entire range of coupling modifier scans. Dedicated machine learning techniques are also applied to signal extraction, with BDTs improving background modeling by re-weighting non-conforming events, thereby generating more reliable background models with reduced statistical uncertainty. We report observed (expected) upper limits at the 95% confidence level on the VHH production cross section, established at 294 (124) times the SM prediction. Constraints are also set on κ_λ, assuming κ_{VV} equals 1, and vice versa. The observed (expected) 95% confidence intervals for these coupling modifiers are $-37.7 < \kappa_\lambda < 37.2$ ($-30.1 < \kappa_\lambda < 28.9$) and $-12.2 < \kappa_{VV} < 13.5$ ($-7.2 < \kappa_{VV} < 8.9$), respectively.

From the VHH analysis, the significant contribution of machine learning technologies to high-energy physics data analysis was observed, enhancing physics performance and simplifying the analytical processes for researchers.

Further exploration into the integration of machine learning algorithms is conducted through a prospective study on HH decay into $b\bar{b}\tau^+\tau^-$ and $b\bar{b}\mu^+\mu^-$ final states. In the boosted study of $b\bar{b}\tau^+\tau^-$, utilizing CMS 2018 MC samples, an increase of at least 20% in statistics and a substantial improvement in background suppression were achieved by adopting a state-of-the-art ParticleNet boosted di-tau tagger.

For the $b\bar{b}\mu^+\mu^-$ analysis, both cut-based and machine-learning analyses, employing boosted decision trees, were conducted. These analyses were tailored to the variations in coupling strengths, with expected sensitivities derived for various integrated luminosities up to the entire high luminosity LHC phase. The anticipated 95% confidence level upper limit on Higgs boson pair production is estimated to be 47 (28) times the Standard Model cross-section for gluon-gluon fusion production using the cut-based method (boosted decision trees). The projected 95% confidence level constraints on the couplings are -13.8 < κ_λ < 19.1 (-10.0 < κ_λ < 15.5) using the cut-based method (boosted decision trees), respectively, with an assumed integrated luminosity of 3000 fb^{-1}.

The advancement of physics research is contingent not only on software innovations but crucially on the development of hardware for experiments.

In the final, yet critical, section of this thesis, we introduce a significant upgrade project for the CMS sub-detector system, designed to address the challenges posed by the high-luminosity LHC operation environment. This includes the high radiation doses that can affect detector longevity and the high pile-up rates that may compromise the precision of reconstructions and measurements. The Endcap Muon system will undergo an upgrade with the addition of new gaseous electron multiplier (GEM) chambers to enhance trigger acceptance and efficiency. The assembly and quality control processes have been established, with one model (GE1/1) already installed and tested during Run-3. To mitigate pile-up effects, a new timing layer will be implemented in both the barrel and endcap regions. The introduction of an extra time dimension is poised to significantly reduce the impact of high pile-up, thereby unlocking additional physics potential. Test beams and dedicated reconstruction algorithms are currently being developed to accommodate the upcoming operational scenarios.

Appendix

.1 ZHH NNLO vs LO Reweighting

In this analysis, the cross sections of ZHH and WHH processes are corrected to NNLO and NLO respectively. The k-factors are derived using corresponding NNLO and NLO signal samples with SM-like couplings and applied to all other modified couplings. The study shows that the differences between higher order and leading order did not only affect larger cross section (normalisation) but also depend on kinematics of the bosons. The vector boson and leading Higgs boson from loop-induced gluon fusion process tend to be more boosted as shown in Fig. 1, while the second Higgs boson shows no difference.

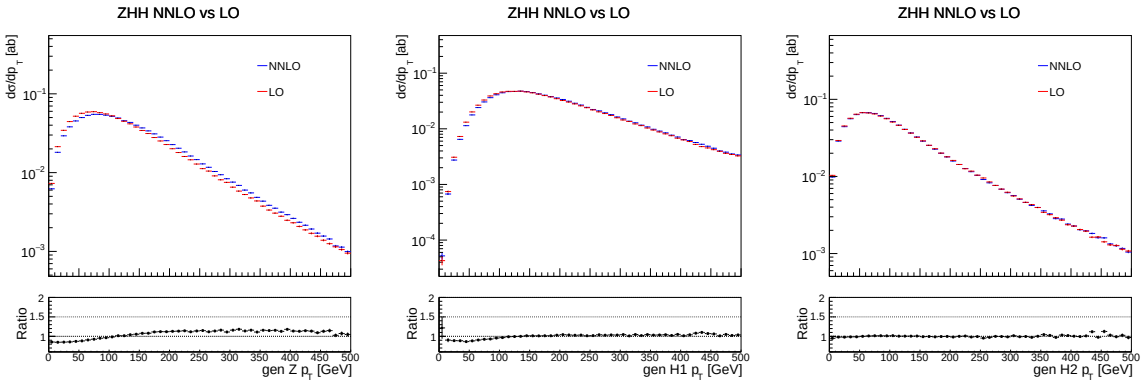

Figure 1 Distributions of transverse momenta of the Z (left), leading Higgs (middle) and second Higgs bosons (right) comparing between NNLO and LO at generator level and scaled to NNLO cross section.

Therefore, we also derived the k-factor as a function of transverse momentum of the Z bosons at generator level using ZHH signal samples without signal selection. The distributions of transverse momenta of the Z and Higgs bosons after NNLO reweighting are shown in Fig. 2. And the k-fractors are the black line in Fig. 4.

After signal selection with 4 b-jets requirement and NNLO reweighting, there is additional difference on transverse momenta of the Z and leading Higgs boson at generator level, see Fig. 3. The residual difference on these distributions is considered as systematic uncertainty on the NNLO reweighting method and applied to final statistical analysis. The up and down variations, together with the nominal k-factor are parametrized with polynomial degree two function (quadratic) in order to get smooth k-factors along the p_T range, shown in Fig. 4.

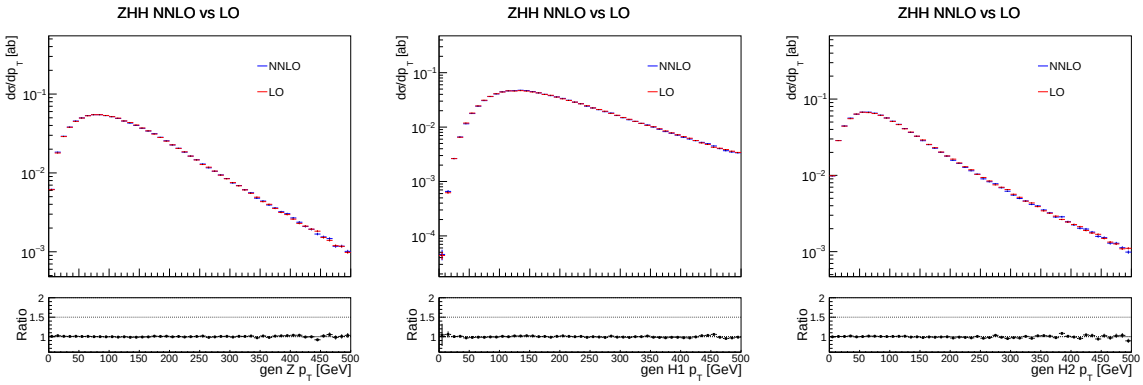

Figure 2 Distributions of transverse momenta of the Z (left), leading Higgs (middle) and second Higgs bosons (right) comparing between NNLO and LO at generator level and scaled to NNLO cross section after NNLO reweighting.

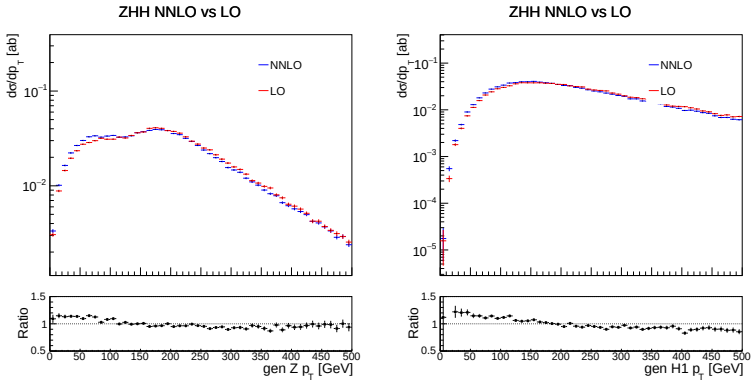

Figure 3 Distributions of transverse momenta of the Z boson (left) and leading Higgs boson (right) comparing between NNLO and LO at generator level after signal selection and NNLO reweighting, and scaled to NNLO cross section.

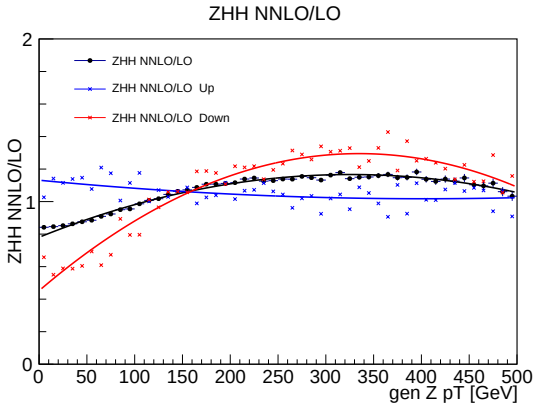

Figure 4 ZHH NNLO/LO as a function of transverse momentum of the Z boson at generator level (Fig. 2 left bottom plot) with up and down variations taken from residual difference appeared after signal selection (Fig. 3 left bottom plot). The curves are further parametrized and used in the analysis.

.2 VHH topology priority

Since multiple topologies are considered and dedicated selections are applied, some events can be classified into more than 1 topology. We use the expected limit as the figure of merit and did 2 tests. First categorize all these events as Resolved events, the expected limits are shown in Fig. 5 with label ”R priority”. Then we repeat the limit scan but this time categorize all these events as Boosted events. the expected limits are shown in Fig. 5 with label ”B priority”. Fig. 5 shows classifying events as Boosted is better for both 1L and MET channels. Of course one might come up with a strategy to categorize overlapped events event by event, but we think the current categorization is already good enough if not optimal.

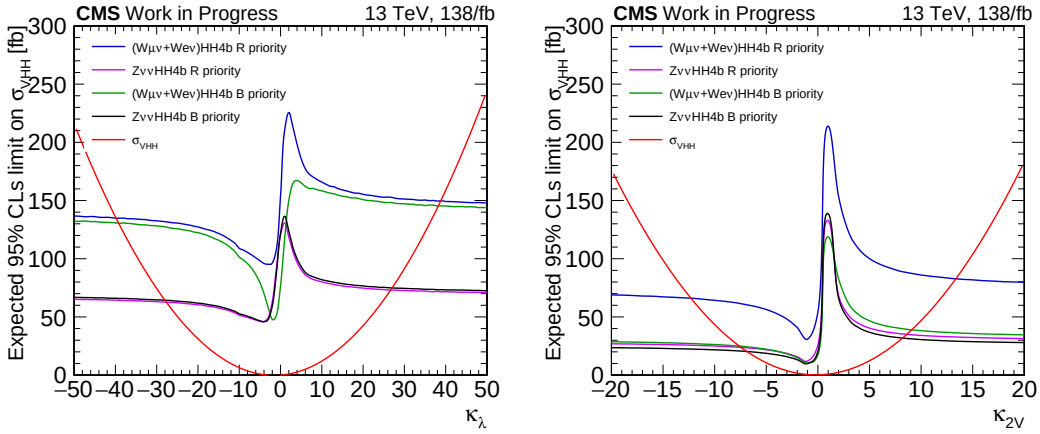

Figure 5 combination of limit scans to show what’s the best strategy to classify the events that can be included in both resolved and boosted topology. The ”B priority” is better so we prioritize boosted topology in this analysis.

.3 Nuisance pulls and impacts from fit of VHH

Only the leading significant nuisance are listed in this section.

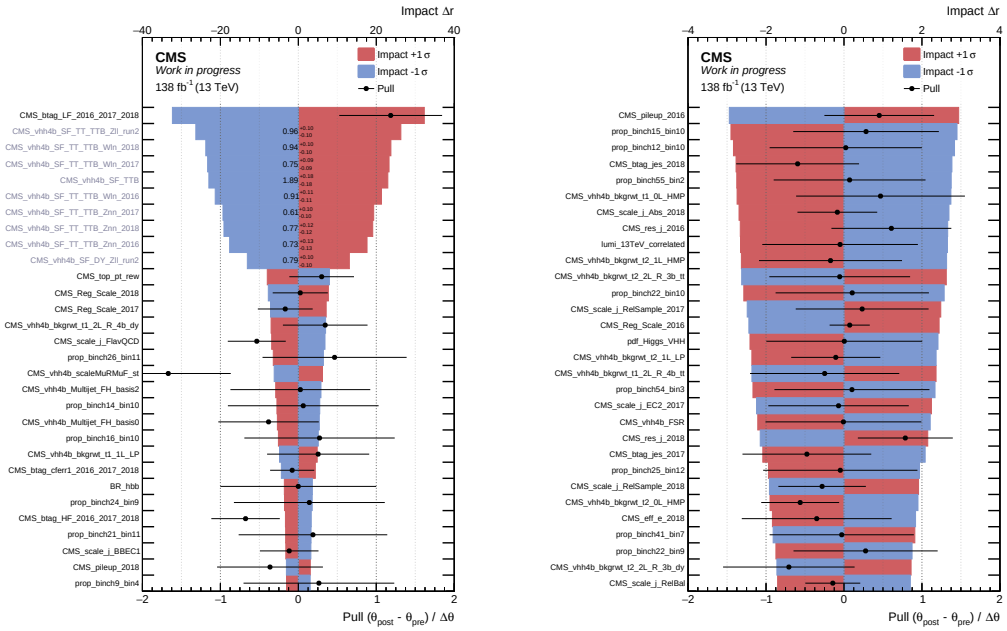

Figure 6 Pulls and impacts of nuisance parameters in the combined fit.

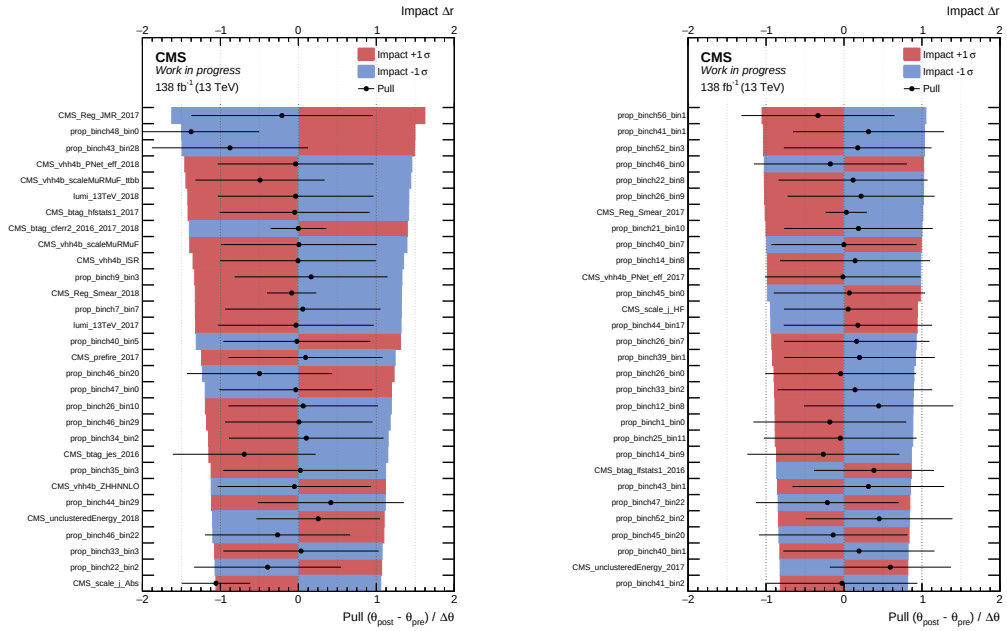

Figure 7 Pulls and impacts of nuisance parameters in the combined fit (continued).

References

[1] Chicago Sandbox Studio. Image courtesy of symmetry magazine, a joint fermilab/slac publication. artwork by sandbox studio, chicago., 2020. Accessed on Date (January 18, 2024).

[2] SIzaak Neutelings. Graphical representation of the weak hypercharge y and isospin i3 quantum number (of u(1)y and su(2)l) of the standard model particles, as well as for different types of leptoquarks., 2022. Accessed on Date (January 30, 2024).

[3] François Englert and Robert Brout. Broken symmetry and the mass of gauge vector mesons. *Physical review letters*, 13(9):321, 1964.

[4] Peter W Higgs. Broken symmetries and the masses of gauge bosons. *Physical review letters*, 13(16):508, 1964.

[5] Gerald S Guralnik, Carl R Hagen, and Thomas WB Kibble. Global conservation laws and massless particles. *Physical Review Letters*, 13(20):585, 1964.

[6] Jeffrey Goldstone. Field theories with «superconductor» solutions. *Il Nuovo Cimento (1955-1965)*, 19:154–164, 1961.

[7] Gerardus' t Hooft. Renormalizable lagrangians for massive yang-mills fields. *Nuclear physics: B*, 35(1):167–188, 1971.

[8] J Baglio, Abdelhak Djouadi, R Gröber, Margarete M Mühlleitner, Jérémie Quevillon, and Michael Spira. The measurement of the higgs self-coupling at the lhc: theoretical status. *Journal of High Energy Physics*, 2013(4):1–40, 2013.

[9] R Frederix, S Frixione, V Hirschi, Fabio Maltoni, Olivier Mattelaer, P Torrielli, Eleni Vryonidou, and M Zaro. Higgs pair production at the lhc with nlo and parton-shower effects. *Physics Letters B*, 732:142–149, 2014.

[10] Massimiliano Grazzini, Gudrun Heinrich, Stephen Jones, Stefan Kallweit, Matthias Kerner, Jonas M Lindert, and Javier Mazzitelli. Higgs boson pair production at nnlo with top quark mass effects. *Journal of High Energy Physics*, 2018(5):1–21, 2018.

[11] Biagio Di Micco, Maxime Gouzevitch, Javier Mazzitelli, and Caterina Vernieri. Higgs boson potential at colliders: Status and perspectives. *Reviews in Physics*, 5:100045, 2020.

[12] Fabio Maltoni, Giovanni Ridolfi, and Maria Ubiali. b-initiated processes at the lhc: a reappraisal. *Journal of High Energy Physics*, 2012(7):1–49, 2012.

[13] Daniel de Florian, D Fontes, J Quevillon, M Schumacher, FJ Llanes-Estrada, AV Gritsan, E Vryonidou, A Signer, P de Castro Manzano, D Pagani, et al. *arXiv: Handbook of LHC Higgs Cross Sections: 4. Deciphering the Nature of the Higgs Sector*. Number arXiv: 1610.07922. Cern, 2016.

[14] Luca Cadamuro. *Search for Higgs Boson Pair Production in the bb $\tau+\tau$-Decay Channel: with the CMS detector at the LHC*. Springer, 2018.

[15] Morad Aaboud et al. Search for pair production of Higgs bosons in the $b\bar{b}b\bar{b}$ final state using proton-proton collisions at $\sqrt{s}$ = 13 TeV with the ATLAS detector. *JHEP*, 01:030, 2019.

[16] Albert M Sirunyan et al. Search for nonresonant Higgs boson pair production in the $b\bar{b}b\bar{b}$ final state at $\sqrt{s}$ = 13 TeV. *JHEP*, 04:112, 2019.

[17] Morad Aaboud et al. Search for resonant and non-resonant Higgs boson pair production in the $b\bar{b}\tau^+\tau^-$ decay channel in pp collisions at $\sqrt{s}$ = 13 TeV with the ATLAS detector. *Phys. Rev. Lett.*, 121:191801, 2018. [Erratum: Phys.Rev.Lett. 122, 089901 (2019)].

[18] Albert M Sirunyan et al. Search for Higgs boson pair production in events with two bottom quarks and two tau leptons in proton-proton collisions at $\sqrt{s}$ =13TeV. *Phys. Lett. B*, 778:101, 2018.

[19] Morad Aaboud et al. Search for Higgs boson pair production in the $b\bar{b}WW^*$ decay mode at $\sqrt{s}$ = 13 TeV with the ATLAS detector. *JHEP*, 04:092, 2019.

[20] Albert M Sirunyan et al. Search for resonant and nonresonant Higgs boson pair production in the $b\bar{b}\ell\nu\ell\nu$ final state in proton-proton collisions at $\sqrt{s}$ = 13 TeV. *JHEP*, 01:054, 2018.

[21] M. Aaboud et al. Search for Higgs boson pair production in the $\gamma\gamma b\bar{b}$ final state with 13 TeV pp collision data collected by the ATLAS experiment. *JHEP*, 11:040, 2018.

[22] Albert M Sirunyan et al. Search for Higgs boson pair production in the $\gamma\gamma b\bar{b}$ final state in pp collisions at $\sqrt{s}$ = 13 TeV. *Phys. Lett. B*, 788:7, 2019.

[23] Morad Aaboud et al. Search for Higgs boson pair production in the $\gamma\gamma WW^*$ channel using pp collision data recorded at $\sqrt{s}$ = 13 TeV with the ATLAS detector. *Eur. Phys. J. C*, 78:1007, 2018.

[24] Morad Aaboud et al. Search for Higgs boson pair production in the $WW^{(*)}WW^{(*)}$ decay channel using ATLAS data recorded at $\sqrt{s}$ = 13 TeV. *JHEP*, 05:124, 2019.

[25] Georges Aad et al. Search for non-resonant Higgs boson pair production in the $bb\ell\nu\ell\nu$ final state with the ATLAS detector in pp collisions at $\sqrt{s}$ = 13 TeV. *Phys. Lett. B*, 801:135145, 2020.

[26] Albert M Sirunyan et al. Search for nonresonant Higgs boson pair production in final states with two bottom quarks and two photons in proton-proton collisions at $\sqrt{s}$ = 13 TeV. *JHEP*, 03:257, 2021.

[27] Sandeep Bhowmik. Search for di-higgs boson production in multi-lepton final states at cms. Technical report, 2023.

[28] Georges Aad et al. Search for the $HH \to b\bar{b}b\bar{b}$ process via vector-boson fusion production using proton-proton collisions at $\sqrt{s}$ = 13 TeV with the ATLAS detector. *JHEP*, 07:108, 2020.

[29] Lyndon Evans and Philip Bryant. Lhc machine. *Journal of instrumentation*, 3(08):S08001, 2008.

[30] Esma Anais Mobs. The cern accelerator complex. Technical report, 2016.

[31] Maria Florencia Canelli, Thea K Aarrestad, Danyyl Brzhechko, Lea Caminada, Annapaoloa De Cosa, Riccardo Del Burgo, Silvio Donato, Camilla Galloni, Tomas Hreus, Stefanos Leontsinis, et al. Measurement of the inelastic proton-proton cross section at *sqrts*= 13 tev. *Journal of High Energy Physics*, 7:161, 2018.

[32] Technical Proposal for the Phase-II Upgrade of the CMS Detector. 6 2015.

[33] HiLumi Collaboration et al. The hl-lhc project. *URL https://hilumilhc. web. cern. ch/content/hl-lhc-project*, 2020.

[34] ATLAS Collaboration et al. The atlas experiment at the cern large hadron collider jinst 3. *S08003*, pages 1–407, 2008.

[35] Oscar Adriani, Lorenzo Bonechi, Massimo Bongi, G Castellini, Raffaello D'Alessandro, DA Faus, K Fukui, M Grandi, M Haguenauer, Y Itow, et al. The lhcf detector at the cern large hadron collider. *Journal of Instrumentation*, 3(08):S08006, 2008.

[36] ALICE collaboration, K Aamodt, et al. The alice experiment at the cern lhc. jinst 3, s08002 (2008), 2008.

[37] CMS Collaboration, S Chatrchyan, G Hmayakyan, V Khachatryan, AM Sirunyan, W Adam, T Bauer, T Bergauer, H Bergauer, M Dragicevic, et al. The cms experiment at the cern lhc. *Jinst*, 3:S08004, 2008.

[38] Giovanni Anelli, G Antchev, P Aspell, V Avati, MG Bagliesi, V Berardi, M Berretti, V Boccone, Ubaldo Bottigli, M Bozzo, et al. The totem experiment at the cern large hadron collider. *Journal of Instrumentation*, 3(08):S08007, 2008.

[39] TL Collaboration, A Augusto Alves, LM Andrade Filho, AF Barbosa, I Bediaga, G Cernicchiaro, G Guerrer, HP Lima, AA Machado, J Magnin, et al. The lhcb detector at the lhc. *Journal of instrumentation*, 3(08):S08005–S08005, 2008.

[40] James Pinfold, K Kinoshita, R Soluk, J Jakubek, Y Yao, D Felea, DH Lacarrère, L Patrizii, S Cecchini, T Hott, et al. Technical design report of the moedal experiment. Technical report, 2009.

[41] Tai Sakuma. Cutaway diagrams of cms detector. In *J. Phys.: Conf. Ser. 513 022032*, number CMS-OUTREACH-2019-001, 2019.

[42] Izaak Neutelings. How to draw diagrams in latex with tikz. *URL https://wiki. physik. uzh. ch/cms/latex: tikz.[44] CMS Collaboration. CMS Physics Technical Design Report*, 1, 2017.

[43] G Acquistapace, CMS Collaboration, et al. Cms, the magnet project: Technical design report. *Technical Design Report CMS*, 1997.

[44] COSMIC RAYS. Precise mapping of the magnetic field in the cms barrel yoke using cosmic rays.

[45] CMS Collaboration. Cms muon project technical design report. *Preprint*, pages 97–32, 1997.

[46] CMS collaboration et al. The cms tracker: addendum to the technical design report. Technical report, CERN-LHCC-2000-016, 2000.

[47] CMS Collaboration. Images for us lhc cms detector upgrade project. Accessed on Date (January 18, 2024).

[48] CMS collaboration et al. Description and performance of track and primary-vertex reconstruction with the cms tracker. *Journal of Instrumentation*, 9(10):P10009, 2014.

[49] CMS Collaboration. The electromagnetic calorimeter project, technical design report cern. *LHCC 97*, 33, 1997.

[50] GL Bayatian, A Korablev, A Soha, O Sharif, M Chertok, W Mitaroff, F Pauss, V Genchev, M Wensveen, V Lemaitre, et al. Cms physics: technical design report volume 1: detector performance and software. Technical report, CMS-TDR-008-1, 2006.

[51] A. M. Sirunyan et al. Performance of the CMS muon detector and muon reconstruction with proton-proton collisions at $\sqrt{s}$ = 13 TeV. *JINST*, 13(06):P06015, 2018.

[52] A Bell, E Castro, R Hall-Wilton, W Lange, W Lohmann, A Macpherson, M Ohlerich, N Rodriguez, V Ryjov, RS Schmidt, et al. Fast beam conditions monitor bcm1f for the cms experiment. *Nuclear Instruments and Methods in Physics Research Section A: Accelerators, Spectrometers, Detectors and Associated Equipment*, 614(3):433–438, 2010.

[53] CMS Luminosity Measurements for the 2016 Data Taking Period. 2017.

[54] CMS luminosity measurement for the 2017 data-taking period at $\sqrt{s}$ = 13 TeV. 2018.

[55] CMS luminosity measurement for the 2018 data-taking period at $\sqrt{s}$ = 13 TeV. 2019.

[56] Georges Aad, Tatevik Abajyan, B Abbott, J Abdallah, S Abdel Khalek, Ahmed Ali Abdelalim, R Aben, B Abi, M Abolins, OS AbouZeid, et al. Observation of a new particle in the search for the standard model higgs boson with the atlas detector at the lhc. *Physics Letters B*, 716(1):1–29, 2012.

[57] Serguei Chatrchyan, Vardan Khachatryan, Albert M Sirunyan, Armen Tumasyan, Wolfgang Adam, Ernest Aguilo, Thomas Bergauer, M Dragicevic, J Erö, C Fabjan, et al. Observation of a new boson at a mass of 125 gev with the cms experiment at the lhc. *Physics Letters B*, 716(1):30–61, 2012.

[58] John D Barrow and Michael S Turner. Baryosynthesis and the origin of galaxies. *Nature*, 291(5815):469–472, 1981.

[59] Daniel de Florian, D Fontes, J Quevillon, M Schumacher, FJ Llanes-Estrada, AV Gritsan, E Vryonidou, A Signer, P de Castro Manzano, D Pagani, et al. *arXiv: Handbook of LHC Higgs Cross Sections: 4. Deciphering the Nature of the Higgs Sector*. Number arXiv: 1610.07922. Cern, 2016.

[60] Lhc higgs cross section hh sub-group (a.k.a lhc-hh). `https://twiki.cern.ch/twiki/bin/view/LHCPhysics/LHCHWGHH`.

[61] HH Inference Tools. `https://gitlab.cern.ch/hh/tools/inference`, 2021.

[62] E.H. Moore. On the reciprocal of the general algebraic matrix. *Bull. Amer. Math. Soc.*, 26:385–396, 1920.

[63] R. Penrose. A generalized inverse for matrices. *Nature*, 51:406–413, July 1955.

[64] Johan Alwall, R Frederix, S Frixione, V Hirschi, Fabio Maltoni, Olivier Mattelaer, H-S Shao, T Stelzer, P Torrielli, and M Zaro. The automated computation of tree-level and next-to-leading order differential cross sections, and their matching to parton shower simulations. *Journal of High Energy Physics*, 2014(7):1–157, 2014.

[65] Andrej Saibel. Study of $\bar{t}t$ + $b\bar{b}$ modelling and uncertainties of monte carlo generators for the $\bar{t}th$ ($b\bar{b}$)-analysis at the cms experiment. 2017.

[66] Maximilian Maria Horzela. Merging of $t\bar{t}$ and $t\bar{t}$+$b\bar{b}$ simulations for an improved background modeling for $t\bar{t}$H($b\bar{b}$) measurements. Master's thesis, Karlsruhe Institute of Technology (KIT), 2019.

[67] A. M. Sirunyan et al. Particle-flow reconstruction and global event description with the CMS detector. *JINST*, 12:P10003, 2017.

[68] Albert M Sirunyan et al. A deep neural network for simultaneous estimation of b jet energy and resolution. *Comput. Softw. Big Sci.*, 4:10. 20 p, Dec 2019. Submitted to Computing and Software for Big Science. All figures and tables can be found at http://cms-results.web.cern.ch/cms-results/public-results/publications/HIG-18-027 (CMS Public Pages).

[69] E. Bols, J. Kieseler, M. Verzetti, M. Stoye, and A. Stakia. Jet flavour classification using deepjet. *Journal of Instrumentation*, 15(12):P12012–P12012, Dec 2020.

[70] Huilin Qu and Loukas Gouskos. Jet tagging via particle clouds. *Physical Review D*, 101(5):056019, 2020.

[71] Albert M Sirunyan, Armen Tumasyan, Wolfgang Adam, Janik Walter Andrejkovic, Thomas Bergauer, Suman Chatterjee, Marko Dragicevic, A Escalante Del Valle, Rudolf Fruehwirth, Manfred Jeitler, et al. Precision luminosity measurement in proton–proton collisions at s= 13\, tev s= 13 tev in 2015 and 2016 at cms. *The European Physical Journal C*, 81:1–42, 2021.

[72] CMS collaboration, CMS Collaboration, et al. Cms luminosity measurement for the 2017 data-taking period at $\sqrt{S}$ = 13 tev. *CMS Physics Analysis Summary CMS-PAS-LUM-17-004*, page 90, 2018.

[73] CMS Collaboration et al. Cms luminosity measurement for the 2018 data-taking period at $\sqrt{S}$ = 13 tev. cms physics analysis summary cms-pas-lum-18-002 (2019). *URL: https://cds. cern. ch/record/2676164*.

[74] Albert M Sirunyan et al. Performance of missing transverse momentum reconstruction in proton-proton collisions at $\sqrt{S}$ = 13 tev using the cms detector. *Journal of Instrumentation*, 2019.

[75] J. Ross Quinlan. Simplifying decision trees. *International journal of man-machine studies*, 27(3):221–234, 1987.

[76] Helge Voss, Andreas Höcker, Jörg Stelzer, and Fredrik Tegenfeldt. Tmva, the toolkit for multivariate data analysis with root. In *XI International Workshop on Advanced Computing and Analysis Techniques in Physics Research*, volume 50, page 040. Sissa Medialab, 2009.

[77] Fabian Pedregosa, Gaël Varoquaux, Alexandre Gramfort, Vincent Michel, Bertrand Thirion, Olivier Grisel, Mathieu Blondel, Peter Prettenhofer, Ron Weiss, Vincent Dubourg, et al. Scikit-learn: Machine learning in python. *J. Mach. Learn. Res.*, 12:2825, 2011.

[78] J. Thaler and K. Van Tilburg. Identifying boosted objects with N-subjettiness. *JHEP*, 03:015, 2011.

[79] Search for Higgs boson pair production with one associated vector boson in proton-proton collisions at $\sqrt{s}$ = 13 TeV. 2023.

[80] J. Alison, P. Bryant and C. Liu. Search for zz, zh and hh production in the four b-jet final state. (AN-19-254), 2022. CMS AN-19-254.

[81] The ATLAS collaboration. Search for pair production of higgs bosons in the bbbb final state using proton-proton collisions at sqrt(s)=13 tev with the atlas detector. *Journal of High Energy Physics*, 2019(1):30, Jan 2019.

[82] Sm higgs branching ratios and total decay widths. *CMS twiki*, CERN Yellow Report Page Branch Ratio twiki, 2016.

[83] Procedure for the LHC Higgs boson search combination in Summer 2011. 8 2011.

[84] Glen Cowan, Kyle Cranmer, Eilam Gross, and Ofer Vitells. Asymptotic formulae for likelihood-based tests of new physics. *The European Physical Journal C*, 71:1–19, 2011.

[85] Thomas Junk. Confidence level computation for combining searches with small statistics. *Nuclear Instruments and Methods in Physics Research Section A: Accelerators, Spectrometers, Detectors and Associated Equipment*, 434(2-3):435–443, 1999.

[86] Alexander L Read. Presentation of search results: the cls technique. *Journal of Physics G: Nuclear and Particle Physics*, 28(10):2693, 2002.

[87] Robert D Cousins. Generalization of chisquare goodness-of-fit test for binned data using saturated models, with application to histograms. *URL: http://www. physics. ucla. edu/~ cousins/stats/cousins_saturated. pdf (visited on 11/04/2021)*, 2013.

[88] ATLAS and CMS Collaborations, and LHC Higgs Combination Group. Procedure for the LHC Higgs boson search combination in Summer 2011. Technical Report CMS-NOTE-2011-005, ATL-PHYS-PUB-2011-11, 2011.

[89] Eilam Gross and Ofer Vitells. Trial factors for the look elsewhere effect in high energy physics. *Eur. Phys. J. C*, 70:525, 2010.

[90] CMS Collaboration. Search for nonresonant Higgs boson pair production in final state with two bottom quarks and two tau leptons in proton-proton collisions at $\sqrt{s}$ = 13 TeV. *Phys. Lett. B*, 842:137531, 2023.

[91] Armen Tumasyan et al. Search for Nonresonant Pair Production of Highly Energetic Higgs Bosons Decaying to Bottom Quarks. *Phys. Rev. Lett.*, 131(4):041803, 2023.

[92] CMS collaboration et al. Identification of hadronic tau lepton decays using a deep neural network. *arXiv preprint arXiv:2201.08458*, 2022.

[93] CMS collaboration et al. Performance of τ-lepton reconstruction and identification in cms. *Journal of Instrumentation*, 7(01):P01001, 2012.

[94] Albert M Sirunyan, Armen Tumasyan, Wolfgang Adam, Thomas Bergauer, Marko Dragicevic, Janos Erö, Alberto Escalante Del Valle, Rudolf Fruehwirth, Manfred Jeitler, Natascha Krammer, et al. Evidence for higgs boson decay to a pair of muons. *Journal of High Energy Physics*, 2021(1):1–68, 2021.

[95] ATLAS collaboration et al. A search for the dimuon decay of the standard model higgs boson with the atlas detector. *arXiv preprint arXiv:2007.07830*, 2020.

[96] Ulrich Baur, Tilman Plehn, and David Rainwater. Probing the higgs self-coupling at hadron colliders using rare decays. *Physical Review D*, 69(5):053004, 2004.

[97] Amit Adhikary, Rahool Kumar Barman, and Biplob Bhattacherjee. Prospects of non-resonant di-higgs searches and higgs boson self-coupling measurement at the he-lhc using machine learning techniques. *Journal of High Energy Physics*, 2020(12):1–47, 2020.

[98] G Heinrich, Stephen Philip Jones, M Kerner, G Luisoni, and E Vryonidou. Nlo predictions for higgs boson pair production with full top quark mass dependence matched to parton showers. *Journal of High Energy Physics*, 2017(8):1–26, 2017.

[99] G Heinrich, SP Jones, M Kerner, G Luisoni, and L Scyboz. Probing the trilinear higgs boson coupling in di-higgs production at nlo qcd including parton shower effects. *Journal of High Energy Physics*, 2019(6):1–17, 2019.

[100] Armen Tumasyan, Wolfgang Adam, Janik Walter Andrejkovic, Thomas Bergauer, Suman Chatterjee, Konstantinos Damanakis, Marko Dragicevic, A Escalante Del Valle, Rudolf Fruehwirth, Manfred

Jeitler, et al. Search for higgs boson pair production in the four b quark final state in proton-proton collisions at $\sqrt{S}$ = 13 tev. *Physical review letters*, 129(8):081802, 2022.

[101] Botao Guo, Xiaohu Sun, Licheng Zhang, Zhe Li, and Yong Ban. Search for higgs boson pair production in the b b^{-} μ+ μ- final state at the lhc. *Physical Review D*, 107(3):034014, 2023.

[102] Albert M Sirunyan, Armen Tumasyan, Wolfgang Adam, Thomas Bergauer, Marko Dragicevic, Alberto Escalante Del Valle, Rudolf Fruehwirth, Manfred Jeitler, Natascha Krammer, Lukas Lechner, et al. Search for nonresonant higgs boson pair production in final states with two bottom quarks and two photons in proton-proton collisions at $\sqrt{S}$ = 13 tev. *Journal of High Energy Physics*, 2021(3):1–57, 2021.

[103] Tianqi Chen and Carlos Guestrin. Xgboost: A scalable tree boosting system. In *Proceedings of the 22nd acm sigkdd international conference on knowledge discovery and data mining*, pages 785–794, 2016.

[104] Albert M Sirunyan, Armen Tumasyan, Wolfgang Adam, Federico Ambrogi, Thomas Bergauer, Marko Dragicevic, Janos Erö, A Escalante Del Valle, Martin Flechl, Rudolf Fruehwirth, et al. A measurement of the higgs boson mass in the diphoton decay channel. *Physics Letters B*, 805:135425, 2020.

[105] Projected sensitivity of Higgs boson pair production combining the $b\bar{b}\gamma\gamma$ and $b\bar{b}\tau^{+}\tau^{-}$ final states with the ATLAS detector at the HL-LHC. 2022.

[106] J Butler, D Contardo, M Klute, J Mans, L Silvestris, CMS collaboration, et al. Technical proposal for the phase-ii upgrade of the cms detector. *CERN-LHCC-2015–010*, 2015.

[107] J Butler, M Klute, L Silvestris, J Mans, D Contardo, et al. Cms phase ii upgrade scope document. Technical report, 2015.

[108] Malte Backhaus. The upgrade of the cms inner tracker for hl-lhc. *Journal of Instrumentation*, 14(10):C10017, 2019.

[109] Matteo Bonanomi. The cms endcap calorimeters upgrade for the hl-lhc. In *Response of the High Granularity Calorimeter HGCAL and Characterisation of the Higgs Boson: With the CMS Experiment at the LHC*, pages 65–118. Springer, 2023.

[110] Charlotte Cooke. Upgrade of the cms barrel electromagnetic calorimeter for the high luminosity lhc. *Instruments*, 6(3):29, 2022.

[111] Thomas Hebbeker and Andrey Korytov. The Phase-2 Upgrade of the CMS Muon Detectors. 9 2017.

[112] Joel N. Butler and Tommaso Tabarelli de Fatis. A MIP Timing Detector for the CMS Phase-2 Upgrade. 2019.

[113] The CMS muon project: Technical Design Report. 1997.

[114] CMS Technical Design Report for the Level-1 Trigger Upgrade. 6 2013.

[115] Piet Verwilligen et al. Gem detectors for the cms endcap muon system: status of three new detector stations. *Journal of Instrumentation*, 18(07):C07006, 2023.

[116] Fabio Sauli. Gem: A new concept for electron amplification in gas detectors. *Nuclear Instruments and Methods in Physics Research Section A: Accelerators, Spectrometers, Detectors and Associated Equipment*, 386(2-3):531–534, 1997.

[117] CMS GEM Collaboration et al. Cms-tdr-013. Technical report, CERN-LHCC-2015-012, 2015.

[118] Duccio Abbaneo, M Abbas, M Abbrescia, AA Abdelalim, M Abi Akl, W Ahmed, P Altieri, R Aly, C Armaingaud, C Asawatangtrakuldee, et al. Quality control and beam test of gem detectors for future upgrades of the cms muon high rate region at the lhc. *Journal of Instrumentation*, 10(03):C03039, 2015.

[119] Branislav Sitar, Gabriel I Merson, Valery A Chechin, Yury A Budagov, GB Pontecorvo, Gerhard Höhler, and Ernst A Niekisch. Physical processes in gas ionization detectors. *Ionization Measurements in High Energy Physics*, pages 61–105, 1993.

[120] D Mörmann, Amos Breskin, Rachel Chechik, and D Bloch. Evaluation and reduction of ion back-flow in multi-gem detectors. *Nuclear Instruments and Methods in Physics Research Section A: Accelerators, Spectrometers, Detectors and Associated Equipment*, 516(2-3):315–326, 2004.

[121] Addendum to the Technical Design Report for the Upgrade of the ALICE Time Projection Chamber. 2 2015.

[122] Heinz Raether. Electron avalanches and breakdown in gases. *(No Title)*, 1964.

[123] S Bachmann et al. Discharge mechanisms and prevention in the gas electron multiplier. *Nucl. Instr. and Meth*, 2000.

[124] Senta V Greene, Julia Velkovska, Brandon Blankenship, Michael Z Reynolds, and Sourav Tarafdar. Effective gain and ion back flow study of triple and quadruple gem detector. *Journal of Instrumentation*, 17(12):T12004, 2022.

[125] et al. Rob Veenhof. Garfield++, 2024. Accessed on Date (January 18, 2024).

[126] Yue Wang, Licheng Zhang, Aera Jung, Dayong Wang, and Yong Ban. Simulation study of the performance of quadruple-gem detectors. *Radiation Detection Technology and Methods*, 7(1):107–116, 2023.

[127] R Farinelli, M Alexeev, A Amoroso, S Bagnasco, R Baldini Ferrioli, I Balossino, M Bertani, D Bettoni, A Bortone, F Bianchi, et al. A fast and parametric digitization for triple-gem detectors. In *Journal of Physics: Conference Series*, volume 1525, page 012113. IOP Publishing, 2020.

[128] Jason Rosa. *submitter: Characterizing the VFAT3 chip for the DAQ electronics of the CMS detector*. PhD thesis, Brussels U., IIHE, 2017.

[129] Rajendra Nath Patra. *Development of GEM Detectors for the ALICE TPC Upgrade and Study of Particle Production at LHC Energies*. PhD thesis, HBNI, Mumbai, 2019.

[130] Rajendra Nath Patra, Rama Narayan Singaraju, Saikat Biswas, Yogendra P Viyogi, and Tapan K Nayak. Characteristic study of a quadruple gem detector and its comparison with a triple gem detector. *Nuclear Instruments and Methods in Physics Research Section A: Accelerators, Spectrometers, Detectors and Associated Equipment*, 906:37–42, 2018.

[131] D Abbaneo, M Abbrescia, C Armagnaud, P Aspell, MG Bagliesi, Y Ban, S Bally, L Benussi, U Berzano, S Bianco, et al. Test beam results of the ge1/1 prototype for a future upgrade of the cms high-η muon system. In *2011 IEEE Nuclear Science Symposium Conference Record*, pages 1806–1810. IEEE, 2011.

[132] TJ Paulus. Timing electronics and fast timing methods with scintillation detectors. *IEEE Transactions on Nuclear Science*, 32(3):1242–1249, 1985.

[133] Yasser Assran and Archana Sharma. Transport properties of operational gas mixtures used at lhc. *arXiv preprint arXiv:1110.6761*, 2011.

[134] G Bencivenni, G Felici, F Murtas, P Valente, W Bonivento, A Cardini, A Lai, D Pinci, B Saitta, and C Bosio. A triple gem detector with pad readout for high rate charged particle triggering. *Nuclear Instruments and Methods in Physics Research Section A: Accelerators, Spectrometers, Detectors and Associated Equipment*, 488(3):493–502, 2002.

[135] Thierry Maerschalk. Study of triple-gem detector for the upgrade of the cms muon spectrometer at lhc. 2016.

[136] Shaokun He, Qianming Huang, Hao Qiao, Dayong Wang, and Yong Ban. Simulation study of the performance of new micropattern gaseous detectors. *Radiation Detection Technology and Methods*, 2:1–7, 2018.

[137] S Bachmann, Andrea Bressan, Leszek Ropelewski, Fabio Sauli, A Sharma, and D Mörmann. Charge amplification and transfer processes in the gas electron multiplier. *Nuclear Instruments and Methods in Physics Research Section A: Accelerators, Spectrometers, Detectors and Associated Equipment*, 438(2-3):376–408, 1999.

[138] Martin Killenberg, S Lotze, J Mnich, Stefan Roth, R Schulte, B Sobloher, W Struczinski, and M Tonutti. Modelling and measurement of charge transfer in multiple gem structures. *Nuclear Instruments and Methods in Physics Research Section A: Accelerators, Spectrometers, Detectors and Associated Equipment*, 498(1-3):369–383, 2003.

[139] Dengming Xiao. *Gas discharge and gas insulation*. Springer, 2016.

[140] Purba Bhattacharya, Supratik Mukhopadhyay, Nayana Majumdar, and Sudeb Bhattacharya. A comparative numerical study on gem, mhsp and msgc. *Journal of Instrumentation*, 7(09):P09007, 2012.

[141] M Alfonsi, G Croci, S Duarte Pinto, E Rocco, L Ropelewski, F Sauli, R Veenhof, and M Villa. Simulation of the dielectric charging-up effect in a gem detector. *Nuclear Instruments and Methods in Physics Research Section A: Accelerators, Spectrometers, Detectors and Associated Equipment*, 671:6–9, 2012.

[142] Collaboration Cms. A mip timing detector for the cms phase-2 upgrade. Technical report, 2019.

[143] P Elmer, B Hegner, and L Sexton-Kennedy. Experience with the cms event data model. In *Journal of Physics: Conference Series*, volume 219, page 032022. IOP Publishing, 2010.

[144] Daniele Bertolini, Philip Harris, Matthew Low, and Nhan Tran. Pileup per particle identification. *Journal of High Energy Physics*, 2014(10):1–22, 2014.

[145] Andrea Coccaro, David Curtin, HJ Lubatti, Heather Russell, and Jessie Shelton. Data-driven model-independent searches for long-lived particles at the lhc. *Physical Review D*, 94(11):113003, 2016.

[146] R Abbott, A Abreu, F Addesa, M Alhusseini, T Anderson, Y Andreev, A Apresyan, R Arcidiacono, M Arenton, E Auffray, et al. Test beam characterization of sensor prototypes for the cms barrel mip timing detector. *Journal of instrumentation*, 16(07):P07023, 2021.

Publications

CMS Collaboration, *Search for Higgs boson pair production with one associated vector boson in proton-proton collisions at* $\sqrt{s}$ = 13 *TeV*, CMS-PAS-HIG-22-006, **(Submitting to Journal of High Energy Physics.)**

G. Botao, X. Sun, **L. Zhang**, et al, *Search for Higgs boson pair production in the* $b\bar{b}\mu^+\mu^-$ *final state at the LHC*, Phys. Rev. D **107** (2023) no.3, 034014, arXiv:2207.10912

W. Yue, **L. Zhang**, et al, *Simulation study of the performance of quadruple-GEM detectors*, Rad. Det. Tech. and Met. **7** (2023), 107–116

J. Aera, et al, *Simulations of Multi-layer GEM Systems from Single to Quadruple GEMs*, Advanced Radiation Detector and Instrumentation in Nuclear and Particle Physics . RAPID 2021. Springer Proceedings in Physics, Vol.282 (2023)

W. Jialu, **L. Zhang**, et al, *Experimental progress of Higgs and flavor physics at the LHC*, Science China-Physics Mechanics and Astronomy, Vol.53, **10** (2023), 100007

L. Zhang, et al, *Gas-Electron Amplifiers (GEM) in CMS Detector Upgrades*,Modern Physics. Vol.33 **4** (2021), 15-21

W. Siguang, et al, *Simulation of Relativistic Momentum-Energy Relationship in* β *Particle Experiments Using BetaSim*, Physics Experiment, **6** (2020) no.40, 12

Conferences

Nov. 2023, *Search for Di-Higgs production associated with a vector boson in CMS*, **157th LHCC PhD poster session, CERN, Switzerland**

Nov. 2023, *VHH study on CMS detector*, **Chinese LHC Physics Workshop, Shanghai, China**

May. 2021, *Simulation study of Multi-layer GEM Systems*, **CMS China Workshop, Hangzhou, China**

Nov. 2021, *Search for Di-Higgs production associated with a vector boson in CMS*, **Chinese LHC Physics Workshop, Nanjing, China**

Other contributions

2022-present **Reviewer** of Radiation Science and Technology(RST),

2022-present Responsible for data analysis (energy sharing study) and Test Beam shift for CMS Phase-II Timing detector(MTD) upgrade project,

2022-present Responsible for Commissioning of B-tagging High Level Triggers in Run3 Data in CMS BTV Group,

2021-present Serving as a member of the administrative team for the PKU Physics Cluster Server,

2020-2022 Responsible for Training of B-tagging Machine Learning Models for High Level Triggers in Run2 and Phase-2 in CMS BTV Group,

Acknowledgment

汩余若将不及兮，恐年岁之不吾与。求学数载，总是处于盼望时间既快又慢的叠加态，希望时间在阶段转进时快，却又深感自身之不足，吸收太慢。幸而在北大遇到了高能组的老师和同学们，助推我更快成长，也愉悦了我的生活。

班勇教授在生活与学习环节中对我的照顾细致入微，他解决问题不急不躁，总是让人如沐春风。孙小虎老师亦师亦友，在近四年的时间里，在紧张活泼的氛围中，把我领入到科学的世界和研究的生活中。系里的冒亚军，李强，王大勇，周辰老师，时而提纲挈领，时而明察秋毫，无私地将智慧传递给我们。

感谢同窗秦雪龙, 在五年的无话不谈中，我们共同成长，直到寻找吃饭窗口的能力远胜寻找信号窗口的能力。还有李聪乔、钱思天、谢昕海、罗棱尹、张轩豪、邓森、关哲都是同窗好友，和他们交往，激扬文字，在获得快乐的同时还能取长补短。另外感谢师兄蒋楚翘、李致源、肖杰、卢梦、宋昀轩，师姐安莹、王珂等从 2018 年起在生活学术的种种方面给予我无微不至的帮助。还有郭波涛、王锦、耿新月、何宗晟等同学们，希望我们可以一起在未来的物理学习中获得更多的快乐。

特别感谢亲友的无私支持，我的父母始终支持着我的任何决定，让我可以在世界这个巨大的开架阅览室里畅游, 让我的身体和精神都完全自由, 去争取知行合一。我的祖父母 (蒋文族，俞琴)，他们从我学语学步时期一路陪伴着我，塑造着我的人格和世界观。还有李茜茜，柔和了我的性格，增长了生活的智慧。Thank you, Tetiena Yushkevych, for revealing the joy of the life. We continue to delve deeper into the pursuit of happiness in physics and beyond.

I want to express my deepest gratitude to Prof. Tommaso Tabarelli de Fatis. He is such an energetic gentleman, always uplifting our spirits. I constantly feel that both our work and well-being are well taken care of. In the Bicocca CMS group, I also had the pleasure of meeting Dr. Raffaele Gerosa, Dr. Martina Malberdi, Dr. Andrea Benaglia, and Dr. Simone Gennai, as well as Simona Palluoto and Dr. Flavia Cetorelli. They have created a friendly and enjoyable environment. Sono abbastanza sicuro che sia solo questione di tempo prima che lavoriamo insieme o trascorriamo del tempo insieme in futuro. (Forse con me che parlo un Italiano non troppo strano.) I would like to extend my heartfelt thanks to Giulia Liguori. Without her selfless assistance, I was not able to overcome the fear of the new environment and unfamiliar systems.

I also want to express my deepest appreciation to Prof. Christopher Palmer, Yihui Lai (赖

奕辉), Dr. Chayanit Asawatangtrakuldee, Chuyuan Liu and Prof. John Alison, who formed the first HEP analysis team I joined. Working alongside each other, we extended our friendship beyond the boundaries of physics topics. This was the first time I experienced the joy of being part of a large group and collaboration, which inspired me to continue working in this field for a longer time.

北京大学学位论文原创性声明和使用授权说明

原创性声明

本人郑重声明：所呈交的学位论文，是本人在导师的指导下，独立进行研究工作所取得的成果。除文中已经注明引用的内容外，本论文不含任何其他个人或集体已经发表或撰写过的作品或成果。对本文的研究做出重要贡献的个人和集体，均已在文中以明确方式标明。本声明的法律结果由本人承担。

论文作者签名：章立诚 日期：2024年 5月 15日

学位论文使用授权说明

（必须装订在提交学校图书馆的印刷本）

本人完全了解北京大学关于收集、保存、使用学位论文的规定，即：

- 按照学校要求提交学位论文的印刷本和电子版本；
- 学校有权保存学位论文的印刷本和电子版，并提供目录检索与阅览服务，在校园网上提供服务；
- 学校可以采用影印、缩印、数字化或其它复制手段保存论文；
- 因某种特殊原因需要延迟发布学位论文电子版，授权学校□一年/□两年/□三年以后，在校园网上全文发布。

（保密论文在解密后遵守此规定）

论文作者签名：章立诚 导师签名：

日期：2024年 5月 15日

学位论文答辩委员会名单

论文题目	CMS实验上双希格斯粒子寻找与探测器升级			
作　者	章立诚			
专　业	粒子物理与原子核物理			
答辩委员会成员	**姓　名**	**专业技术职称**	**从事专业**	**工作单位**
主席	李强	教授	粒子物理与原子核物理	北京大学
委员	陈明水	研究员	粒子物理与原子核物理	中科院高能物理研究所
	胡震	副教授	粒子物理与原子核物理	清华大学
	王大勇	副教授	粒子物理与原子核物理	北京大学
	周辰	助理教授	粒子物理与原子核物理	北京大学

北京大学博士学位论文答辩委员会决议书

（本表由博士答辩委员会秘书填写，一式两份，一份存学校档案，一份存研究生个人档案）

院、系：物理学院　　专　　业：粒子物理与原子核物理

姓　名：章立诚　　研究方向：高能物理实验

学　号：1901110115　　导师姓名：班勇

学位论文题目： CMS实验上双希格斯粒子寻找与探测器升级

答辩委员会对学位论文和答辩情况的学术评语 **（主要就论文选题意义，创新性成果及学术水平；论文存在的主要不足之处，以及博士生答辩情况等方面）。**

对希格斯粒子自耦合的研究是粒子物理的前沿热门课题，在对撞机实验中寻找并测量双希格斯粒子产生过程是理解希格斯粒子自耦合性质的关键途径。章立诚在其博士论文中研究相关物理过程，选题具有重要科学意义。

该论文分析了CMS实验2016-2018年采集的质心能量为13TeV的数据，通过运用机器学习方法及对物理对象标定、事例分类和信号提取的详细研究提高了分析的灵敏度，首次在CMS实验上寻找了VHH产生过程，在95%置信水平下给出了其产生截面上限，并给出了相关的耦合强度限制。同时探索了boosted HH->bbtautau衰变道。这些工作为深入理解希格斯机制、电弱对称性破缺等提供了重要实验依据。作者还参与了CMS实验端部缪子探测器及快时间探测器的二期升级工作，为探测器在高亮度LHC运行提供了重要基础。

论文写作规范、逻辑清晰、结果可靠、文献引用详实，研究成果获得所在实验合作组的认可，反映出论文作者掌握了粒子物理理论基础和实验方法，具备了独立从事科研工作的能力。

答辩过程中，答辩人表述清楚，回答问题正确。答辩委员会一致通过其论文答辩，认为这是一篇优秀的博士论文，建议授予章立诚理学博士学位。

答辩委员会表决结果：　实到答辩委员：　5　人，

同意博士毕业者　5　人，不同意博士毕业者　0　人，结论为　准予毕业

同意建议授予博士学位者　5　人，不同意建议授予博士学位者　0　人，结论为　建议授予学位

答辩时间：　2024 年 05 月 24 日 14 时

答辩委员会主席（签字）：

委员（签字）：

本表不得折叠、不得跨页

提交终版学位论文承诺书

本人郑重承诺，所呈交的学位论文为最终版学位论文。本人知晓，该版学位论文将用于校学位评定委员会审议学位、国家和北京市学位论文抽检。论文版本呈交错误带来的结果将由本人承担。

论文作者签名：章之城

日期：2024年 6月 10日